Nano TiO$_2$ hydrosols-based photocatalytic self-cleaning cementitious materials

FUNCTIONAL PERFORMANCES AND APPLICATIONS

Zixiao Wang

,

Nano TiO₂ hydrosols-based photocatalytic self-cleaning cementitious materials

FUNCTIONAL PERFORMANCES AND APPLICATIONS

Zixiao Wang

Nano TiO₂ hydrosols-based photocatalytic self-cleaning cementitious materials

FUNCTIONAL PERFORMANCES AND APPLICATIONS

PROEFSCHRIFT

ter verkrijging van de graad van doctor aan de Technische Universiteit Eindhoven,

op gezag van de rector magnificus, prof.dr.ir. S. K. Lenaerts,

voor een commissie aangewezen door het College voor Promoties,

in het openbaar te verdedigen op donderdag 1 mei 2025 om 16:00 uur

door

Zixiao Wang

geboren te Nanyang, China

Dit proefschrift is goedgekeurd door de promotoren en de samenstelling van de promotiecommissie is als volgt:

Voorzitter: prof. dr. ir. T.A.M. Salet

1e Promotor: prof. dr. ir. H.J.H. Brouwers

2e Promotor: dr. Q.L. Yu

Promotiecommissieleden: prof. dr. Z. Li (Macau University of Science and Technology)

                                      prof. dr. H. Justnes (Norwegian University of Science and Technology)

                                      prof. dr. H. Wong (Imperial College London)

                                      prof. dr. J.P. Hofmann (Technical University of Darmstadt)

                                      prof. dr. A.P.H.J. Schenning

Het onderzoek of ontwerp dat in dit proefschrift wordt beschreven is uitgevoerd in overeenstemming met de TU/e Gedragscode Wetenschapsbeoefening.

To my parents, Mr. Kefei Wang and Mrs. Yali Hai

Preface

My learning journey began on 3rd September 2018 in the Building Materials group of the Department of Built Environment at Eindhoven University of Technology (TU/e), in the Netherlands, under the leadership of Prof. H.J.H. (Jos) Brouwers. The China Scholarship Council and the Eindhoven University of Technology support this research. I have many unforgettable memories of the Netherlands over the years. The people I meet here and the latest theories and advanced technologies I learn here will be my precious treasure for the rest of my life.

First of all, I would like to express my sincere appreciation to my promotor and supervisor, Prof. H.J.H. (Jos) Brouwers. Thanks for providing world-class experimental conditions and academic platforms in the field of concrete science and engineering for my research project. In the past few years of working with you, your serene attitude towards life, broad-mindedness, and commitment to seeking truth have subtly yet profoundly influenced my philosophy, values, and worldview, much like the gentle spring breeze and nourishing rain. This doctoral thesis has been going on for too long since its inception. In the past two years, my life has seen an unprecedented crisis and uncertainty, and I once wondered whether I should give up applying for this Ph. D. degree. It is your appraisal support and affirmation that helped me to finish this dissertation. Here again, I would like to extend my sincere thanks and infinite respect to Prof. Brouwers.

In addition, I am grateful to my daily supervisor and co-promotor, Prof. Qingliang Yu. You helped me a lot with the revision of my many manuscripts and provided professional suggestions. You gave me enough freedom and trust to finish my research projects. You always encouraged and inspired me when I was in trouble with my research. I cannot finish this thesis without your help. It has been my pleasure to work with you, and you have taught me how to be a passionate, independent and responsible researcher.

My appreciation to my promotion committee, Prof. Zongjin Li (Macau University of Science and Technology), Prof. Harald Justnes (Norwegian University of Science and Technology), Prof. Hong Wong (Imperial College London), Prof. Albert P.H.J. Schenning (Eindhoven University of Technology), and Prof. Jan Philipp (Hofmann Technical University of Darmstadt) for accepting to be a member. Thank you all for reading and evaluating my work.

Furthermore, the thesis cannot be finished without the efforts and help from my colleagues and friends. I would like to thank the technical staff in the Laboratory of Building Physics and Services. Thanks for the contributions from Ing. J. F. L. Diepens, Ing. A.C.A Delsing, and Mr. H.L.W Smulders and   for the tests and technical support during my research. Their valuable suggestions and inputs for the experimental work in the lab are helpful. Also, I am

Jan. 2025

Zixiao Wang

Summary

Affected by the adhesion of dust and organic matter in the environment, the concrete building facade exposed to the service environment for a long time makes it challenging to maintain the aesthetic quality requirements of the building, which will increase many building maintenance costs. Cementitious materials containing nano photocatalysts can reduce air pollution near buildings and the specks of dirt on buildings' facades. This thesis first focuses on the photocatalytic properties of nano-dispersed TiO_2 hydrosols. Secondly, the dispersion and photocatalytic activity of the nano TiO_2 particles in cement base materials have been investigated. Thirdly, the effects of the formation and degradation of cement hydration products on nano TiO_2 particles' electronic structure have been studied. Fourthly, the photocatalytic self-cleaning mechanisms of nano TiO_2 hydrosols-modified cementitious materials and the self-cleaning performance decay in carbonization and pure water wetting and drying cycles are investigated. Subsequently, cellulose nanofibrils are used to improve the visible-light photocatalytic activity of nano TiO_2 hydrosols. The early age and hardened performances of visible-light photocatalytic concrete with ultra-low dosages of CNF-TiO_2 hydrosols have been studied. Finally, the CNF-TiO_2 hydrosols have been applied to the photocatalytic concrete with designed directional porous channels to improve the NO_x degradation rate and the radiative cooling performance.

In Chapter 2, the existence of electrolytes in an aquatic environment on the photocatalytic performance and coagulation of nano-dispersed TiO_2 hydrosols and the corresponding photocatalytic alteration are investigated by studying cations (Na^+, K^+, Ca^{2+}, Mg^{2+}, and Al^{3+}). The photocatalysis reactions of nano TiO_2 with different dosages of electrolytes are measured by monitoring the degradation of Rhodamine B (RhB) under ultraviolet A (UV-A) irradiation over time. The results showed that the presence of Al^{3+} improved the photocatalytic performance of TiO_2, while the other tested cations impaired the performance. The negative influences of divalent ions on the photocatalytic performance of TiO_2 are more significant than monovalent ions. The TiO_2 hydrosols dispersed stably at the nanoscale at a low concentration of electrolyte (<0.01 mol/L) with a slight change of pH and coagulated into micro sizes at high concentrations of electrolytes (>0.1 mol/L) with larger increase or decrease of pH. The positive effects of Al^{3+} on the photodegradation rate of RhB might relate to the strong hydrolytic action of Al^{3+} in aquatic solutions. The photocatalytic processes of TiO_2 in the presence of all ions followed the Langmuir-Hinshelwood model, and the reaction kinetic constant is increased with the decrease of pH caused by different cations. It suggests a new perspective on the relationship between coagulation and photocatalytic performance of TiO_2 hydrosols in electrolytes with hydrolysable cations, demonstrating that TiO_2 hydrosols may be suitable as photocatalysts in aquatic environments.

In Chapter 3, the self-cleaning performance of photocatalytic cement paste is related to the

dispersion of nano TiO₂ in the hardened matrix. This section aims to study the influences of Portland cement hydration on the self-cleaning behaviours of acidic anatase TiO_2 hydrosols-modified hardened Portland cement paste (HPCP) and the working mechanisms. The presence of TiO_2 hydrosols causes the retardation of hydration at an early age and better self-cleaning performance of HPCP. The additional surface defects of TiO_2 in HPCP are the main reason for self-cleaning performance enhancement. The morphology and the pore size distribution of hydration products also contribute to the enhancement of self-cleaning performance by the surface electron capture effect, supported by the analyses of Confocal Raman Microscopy and Scanning Electron Microscope. A new mechanism is suggested to explain the role of photocatalytic property and cement hydration on the enhancement of self-cleaning performance of HPCP with different concentrations of TiO_2 hydrosols.

In Chapter 4, the photocatalytic self-cleaning performance variations of mortar containing different dosages of nano TiO_2 hydrosols at different carbonization durations are studied. The colourimetric analysis is used to evaluate the self-cleaning performances of carbonated mortar samples. The distribution areas of anatase TiO_2, hydrates, and carbonates in the mortar surface are characterised by the Confocal Raman Microscopy. The data recorded during the 28 days of carbonation show that the self-cleaning performance of mortar surfaces features a recovery phenomenon during carbonation. The correlations between photocatalytic self-cleaning performance and the possible parameters are analysed. A predictive model is suggested to evaluate the influence of carbonation degree on the photocatalytic self-cleaning ability of nano TiO_2 hydrosols-modified mortar.

In Chapter 5, the evolution of the photocatalytic self-cleaning performance of nano TiO_2 hydrosols-modified mortar with different cycles under the action of wetting and drying cycles of pure water has been studied. The wetting and drying cycles of pure water affect the microstructure of cement mortar and the distribution of hydration products, making the self-cleaning capacity of photocatalytic mortar with low nano TiO_2 hydrosols contents fluctuate regularly with the number of cycles. However, it does not reduce its self-cleaning capacity below the expected value. The distribution area of nano TiO_2, cement hydration products, and carbonization products on cement mortar surfaces is correlated with the number of wetting and drying cycles. The wetting and drying cycles cause periodic changes in the exposed areas and particle surface states of nano TiO_2 on the mortar samples' surfaces.

In Chapter 6, bio-based nano TiO_2 photocatalysts with visible light activity are prepared. This chapter investigates the negative influences and potential solutions of pure nano TiO_2 hydrosols with ultra-low dosages to cement paste. Cellulose nanofibrils (CNF) are used to modify the TiO_2 hydrosols to prepare visible-light photocatalysts (CNF-TiO_2 hydrosols). The mass ratios of CNF influence the rheological parameters of paste slurries containing

CNF-TiO$_2$ hydrosols. Compared with the reduction of compressive property caused by adding pure nano TiO$_2$ hydrosols, the compressive strength values of hardened cement paste samples containing CNF-TiO$_2$ hydrosols increase apparently when the CNF to TiO$_2$ ratio is less than 1.5. The presence of CNF-TiO$_2$ hydrosols does not affect the phase patterns of hardened paste but improves the portlandite mass ratios and the porosities of macro pores.

In Chapter 7, the influences of artificial directional microchannels on the compressive strength and the functional performances (NO$_x$ degradation rate and radiative cooling property) of CNF-TiO$_2$ hydrosols-modified cement paste are investigated. The cost-effectiveness of photocatalytic cementitious materials hindered their applications in construction and buildings. This chapter tries to propose a possibility of improving the functional properties of visible-light photocatalysts modified cement paste by using CNF-TiO$_2$ nano-refrigerants and freeze-casting methods. The results show that 0.10 w/w % CNF-TiO$_2$ modified hardened paste prepared via freeze-casting obtains much better compressive properties at both early ages and 28-day-age. Due to the pore structure rearrangement effects by freeze-casting processes optimised by CNF-TiO$_2$ hydrosols, the photocatalytic NO$_x$ degradation rates of hardened cement paste improved more than 1000 times than that of the sample with the same nano-refrigerants prepared via regular casting methods. The CNF-TiO$_2$ hydrosols-modified hardened paste containing directional micro channels with widths of 0.38 to 2.5 μm obtains much better radiative cooling performance and receives less solar energy.

The last chapter collected all the findings of this chapter, and the prospects of future research are drawn.

Contents

Chapter 1 Introduction

1.1 Background and motivations

Sunlight plays a major role in biological processes and environmental balance. Until the early 20th century, the production of energy and materials is obtained directly or indirectly from sunlight. Over the past century, however, the growing prosperity of the population, the continuous creation of new materials, and the increasing use of oil and nuclear energy for energy consumption have led to a widening gap between natural and human societies. Solar energy is rarely considered in modern architectural engineering structures; instead, a large amount of infrastructure is built to resist the negative effects of sunlight. The amount of solar energy that reaches the Earth's surface every year is about 5×10^{24} J, which is 104 times the amount of energy the world consumes each year. In order to make full use of solar energy, architects and designers are reconsidering the use of sunlight in combination with building materials to achieve the purpose of reducing the energy consumption of buildings and reducing pollutants in the environment. In modern civil engineering construction, cementitious materials are still the most widely used and easily available building materials. According to a study of the global cement market by Fortune business insights, the global cement market is expected to grow to an estimated USD 686.41 billion by 2032. Cementitious materials, which are heavily used in buildings, have a large surface area, providing the possibility for efficient use of light energy.

Due to the diversity of building service environments, cement-based materials, especially those exposed to outdoor conditions, are directly and continuously exposed to many atmospheric pollutants. Microorganisms under different weather or climate conditions, such as algae and fungi, will accelerate the deterioration of cementitious materials. In many cases, this can lead to significant changes in the properties of cementitious materials, including a decline in the aesthetic properties of the building, such as a change in the colour of the building facades. The main reason for the change in the surface colour of cementitious materials is the decrease in solar reflectivity, which is mainly caused by atmospheric aerosol pollutants such as nitrogen oxides, carbon-based materials and volatile organic compounds [1,2]. These pollutants are soluble in water (such as rain and water vapour condensation on the surface, etc.) and can penetrate the pores of facade materials such as brick, paint or mortar, causing changes in the appearance of buildings and promoting physical degradation of the outer surface [3–5]. The mineral composite properties of the cementitious material eventually cause severe colour changes in buildings and structures. The environment causes high porosity and roughness, which causes the deposition of coloured organic pollutants or particulate matter, which will partially promote the growth of microorganisms and the attachment of pollutants. To avoid and control the discolouration of cementing materials, common practices widely used in buildings or structures include the use of additives, sealants,

chemical cleaners, paints, regular cleaning, repair and maintenance. However, due to the complexity and variability of the natural environment, the multi-component inherent characteristics of the cementitious material, and the influence of atmospheric pollutants and microorganisms on the cementitious material, these measures cannot completely eliminate the colour change of the cementitious material [6,7]. In addition to the direct costs of these measures, indirect costs related to operational and environmental losses also need to be considered in maintenance costs. The regular cleaning processes of building facades also create other durability problems for cementitious materials, such as crack propagation and aggressive material migration. Therefore, it is important to develop and apply effective, innovative and environmentally friendly gelling materials to solve these problems.

Nano titanium dioxide (TiO_2) photocatalysis technology has been proved to be a potential technology for the efficient degradation of a series of organic and inorganic compounds in different application scenarios, such as volatile organic compounds and some inorganic compounds (such as nitrogen oxides and sulfur dioxide) in busy streets and canyons, highway tunnels and urban environments [8]. In addition, TiO_2 and cementitious materials have some synergistic advantages because the products of photocatalytic reactions attached to building surfaces can be washed away by rain [9]. Therefore, nano TiO_2 can be used to increase the service cycle of cementitious materials, and it can also greatly reduce the concentration of some air pollutants in urban air, especially in closed spaces such as canyons, streets, tunnels, parking lots, heavily polluted open spaces, such as gas stations or refineries. Since the late 1990s, nano TiO_2-based photocatalytic building materials such as tiles, sheets, plastic films, tents and cement have been marketed, especially in Japan, Italy and other countries [10,11].

The photocatalytic oxidation reaction of nano TiO_2 mainly occurs in the areas where particles are in contact with surface pollutants. Therefore, the higher the dispersion and the larger the specific surface area of nanoparticles, the more reactive sites they can provide. That is, the higher the photocatalytic reaction activity, the better the degradation effect of pollutants [12–15]. In the preparation of commonly used powdered nano TiO_2 particles, an important process is to promote the crystallization of TiO_2 through high-temperature calcination, which also brings inherent defects, namely the phenomenon of hard agglomeration between grains [16,17]. As a result, the crystal size of powdered nano-sized TiO_2 particles is nanometer, but the hydration diameter of the aggregate measured in the dispersion medium can generally reach several hundred microns. Due to the agglomeration of nano TiO_2 particles, the specific surface area of the aggregate decreases significantly compared with the initial grain. In addition, the surface charge type and dispersion stability of nano TiO_2 aggregates in aqueous dispersions are greatly affected by the pH of the medium, types and concentrations of ions.

In the highly alkaline environment of the porous solution of cementitious materials, there are rich cations, such as sodium, potassium, calcium, magnesium, aluminium, and rich anions, such as hydroxide and silicate. [18,19]. The ionic environment in the pore solution is usually

not conducive to the dispersion of nano TiO_2 particles, which will cause a serious agglomeration phenomenon. This greatly affects its photocatalytic activity and weakens its self-cleaning effect on cementitious materials. Therefore, in the existing studies, the recommended dosage of powdered nano TiO_2 particles in cementitious materials is about 3- 5 w/w % of cement mass [20–22]. At such a high dosage, cementitious materials can show an ideal effect of photocatalytic degradation of NO_x and other pollutants in the air. Therefore, improving the dispersion stability of nano TiO_2 particles in cementitious materials and reducing the agglomeration in the processes of preparation and redispersion are one of the urgent problems to improve the photocatalytic degradation performances of photocatalytic cementitious materials and promote the production and application of photocatalytic cementitious materials.

In addition, during the entire service process, under the coupling effect of service time, CO_2 and rain wetting and drying cycles, the main components of cementitious materials, such as cement hydration products, will inevitably carbonize and durability declination. The main effect of photocatalytic oxidation of cementitious materials modified by nano TiO_2 on pollutant degradation is produced by the doped nano TiO_2 particles. Changes in the composition of cementitious materials will inevitably lead to changes in the molar volume of hydration products, which is likely to affect the interface between hydration products and nano TiO_2 particles, affect the effective reaction area between nano TiO_2 particles and pollutants and further affect the photocatalytic degradation of pollutants in cementitious materials. Exploring the relationship and influence between the phase change of cementitious materials and their photocatalytic self-cleaning performance and studying the long-term stability and decay rules of the photocatalytic self-cleaning performance of nano TiO_2 modified cementitious materials can lay a theoretical foundation for the promotion and application of nano TiO_2 modified cementitious materials.

In addition, the self-cleaning mechanism of photocatalytic cementitious materials modified by nano TiO_2 in the existing literature has not been uniformly explained. Due to the different forms of pollutants, the reaction between pollutants and photocatalytic cementitious materials is classified as heterogeneous catalysts, such as liquid pollutants and cementitious materials solid-liquid surface contact, gaseous pollutants, solid pollutants and cementitious materials gas-solid surface contact. Cementitious materials are mostly porous materials with rough surfaces, and solid pollutants in the service environment are easy to adhere to the surface of the substrate. Therefore, an in-depth study of the self-cleaning mechanisms of photocatalytic cementitious materials modified by nano TiO_2, especially the photodegradation mechanism of solid pollutants attached to the surface of cementitious materials, can help us further understand what roles cementitious materials play in the processes of photocatalytic degradation of pollutants.

1.2   Scope and objective

This thesis aims to study the photocatalytic self-cleaning effects of nano-dispersed TiO_2 hydrosols in cementitious materials, study the self-cleaning effects of cementitious materials modified by TiO_2 hydrosols in the simulated actual service environment such as carbonization, wetting and drying cycles, and deeply explore the self-cleaning mechanisms of cementitious materials. The influences and functions of cement hydration products and their evolution products in the photocatalytic reaction processes are clarified. The key problems to be solved in this thesis are as follows:

1. How to further realize the uniform dispersion and high photocatalytic activity of nano TiO_2 in cementitious materials by improving the water dispersion stability of nano TiO_2 and reducing the aggregation of primary nanoparticles?

2. What are the effects of the generation and degradation of cement hydration products on the photocatalytic degradation of solid pollutants of cementitious materials modified by nano TiO_2 hydrosols?

3. What is the formation mechanism of the photocatalytic self-cleaning effects of cementitious materials modified by nano TiO_2, and what are the roles of hydration products in the photochemical reaction processes?

4. Are there any cost-effective ways for cementitious materials to obtain better photocatalytic degradation of air pollution by using very low dosages of nano TiO_2-based hydrosols?

1.3   Outline of the thesis

According to the above main research contents, the following paragraphs briefly introduce the thesis chapters:

In Chapter 1, the motivation and background, as well as the scope and objective of the research topic in this thesis, are discussed.

In Chapter 2, the photocatalytic performances and dispersion stability of commercial nano TiO_2 hydrosols in different cationic electrolyte solutions are introduced. The correlations between photocatalytic performance and stability of TiO_2 hydrosols in five different cationic solutions are studied.

In Chapter 3, the effects of Portland cement hydration on the self-cleaning performances of acidic anatase TiO_2 hydrosols-modified hardened cement paste are studied.

In Chapter 4, the effects of crystal phase changes of cement hydration products with different carbonization degrees on photoactivity and self-cleaning properties of Portland cement mortar modified by nano TiO_2 hydrosols are studied.

In Chapter 5, the evolution processes of photoactivity and self-cleaning effect of Portland cement mortar modified by nano TiO_2 hydrosols under the action of wetting and drying cycles of pure water are studied.

In Chapter 6, bio-based modified nano TiO_2 photocatalysts with visible light activity are prepared. This chapter investigates the negative influences and potential solutions of pure nano-dispersed TiO_2 hydrosols with ultra-low dosages to cement paste.

In Chapter 7, the influences of artificial directional microchannels on the compressive strength and the functional performances (NO_x degradation rate and radiative cooling property) of CNF-TiO_2 modified cement paste are investigated. The possibility of a strategy for improving the functional properties of modified visible-light photocatalysts is suggested.

In Chapter 8, the main conclusions, innovations of this chapter and recommendations for future research are drawn.

Chapter 2   Photocatalytic properties of nano TiO₂ particles with different surface conditions

The existence of electrolytes in aquatic environment on the photocatalytic performance and coagulation of nano-dispersed TiO_2 hydrosols and the corresponding photocatalytic alteration are investigated by studying cations (Na^+, K^+, Ca^{2+}, Mg^{2+}, and Al^{3+}). The photocatalysis reactions of nano TiO_2 with different dosages of electrolytes are measured by monitoring the degradation of Rhodamine B (RhB) under ultraviolet A (UV-A) irradiation over time. The results showed that the presence of Al^{3+} improved the photocatalytic performance of TiO_2, while the performance is impaired by the other tested cations. The negative influences of divalent ions on the photocatalytic performance of TiO_2 are more significant than monovalent ions. The TiO_2 sol dispersed stable at nano scale at low concentration of electrolyte (<0.01 mol/L) with slight change of pH, and coagulated into micro sizes at high concentration of electrolytes (>0.1 mol/L) with larger increase or decrease of pH. The positive effects of Al^{3+} on the photodegradation rate of RhB might relate to the strong hydrolytic action of Al^{3+} in aquatic solutions. The photocatalytic processes of TiO_2 in the presence of all ions followed the Langmuir-Hinshelwood model, and the reaction kinetic constant is increased with the decrease of pH caused by different cations. These results suggested a new perspective on the relationship between coagulation and photocatalytic performance of TiO_2 hydrosols in electrolytes with hydrolysable cations, which demonstrated that TiO_2 hydrosols may be suitable as photocatalysts in aquatic environments.

2.1   Introduction

The photocatalytic reaction is one of the most widely studied topics in the fine chemical industry, building materials, water and air treatment, sanitation, environmental protection, automobile industry, etc [23–30]. Among the photocatalysts, titanium dioxide (TiO_2) particles have received the greatest attention. The multi-faceted functional properties of TiO_2, such as its chemical and thermal stability and strong mechanical properties have promoted its wide application in various fields like water treatment, air purification, etc. [31]. Nano-dispersed TiO_2 hydrosols are known to contain mainly anatase nanoparticles and are aggregation-stable even at high concentrations of dispersed phase and electrolytes mainly refer to strong acid solutions, which means the surface charge of nano-dispersed TiO_2 hydrosols particles is normally positive [32–37]. In the field of photocatalytic degradation of organic pollutants, hydrosols catalysts can be easily separated, collected and re-dispersed for continuous reuse because of its sensitivity to pH value and electrolyte strength of medium [32–35,38,39]. Moreover, some research results show nano-dispersed TiO_2 hydrosols exhibit high photo-chemical reactivity even superior to nano TiO_2 powders [40,41].

However, agglomeration and coagulation are the main physicochemical processes affecting the photocatalytic performance of nano-dispersed TiO_2 hydrosols or nanopowders [42]. The cations like Fe^{3+} [43] would improve the efficiency of photocatalytic oxidation of TiO_2 hydrosols in solutions by influencing the complex hydroxyl groups bond between TiO_2 surface and Fe^{3+}. Volkova et al. [44,45] had studied the coagulation properties and fractionation of TiO_2 hydrosols in haloid salts solutions, and the results supported that the sol stability is strongly affected by the coion (refers to cation) nature and valence.

Compared with nano-dispersed TiO_2 hydrosols, the stability of nano TiO_2 powders influenced by inorganic cations in aquatic environments [46–51] has been studied relatively comprehensive. Common cations such as Na^+ [52], Ca^{2+} [52,53] and Mg^{2+} [54] are found to enhance agglomeration and sedimentation of nano TiO_2 particles by absorbing on the surface of particles surfaces, and the enhancement of divalent cations are greater because of the higher negative charge. For nano TiO_2 powders, aluminium salts, like $Al_2(SO_4)_3$, Al_2O_3, are usually used as the coagulants to remove the particles during the primary water treatment [55,56]. Some heavy cations, like Cu^{2+} [57,58], Pb^{2+} [57–59], Fe^{3+} [58], Mn^{2+} [57,58] and Zn^{2+} [57,58], can absorb on the surface of nano TiO_2 powders in aquatic solutions, because of the deprotonated surface hydroxyls yield negatively-charged surface of nano TiO_2 powders. Due to the increasing application of TiO_2 catalyst for obtaining functional cementitious materials, the influences of Portland cement-like ionic environment on the surface chemical of nano TiO_2 powders had been studied in some researches [18,19].

Since the synthesis processes of nano-dispersed TiO_2 hydrosols and nano TiO_2 powders are

different, their phase, disperse composition and condition are totally different [33]. For example, heat treatment is a requirement for synthesizing crystallized nano TiO_2 powders by sol-gel method, which causes the irreversible aggregation of particles. Namely, it is difficult to obtain nano-dispersed systems by re-dispersing nano TiO_2 powders because of the initial aggregation of particles. Moreover, the particles surfaces in nano-dispersed TiO_2 hydrosols are normally positive, while the particle surfaces in nano TiO_2 powders aqueous suspensions are normally negative. Thus, the interaction mechanism between the cations and TiO_2 particles studied in literature via nano TiO_2 powders can hardly explain the influence of cations to TiO_2 particles in nano-dispersed hydrosols systems. In addition, few studies focus on the photochemical reactivity of nano-dispersed TiO_2 hydrosols in aqueous solutions contaminated by cations with different valence. According to literature [44,45,60], the effect of certain cations on the coagulation of TiO_2 hydrosols particles is very pronounced, and the effect is closely related to the valance of cations and the pH of the aquatic systems.

The goal of this chapter is to investigate the probable relationship between photocatalytic properties and stability of TiO_2 hydrosols with different kinds of inorganic cations. Ghenne et al. [32] reported that in acidic media, the critical coagulation concentration of anions of NO_3^- and Cl^- is nearly 0.5 mol/L at pH = 2, and the critical coagulation concentration of anions decreased with the increase of pH values. Budarz et al. [61] showed that the adverse impacts of NO_3^- on the photocatalytic property of nano TiO_2 are less than that of Cl^- in aqueous solutions. Therefore, in this chapter, the aqueous solutions of Na^+, K^+, Ca^{2+}, Mg^{2+} and Al^{3+} with a concentration of 0.005 to 0.5 mol/L are chosen as the tested cations, and NO_3^- is selected as the anion in this chapter. The photocatalytic activity of nano-dispersed TiO_2 hydrosols is assessed by the photodegradation performance on Rhodamine B (RhB). The stability of particles in hydrosols over time is evaluated by the particle size and zeta potential values.

2.2   Materials and methods

2.2.1   Reagents and solutions

$NaNO_3$, KNO_3, $Ca(NO_3)_2$, $Mg(NO_3)_2$ and $Al(NO_3)_3$ and RhB are analytical pure commercial regents and applied without further purification. Solutions of salts (0.005, 0.1, and 0.5 mol/L) are prepared with deionized (DI) water. A 30 mg/L RhB solution is prepared as the target pollutant in the test. The solid content of the commercial nano anatase TiO_2 is 10 % in the hydrosols, the pH is 1.17 at 20 °C and the mean particle size is 30.3 nm. In order to purify the TiO_2 hydrosols, the commercial TiO_2 hydrosols are filtrated by an ultrafiltration system for ten cycles, and the 80 mm 100 kDa ultrafiltration membranes are used to remove the impurities. After purification, the pH of hydrosols is 2.32 at 20 °C and the mean particle size is 37 nm. The detailed method of TiO_2 purification can be found in supporting information.

2.2.2   Degradation experiments

The photocatalytic performance of TiO_2 is evaluated by examining the degradation of 50 mL solution with the initial RhB concentration of 30 mg/L under ultraviolet (UV) illumination. A 400 W ultraviolet metal halogen lamp (UV-400, Shanghai Libi Company of Vacuum Technique, China) is used as the source of the UV irradiation light. The UV lamp is placed outside the reactor and the distance between the lamp and the reactor is 10 cm, the wavelength (λ) of the ultraviolet lamp ranges from 253.7 to 600 nm (centered at λ = 365 nm). The intensity of the UV light is 34.9 mW/cm². The 2 g/L TiO_2 and 30 mg/L RhB solution are put into the reactor and mixed with a magnetic stirrer at 400 r/min during the test. The UV lamp is turned on after the 30 min adsorption-desorption equilibrium at dark. The UV light and the reactor are both inside the intelligent artificial climate box (PRX-350C, Saifu Experimental Apparatus Technology Company, China), by which the test temperature is controlled at 25 ± 2 ℃. A 4.5 mL aliquot is sampled every five mins. The liquid sample is centrifuged for 5 min at 10,000 r/min and then filtered through a nylon syringe membrane filter with pore size of 0.45 µm (BS-QT-014, Biosharp, Japan) prior to analysis. Variations in the concentration of RhB in each degraded solution are monitored by UV-visible spectroscopy (UV-Vis) (UV-2600 spectrophotometer, Shimadzu, Japan). There are two different photodegradation processes of RhB, photobleaching and N-deethylation. With the increased radiation time, the N-deethylation of RhB causes the blue shift in the maximum absorption of the dye solution, and then absorption peak disappears rapidly after the N-deethylation[62]. The photocatalytic oxidation rate of TiO_2 can be represented by the absorption of RhB at 554 nm, and can be calculated by the following formula [63]:

$$R = \frac{C_0 - C_t}{C_0} \times 100\% \tag{2.1}$$

where, R is the photo-degradation rate of RhB, C_0 (g/L) is the initial absorption of RhB at 554 nm before the illumination, and C_t (g/L) is the absorption of RhB at 554 nm at different illumination time.

2.3   Dispersion stability

Laser particle sizer (Microtrac S3500, Microtrac Inc., USA) is used to measure nano TiO_2 aggregate size. Time-resolved size measurements, reported in terms of median diameter (D50), are taken every 2 min for 30 min. To characterize the dispersion stability of nano TiO_2, zeta potential of the Nanoparticles is measured by electroacoustic zeta potentiometer at each test time point (DT-310, Dispersion Technology Instrument, USA).

2.4 Results and discussions

2.4.1 Effect of cations on the photocatalytic degradation

Fig. 2.1 shows the photo-degradation rate of RhB in all the solutions over time. It can be seen that the degradation rate of pure TiO_2 hydrosols is 86.06 % during the first 15 min, which is higher than that of TiO_2 in monovalent and bivalent cationic solutions. After 20 min illuminating, the photo-degradation rates of RhB in all electrolyte solutions are very close and the rate values are higher than 95 %. The photo-degradation rate of RhB decreased with the increase of monovalent and bivalent cation contents. But in the $Al(NO_3)_3$ solutions, the photo-degradation rate showed different results. The photo-degradation rate of RhB increased with the increase of $Al(NO_3)_3$ contents, and the rate values are higher than that in pure TiO_2 hydrosols after 10 min illumination.
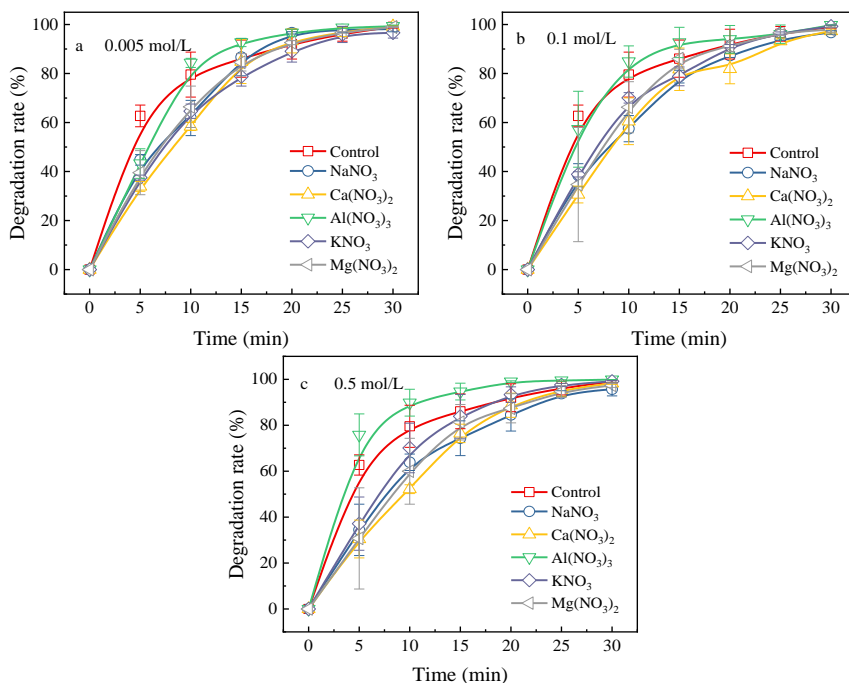

Fig. 2.1 Photodegradation rate of Rhodamine B (RhB) in solution within 30 min at (a) 0.005 mol/L, (b) 0.1 mol/L and (c) 0.5 mol/L cations.
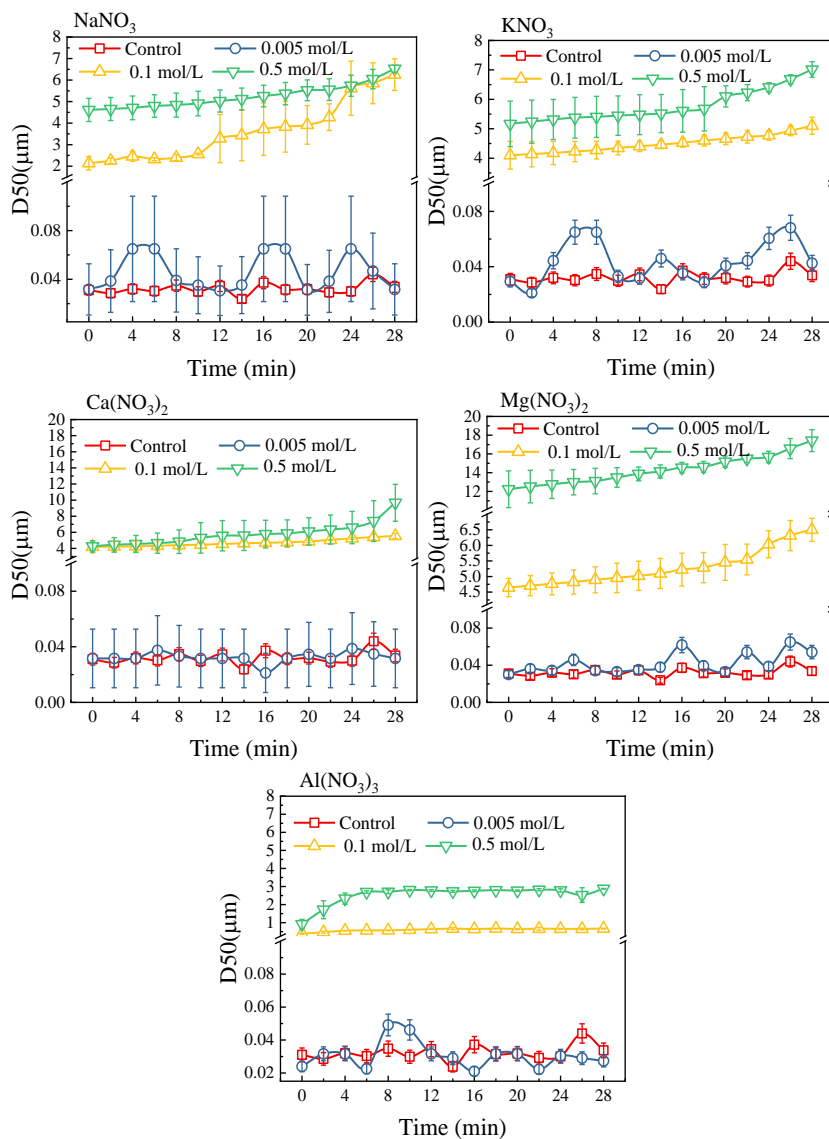
2.4.2 Coagulation of TiO₂ particles

Fig. 2.2 Median diameter (D50) of TiO₂ particles in electrolytes over 30 min in the presence of NaNO₃, KNO₃, Ca(NO₃)₂, Mg(NO₃)₂, and Al(NO₃)₃.

Due to TiO₂ hydrosols consisting of anatase nanoparticles are stable to disperse at high concentration and certain electrolytes and certain pH range, the stability of TiO₂ hydrosols caused by electrolytes has been studied both experimentally and theoretically [33,38,44,45].

In most studies, the optical density increment is chosen as the evaluation index for the stability of TiO_2. Moreover, the photocatalytic oxidation process is related to the production and annihilation of electrons and holes, which are influenced by the particle size of TiO_2 in electrolyte solutions. To represent the stability of TiO_2 hydrosols in electrolytes intuitively, the particle sizes during coagulation process are measured in this chapter.

Significantly, the aggregate sizes of sols in $Al(NO_3)_3$ solution are obviously smaller than that in $Ca(NO_3)_2$ and $Mg(NO_3)_2$ solutions at 0.1 and 0.5 mol/L. In addition, the aggregate sizes in 0.5 mol/L $Al(NO_3)_3$ solution are smaller than 4.0 µm, while the sizes in $Ca(NO_3)_2$ solution are between 4.0 and 11.0 µm and in $Mg(NO_3)_2$ solution are between 12.0 and 18.0 µm.

2.4.3   Zeta potential of TiO_2 and pH in solutions

Zeta potential is a physicochemical parameter of particular importance in describing the ion adsorption and electrostatic interactions between charged particles [39], which reflect the dispersion-agglomeration properties of nanoparticles in aqueous media. Since the pH of solutions significantly affects the stability of TiO_2 hydrosols, monitoring the pH changing of solutions over time is helpful for evaluating the stability of sols.

The zeta potential of nano TiO_2 and the pH changes of electrolytes are shown in Fig. 2.3. It can be seen that the zeta potential of nano TiO_2 in the control group is about 60 mV, and the pH value is about 3.0. When the electrolytes content is 0.005 mol/L, the zeta potential of TiO_2 in $NaNO_3$, KNO_3, $Mg(NO_3)_2$, $Ca(NO_3)_2$ and $Al(NO_3)_3$ solutions decreased to around 30, 41, 27, 37 and 43 mV, respectively. When the salt content is 0.1 mol/L, the zeta potential of TiO_2 in $NaNO_3$, KNO_3, $Mg(NO_3)_2$, $Ca(NO_3)_2$ and $Al(NO_3)_3$ solutions increased by 85.94 %, 35.15 %, 60.17 %, 89.85 % and 0.91 % of the initial value, respectively. When the salt content is 0.5 mol/L, the zeta potentials of that are grown by 180.56 %, 55.63 %, 133.68 %, 38.91 %, and 4.91 % of the initial value, respectively. These results revealed that in the presence of Al^{3+}, the zeta potential of TiO_2 did not change significantly over time, which meant that the interaction between nanoparticles was relatively limited.

It is clear that the pH values of solutions during the 30 min test are stable in each cations contents. As to $Al(NO_3)_3$ solutions, the pH of the solutions decreased with the contents of aluminium ion and the zeta potential of TiO_2 is relatively stable. In the presence of Na^+ and K^+, when the electrolyte contents increased from 0 to 0.5 mol/L. Fig. 2.3a and b shows that the pH values of solutions increased from 3.0 to about 3.6. Fig. 2.3c and d shows that in the presence of Ca^{2+} and Mg^{2+}, the pH values increased from 3.0 to about 3.6 when the metal ion contents increased from 0 to 0.1 mol/L, then the pH values decreased slightly when the metal ions content increased to 0.5 mol/L. As to Al^{3+}, Fig. 2.3e shows that the pH of solutions decreased obviously from about 3.0 to about 2.0, when the electrolyte contents increased from 0 to 0.5 mol/L.
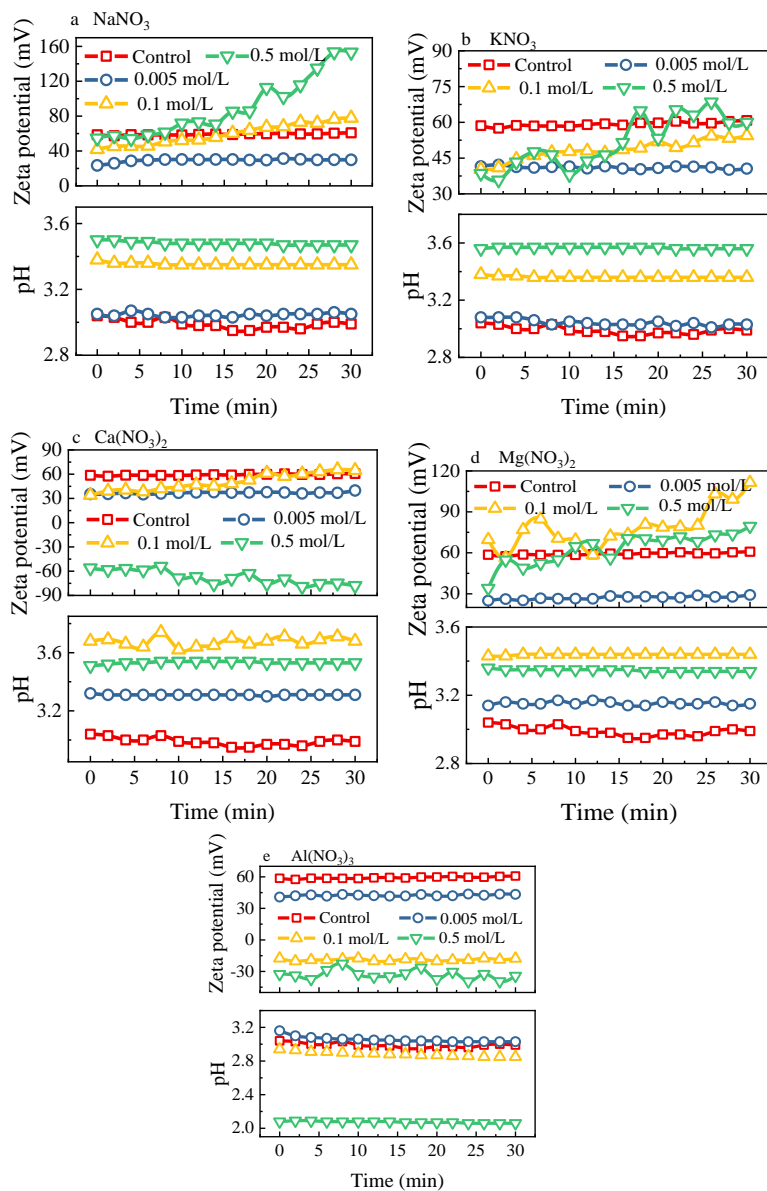
Fig. 2.3 Zeta potential of TiO$_2$ and the pH of solution over 30 min in the presence of (a) NaNO$_3$, (b) KNO$_3$, (c) Ca(NO$_3$)$_2$, (d) Mg(NO$_3$)$_2$, (e) Al(NO$_3$)$_3$.

It is worth mentioning that in the pH range of 2.0 to 4.0, according to the study of Ghenne et al. [32], the critical coagulation concentration of NO$_3^-$ affecting TiO$_2$ hydrosols are less than 0.5 mol/L. However, in the presence of 0.5 mol/L Al(NO$_3$)$_3$, the D50 of TiO$_2$ particles are not larger than those in other electrolyte solutions, and the photo-degradation of RhB is

the highest. As a result, the influence of Al^{3+} on photocatalytic performance and stability in aquatic systems needs further discussion.

2.4.4 Relationship between photocatalysis, coagulation of TiO_2 hydrosols and cations

(1) Explanations in terms of photocatalytic kinetics

According to previous research [64–68], the influence of the initial concentration of the solute on the photocatalytic degradation rate of most organic compounds is described by pseudo-first-order kinetics, which is rationalized in terms of the Langmuir–Hinshelwood model (LH model), modified to accommodate reactions occurring at a solid-liquid interface [69].

Table 2.1 Apparent-first-order reaction rate constants (kapp (min^{-1})) of different cations.

Content (mol/L)	$NaNO_3$	KNO_3	$Ca(NO_3)_2$	$Mg(NO_3)_2$	$Al(NO_3)_3$
0	0.158	0.158	0.158	0.158	0.158
0.005	0.142	0.119	0.150	0.150	0.178
0.1	0.116	0.109	0.118	0.133	0.194
0.5	0.107	0.101	0.102	0.125	0.215

Fig. 2.4 shows the reaction rate kinetics in different cationic nitrate solutions. The slope values of the fitting equations are the k_{app} (the apparent first-order rate constant), as shown in Table 2.1. From Fig. 2.4, the LH model fits the experimental data very well ($R^2 > 0.950$). The high R^2 values indicate that the LH model is appropriate for describing the RhB oxidation in cationic nitrate solutions, which means the reaction rate is mainly controlled by the concentration of the reactants rather than the irradiation intensity or time. From Table 2.1, it can be seen that the k_{app} of the control group is 0.158 min^{-1}, and the k_{app} values decreased with the contents of cations except for the aluminium ion. The k_{app} values for sodium and potassium are similar, and the k_{app} values for magnesium at high contents (0.1 and 0.5 mol/L) are higher than that for calcium. Fig. 4.4e shows that the k_{app} values at 0.005, 0.1 and 0.5 mol/L are 0.178, 0.194 and 0.215 min^{-1}, respectively, and indicated a greater reaction rate of the photo-degradation process.

As seen from Table 2.2, the k_{app} reported in the literature showed that the k_{app} for nano TiO_2 powders degradation of RhB is lower than 0.1 min^{-1}, even for some surface-modified nano TiO_2 powders. In this chapter, the k_{app} of TiO_2 hydrosols (10 w/w %) without cations is 0.158 min^{-1}, which is more than ten times higher than the results in the literature mentioned in Table 2.2. The re-dispersion of nano TiO_2 powders in aqueous solution is still a thorny problem. There is no doubt that the nano TiO_2 particles are agglomerated irreversibly during the drying process of producing nano TiO_2 powders. This instinctive agglomeration is one of the main reasons for the low photocatalytic performance of nano TiO_2 powders in

aquatic environments. According to Fig. 2.2, the D50 of TiO_2 in the control group is nearly 35 nm during the irradiation in 30 min, the better dispersity in the aqueous solution of TiO_2 hydrosols tested in this chapter could explain the higher k_{app} and shorter half period of RhB degradation.

Table 2.2 k_{app} for nano TiO_2 powders degradation of RhB in literature.

Catalyst	Solid content (g/L)	Light intensity (W/m²)	k_{app} (min⁻¹)	Half period of RhB degradation (min)	Reference
Nano TiO_2 powder suspension	10	450	0.0658	10.53	Asilturk et al., 2006
Nano TiO_2 powder	2	Not mentioned	0.00793	87.41	Pang and Abdullah, 2012
TiO_2 nanotubes	2	Not mentioned	0.03271	21.19	Pang and Abdullah, 2012
TiO_2 nanotubes + ultrasonic	2	Not mentioned	0.005	138.63	Pang et al., 2011
Nano TiO_2 powder	2	Not mentioned	0.005	138.63	Song et al., 2012
Nano TiO_2 powder	1	3.6×10^5	0.0165	42.01	Priya and Madras, 2006
P25	1	3.6×10^5	0.0114	60.80	Priya and Madras, 2006
Nano TiO_2 coated activated carbon	2.5	1.8×10^4	0.0207	33.49	Zhang et al., 2011
TiO_2 nano-dispersed hydrosols	0.02	349	0.158	4.39	This chapter
TiO_2 nano-dispersed hydrosols + 0.5 mol/L Al^{3+}	0.02	349	0.215	3.22	This chapter

P25: A commercial nano TiO_2 powder, produced by Degussa (Evonik) Company.

According to the test results about D50 of TiO_2 particles and degradation of RhB in this chapter, these explanations can partly interpret the inhibition of Na^+, K^+, Ca^{2+} and Mg^{2+}. Due to the aggregation of TiO_2 particles in the presence of these cations, the photocatalytic activity of TiO_2 is hindered and the degradation of RhB is decreased. However, these explanations cannot explain the acceleration effect of Al^{3+} on the degradation of RhB, because the agglomeration is also measured when the content of Al^{3+} is higher than 0.1 mol/L.
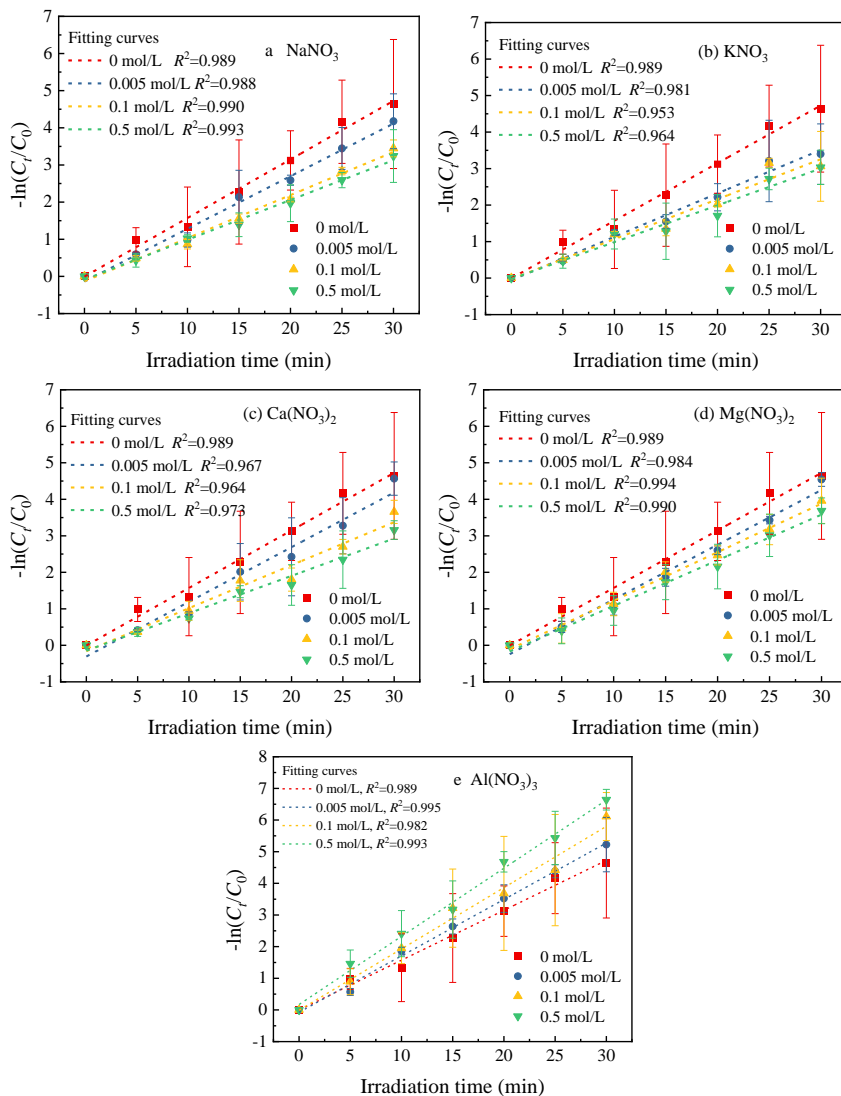
Fig. 2.4 Reaction rate kinetics at different contents in the presence of (a) NaNO₃, (b) KNO₃, (c) Ca(NO₃)₂, (d) Mg(NO₃)₂, and (e) Al(NO₃)₃. R^2: the coefficients of determination; C_0 (g/L) is the initial absorption of RhB at 554 nm before the illumination, and C_t (g/L) is the absorption of RhB at 554 nm at different illumination time.

(2)   Explanations in terms of spectroscopy

As reported in the literature [76], the degradation mechanism of RhB caused by nano TiO₂ is proposed as two ways, one way is de-ethylation process that has been reported in other studies[62,77], another way is the degradation process of the chromophore structure. The changing trend of UV-Vis spectra of RhB in five kinds of electrolyte is similar in the test, to

reduce the space, the groups in Al(NO$_3$)$_3$ solutions are taken as the analysis example. Other spectra images can be found in Appendix I.
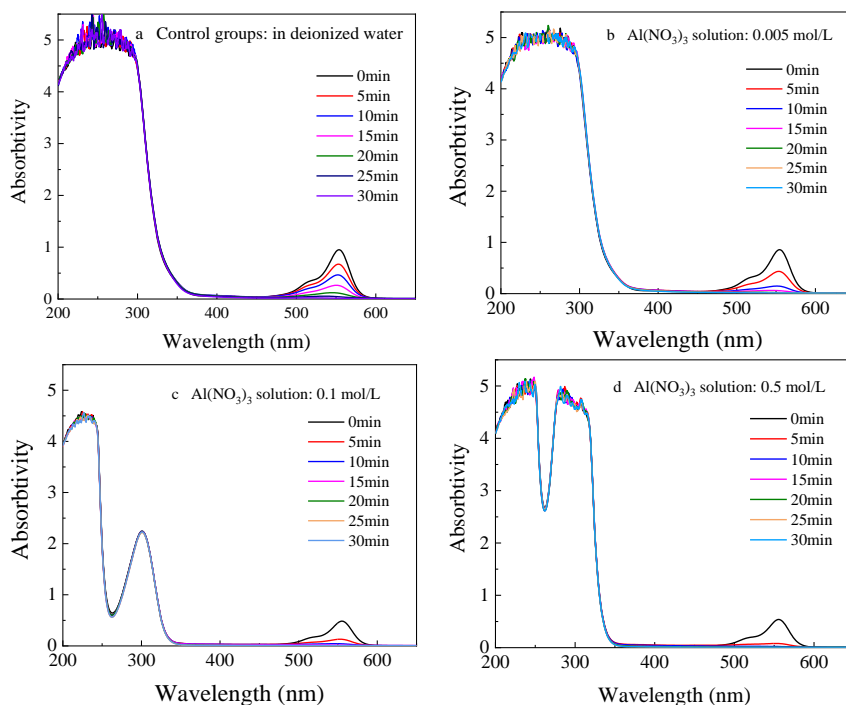
Fig. 2.5 Absorption spectra of RhB with TiO$_2$ hydrosols in Al(NO$_3$)$_3$ solutions in the photocatelytic degradation under ultreviolet (UV) light irradiation (a) without cations (Control groups), in the presence of (b) 0.005 mol/L, (c) 0.1 mol/L, and (d) 0.5 mol/L Al^{3+}.

The UV-Vis absorption spectra of nano TiO$_2$ powder degrading RhB have been studied in several reports (Lei et al., 2012; Wahyuningsih et al., 2014; Wang and Zhang, 2011; Wang et al., 2009; Zhao et al., 1998; Zhu et al., 2014). In these literature, the absorbing peak values at the range of 230-270 nm in the spectra of nano TiO$_2$ powder degrading RhB are smaller than the peak values at 554 nm, and there is only one peak at the range of 200-350 nm. While, in this chapter, Fig. 2.5 shows the UV-Vis spectra of RhB collected during 30 min of irradiation at Al(NO$_3$)$_3$ solutions. De-ethylation of RhB causes a blue shift of the main absorption band at visible light range, as can be seen in Fig. 2.5, the main absorption spectra of RhB decreased rapidly with the blue shift over irradiation time. The main absorption band at 554 nm is due to the chromophore structure, like C = N and C = O, of RhB, and the wide and strong absorption band in 230-270 nm is due to the benzene rings of RhB. The results showed that in the relatively low concentration ($\leq$ 0.01 mol/L) of electrolyte, the absorption peak of RhB is wide in ultraviolet range indicating the typical benzene rings absorption peak

in polar solvent for example water. When the concentration of electrolyte is high ($\geq$ 0.01 mol/L), beside the sharply decrease of absorption at 554 nm and the blue shift, the absorption peak of RhB in ultraviolet range is divided into two peaks near 230 and 290 nm that are the typical absorption peaks of pyrocatechol salts [84]. These phenomenon means the chromophore structure in RhB had been destroyed in electrolyte with high concentration.

The presence of cations and the positive surface of TiO_2 particles might lead to the obvious different results between this chapter and literature mentioned before. As shown in Fig. 2.5, there are still absorbing peaks near 290 nm when the UV light is turned off with high content (> 0.01 mol/L) of the Al^{3+}. RhB is a typical ionic dye [85], in aqueous solution, RhB molecule has both anionic group COO^-, cationic $N(C_2H_5)_2^+$, and Cl^- (one RhB molecule contains one Cl^-). Without the disturbance of impurity cations, RhB molecule may absorb on the surface of TiO_2 particles in hydrosols by COO^- and Cl^- via Coulomb force. However, in the presence of electrolytes with high content (> 0.01 mol/L), the cations may partly break the structure of RhB molecule by combining with COO^-, which lead to the increase of the absorption peak of benzene rings. In the presence of Al^{3+}, the absorption peak of benzene rings is higher than that of other cations because of the greater Coulomb force between Al^{3+} and COO^-. Besides, it is easily understood that there may be competitive absorption between RhB molecules and anion (NO_3^-) on the positive surface of TiO_2 particles of hydrosols, which may inhibit the degradation rate of RhB. Unfortunately, these explanations seem not to be able to explain the enhance effect of Al^{3+} on the process of TiO_2 hydrosols degrading RhB. Therefore, the role of Al^{3+} on the photocatalytic activity of TiO_2 hydrosols needs further discussion, which is presented in Section 2.4.4(4).

(3) Explanations in terms of pH and the dispersion stability of TiO_2

The pH and dissolved ionic solutes play crucial roles in dispersion stability of nano TiO_2 in engineered and natural systems. These parameters can be controlled in laboratory settings, but they may vary spatially and temporally in practice. Spatial heterogeneity of minerals in the subsurface alters the concentration of ionic species present in different systems (e.g., groundwater versus surface water). Variation in aquatic environment pH stems from the same phenomenon [86]. In some specific environment, like concrete pore solution, the high contents of some inorganic ions and high pH may affect the dispersion stability of TiO_2 if adding the nano TiO_2 in the concrete by mixing water. Thus, a better understanding of how pH and dissolved ionic solutes affect the photocatalytic behavior of TiO_2 in the aqueous environment is needed.

In most studies on the dispersion stability of nano TiO_2 powders in aqueous system, due to the pH of tested solutions is controlled by added extra acid and alkaline solution, the influence of inorganic cations on the change of pH is ignored. In this chapter, the change of pH in the tested solutions is mainly caused by adding different amounts of the studied cations. From the results shown in Fig. 2.4 and Table 2.1, the relationship between the pH and the

k_{app} is derived. In addition, the results are shown in Fig. 2.6, it could be seen that the k_{app} is linear with the pH of the solution, and R^2 is 0.954, indicating the very good relativity. The photo-degradation rate decreased with the increase of pH of the solution. Yu et al. (2012) had studied photo-degradation rate of Methylene Blue by TiO_2 hydrosols with different solution pH (adjusted by HNO_3 solution) under sunlight irradiation, and the results showed that hydrosols with pH ranging from 1 to 4 all had high photocatalytic activity toward Methylene Blue, and the photo-degradation rate is higher with lower pH. Although the dispersion stability of nano TiO_2 particles is directly related to the pH of system, the causes of the change of pH need further study, for example the presence of inorganic cations studied in this chapter.

From Fig. 2.2 and 2.3, the variation trend of the zeta potentials of TiO_2 affected by the cations is intuitively similar to the particle size. TiO_2 particles agglomerated significantly over time and the zeta potential also obviously increased with time, which indicated that the nano TiO_2 particles showed dynamic instability with the presence of cations like Na^+, K^+, Ca^{2+} and Mg^{2+} at higher contents (0.1 and 0.5 mol/L). Moreover, TiO_2 particles showed much stable zeta potentials in the presence of Al^{3+} with the same contents, and the TiO_2 particles increased much slower than that in other groups. These results suggested that TiO_2 particles presented better dispersion stability in solutions with the presence of high content of Al^{3+}. According to the literature data [39,88], the isoelectric point of TiO_2 nanoparticles without extra electrolytes are in a pH range of 5.6-6.0. When at a pH near 5.6-6.0, the TiO_2 sols undergo coagulation that results in a relatively low ion-electrostatic repulsion barrier, which cannot terminate particles agglomeration [45]. According to Volkova et al.[44,45], mental ions (Na^+, K^+, Ba^{2+} and La^{3+}) caused the point of zero charge (PZC) shift to the acidic region, and the single charge anions (Cl^-, Br^- and I^-) did not affect the surface charge of anatase TiO_2 and the position in solutions of 1:1 background electrolytes. These may additionally explain the agglomeration of TiO_2 particles in large dosages of nitrates with Na^+, K^+, Ca^{2+}, Mg^{2+} and Al^{3+}. In addition, in literature [44,45], compared with other low valance cations the higher valence of La^{3+} caused the worst agglomeration of TiO_2 sol and the greatest PZC shifting at the presence of 0.1 mol/L La^{3+}. However, in this chapter, Al^{3+}, which is also a cation with high valence, caused little coagulation of TiO_2 hydrosols and enhanced the photocatalytic performance of TiO_2.

According to the above analysis in this section, the negative influence of Na^+, K^+, Ca^{2+}, Mg^{2+} on the photocatalytic performance might be explained by exacerbating the competitive absorption among RhB molecule and anions on the surface of TiO_2. The competitive absorption led to the unstable surface charge of the TiO_2 surface and resulted in the agglomeration and lower photodegradation of RhB. However, the acceleration of Al^{3+} on the photocatalytic performance of TiO_2 cannot be explained by these explanations. In the following section, we are trying to explain the role of Al^{3+} on the photocatalytic activity of TiO_2 hydrosols in degrading RhB.
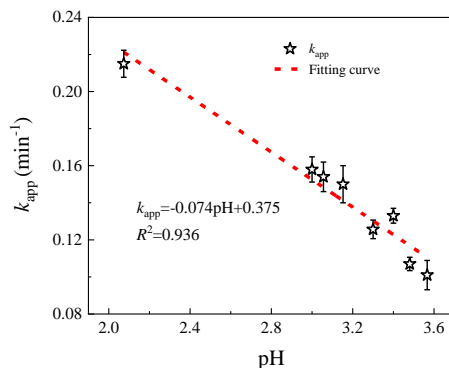
Fig. 2.6 Relationship between apparent-first-order reaction rate constants (k_{app}) and the pH of solutions.

(4) Role of Al^{3+} on the photocatalytic activity of TiO_2 hydrosols

The UV-light induced TiO_2 photocatalytic reaction mechanism is well studied by many researchers [89–93]. Based on the previous analysis, Fig. 2.7 shows the probable degradation process of RhB in the studied system of this chapter. It is clear that H^+ plays a significant role in the photo-oxidation process. The higher concentration of H^+ is favored for accelerating the reduction reaction and hindering the recombination of holes (h^+) and electrons (e^-) of TiO_2 surface inspired by UV light.
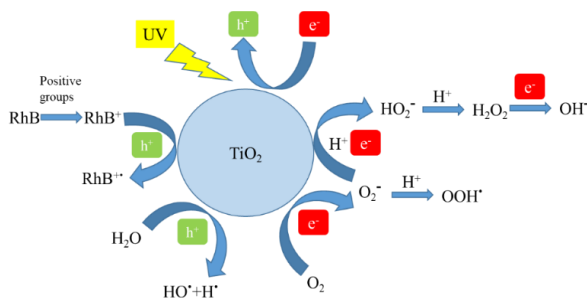
Fig. 2.7 Photocatalytic reactions of TiO_2 for degrading RhB. h^+: holes; e^-: electrons.

In general, the transformations and distributions of Al^{3+} are very complicated in aqueous solution because of the hydrolytic action. The hydrolytic form of Al^{3+} in water can be divided into three types, the monomeric hydroxyl group, the polymeric hydroxyl group, the colloidal polymerization form or amorphous aluminium hydroxide sol. Al^{3+} also show amphoteric characteristics in aquatic systems. In addition, the species distribution of aluminium hydrolysates varies with the pH value of solutions. The hydroxy aluminium complex ions in water tend to polymerize strongly to form dimer, oligomer, and hyper-polymer [94,95]. In the aquatic environment, aluminium is colloidal poly-aluminium hydroxide under the normal pH. The aluminium can convert into soluble hydroxyl polymerized aluminium with the decrease of pH value:

$$p \, Al^{3+} + q \, H_2O \rightarrow Al_p(OH)_q^{(3p-q)+} + q \, H^+ \tag{2.2}$$
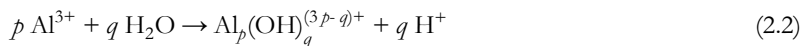
where, p ($1 \leq p \leq 24$) and q ($1 \leq q \leq 60$) are stoichiometric indexes [96]. The hydrolytic polymerization forms of aluminium are a series of metastable states (poly (hydroxo) species) from Al^{3+} to $Al_m(OH)_{3m}$. However, these forms can hardly coexist in the same solution, and the dominant form will vary with the conditions [96].

To distinguish the effects of Al^{3+} and H^+ on the photocatalytic process of TiO_2 hydrosols, the influences of H^+ at different pH values induced by acid are also studied (the detail information can be found in Appendix I and Table 2.3). It can be seen from Table 2.3 that the apparent first-order rate constant k_{app} values in the two groups increased with the decrease of pH value. The k_{app} of TiO_2 hydrosols in the group of pH induced by HNO_3 is smaller than that of pH induced by $Al(NO_3)_3$.

Because of the flocculation effect of the hydrolysates of aluminium, they have a strong adsorption effect on impurities in water [97–99]. The solution pH plays an important role in the hydrolysis process of aluminium [100], i.e. at lower pH (< 6), the amount of monomer aluminium and oligomeric state aluminium increase with the decrease of pH, and the amounts of middle and high polymer state aluminium ions are revised. The monomer aluminium and oligomeric state aluminium could produce cohesive force in sludge flocculation [99], and the formed flocs are larger and looser, so the sludge flocs can re-grow more easily after shearing. In solutions, the attractive force between the impurity particles is reduced by compressing the diffusion layer and reducing the surface potential, the adsorbed positively charged complex ions (for example, RhB^+ of RhB) are interconnected and agglomered when the attractive force gains the upper hand. This flocculation of aluminium probably enhances the surface contact between TiO_2 particles and RhB molecules in solution, which leads to a higher degradation rate and larger k_{app}.

In brief, the existence of TiO_2 hydrosols successfully creates the low pH system in solution. Moreover, according to Eq. (2.2), the hydrolytic action of Al^{3+} produces more H^+ into the solution that leads to a lower pH system, and the agglomeration of TiO_2 hydrosols is relieved because the looser and easy-to-shear floc structures caused by monomer aluminium and oligomeric state aluminium. As mentioned before [70], the high content (1 w/w %) of nano TiO_2 suspension decreased the photodegradation rate of RhB because of the agglomeration and sedimentation of the TiO_2 particles caused by the collision between excited state molecules and ground state molecules. Compared with the results in this chapter, the H^+ produced by Al^{3+} hydrolytic action promotes the photocatalytic actions of nano-dispersed TiO_2 hydrosols notably, which may buffer the collision between TiO_2 molecules in different states. Moreover, the hydroxy aluminium groups have a higher valence that can break the RhB molecule by absorbing COO^-. Hence, the photo-induced degradation rate of RhB increased in the presence of Al^{3+} in TiO_2 hydrosols.

2.5   Summaries

The effects of five inorganic electrolytes in the concentration range of 0.005 to 0.5 mol/L on the photocatalytic degradation rate of RhB solution by TiO_2 hydrosols are investigated. The relationship between photocatalysis coagulation of TiO_2 hydrosols and cations are evaluated. Firstly, the effects of cations on the photocatalytic activity of TiO_2 hydrosols are discussed from the angle of the change of photocatalytic reaction kinetics. Secondly, the influences of cations on the UV-Vis absorption spectra of RhB are discussed from the view of the interaction between ions. Thirdly, the relationships between TiO_2 dispersion stability and the pH of solution caused by cation contents and types are discussed. The enhancement mechanism of Al^{3+} on the photocatalytic performance of TiO_2 hydrosols is studied specially.

The presence of monovalent and bivalent, like Na^+, K^+, Ca^{2+} and Mg^{2+}, inhibited RhB degradation, and the inhibition effect increased with the increased concentration of cations because of exacerbating the competitive absorption among RhB molecules and anions on the surface of TiO_2. Due to the higher valence, the negative effects of Ca^{2+} and Mg^{2+} are greater than that of monovalent. The reaction kinetic constants of the pseudo-first-order reaction kinetics model are linearly inversely proportional to the pH value of solutions with cations, revealing that the photocatalytic performance of TiO_2 hydrosols would be enhanced when containing hydrolysable cations like aluminium. Due to the hydrolytic effect of Al^{3+} in electrolytes, the risk of agglomeration of TiO_2 particles in hydrosols is reduced; the photochemical reactivity of TiO_2 hydrosols is improved, resulting in an enhanced reaction rate. In the presence of 0.5 mol/L Al^{3+}, the apparent first-order rate constant is 0.215 min^{-1}, and the half period of RhB degradation (the time of degrading 50 % RhB) is 3.22 min. The results in this chapter revealed different mechanisms for the coagulation of TiO_2 hydrosols in electrolytes with hydrolysable metal ions. The acidic shift of the point of zero charge caused by electrolytes could be partially offset by the hydrolytic action of Al^{3+} in the examined systems. Therefore, the coagulation of TiO_2 particles could be hammered, and the stability of TiO_2 hydrosols could be improved. These results support the idea that the nano-dispersed TiO_2 hydrosols are suitable for use as photocatalysts in an environment containing Al^{3+}, such as urban sewage and Portland cement-like ionic environment.

Chapter 3 Nano-dispersed TiO₂ hydrosols modified Portland cement paste: The underlying role of hydration on self-cleaning mechanisms

The self-cleaning performance of photocatalytic cement paste is related to the dispersion of nano TiO$_2$ in the hardened matrix. This chapter aims to study the influences of Portland cement hydration on the self-cleaning behaviour of acidic anatase TiO$_2$ hydrosols modified hardened Portland cement paste (HPCP), as well as the working mechanisms. The presence of TiO$_2$ hydrosols results in the retardation of hydration at an early age and better self-cleaning performance of HPCP. The additional surface defects of TiO$_2$ in HPCP are the main reason for self-cleaning performance enhancement. The morphology and the pore size distribution of hydration products also contribute to the enhancement of self-cleaning performance by the surface electron capture effect, which is supported by the analyses of Confocal Raman Microscopy and Scanning Electron Microscope. A new mechanism is suggested to explain the role of photocatalytic property and cement hydration on the enhancement of self-cleaning performance of HPCP with different concentrations of TiO$_2$ hydrosols.

3.1   Introduction

Cementitious materials, especially those exposed to outdoor conditions, are directly and continuously exposed to many pollutants (e.g. organic, inorganic and particulate matter) and microorganisms under different weather. These pollutants can aggravate the deterioration process of concrete structures and cause important changes in the materials properties, like aesthetic and physical properties degradation [1,2]. Nano TiO_2-based photocatalysis has proved to be a promising technology for the efficient degradation of a range of organic compounds (e.g. volatile organic compounds) and inorganic compounds (e.g. NO_x and SO_2), in busy canyon streets [101,102], road tunnels and urban environments [8], etc.

Due to the different synthesis processes, nano-dispersed TiO_2 hydrosols [36,37,40,41,103] and TiO_2 nanopowder [104–107] present different agglomeration morphology and surface charge distribution in aqueous solutions. In general, the TiO_2 particles in hydrosols are positively charged, and the hydrodynamic diameter is less than 100 nm [32–37]. Though the crystal size of TiO_2 particles in nanopowder is on the nanoscale, it is difficult to obtain the nano-dispersed TiO_2 suspension by re-dispersing nanopowders in water [108]. Moreover, the surface charge of nano TiO_2 is influenced by the pH of the system. According to several studies, the isoelectric point of TiO_2 nanopowders [38,39,109,110] and hydrosols [36,60] varies in the pH range of 5-6.8, meaning the positively charged TiO_2 nanoparticles will become negatively charged when the pH is higher than the isoelectric point. As to the strong ionic alkaline system of cementitious materials, the surface charge and agglomeration behaviours of nano TiO_2 should be influenced in theory. In addition, cement hydration involves a collection of coupled chemical processes of dissolution, diffusion, growth, nucleation, complexation and adsorption, each of which occurs at a rate that is determined both by the nature of the process and by the state of the system at that instant [111]. Based on the previous studies [112–116], the nano TiO_2 powders are often understood as accelerating the cement hydration because of the filler effect or nucleation effect. Since the TiO_2 particles are positively charged in hydrosols and negatively charged in water suspensions made of nanopowders, different factors may exist that can influence the hydration process of cement, particularly at an early age. Moreover, due to the inorganic or organic acids being selected as the peptizators in the synthesis process of TiO_2 hydrosols [36], the catalogue of surface banded functional groups might be influenced by the different peptizators, which might also influence the cement hydration process.

The dispersion of nano TiO_2 and the aggregation morphology affected by cement hydration products on the surface of hardened cement paste is the key factor to the self-cleaning performance of the modified cement paste. Many studies [117–122] have investigated photocatalytic and self-cleaning performances, mechanic properties and durability of cementitious materials modified by nano TiO_2 powders in relatively large dosages. Most results reveal that typically 3-5 w/w % of TiO_2 nanopowders (of cement) modified cement-based material

presents satisfying photocatalytic performance, indicating the lower concentration of TiO_2 nanopowders cannot have good photocatalytic performance in cementitious materials. These may be caused by the faster recombination of photo-excited electrons and holes on the surfaces of agglomerated TiO_2 particles [123]. Unlike the TiO_2 nanopowders, TiO_2 hydrosols catalysts can be easily separated, collected and re-dispersed for continuous reuse because of its sensitivity to pH value and electrolyte strength of medium [32–35,38,39]. Some research results show that nano-dispersed TiO_2 hydrosols exhibit high photochemical reactivity, even superior to nano TiO_2 powders in aqueous environment [40,41]. Stable TiO_2 hydrosols have great specific surface areas and high photocatalytic properties, and they have been used to prepare coatings [40,124]. The preparation of cement paste is the reaction between water and cement clinkers, and the TiO_2 hydrosols can be blended into water, like superplasticizers, without agglomeration, which means nano TiO_2 particles via hydrosols may be easily and well dispersed in cement paste matrices.

Some studies [125,126] suggested hypotheses of self-cleaning mechanism concerning TiO_2 nanopowders modified mortar, for example, the chemical composition of cement seems to prevail over the effect of the optical parameters and electronic band structure for mortar made of slag cement; the final microstructure of the material influenced the photocatalytic property of mortar. The research on the self-cleaning performance of TiO_2 hydrosols modified Portland cement paste is also rare, let alone explaining the self-cleaning mechanism of TiO_2 hydrosols in hardened cement paste [127]. Moreover, because of the potential concerns about the negative effects of low pH induced by the TiO_2 hydrosols, few works have studied the effects of the surface charge and surface functional group of nano TiO_2 on the Portland cement hydration process.

This chapter aims to investigate the influences of surface-bonded functional groups of TiO_2 hydrosols on the cement hydration processes and the self-cleaning performance of cement paste modified by nano-dispersed TiO_2 hydrosols in very low dosages, measured at different hydration ages. The possible self-cleaning enhancement mechanisms of TiO_2 hydrosols-modified cement paste are suggested in view of the semiconductor properties of TiO_2 in hardened cement paste and the morphology of cement hydration products.

3.2   Experimental

3.2.1   Materials

(1)   Nano-dispersed TiO$_2$ hydrosols

TiO_2 hydrosols are synthesized based on the precipitation-peptization methods [128] but at the lower temperature (40 °C), because the TiO_2 hydrosols present smaller hydrodynamic particle sizes synthesized at lower temperatures [37]. Titanium tetra-isopropoxide (TTIP,

97.0 %) is purchased from Sigma-Aldrich. Acetic acid glacial (CH_3COOH, 99.6 %) and absolute ethanol (C_2H_5OH, 99.9 %) purchased from VWR Chemicals and deionized water (18.2 MΩ.cm) are used in the preparation process. The physical and chemical parameters of synthesized TiO_2 hydrosols are listed in Table 3.1. To evaluate the crystal type and specific surface area of TiO_2, the TiO_2 xerogel is made by drying hydrosols with unhindered shrinkage at 105 ℃ for 24 hours.

Table 3.1 The physical and chemical parameters of nano TiO_2.

	Hydrodynamic size ± SD (d. nm)	Zeta potential (mV)	Polydispersity Index	Crystal pattern	BET specific surface area (m²/g)	Absorption average pore width(nm)
Hydrosols	18.92±6.358	43.4	0.114	-	-	-
Xerogel	-	-	-	Pure anatase	244.75	5.76

(2)   Sample preparation

CEM I 52.5 R cement and tap water are used to prepare the cement paste. The water-to-cement mass ratio is 0.4. The samples are wet mixed for four minutes before being moulded in 4 cm × 4 cm × 4 cm moulds and covered with a plastic sheet. Different amounts of TiO_2 hydrosols are mixed in mixing water before being added to the cement. The TiO_2 to cement mass ratios are 0 %, 0.01 %, 0.05 % and 0.10 %, respectively. After one day of curing, the samples are demoulded and cured in the climate chamber (RH > 95 %, 20 °C) until the test ages.

3.2.2   Methods

The TiO_2 hydrosols samples are tested three times by a Zetasizer Nano Series (Malvern Panalytical, United Kingdom) applying the dynamic light scattering (DLS) principle. The basic distribution of particle size obtained from a DLS measurement is intensity. The Zetasizer Nano Series calculates the zeta potential by determining the electrophoretic mobility and then applying the Henry equation. The electrophoretic mobility is obtained by performing an electrophoresis experiment on the sample and measuring the velocity of the particles using laser Doppler velocimetry. Prior to the test, the initial hydrosols are diluted in distilled water 100 times.

The calorimetry test is performed using an isothermal calorimeter (TAM Air, TA Instruments, United States) at 20 °C. Cement is firstly mixed with distilled water and TiO_2 hydrosols. Then, the resulting paste is injected into a sealed ampoule. The phase compositions of TiO_2 xerogel and TiO_2 modified cement paste samples are investigated by comparing X-ray diffraction (XRD) patterns (Bruker D4 PHASER, Philips, The Netherlands) with a Co tube (40 kV, 40 mA). A typical run is made with a step size of 0.02°/min and a dwell time of

0.5s.The thermal-gravimetric (TG) analysis is conducted using an STA 449 F1 instrument, and cement paste samples are heated up to 1000 °C from 40 °C at a rate of 10 °C/min with nitrogen as the carrier gas. Before the test, samples at the age of one day, three days, 14 days and 28 days are crushed and immersed in acetone for seven days and then dried in the oven at 40 °C to cease further hydration.

ATR-FTIR is used to analyse the functional groups around the surface of the TiO_2 particles in hydrosols. A Fourier-transform infrared spectroscopy (FTIR) spectrometer (PerkinElmer, United States) equipped with an attenuated total reflectance (ATR) accessory (GladiATR, PIKE technologies, United States) is used here. Liquid samples are dropped evenly onto the surface of the ATR Ge crystal, and the FTIR spectra are recorded from 400 to 4000 cm^{-1} at a resolution of 4 cm^{-1} by 32 scans. For each scanning, the spectrum is collected by subtracting the original spectrum from the air background spectrum. Then, the obtained spectra are baseline-corrected. The reflectance spectra of TiO_2-modified hardened cement paste samples at 28 days are measured by the UV-VIS-NIR spectrophotometer (Perkin Elmer Lambda 750). The tested range is 200 nm to 800 nm, 2 nm per second. To meet the test requirement, the paste samples are cut into slices with a thickness of 1 cm. The distribution of phases at the surface of hardened cement paste at 28 days is observed by Confocal Raman Microscopy (Witec alpha300S, Witec, Ulm, Germany). Raman spectra are recorded over a spectral range from 0 cm^{-1} to 3900 cm^{-1}. Confocal Raman measurements are accomplished using a 532.306 nm excitation laser with a power of 30.159 mW. The scan area is 20 μm × 20 μm, the size of the Raman images is 20 × 20 pixels with the integration time per pixel of 2 s. The collected Raman spectra are analysed by using WITec Suite 5.2 software (Witec, Ulm, Germany). For the results obtained by CRM, cosmic ray removal and background subtraction are performed.

The Brunauer, Emmett and Teller (BET) method, which is the most used method to deduce the internal specific area of pores based on the multi-molecular adsorption assumptions, is used to measure the specific surface area of cement paste containing different dosages of TiO_2 hydrosols. The pore size distribution from the adsorption isotherm is evaluated by the Barrett-Joyner-Halenda (BJH) interpretation. Nitrogen sorption isotherm experiments are carried out at 77 K temperature by a NAD device of type TriStar II 3020 with a nitrogen pressure range of up to 950 mmHg, and the measurement range of the specific surface area is from 0.01 m^2/g, nitrogen unit. The cement paste samples at one day and 28 days are dried at 40 °C and degassed in an external degassing station at 40 °C under N_2 flow for 4 h. In these degassing conditions, the microstructure of early hydration products in the cement pastes is not affected.

The cement paste samples are prepared based on the process described in Section 3.2.1. The paste samples are cut into thin slices at one day and 28 days, and the hydration of the samples for SEM tests is ceased for further hydration. Before the tests, all the samples are sputtered with gold to enhance the electrical conductivity. In order to obtain the microstructure of the

samples with different concentrations of TiO$_2$ hydrosols, micrographs are recorded by using a Quanta 250 FEG scanning electron microscope (ThermoFisher scientific, USA) with a secondary electrons detector at an accelerating voltage of 15 kV.

Rhodamine B(RB) is an organic dye, the chromophoric group of which has the maximum lightweight absorption at about 554 nm [129]. Normally, the RB water solution presents the colour of red to violet red, and the dried RB film on solid materials also presents the same colour. Since the chromophoric group of RB molecules can be destroyed by the photo-degrading process [77,130], the colour change of dried RB film on the surface of hardened cement paste can be used to interpret its degradation. In this chapter, the self-cleaning ability of the TiO$_2$ hydrosols-modified HPCP is evaluated by colourimetric analysis of the degradation of Rhodamine B (RB). Before the tests, the paste top surfaces are polished with SiC sandpapers to obtain a relatively smooth surface with roughness in the range of 10 to 14 micrometres. Each surface area of the paste sample is stained by painting 600 μL of 0.1 mM RB aqueous solution. Then, the samples are kept overnight in the dark at room temperature for drying. For each coated sample, 9 points are tested for the colourimetric tests, and each point is tested 4 times. The samples are exposed to a UV lamp (10 ± 0.05 W/m^2) to simulate UV light in natural conditions, and the discolouration of the stains is monitored. The reflected colour measurements are taken directly on the surface of each point on each sample at different illumination times with a spectrometer (USB4000, Ocean optics, United Kingdom), which is optimized for the 380- 780 nm wavelength range and analysed mathematically to yield colourimetric quantities like xyz, RGB or L*a*b*. In this chapter, the percentage of discolouration (R$_t$) is expressed with the coordinate of the dominant colour of dye a*, the value of the CIE Lab colour space for RB [120,121,131], according to:

$$R_t = \frac{a_0^* - a_t^*}{a_0^*} \times 100 \text{ \%} \tag{3.1}$$

Where, a$_0$* is the value of a* at time 0 before irradiation, a$_t$* is the value after t minutes irradiation.

3.3 Results

3.3.1 Dispersion and surface functional group of TiO$_2$ in hydrosols

Fig. 3.1 presents the ATR-FTIR spectra of the TiO$_2$ hydrosols and xerogel. The measured solid content of TiO$_2$ particles in hydrosols is about 1.54 %, the majority parts in hydrosols are water and acetic acid. As to the red curve in Fig. 3.1, the absorbance peaks are –OH of water and –COO$^-$ and –C–OH of acetic acid, the typical peaks of TiO$_2$ are covered by those strong peaks. So, the spectrum of TiO$_2$ xerogel reflected the functional groups on the nano TiO$_2$ particles much clearer. As to the black curve in Fig. 3.1, the strong C = O peak near 1527 cm^{-1} [132,133] of TiO$_2$ xerogel is assigned to carboxyl groups on the surface of TiO$_2$,

resulting from the acetic acid used in the peptization process [40]. The appearance of vibrations around 1440 cm^{-1} in the fresh xerogel suggests a substantial surface coverage of $-CO_3^{2-}$ resulting from the reaction of carbonation during the drying process [134]. The strong wide peak near 3500- 2800 cm^{-1} is due to the stretching vibration of $-OH$ group, which represented the $-OH$ groups on the surface of TiO_2 [40]. The peaks corresponding to O–O, O–Ti–O and Ti–O–Ti bonds are identified at 912 cm^{-1}, 794 cm^{-1} and 655 cm^{-1} [134,135]. These results indicated that sufficient hydroxyl groups like $-OH$ and $-COOH$ are absorbed on the surface of TiO_2 nanoparticles. It is seen that in TiO_2 hydrosols, the TiO_2 particles are positively charged and surface absorbed by $-OH$ and $-COOH$ via chemisorption, which is negatively charged in suspension by re-dispersing nano TiO_2 powder in solution at neutral or higher pH because of the absorption of O$^-$ and $-OH$ [136,137]. The absorption of $-COOH$ makes the TiO_2 hydrosols different from the suspension made of nano TiO_2 powders. When mixing these TiO_2 hydrosols into cement paste, the hydration process might be influenced by the surface functional groups and charges, which will be discussed in the next section.
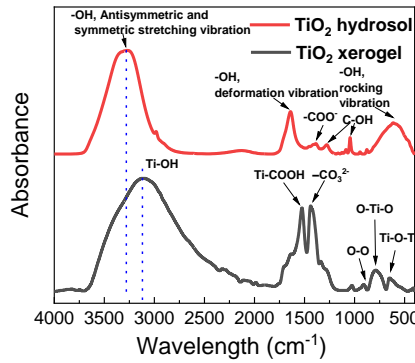
Fig. 3.1 The FTIR absorbance spectra of TiO_2 hydrosols and dried xerogels.

3.3.2　　Effects of TiO_2 hydrosols on cement hydration

(1)　Hydration heat
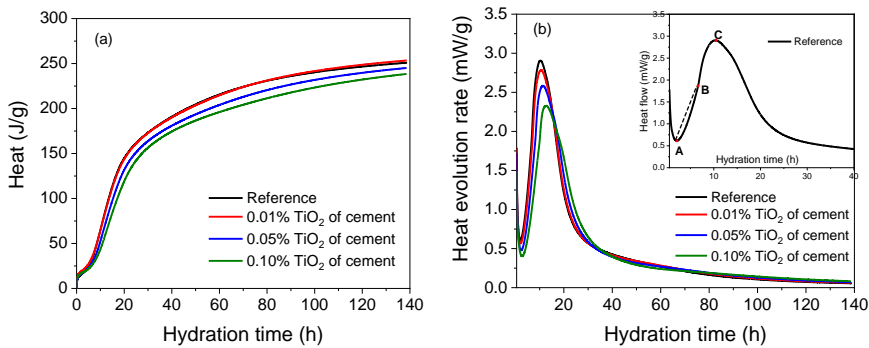
Fig. 3.2 Influence of different concentrations of TiO_2 hydrosols on the exothermic heat flow per mass of binder and total heat of cement paste.

The cumulative heat release and rate of hydration of cement paste containing TiO_2 hydrosols are shown in Fig. 3.2. Fig. 3.2(a) indicates that the total hydration heat remained similar as the TiO_2 dosage is 0.01 % and beyond that dosage the hydration heat decreased with the increase of TiO_2 amount. As can be seen from Fig. 3.2(b), after mixing with TiO_2 hydrosols, the hydration rate decreases and the descent scope is greater as the dosage of TiO_2 increased. Meanwhile, the time of occurrence of heat flow peaks in the blank and TiO_2 modified cement is different, and a delay is observed when TiO_2 hydrosols are used in the cement paste. The retardation of that exothermic peak is greater with the increase content of TiO_2.

To analyse the influences of TiO_2 hydrosols on the hydration kinetics, six parameters are calculated from the heat evolution curves in Fig. 3.2, see the illustration shown in the detailed view of the heat evolution curve of the reference sample in Fig. 3.2(b). The obtained hydration parameters are listed in Table 3.2. The hydration rate in the induction period and the duration of the induction period t_A [138] are related to the diffusion rate of various ions from the mineral phases to the aqueous phase [111,139,140]. The ions diffusion rates are mainly dominated by the contact surface between the mineral grains and water. In Table 3.2, the ending time point of the induction period (t_A) of cement hydration is delayed due to the presence of TiO_2 hydrosols, and the retardation increased with the concentration of TiO_2 hydrosols in cement paste. Adding 0.05 % and 0.10 % TiO_2 hydrosols evidently prolongs the induction period and depresses the hydration rate $(dQ/dt)_A$ in the induction period, implying the decelerated ion diffusion causes by the prominent adsorption of TiO_2 particles on cement surface. The slight influences on the heat evolution parameters of cement hydration are found when 0.01 % TiO_2 hydrosols are added, which is because of the low amount of adsorption functional groups on cement grains surfaces.

Table 3.2 Parameters of cement hydration extracted from the calorimetry curves of the reference cement paste and the cement pastes containing different concentration of TiO_2 hydrosols.

Item	t_A (h)	$(dQ/dt)_A$ (mW/g)	Q_A (J/g)	t_C (h)	$(dQ/dt)_C$ (mW/g)	Q_C (J/g)	K_{A-B} (mW/(g·h))	Q_{A-C} (J/g)
Reference	2.06	0.61	17.19	10.34	2.91	68.56	0.26	51.37
0.01 %	2.12	0.57	19.33	10.52	2.78	69.83	0.24	50.50
0.05 %	2.36	0.48	16.67	11.35	2.58	65.08	0.22	48.42
0.10 %	2.78	0.40	17.94	12.67	2.33	64.80	0.21	46.86

t_A: the ending time point of the induction period.
t_C: the time point of the maximum heat generation rate.
t_B: the inflection point between A and C on the heat evolution curve, refers to the time point of the maximum acceleration rate.
$(dQ/dt)_A$: the heat generation rate during the induction period, the cumulative heat flow at the beginning of the acceleration period Q_A.
$(dQ/dt)_C$: the maximum hydration rate in the acceleration period.
Q_{A-C}: the cumulative heat flow during the acceleration period.
K_{A-B}: The secant slope on the heat evolution curve between A and B, which represents the acceleration rate of hydration rate at the early stage of the acceleration period.

After the induction period, cement hydration steps into the acceleration period with rapid nucleation and growth of hydrates. The hydration rate in the acceleration period is determined by the total amount of hydrate nuclei of C-S-H [140–142]. Thus, K_{A-B} reflects the nucleation rate of C–S–H at the early stage of the acceleration period. In Table 3.2, K_{A-B} and $(dQ/dt)_C$ visibly drop with the concentration of TiO_2 hydrosols, suggesting that TiO_2 depresses the nucleation of hydrates during the acceleration period, which may be ascribed to the absorbance of TiO_2 particles with calcium. As described in Section 3.3.1, the –COOH, –OH and $-CO_3^{2-}$ are observed on the surface of TiO_2 xerogel and TiO_2 particles in hydrosols. The measured zeta potential of TiO_2 hydrosols are positive, indicating the positive charge of functional groups ($-OH_2^+$ [136,137]) played a dominant role on the surface of TiO_2 particles in acidic solution. While in cement pore solution with very high pH, the surface of TiO_2 nanoparticles turns into negative because the solution pH is higher than the isoelectric point (in a pH range of 5.6-6.0 [39,88]). The TiO_2 particles can absorb on the surfaces of positively charged cement grains hinder the exchange of water and ions, and poison nucleation sites.

With the growth of hydration products, a hydrate layer is gradually formed over the surfaces of cement grains, which further hinders the exchange of water and the ions and then advances to the deceleration period of cement hydration (diffusion-controlled reaction) at time point t_C. The maximum hydration rate is mainly determined by the number of nuclei formed during the periods A to C. The lower hydration peak is related to fewer nuclei existing during A to C. Thus, from the lower hydration peak $(dQ/dt)_C$, it can be deducted that the total nuclei number is reduced when more TiO_2 hydrosols are added into cement paste. In addition, the higher concentration of TiO_2 hydrosols decreases the cumulative heat flow Q_{A-C} during the acceleration period, which is due to the decrease of nuclei from point A to point C. These results revealed TiO_2 hydrosols prolonged the induction period, and delayed the hydration peak due to the absorption on cement surface, and a higher concentration of TiO_2 indicated a larger absorption amount. The high adsorption of TiO_2 reduced the diffusion rate of ions and water transport to the interface between the cement and aqueous phases, consequently depressing the nucleation process of cement hydration. These retardation effects of nano-dispersed TiO_2 hydrosols on cement hydration are similar to the retardation effect of polycarboxylate salts on cement hydration. Compared with the polycarboxylate salts, like polycarboxylate-based superplasticizers or polymers, the retardation effect is not significant because the isolated carboxyl groups on TiO_2 surfaces are less effective for retardation of cement hydration compared with triad, tetrad, pentad, etc. [138,143,144].

(2)   Hydration products

The XRD patterns of cement with different concentrations of TiO_2 at one day and 28 days are shown in Fig. 3.3. The reference and TiO_2-modified samples presented similar mineral compositions and hydration products. The main clinkers are C_3S, C_2S, C_3A and C_4AF. The

main hydration products are CH, C-S-H and AFt, which means the kinds of hydration products are not influenced by the TiO_2 hydrosols. The TGA curves of cement pastes can be divided into two major parts, representing three different kinds of reactions [145–147]: (1) 105 °C to 300 °C: the primary range of dehydration of C-S-H gel. (2) 400 °C to 500 °C: dehydroxylation of calcium hydroxide (CH). (3) 600 °C to 800 °C: decarbonation of calcium carbonate. According to the suggested calculation method in literature [145,148,149], the CH and non-evaporation water in cement paste samples measured by TGA are shown in Table 3.3. Both CH and non-evaporable water are expressed as a percentage of the weight of the dried paste samples. In Table 3.3, the CH contents in paste mixed with TiO_2 at the age of one day decreases with the concentration of TiO_2 hydrosols, indicating the cement hydration is retarded. At 28 days, the CH contents in the paste containing TiO_2 are very close to the reference cement paste. These results indicated that the presence of TiO_2 hydrosols had delayed the hydration of clinker grains at an early age but had insignificant influence on the hydration at later stage.
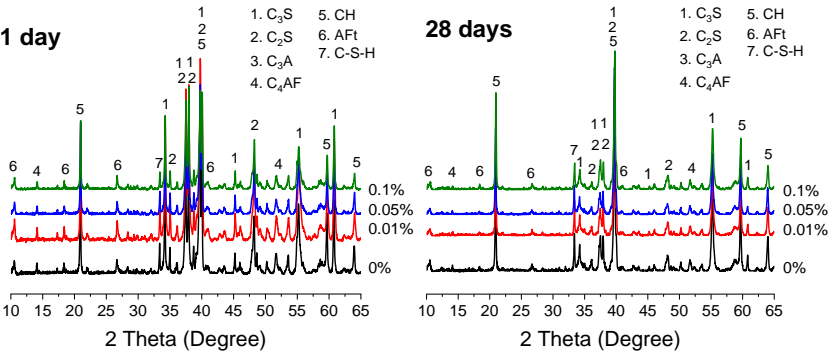
Fig. 3.3 The XRD pattern spectra of cement paste containing different amounts of TiO_2 hydrosols at one day and 28 days.

Table 3.3 Non-evaporable water and $Ca(OH)_2$ content of hydrated cements.

Dosage of TiO_2	Non-evaporable water (%)				$Ca(OH)_2$ (%)			
	1 d	3 d	14 d	28 d	1 d	3 d	14 d	28 d
0 %TiO_2	11.19	14.82	15.49	17.19	16.61	22.10	22.83	23.22
0.01 %TiO_2	11.16	14.57	16.77	17.75	16.45	21.90	21.55	22.24
0.05 %TiO_2	11.12	14.56	17.42	18.16	16.23	21.74	21.68	22.51
0.10 %TiO_2	9.62	14.79	17.56	17.19	14.86	20.53	22.39	22.92

Based on the analysis of hydration heat, XRD pattern and thermal decomposition behaviour of cement paste, it can be confirmed that the chemical reactions during the cement hydration process have been altered with the introduction of TiO_2 hydrosols, by consuming portlandite

crystals and influencing the contents of hydration products. For further analysing the influence of TiO_2 hydrosols on the hardened cement paste, the specific surface, pore size distribution, and SEM images of hardened cement paste will be discussed in Section 3.3.4.

3.3.3   Self-cleaning performance and optical parameters determination

(1)   Self-cleaning performance
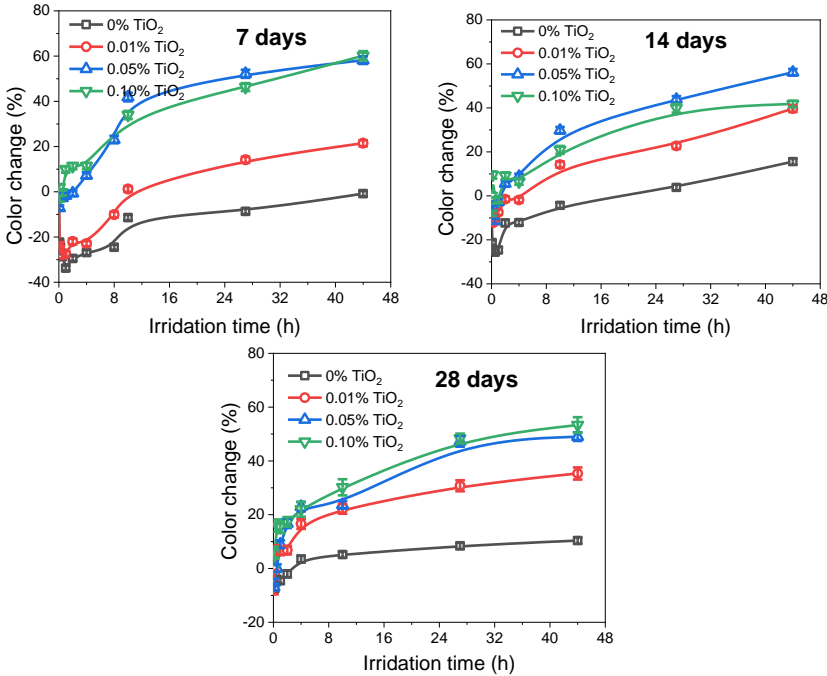
Fig. 3.4 Percentage of the colour change rate of a* for RB on the surface of hardened cement paste with different concentrations of TiO_2 at different ages.

The percentage of colour change for a* for RB caused by the self-cleaning effect of TiO_2 containing cement paste is presented in Fig. 4. The colour change of samples containing TiO_2 increases quickly during the first 6h irradiation, the differences between TiO_2 hydrosols contents are significant. In addition, the colour change of the samples' surfaces is also influenced by the hydration ages of cement, as shown in Fig. 3.4. At early age, for example seven days, the sample containing 0.05 % and 0.10 % nano TiO_2 are very close in self-cleaning performance, and the highest colour change rate (60.15 %, 0.10 % TiO_2) is obtained after 44h irradiation. Moreover, compared with the control cement paste sample, the paste containing 0.01 % TiO_2 at seven days shows a certain self-cleaning property, the colour change rate is 21.47 % after 44 hours UV irradiation. Because the cement hydration is not completely in the paste samples, the surface colour change of the samples is influenced by the colour

change of cement matrix at seven days and 14 days, and the colour change rates are negative at the first 2 h UV irradiation. At 28 days, the tested data at first 2 h are much more stable. The colour change rate of sample surfaces increases with the increased concentration of TiO_2 hydrosols, namely the colour change rates are 35.3 %, 49.0 % and 53.4 % after 44 h UV irradiation with 0.01 %, 0.05 % and 0.10 % TiO_2 hydrosols, respectively.

According to the previous studies [70,77,130,150], the maximum absorbance band of RB in the visible light range is about 554 nm, which is the typical absorbance peak of chromophoric groups of RB. To eliminate the interference of the light absorbance of cement paste matrix, the absorbance spectra of baseline at the range of 400 to 800 nm are removed from HPCP samples contains 0.05 % TiO_2, which are tested at three curing ages under different duration of UV irradiation, as shown in Fig. 3.5. The full information of the absorbance spectra curves with and without baselines of each tested HPCP samples are presented in Fig. B-1 and Fig. B-2 in Appendix II. For further clarification, several photos of the surface colour of HPCP samples after 44 hours of UV irradiation are selected and shown in Table B-1 in Appendix II. The peak positions of absorbance spectra before and after 44 hours of UV irradiation are marked in Fig. 3.5. After seven days and 14 days of curing, in all TiO_2 hydrosols modified HPCP, the absorbance at 554 nm increases in the first 0.5 to 2 hours of UV irradiation, then decreases in the rest of UV irradiation duration. The variation of peak values at 554 nm presents the similar changing trend as the variation of surface colour shown in Fig. 3.4, which confirms that the colour change of RB on the surface of mortar is caused by photo-bleaching [77].

Although the slow photobleaching of RB in air can still be observed under sunlight, it can be seen from Fig. 3.4 and Fig. 3.5 that the presence of TiO_2 hydrosols in mortar has promoted the photobleaching effect on the degradation of RB. In Fig. 3.5, another obvious phenomenon, the so called peak hypsochromic shift (or blue shift), is also observed in HPCP modified by TiO_2 hydrosols. It has been previously reported that the blue shift in the maximum absorption of RB water solution and dried RB film on the surface of mortar is induced by the N-deethylation of RB molecules [77,130,151], which is a significant indicator of photocatalytic degradation of RB by photocatalysts. It's noted that these two degradation processes are different processes in the primary steps of the photo-degradation of RB. The decrease of peak value refers to the photo-bleaching process, while the blue shift value refers to the N-deethylation process. As a result, for HPCP modified by a lower content (<0.05 %) of TiO_2 hydrosols, the weight of N-deethylation process increases with the age of cement paste. While, for the HPCP modified by a higher content (>0.05 %) of TiO_2, the maximum weight of the N-deethylation process appears at the age of 14 days. It is concluded that the degradation of dried RB film on the surface of HPCP goes via both the photo-bleaching process and N-deethylation process, which are both influenced by the age of the cement paste and the concentration of TiO_2 in the paste. In other words, the weight of the photo-bleaching and N-deethylation processes could be directed by designing the mix proportion

of TiO$_2$ hydrosols-modified cement paste.

(a) 7-day-age

(b) 14-day-age

(c) 28-day-age
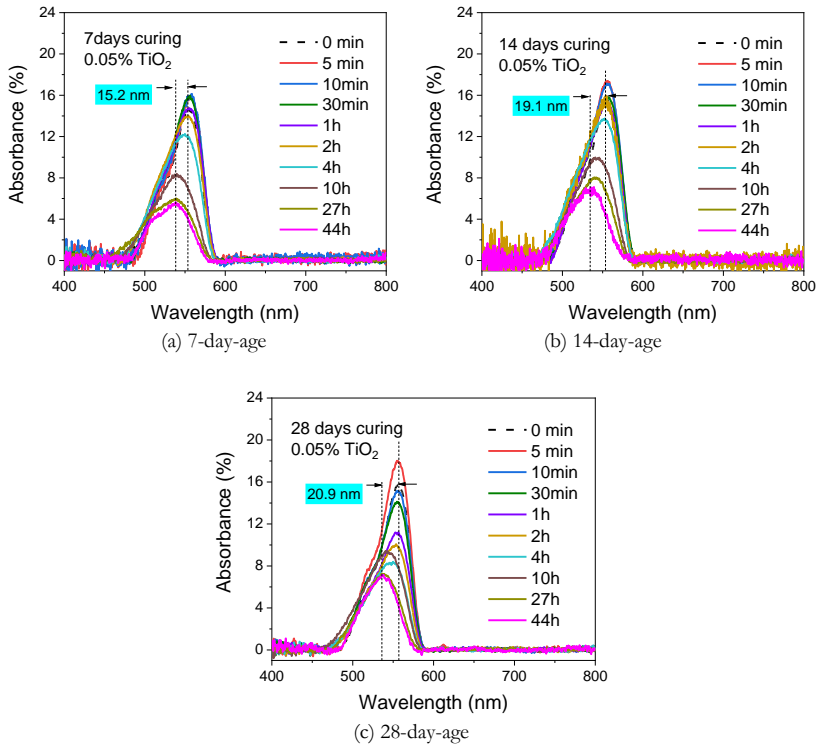
Fig. 3.5 The absorbance spectra curves with the baseline removed of HPCP modified by 0.05 % TiO$_2$ at different curing ages under UV irradiation during UV irradiation (a, b, c) are spectra of the HPCP with 0.05 % TiO$_2$ tested at 7, 14, and 28 days.

Table 3.4 The self-cleaning performance of nano TiO$_2$ (RB degradation rate) reported in literature.

TiO$_2$ type	TiO$_2$ w/w % of cement	Sample	W/B ratio	UV density (W/m^2)	About 4 hours degradation (%)	About 24 hours degradation (%)	Literature
nano powder	2	mortar	0.5	10	35	60	[126]
	5	paste	0.48	0.4	15	25	[118]
	2 % suspension+ 3 % powder	mortar	0.5	10	40	56	[121]
hydro-sols	0.1	paste	0.4	10	22	48	This chapter

Table 3.4 summaries some results of the self-cleaning performance of photocatalytic cement paste or mortar in literature. Compared with the RB degradation rate in Table 3.4, the tested TiO$_2$ hydrosols present good self-cleaning performance at such low concentrations in hardened cement paste. Thus, an excellent self-cleaning performance of samples is yielded by

adding such low dosages of TiO_2 hydrosols in the mixing water.

However, it is observed that the colour change rate of hardened cement paste at higher concentrations, for example 0.05 %, reduced with the increase of hydration age. Moreover, the colour change rate induced by 0.05 % TiO_2 is close to that induced by 0.10 % TiO_2, indicating the self-cleaning performance of hardened cement paste does not increase proportionally with the concentration increase of TiO_2 in the matrix at higher contents. Particularly, at 28 days, the self-cleaning performance of samples containing 0.10 % TiO_2 is only slightly better than that of samples containing 0.05 % TiO_2, revealing the cement hydration products affect the self-cleaning performance. As discussed in Section 3.3.2, the hydration rate and hydration products amounts are influenced by the mixing with TiO_2 hydrosols, in other words, the microstructure of the hardened cement paste samples modified by TiO_2 hydrosols are different from the reference paste at the same hydration age. From the view of the compound photocatalyst, the optical parameters of TiO_2-Cement paste can explain the self-cleaning ability of TiO_2 modified paste, which will be discussed in the Section 3.4.2.

(2)   Optical band energy and Urbach energy determination
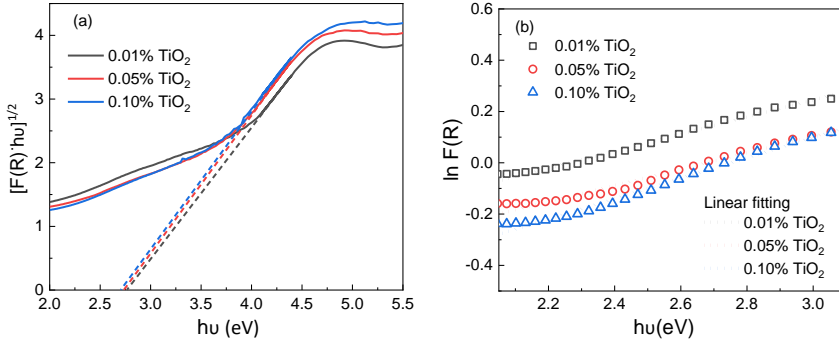
Fig. 3.6 Tauc's plots and determination of Urbach energy of the hardened cement pastes.

The properties of UV-VIS reflectance of hardened cement paste samples containing different concentrations of TiO_2 at 28 days are measured. To obtain the band energy (E_g) of TiO_2 modified cement paste samples, the Kubelka-Munk optical absorption coefficient $F(R)$ is first calculated. $F(R)$ and E_g are calculated using the Eq.(3.5),

$$F(R) = (1 - R)^2 / 2R \qquad (3.5)$$

and the Tauc's relation:

$$F(R)h\upsilon = (h\upsilon - E_g)^n \qquad (3.6)$$

Where, R is the reflectance of TiO_2-Cement paste compound; n is the exponent that depends on the type of transition, h is the Planck constant, and υ is the photon's frequency. n

= 2 for indirect allowed transitions, and n = 1/2 for direct allowed transitions. As to TiO_2 photocatalyst, the modified Kubelka-Munk function with n = 2 is used in some reports [152,153]. The band energy E_g is derived from the intercept of this straight line with the photon energy axis at F(R) = 0 [154] (Fig. 3.6(a)).

Fig. 3.6(a) shows the Tauc's plot of the TiO_2-modified hardened cement paste samples. The optical energy band edges of TiO_2-modified cement paste slightly decrease with the concentration of TiO_2, as shown in Table 3.5. The lowering of band edge in TiO_2-modified samples can be caused by the existence of localized defect states in the forbidden zone of TiO_2-photocatalyst near the bottom/top of its conduction/valence band [125]. This result reflects the fact that the hardened cement paste matrix might disturb the semiconductor electronic structure of the semiconductor through the creation of defects [125,155].

Table 3.5 Band energy and Urbach energy of TiO_2 modified hardened cement pastes.

TiO_2 concentration	Band energy (eV)	Urbach energy(eV)
0.01 %	2.79	2.98
0.05 %	2.74	3.20
0.10 %	2.71	2.54

Moreover, this distortion can bring an Urbach-type absorption, which occurs due to the electron transition between the extended band and localized band tail. The structural disorder caused by impurities and defects (Ti^{3+} and oxygen vacancies) produces an absorption tail extending deep into the forbidden gap. This absorption tail is called Urbach tail, and the associated energy is named Urbach energy (E_u), which is the width of the tail states in the bandgap associated with the structural defects and disorder within the crystal. The linear region (exponential tail) is the direct manifestation of the presence of structural defects in the crystal, which results in the formation of band tail states below (above) the conduction (valence) band and their density of states falls sharply with energy [156]. The exponential character of the absorption coefficient near the absorption edge is expressed by the Urbach rule [157,158], which is given by

$$F(R) = k \exp(h\upsilon / E_u) \tag{3.7}$$

$$\ln F(R) = \frac{1}{E_u} h\upsilon + \ln k \tag{3.8}$$

Where k is a characteristic crystal constant, $h\upsilon$ is the incident photon energy, and E_u is the Urbach energy, F(R) is the Kubelka-Munk optical absorption coefficient mentioned before.

Fig. 3.6(b) presents the Urbach energy of TiO_2-modified hardened cement paste samples. The fitting lines of the absorption data near the band edge showed that the absorption edge followed the Urbach tail behaviour indeed. The E_u of TiO_2-modified cement paste increased

when the TiO_2 concentration increased from 0.01 % to 0.05 %, and then decreased when the TiO_2 concentration is 0.10 %. The increase of E_u meant the presence of additional structural or crystalline defects like low angle grain boundaries, additional growth sites on the surface, disorder, oxygen vacancies etc. [156].

The results of Urbach energy indicated that the hardened cement paste containing 0.05 % TiO_2 presents the highest photocatalytic activity, theoretically, the self-cleaning performance of that compound is supposed to be the best in the tested samples. Since the cement paste is a complex multi-phase system, the self-cleaning performance of hardened cement paste may not only be dominated by the additional structural or crystalline defects of the TiO_2-cement compound. In other words, for the TiO_2-cement paste compound, a high photocatalytic activity does not guarantee a better de-colour performance. The surface conditions and microstructures of hardened cement paste samples can also influence the self-cleaning performance, which will be discussed in Section 3.4.1.

3.3.4   Microstructure of hardened cement paste

(1)   *Specific surface area and pore size distribution*

The specific surface area measured by the NAD method is shown in Table 3.6 with the BET interpretation. In Table 3.6, the specific surface area (SSA) of cement paste at one day decreases with the concentration of TiO_2, while at 28 days the SSA of paste increased with the concentration of TiO_2. At 28 days, the SSA in paste containing 0.05 % and 0.10 % TiO_2 reduces by 33.49 % and 15.28 % compared to that of one day, while in the reference paste the SSA reduces by 55.74 %. Moreover, at 28 days, the adsorption average pore width in paste containing 0.05 % and 0.10 % TiO_2 reduces by 37.96 % and 39.83 %, while in reference paste the adsorption average pore width reduces by 24.76 %. As mentioned before, the SSA of TiO_2 xerogel is 244.75 m^2/g. It is obvious that at 28 days the increased values of SSA in hardened cement paste containing 0.05 % and 0.10 % TiO_2 are much greater than the pure growth caused by superposition of the SSA of nano TiO_2 particles and hardened paste. These results indicated that the presence of TiO_2 hydrosols in hardened cement paste could inhibit the decrease of SSA caused by cement hydration, which may be related to the change of morphology of hydration products and distribution of pores.

The cumulative pore size distribution (CPSD) and differential pore size distribution (DPSD) of the paste samples at 1d and 28 d are presented in Fig. 3.7. As can be seen from Fig. 3. 7, after one day hydration, the pore volumes of gel micropores, mesopores and capillary pores [159] are higher than that of hardened cement paste containing TiO_2, and the pore volumes of pores reduced with the concentration of TiO_2. At 28 days, the pore volume of gel micropores in hardened cement paste containing 0.10 % TiO_2 is the highest, and the pore volume of mesopores and capillary pores in hardened cement paste containing 0.01 % is the highest. According to the results in [160], a higher volume of capillary porosity between 10

56

- 50 nm in mortars reveals a stronger photocatalytic activity. In Fig. 3.7(b), the volume of capillary porosity between 10 - 50 nm decreases obviously from one day to 28 days of hydration, and the volumes of capillary porosity in that range of the cement paste containing 0.05 % and 0.10 % TiO_2 are similar while the volume of capillary porosity in that range of cement paste containing 0.01 % TiO_2 is the lowest. These results of pore distribution can successfully explain the reduction of self-cleaning performance of TiO_2-modified cement paste at different hydration ages, an earlier hydration age represents a larger volume of capillary porosity in the range of 10 - 50 nm and a higher value of SSA, which are helpful for the improvement of photocatalytic activity and self-cleaning performance of cement paste.

Table 3.6 BET surface area of the hardened cement paste.

	0 % TiO_2		0.01 % TiO_2		0.05 % TiO_2		0.10 % TiO_2	
	1d	28d	1d	28d	1d	28d	1d	28d
BET surface area (m²/g)	17.06	7.55	15.11	6.52	15.02	9.99	13.81	11.70
Adsorption average pore width (nm)	20.64	15.53	21.87	15.04	21.18	13.14	21.54	12.96
Decrease rate of BET surface area (%)	55.74		61.95		33.49		15.28	
Decrease rate of adsorption average pore width (%)	24.76		31.24		37.96		39.83	
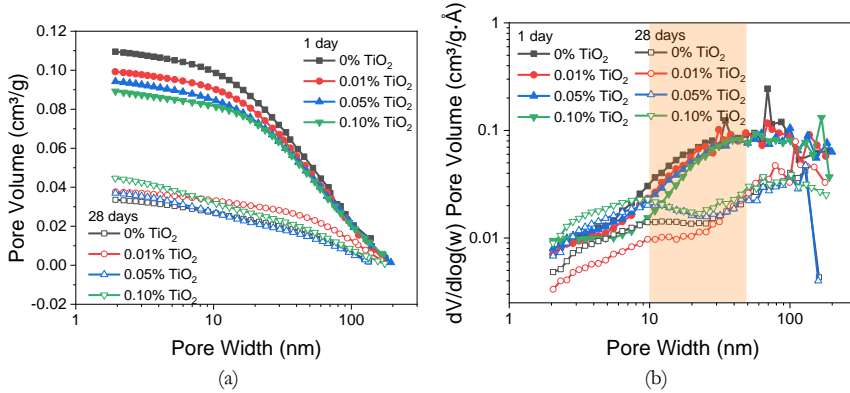
Fig. 3.7 Cumulative (a) and differential (b) pore size distributions of hardened paste at 1d and 28d.

(2)   SEM analysis

The morphology of hardened cement paste modified with different concentration of TiO_2 hydrosols at one day and 28 days are presented in Fig. 3.8 and Fig. 3.9. From Fig. 3.8(a) and (b), it can be seen that the hydration product AFt in the reference sample and sample containing 0.01 % TiO_2 is the typical needle-like shape with relatively uniform size [161,162], and the C-S-H is the dense gelatinous inner product [163]. While in the hardened cement

paste containing 0.05 % TiO$_2$, the AFt presents the shape of hexagonal prisms with shorted length. In Fig. 3.8(d) and (e), in the paste containing 0.10 % TiO$_2$, the hexagonal prisms are tangled by wire like amorphous C-S-H gels [163], which are surrounding the C$_3$S grains. These images directly confirmed that the nucleation and formation of AFt at an early age are inhibited by the TiO$_2$ hydrosols.
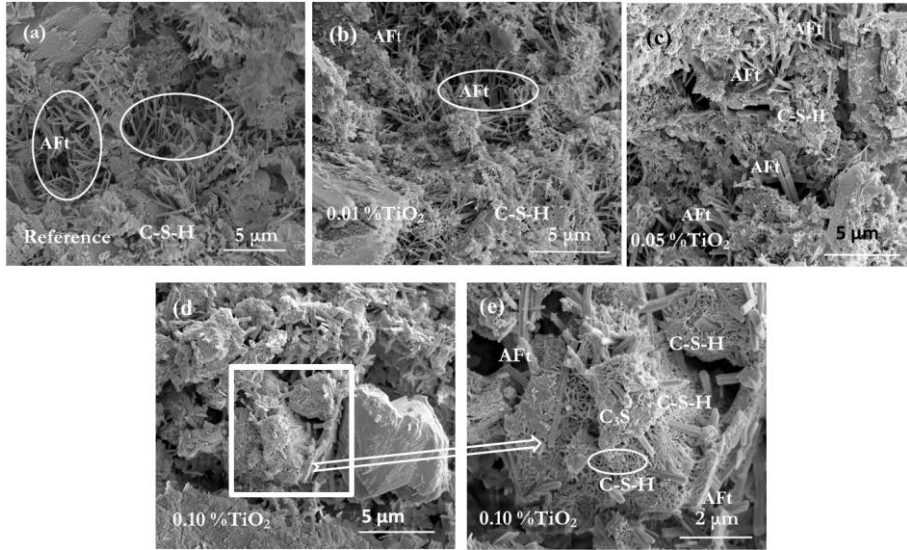
Fig. 3.8 SEM photos of hardened cement paste at one day (a. Reference; b. containing 0.01 % TiO$_2$; c. containing 0.05 % TiO$_2$; d. containing 0.10 % TiO$_2$ magnified 15000 x; e. containing 0.10 % TiO$_2$ magnified 35000 x).
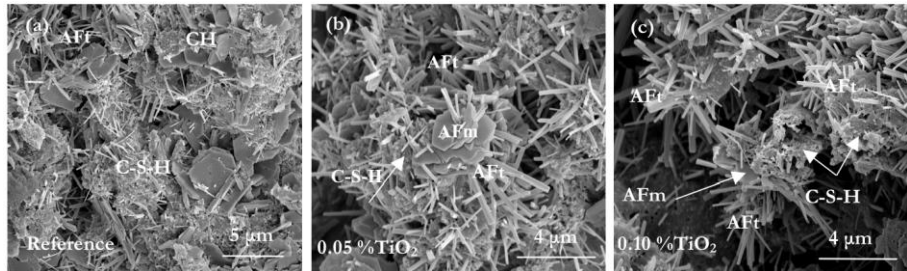
Fig. 3.9 SEM photos of cement paste at 28 days (a. Reference; b. containing 0.05 % TiO$_2$; c. containing 0.10 % TiO$_2$).

In Fig. 3.9(a), after 28 days of hydration, the main hydration products, like calcium hydroxide (CH), C-S-H gel and AFt, can be seen in the reference hardened cement paste, and the amount of AFt greatly reduces compared with that in Fig. 3.8(a). While, in the hardened cement paste containing 0.05 % TiO$_2$ hydrosols (Fig. 3.9(b)), fibrous, radial crystal aggregates of AFt and petal shaped AFm are observed, and a number of small and short rod- shaped Ettringite crystals (Type 2 Ettringite crystals) [164] with about 3 μm length and 0.1 to 0.2 μm

thickness are also observed. In the hardened cement paste containing 0.10 % TiO_2 hydrosols (Fig. 3.9(c)), the clusters of AFt, AFm and C-S-H gel can be seen clearly, and the pores of hardened cement are filled with the areatus crystals.

The results of SEM images of hardened cement paste at one day and 28 days can explain the change of SSA caused by TiO_2 hydrosols. The amount and morphology of cement hydration products at one day and 28 days, like C-S-H and AFt, are impacted more by the concentration of TiO_2 hydrosols. At one day, the retardation of nucleation and formation of AFt and C-S-H led to the smaller SSA of hardened cement paste containing TiO_2 hydrosols. While at 28 days, the pores of hardened cement paste are filled with plenty of clusters of short rod-shaped AFt, flake-like AFm and C-S-H gel, which led to a bigger SSA as compared with the reference paste.

3.4   Discussions

3.4.1   Dispersion of TiO_2 in hardened cement paste matrix

Agglomeration and coagulation are the main physicochemical processes restricting the photocatalytic activity of nano-dispersed TiO_2 hydrosols or nanopowders [42]. However, it is difficult to distinguish nano TiO_2 from cement by energy dispersive X-ray spectroscopy (EDX) element analysis, because the cement also contains titanium [165,166]. The confocal Raman microscope (CRM) is an ideal instrument for heterogeneous materials that show local fluorescence, which has been used to characterize the clinkers and hydration products of hardened cement paste [167–170]. Due to the non-destructive nature of the method, it can easily be applied to aqueous systems and both amorphous as well as crystalline components can be studied. Since TiO_2 is a typical crystalline compound, the distribution of nano TiO_2 crystals on the surface of the hardened cement paste can be observed by CRM more precisely and easily.

The average Raman spectra for hardened cement paste containing TiO_2 measured by CRM are shown in Fig. 3.10. The Raman bands at 144, 197 and 639 cm^{-1} are assigned to e_g modes, and the band at 144 cm^{-1} is very intense and sharp [171,172]. Raman spectroscopy can also be used to determine (approximately) the anatase content of impure rutile and other compounds [171]. In Fig. 3.10, the Raman band of anatase TiO_2 at 144 cm^{-1} is more obvious in the hardened cement paste containing 0.05 % and 0.10 % TiO_2 hydrosols, while the wide Raman band of amorphous carbon [168] is clear in the reference paste and paste containing 0.01 % TiO_2 paste. In hardened cement composites, the Raman spectrum of the ettringite is dominated by the Raman band around 1009 cm^{-1} and weaker band at 628 cm^{-1} [173,174], and the calcite ($CaCO_3$) is dominated by the narrow and intense Raman band at 1085 cm^{-1} [168,175–177] and weaker band at 711 cm^{-1} [168], the Raman modes of pure Portlandite ($Ca(OH)_2$) at 252 cm^{-1}, 356 cm^{-1} and approximate 680 cm^{-1} [178]. In Fig. 3.10, the peak intensity of Ettringite at 1000 cm^{-1} increased with the content of TiO_2 while the peak of

calcite at 1085 cm^{-1} is observed in all samples. The wide peak in the range of 800- 900 cm^{-1} is referred to the unhydrated C$_3$S and C$_2$S [179]. As shown in Fig. 3.10, the peak intensity of unhydrated C$_3$S and C$_2$S is very weak on the surface of hardened cement paste with 0.05 % and 0.10 % TiO$_2$ hydrosols, indicating the more complete hydration of cement clinkers.
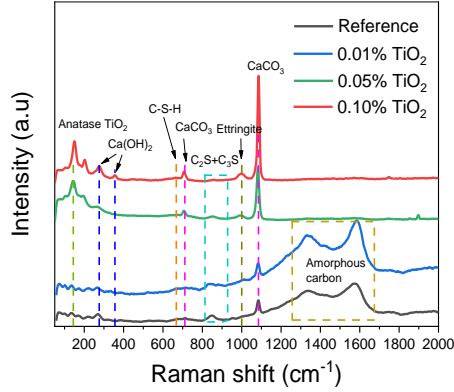
Fig. 3.10 Average Raman spectra of the different cements obtained by CRM (50 -2000 cm^{-1} region).

(a) Contains 0.01 % TiO$_2$ (b) Contains 0.05 % TiO$_2$ (c) Contains 0.10 % TiO$_2$
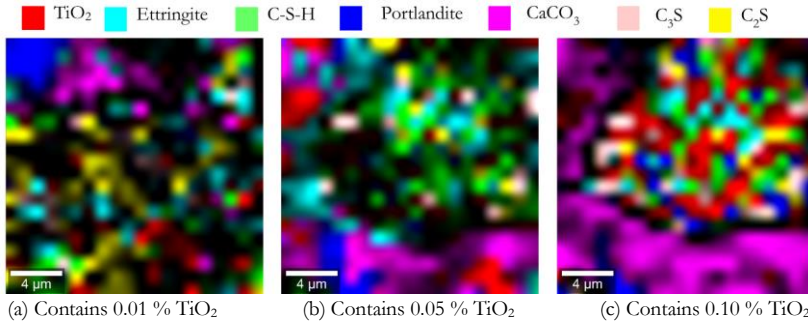
Fig. 3.11 Raman images by CRM of the evolution of the main phases present in the paste at 28 days (the scan area is 20 μm×20 μm).

The Raman images of the anatase TiO$_2$ and the main hydration products' spatial distributions in the hardened cement paste are shown in Fig. 3.11. The Raman band of 144 cm^{-1} [168], 356 cm^{-1} [178], 667 cm^{-1} [169], 839 cm^{-1} [179], 860 cm^{-1} [179], 1000 cm^{-1} [173,174] and 1085 cm^{-1} [168,175–177] are referred to the phase of anatase TiO$_2$, Portlandite, C-S-H, C$_3$S, C$_2$S, ettringite and calcite, respectively. In Fig. 3.11, in hardened cement paste containing 0.01 % TiO$_2$, very little anatase TiO$_2$ is observed in the surface pores, while in the paste containing 0.05 % and 0.10 % TiO$_2$, more anatase TiO$_2$ is observed in the surface pores. In addition, the TiO$_2$ clusters are surrounded by the C-S-H and Ettringite, especially in the pore areas. Compared with a paste containing 0.05 % TiO$_2$, the distribution area of TiO$_2$ in a paste containing 0.10 % is bigger, and the amounts of unhydrated C$_3$S and C$_2$S are smaller.

3.4.2   Self-cleaning mechanism analysis

The degradation mechanisms of RB in cement paste caused by TiO_2 hydrosols are important in the understanding and optimisation of self-cleaning efficiencies. As reported previously [76], the degradation mechanism of RB caused by nano TiO_2 is proposed to happen by two phenomena, one being the de-ethylation process that has also been reported in other studies [77,180], and a second which is the degradation process of the chromophore structure. Several mechanisms for photoinduced self-cleaning of nano TiO_2 have been proposed, including (1) photoinduced surface vacancy generation [181]; (2) photoinduced reconstruction of surface hydroxyl groups [182,183]; and (3) light-induced removal of the carbonaceous layer on the surface of TiO_2 exposed to air [184]. The foundation of these theories is that the nano TiO_2 particles are dispersed evenly on the surface of the matrix, and the surfaces of the nano TiO_2 particles are exposed to the air and pollutants.

Many previous studies [153,185–187] prove that the higher concentration of oxygen vacancies or other defects results in the stronger photoactivity of nano TiO_2, which is usually used to explain the better air purification property of photocatalytic cementitious materials [123,188]. According to the calculation results of Band energy and Urbach energy shown in Table 3.5, the hardened cement paste containing 0.05 % TiO_2 presents the highest photocatalytic activity, however, it does not present the best self-cleaning performance based on the test results in Section 3.3.3(1). Therefore, a new interpretation of the self-cleaning performance enhancement of TiO_2 hydrosols-modified Portland cement paste is proposed here.

For cement paste modified by nano-dispersed TiO_2 hydrosols, the high self-cleaning performance can be interpreted from two parts. Firstly, the nanoscale dispersion of TiO_2 hydrosols are added in the mixing water in preparing cement paste, which means the nano TiO_2 particles can scatter much more evenly in the paste along with the water through mixing compared to the powder TiO_2 particles. The results of CRM analysis confirm that the anatase nano TiO_2 particles are dispersed evenly in the matrix of hardened cement paste. Secondly, there is a retardation effect of TiO_2 hydrosols on cement hydration at the acceleration and the deceleration stages. According to the XRD and TG analyses of hardened cement paste at different hydration ages, the presence of TiO_2 hydrosols does not affect the types of hydration products but affects the content of hydration products at early age. The retardation and nucleation effect of nano TiO_2 hydroosl on cement hydration leads to the obviously different morphology and distribution of hydration products (see the SEM and CRM analyses in Sections 3.3.4 and 3.4.1). As a result, the specific surface area of the hardened cement paste at 28 day modified with greater TiO_2 hydrosols are much higher than that of the reference. The larger specific surface area of cement paste meant the more reaction surface area for TiO_2 to degrade the RB molecules on the surface of cement paste, indicating the better self-cleaning performance of cement paste.

Fig. 3.12 reveals the two routes to explain the self-cleaning mechanism of TiO_2 hydrosols

modified cement paste, one is the additional surface defects causing smaller energy band gap and better photocatalytic activity (see Fig. 3.12 (a)), and another one is the surface electron capture effect of nano sized cement hydration products, like AFt and AFm phases (see Fig. 3.12 (b)). As mentioned in Section 3.3.3, the semiconductor electronic structure of TiO_2 can be disturbed by the hardened cement paste through the creation of defect levels. Moreover, the self-cleaning ability of a photocatalytic cementitious material is not only influenced by photocatalytic activity, but also influenced by the conditions of the nano TiO_2 surface. As mentioned in Section 3.3.1, the surface of TiO_2 nanoparticles turns to negative at high pH system. In other words, in a cement-based environment, the TiO_2 particles tend to absorb on the surface of hydration phases with the positively charged surface, like AFt, AFm phases. The CRM images support that the non-agglomerated TiO_2 particles are surrounded by the positively charged AFt and AFm phases, which could be interpreted as that AFt and AFm can be the receptors of photo-induced electrons. When the electrons on the surface of TiO_2 are promoted by UV illumination, the electrons are trapped by positively charged AFt and AFm phases, which reduces the possibility of the electron-hole recombination. The surface electron capture effect is stronger at a larger concentration of TiO_2 hydrosols based on the results in Section 3.3.1. As a result, the tested TiO_2 modified cement paste shows a good self-cleaning performance.

(a) Surface defects effect

(b) Surface electron capture effect
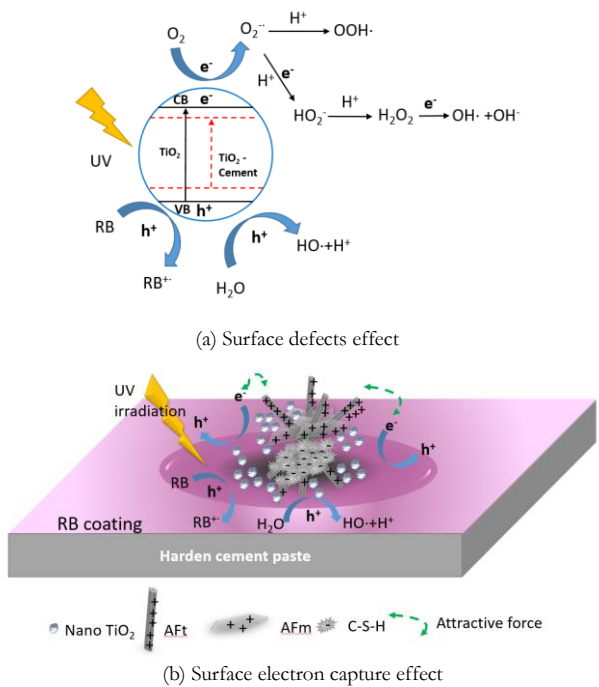
Fig. 3.12 Schematic diagram of the self-cleaning mechanism of TiO_2 hydrosols modified photocatalytic cement paste.

From what has been discussed above, at low concentrations of TiO_2 (< w/w 0.05 % of cement), the self-cleaning performance of hardened cement paste is mainly dominated by the additional surface defects. While, at a high concentration of TiO_2 (> w/w 0.10 % of cement), the surface electron capture effects of cement hydration products predominate the efficiency of de-colour rate of hardened cement paste. Moreover, the enhancement of self-cleaning performance induced by the photocatalytic activity is much higher than that induced by the surface electron capture effect.

3.5   Summaries

In this chapter, the influences of very low concentration nano-dispersed TiO_2 hydrosols on the self-cleaning properties of hardened Portland cement paste (HPCP) are investigated on the cement hydration process and microstructure evolution. The following conclusions are drawn:

(1) Due to the positively charged TiO_2 particles in hydrosols carrying functional group   -COOH, the cement hydration process is slightly retarded when mixing TiO_2 hydrosols in water at an early age. The category of cement hydration products is unaffected, but the microstructure of hardened cement paste is affected. The modified microstructure of hardened cement paste presented a bigger specific surface area at 28 days than that of the reference paste, and the specific surface area of the paste increased with the concentration of TiO_2.

(2) The self-cleaning performance of modified HPCP is influenced by the higher optical photocatalytic activity of TiO_2-cement paste and the morphology of cement hydration products at different ages. At each test hydration age, the colour change rate in modified HPCP is increased with the concentration of TiO_2 hydrosols, but the increment is not proportional to the concentration of TiO_2 hydrosols. The colour change rate of modified HPCP with higher concentrations of TiO_2 (> 0.05 % w/w of cement) decreases with the hydration age of cement.

(3) At lower TiO_2 hydrosols concentration (< 0.05 % w/w of cement), the increase of additional surface defects of TiO_2 dominates the enhancement of self-cleaning performance of hardened cement paste. While in the higher concentration of TiO_2 hydrosols (> 0.05 % w/w of cement), the contribution of the surface electron capture effect of hydration products to the enhancement of self-cleaning performance is larger. Under the UV irradiation, the recombination of electron-hole on the surface of nano TiO_2 can be resisted because the photo-induced electrons trapped by the positively charged AFt and AFm phase.

(4) A new mechanism of the self-cleaning performance enhancement of TiO_2 hydrosols modified hardened cement paste is proposed. The coupling of surface defects of nano TiO_2 particles and a surface electron capture effect generated by the special cluster structures of TiO_2 and main hydration products, like AFt, AFm and C-S-H are observed. Since the TiO_2

hydrosols affect the cement hydration at lower concentration, the lower-impacted HPCP creates more additional surface defects of TiO_2 particles. With the increase of TiO_2 hydrosols, the higher-impacted cement hydration products become the capturers of photo-induced electrons, which effect also improves the self-cleaning performance of HPCP.

Chapter 4 Variation of self-cleaning performance of nano TiO₂ modified mortar caused by carbonation: From hydrates to carbonates

Evaluation and quantification of the effects of the carbonation process on photocatalytic activity are essential for the long-term functional assurance of nano TiO_2 modified photocatalytic concrete. This chapter focuses on the photocatalytic self-cleaning performance variation of mortar containing different dosages of nano TiO_2 hydrosols at different carbonization duration. The colourimetric analysis is used to evaluate the self-cleaning performances of carbonated mortar samples. The distribution areas of anatase TiO_2, hydrates, and carbonates in the mortar surface are characterized by the Confocal Raman Microscopy. The data recorded during the 28 days of carbonation show that the self-cleaning performance of mortar surfaces features a recovery phenomenon during carbonation. The correlations between photocatalytic self-cleaning performance and the possible parameters are analyzed. A predictive model is suggested to evaluate the influence of carbonation degree on the photocatalytic self-cleaning ability of nano TiO_2 hydrosols modified mortar.

4.1   Introduction

Nano TiO$_2$-based photocatalytic cementitious materials have proven excellent air purification and self-cleaning performance in previous studies and field applications [101,120,189–194], and among the available forms, hydrosols TiO$_2$, thanks to its fine size of 5 to 100 nm [17–20], has shown better depollution performance than other types [129,195–198]. However, the photocatalytic ability of nano TiO$_2$ modified cementitious materials can be weakened by the physio-chemical reactions during the service. Among those reactions, carbonation-induced cement hydrates alteration is potentially a serious issue [125,199,200], which includes a series of complex physical and chemical-related dissolution-precipitation reaction processes [201–205], affecting the durability of concrete structures [205–210]. The photocatalytic depollution rates of fully carbonated photocatalytic mortar samples have been reported to reduce significantly [160,199,200,211], for example, about 50 % [26]. The shielding and filling effects of calcium carbonates in carbonated mortar are the main possible reasons for the decrease in photocatalytic performance [211].

The carbonation process of cementitious materials is influenced by CO$_2$ concentration, temperature [212], relative humidity, the types of supplementary cementitious materials [213] and the diffusion ability of CO$_2$ in the matrix, among which the CO$_2$ concentration [202,205,214–216] and relative humidity [214,217–219] significantly affect the chemical changes and crystal phases of cement hydrates during carbonation. In the natural environment with a CO$_2$ concentration of about 0.03 %, it will take several years for the total carbonation of cement hydrates in the depth of 10 mm to take place [220–222], indicating that the phase and crystal shape from hydrates to calcite crystals experience continuous changes during a very long period. During carbonation, the cement hydrates in mortar usually transform into different forms of calcium carbonate (CaCO$_3$) based on the initial conditions, such as the crystal shapes and morphology of the mortar. Calcium carbonate has polymorphic forms [223–226], with different crystal sizes, shapes, and molecular volumes. Calcite, vaterite, and aragonite are the three anhydrous crystalline polymorphs of CaCO$_3$. The calcium carbonate hexahydrate (Ikaite, CaCO$_3$•6H$_2$O) and calcium carbonate monohydrate (CaCO$_3$•H$_2$O) are the two well-defined hydrated crystalline polymorphs of CaCO$_3$. The amorphous CaCO$_3$ also contains a variety of forms. Table 4.1 summarises the parameters such as density and molar volume of cement hydration products and carbonation products.

The interplanar crystal spacing d[hkl] of Ca(OH)$_2$ firstly increases when CCH1, CCH2, and CCH3 are formed. The crystal shape and size of Ca(OH)$_2$ significantly influence the polymorph evolution during the conversion of Ca(OH)$_2$ into CaCO$_3$. As to the C-S-H phase, the crystal pattern and shape of carbonation products are influenced by the Ca/Si ratio [209], mineral morphology [201], and density [203]. The molar volumes of these intermediate carbonization products CCH1 to CCH4 are several times larger than the volumes of the CH and C-S-H. The volume of reactants and products involved in carbonation first increases

sharply and then decreases gradually from hydration products to the final stable state of calcite.

Table 4.1 Compounds participating in the carbonation reactions.

Name	Molecular formula	Density (g/cm^3)	Molar weight (g/mol)	Molar volume (cm^3/mol)
Portlandite	$Ca(OH)_2$	2.23	74	33.18
C-S-H	$(CaO)_{1.7}(SiO_2)(H_2O)_{1.80}$	2.60	187.6	72.15
Calcium carbonate hydroxide (CCH1)	$Ca_3(CO_3)_2(OH)_2$	1.60	274	171.25
Defernite (CCH2)	$Ca_6(CO_{2.65})_2(OH_{0.657})\bullet7(H_2O)_2$	2.50	501.4	200.56
Calcium carbonate hydroxide hydrate (CCH3)	$Ca_3(CO_3)_2(OH)_2\bullet1.5H_2O$	1.82	301	165.38
Ikaite (CCH4)	$CaCO_3(H_2O)_6$	1.78	208	116.85
Monohydrocalcite (CCH5)	$CaCO_3(H_2O)$	2.38	118	49.58
Vaterite	$CaCO_3$	2.54	100	39.37
Aragonite	$CaCO_3$	2.93	100	34.13
Calcite	$CaCO_3$	2.71	100	36.90
Silica gel	SiO_2	2.2	60	27.27

The carbonation reactions of Portlandite and products crystal systems suggested by Stepkowska [227] are shown in the following equation:

$$\underset{\text{hexagonal}}{\text{Portlandite}} \rightarrow \underset{\text{orthorhombic monoclinic}}{\text{CCH1}\rightarrow\text{CCH2}\rightarrow\text{CCH3}} \rightarrow \underset{\text{monoclinic}}{\text{CCH4}} \rightarrow \underset{\text{hexagonal}}{\text{CCH5}} \rightarrow \underset{\text{hexagonal}}{\text{vaterite}} \rightarrow \underset{\text{orthorhombic}}{\text{aragonite}} \rightarrow \underset{\text{rhombohedral}}{\text{calcite}} \quad (4.1)$$
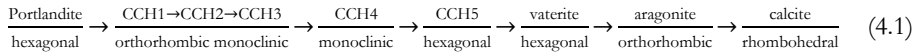
The volume variation of calcium carbonates caused by carbonation of cement hydrates will vitally influence the microstructure of photocatalytic mortar, consequently leading to alteration of its self-cleaning performance. However, only a few researchers [160,199,200,211] studied the influences of fully carbonated cement hydrates on the photoactivity of powder-formed nano TiO_2 in cementitious materials. Therefore, studying the phases and morphology of cement hydrates in photocatalytic self-cleaning mortar during carbonation is essential to understanding the functional ability during the engineering application.

This chapter investigates the potential relationships between crystalline morphology evolutions and photoactivity reductions to control the adverse effects of carbonation on photocatalytic cementitious materials. The accelerated carbonation test with 3 % CO_2 and 65 % RH is used to mimic the natural environment as the variation of the microstructure of ordinary Portland cement paste upon accelerated carbonation is relatively close to that of paste in the natural carbonation [202,205]. The chromatics and optical photocatalytic factors are

determined to characterize the self-cleaning performance of mortar samples. More importantly, a calculation model is established to quantitatively evaluate the influence on the photocatalytic self-cleaning performance declination caused by the carbonation of hydrates.

4.2 Materials and experimental

4.2.1 Materials

The nano-dispersed anatase TiO_2 hydrosols are synthesized based on the method in our previous study [228]. The hydrodynamic size of TiO_2 hydrosols is 18.92 ±6.358 nm, and the percentage of pure TiO_2 in hydrosols are 1.54 w/w %. CEM I 52.5 R cement, standard sand (CEN-EN 196-1), and tap water are used to prepare the mortar samples with the water to cement ratio mass of 0.5 and sand to cement mass ratio of 3. The chemical composition of cement is shown in Table 4.2, which is tested by X-ray fluorescence spectroscopy.

Table 4.2 Chemical composition of CEM I 52.5 R cement.

Components	CaO	SiO$_2$	Fe$_2$O$_3$	SO$_3$	Al$_2$O$_3$	MgO	K$_2$O	TiO$_2$	P$_2$O$_5$	Minor elements*
Content (%)	66.34	18.22	3.81	3.15	5.56	1.68	0.29	0.50	0.16	0.30

   * V_2O_5+Cr_2O_5+MnO+CuO+ZnO+BaO+Cl

The samples are wet mixed for five minutes before being moulded in 4 cm × 4 cm × 16 cm moulds and covered with a plastic sheet. Different amounts of TiO_2 hydrosols are firstly dispersed in the mixing water. The TiO_2 to cement mass ratios are 0 %, 0.01 w/w %, 0.05 w/w %, 0.10 w/w % and 0.50 w/w %, respectively. After one day of curing, the samples are de-moulded and cured in a climate chamber (RH > 95 %, 20 °C) until 28 days.

4.2.2 Methods

(1) Accelerated carbonation tests

For the accelerated condition, mortar samples are placed in a CO_2 incubator (HPP, Memmert, Germany) in which the CO_2 concentration is maintained at 3 ± 0.1 %, the relative humidity at 65 ± 0.1 % and the temperature at 25 ± 0.1 °C. Four different carbonation test durations are set as three days, seven days, 14 days, and 28 days for testing the mortar samples. Before the accelerated carbonation tests, both ends of the prism sample are cut with 1 cm and then cut into three cubes with a side length of 4 cm. For achieving one-dimensional carbonization, the four side faces of each cube are sealed by paraffin and Parafilm (Bemis Company Inc., United States). Before that, the cubes are dried at 40 ℃ in the oven for 48 hours. Two parallel samples are used in each test group.

(2)   Self-cleaning tests

The self-cleaning performances of the TiO_2-modified mortar slice samples are evaluated by the colourimetric analysis of the degradation of the organic dye Rhodamine B (RB). Each surface area of the paste sample is stained by painting 600 µL of 50 mg/L RB aqueous solution. Then, the samples are kept overnight in the dark at room temperature for drying. Subsequently, the samples are exposed to a UV lamp (10 ± 0.05 W/m²) to simulate UV light in natural conditions, and the discolouration of the samples is monitored. The UV lamp is composed of three UV tubes with a power of 25 W. The UV-A wavelength ranges from 300 nm to 400 nm and is centered at 345 nm. The reflected colour measurements are taken on the sample's surface with a spectrometer (USB4000, Ocean optics, United Kingdom) equipped by a light resource with a wavelength range from 380 to 780 nm. For mortar with each dosage of nano TiO_2, two slices are used as the parallel samples. Nine points are recorded for the colourimetric tests for each sample, and each point is tested four times. The colour of each sample is measured after 0.5h, 1h, 2h, 4h, 8h, 16h and 26h of UV irradiation, respectively. The percentage of discolouration of RB on the surface of mortar (R_t) is expressed with a* value coordinate of the dominant colour of dye in the CIE Lab colour space, according to Eq. (3.1) in Chapter 3.

4.2.3   Characterizations

An isothermal calorimeter (TAM Air, TA Instruments, United States) is used to record the heat release of cement hydration containing different concentrations of TiO_2 hydrosols every 10 s for the first 168 h of hydration. The test temperature is 20 °C.

The planetary ball mill (Pulverisette 4, Fritsch, Germany) is used to prepare the powder samples from the slice mortar samples. Then, the powder samples are sieved through a fine sieve with a pore size of 75 µm. The fine powders are dried at 40 °C for 48 hours before the X-ray diffraction and TG analysis. For mortar samples carbonized for different periods, one slice of mortar sample is crushed to prepare a powder sample.

The crystal patterns of cement hydrates before and after the accelerated carbonation test are determined by the X-ray diffraction (XRD) pattern (Bruker D4 PHASER, Philips, The Netherlands) with a Co tube (40 kV, 40mA), with the test step size of 0.02°/min and dwell time of 0.5s. According to the previous study [229], the crystals of the Portlandite with hexagonal-prism shape faceted by {10-10} prismatic and {0001} basal facets, and the exhibit aspect ratio (r_L) of the crystal can be calculated by:

$$r_L = \frac{L_1}{L_2} \tag{4.2}$$

Where L_1 is the characteristic linear size of portlandite crystal in {10-10} growth direction;

L_2 is the characteristic linear size of portlandite crystal in {0001} growth direction.

A nitrogen adsorption-desorption device (TriStar II 3020) is used to test the nitrogen sorption isotherm and Brunauer, Emmett and Teller (BET) specific surface area of the mortar samples. The Barrett-Joyner-Halenda (BJH) plots are analysed to evaluate the pore size distribution. Before the BET test, the slice mortar samples are cut into small blocks with a volume of about 0.5 cm^3 and then dried at 40 °C for 48 hours in the oven, finally degassed in an external degassing station at 40 °C under N_2 flow for 4 hours. The mass of each tested sample is about 0.60 g, and the test pressure ranges from 0.01 to 0.14 atm.

A Quanta 250 FEG scanning electron microscope (ThermoFisher Scientific, USA) and a Phenom Pro Desktop scanning electron microscope (ThermoFisher Scientific, USA) are used to capture the morphology images of mortar samples with secondary electrons detector. The slice mortar samples are cut into blocks of about 1 cm^3 and dried at 40 °C for 48 hours before being put into the SEM test chamber.

The UV–vis diffuse reflectance spectra (UV–vis DRS) of TiO_2 hydrosols modified mortar before and after accelerated carbonation tests are measured by a UV-VIS-NIR spectrophotometer (Perkin Elmer Lambda 750), the tested range is 200 nm to 2500 nm, 2 nm per second. Two mortar slices are used as the parallel samples for obtaining the reflectance spectra. All the samples are dried at 40 °C for 48 hours before tests. The Kubelka-Munk optical absorption coefficient F(R) and the bandgap energy (E_g) of TiO_2 modified cement paste samples are calculated by Tauc's relation [153]. The exponential character of the absorption coefficient near the absorption edge is expressed by the Urbach rule [157,158]. Detailed information can be found in our previous work [228].

The distribution of phases on TiO_2 hydrosols modified mortar is observed by Confocal Raman Microscopy (Witec alpha300S, Witec, Ulm, Germany). The Raman spectra range from 0 cm^{-1} to 3900 cm^{-1}. The 532 nm excitation laser with a power of 60 mW is used in measurements. The scan area on the surface of mortar is 35 µm × 35 µm, the size of the Raman images is 70 × 70 pixels with an integration time per pixel of 0.1 s. One mortar slice is used for CRM mapping analysis.

The TG analysis of mortar samples before and after the accelerated carbonation is conducted using a STA 449 F1 instrument (NETZSCH, Germany) with N_2 as the carrier gas by heating up to 1000 °C from 40 °C at the rate of 10 °C/min. The TGA plots of cement hydrates are usually divided into three main parts [145–147]: (1) The primary range of dehydration of C-S-H gel is 105 °C to 300 °C. (2) Dehydroxylation of calcium hydroxide (CH) is 400 °C to 500 °C. (3) Decarbonisation of calcium carbonate ($CaCO_3$). The decomposition of $CaCO_3$ in the range of 500 °C to 680 °C is related to the amorphous calcium carbonate [230,231]. The poorly-crystalline (including vaterite and aragonite phases) and well-crystalline $CaCO_3$ (calcite phase) are considered to be decomposed between 680 °C and 780 °C,

and between 780 ℃ and 990 ℃, respectively [232]. The carbonation degree (D_c) of mortar can be calculated as follows [233]:

$$D_c = \frac{C - C_0}{C_{max} - C_0} \times 100 \text{ \%} \tag{4.3}$$

C is the amount of CO_2 in the sample (refer to the CO_2 derived from the $CaCO_3$); C_0 is the amount of CO_2 in the non-carbonated sample; C_{max} is the theoretical amount of carbon dioxide needed to combine with the total CaO in the sample to form $CaCO_3$. The C_{max} must be analysed by a reliable method, such as XRF, and the CaO amount in the $CaCO_3$ of raw materials should be deducted.

4.3   Results

4.3.1   Cement hydrates and carbonates

(1)   Hydration kinetics
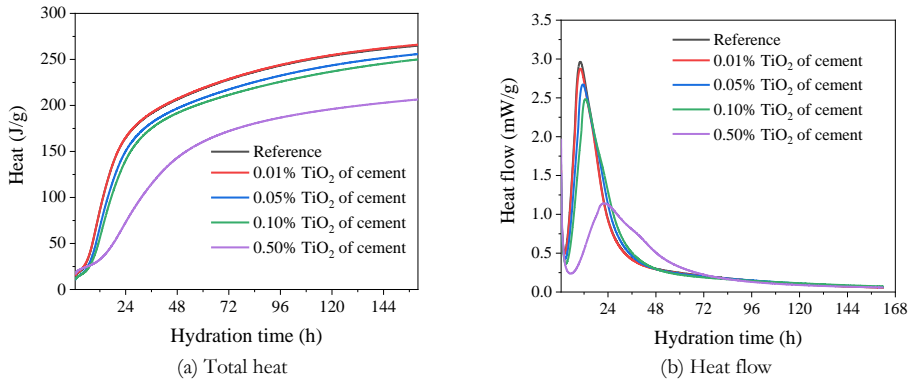
Fig. 4.1 Influences of TiO₂ hydrosols on the exothermic heat flow and total heat of per gram of cement.

The influence of TiO_2 hydrosols concentration on the Portland cement hydration kinetics at the early age is studied, and the cumulative heat release and hydration rate are shown in Fig. 4.1. At a low concentration of TiO_2, for example, 0.01 w/w % of cement, the cumulative hydration heat is primarily unaffected. While with the increase of the concentration of TiO_2 hydrosols, the total released hydration heat decreases clearly, as seen in Fig. 1(A). Moreover, the TiO_2 hydrosols reduces the hydration rate, delays the appearance of the second heat flow peak and extends the acceleration and deceleration periods of cement hydration. The peak value and cumulative heat release of cement are significantly reduced by adding TiO_2 hydrosols at higher concentrations, while the width of the hydration heat flow peak increases with the dosages of nano TiO_2. In the paste containing 0.50 w/w % TiO_2, the heat flow peak appears about 12 hours later than in the reference paste. It is concluded that the presence of

TiO$_2$ hydrosols retards the hydration of Portland cement, prolongs the induction period of early hydration of cement, and reduces the hydration rate in the acceleration and deceleration periods. When TiO$_2$ hydrosols to cement ratio is less than 0.1 w/w %, the influence of TiO$_2$ hydrosols on the hydration heat evolution becomes very small after three days. However, it should be noticed that the retardation of cement hydration may influence the hydrates crystal pattern and morphology after 28 days of curing, which will be discussed in next section.

(2) Hydration products

The X-ray diffractograms of reference mortar and mortar samples containing 0.5 w/w % TiO$_2$ before are shown in Fig. 4.2. Before carbonation, the main hydrates of calcium hydroxide (CH) and C-S-H phases are detected in the TiO$_2$-modified mortar and the reference mortar. The C-S-H phases in mortar sample containing 0.50 w/w % TiO$_2$ contains Tobermorite, Hillebrandite, Xonotlite, and Foshagite phases, while only the Tobermorite phase is detected in the reference mortar sample. Based on the previous study [228] and the results in Section 3.1.1, the formation of C-S-H phases are delayed, and the morphologies of C-S-H phases are different at an early age because the nano TiO$_2$ hydrosols have the surface functional groups of –COO$^-$ and –C–OH.

As shown in Fig. 4.3, the morphology of the C-S-H gel is also influenced by the applied TiO$_2$. In the mortar with a lower content of TiO$_2$ (<0.10 w/w %), a foil-like C-S-H gel is observed. In the mortar with 0.10 w/w % TiO$_2$, the fibrillar and reticular C-S-H phases appear, which co-exist with foil-like C-S-H and CH crystals. More fibrillar C-S-H gels appear when the mortar contains 0.50 w/w % TiO$_2$. Previous studies [127,234] have reported a similar phenomenon: nano TiO$_2$ in the forms of sol and suspension leads to fibrillar C-S-H that contains alumina with a high Ca/Si ratio (-2) in the hardened cement paste. Furthermore, the initial Ca/Si ratios of C-S-H gel in hydrates closely relate to its carbonation rate, the C-S-H with higher Ca/Si ratios shows a faster carbonation rate than the lower Ca/Si ratios [235]. Therefore, the results in Fig. 4.2 and Fig. 3 support that the ratios of Ca/Si in the C-S-H phase are influenced by the amount of nano TiO$_2$ hydrosols, which will affect the carbonation rate and the morphology of carbonates in mature cementitious materials [209,236].
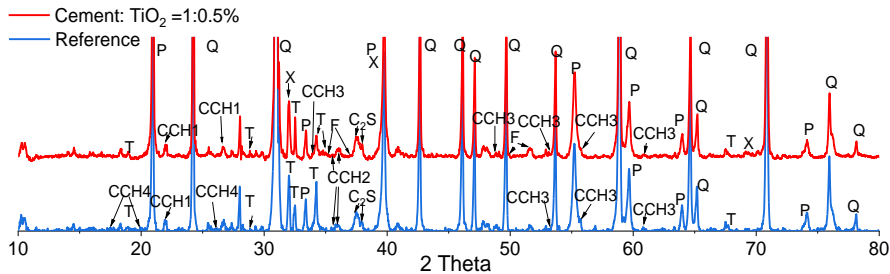
Fig. 4.2 X-ray diffractograms of mortar with and without TiO$_2$ hydrosols before carbonation. Symbols: Portlandite: P, Quartz: Q, Tobermorite: T, Hillebrandite: H, Xonotlite: X, Foshagite: F; Calcium carbonate hydroxide: CCH1; Defernite: CCH2; Calcium carbonate hydroxide hydrate: CCH3; Ikaite: CCH4; Monohydrocalcite: CCH5.
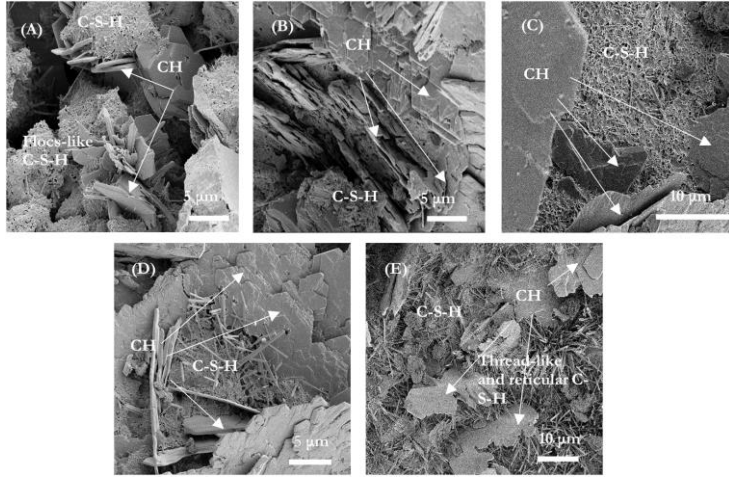
Fig. 4.3 Morphology of Portlandite crystal in the mortar after curing with different amounts of TiO₂ hydrosols; (A) 0w/w % TiO₂; (B) 0.01w/w % TiO₂; (C) 0.05 w/w % TiO₂; (D) 0.10 w/w % TiO₂; (E) 0.50 w/w % TiO₂.
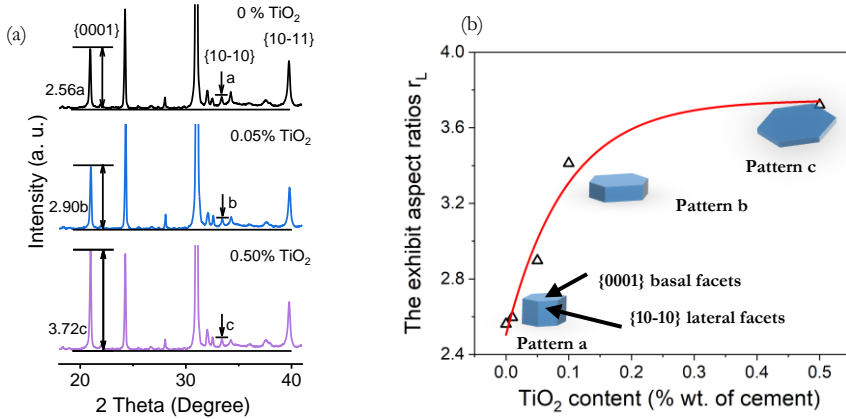
Fig. 4.4 (a) Crystal pattern of hydrates before carbonation test; (b) Plot of the exhibit aspect ratios (r_L) of CH vs. TiO₂ mass fraction.

Fig. 4.4(a) shows the XRD pattern of mortar samples containing different content of nano TiO₂, the typical peaks of Portlandite at {0001}, {10-10} and {10-11} planes appear on the patterns of the reference mortar and TiO₂ modified mortar before carbonation test. In other words, the presence of TiO₂ hydrosols does not affect the lattice parameters of portlandite crystals and does not change the types of cement hydrates. Nevertheless, in the mortar containing a lower content of TiO₂, the intensity of facets of {0001} increases slightly. While at higher contents of TiO₂, the intensity of facets of {0001} exhibits a much sharper peak. In Fig. 4.4(b), the exhibit aspect ratios (r_L) of CH crystal, that is the intensity ratio of {0001}/{10-10}, increase with the increased content of TiO₂ in the mortar, which corresponds well

with the shape change in portlandite crystal [229]. Typically the portlandite crystals are detected in the shape of hexagonal tabular [229,237–239] (Fig. 4.4(b), pattern a). A larger ratio of r_L indicates a shorter length of crystal along the c axis and a more prominent basal facet (shown in Fig. 4.4(b), pattern c). The SEM images of Portlandite crystal in the mortar are shown in Fig. 4.3. As seen in Fig. 4.3(a), the CH crystal is the typical hexagonal tabular with a small area of {0001} basal facet, and the edge of a single CH crystal is relatively regular. With the increase of TiO_2 amount in the mortar, the CH crystals tend to grow in layers, the boundary edges of layers tend to be indistinct, and the amount and area of {0001} basal facet increase. These SEM images of CH crystals confirm that the CH crystals grow into layered thin hexagonal plates in the presence of a higher amount of TiO_2 hydrosols in the mortar, as illustrated in Fig. 4.4(b).

According to previous studies about the formation mechanisms of stable calcite from Portlandite [238,240,241], calcite can directly nucleate and grow after the dissolution of amorphous $CaCO_3$, vaterite and aragonite, or it can nucleate on vaterite and aragonite, then grow via non-classical particle-mediated aggregation or a classical ion-mediated mechanism. Thus, the precipitation of $CaCO_3$ is dominated by the crystal shape and size of Portlandite, atomic defects [242], and environmental conditions like relative humidity [243], temperature [224], water content and the parameters of pore solution, such as the degree of supersaturation and ion activity [244]. Based on the modified Kelvin equation [245,246], larger CH crystals have lower solubility than smaller crystals, resulting in a slower dissolution of CH in CO_3^{2-} saturated pore solution when CO_2 dissolves into the pore solution of mortar. Furthermore, according to [240], the polymorph evolution of calcium carbonate is slower for larger CH crystals. Thus, the presence of TiO_2 hydrosols in the mortar sample will retard the carbonation of CH because of the larger crystalline size and smaller specific surface area.

(3)   Carbonation products

Fig. 4.5 shows the X-ray diffractograms of all mortar samples containing different concentrations of TiO_2 hydrosols before and after carbonation at 28 days. It is seen that, after 28 days of carbonation, the prominent intensity peak of Portlandite in all mortar samples decreases significantly. The CCH1, CCH2, CCH3 and CCH5 peaks are observed in both mortar samples, proving that the intermediate reactions between Portlandite and CO_2 are still ongoing. These results confirm the slower carbonation reaction rate of CH with layered thin hexagonal plates with significant {0001} basal facet and lower specific surface area.
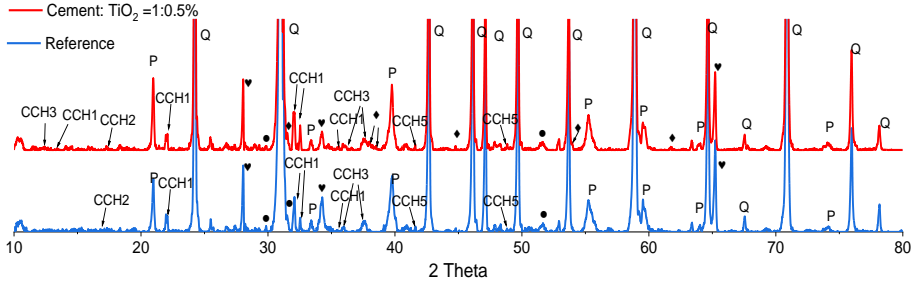
Fig. 4.5 X-ray diffractograms of mortar with and without TiO_2 hydrosols after 28 days of carbonation test. Symbols: Portlandite: P; Quartz: Q; Calcite: ♥; Aragonite: ♦; Vaterite: ●; Calcium carbonate hydroxide: CCH1; Defernite: CCH2; Calcium carbonate hydroxide hydrate: CCH3; Ikaite: CCH4; Monohydrocalcite: CCH5.

The calcite and two kinds of meta-stable aragonite and vaterite phases are detected in the mortar sample containing 0.50 w/w % TiO_2 hydrosols. In contrast, no aragonite peak is detected in the reference mortar samples. According to Black et al. [209], the CaO to SiO_2 ratio (Ca/Si) significantly influences the carbonation products of the synthetic C-S-H(I). When the Ca/Si > 1, the amorphous $CaCO_3$ is always the initial carbonation product, and then the aragonite phase is precipitated with the formation of SiO_2 gel. The initial carbonation product of the C-S-H with Ca/Si of 0.75 and 0.67 is amorphous $CaCO_3$, together with the traces of vaterite. Therefore, it can be deduced that the Ca/Si ratio of C-S-H in the blank mortar is higher than one in the mortar containing 0.5 w/w % of nano TiO_2 hydrosols. The phases of carbonation products also confirm that the C-S-H with a high Ca/Si ratio largely exists in the mortar sample with 0.5 w/w % of nano TiO_2 hydrosols. Because the C-S-H with a higher Ca/Si shows a faster dissolution rate [247], the carbonation rates for C-S-H should increase with the increase of Ca/Si [235].

Based on the above analysis, the presence of TiO_2 hydrosols leads to more CH with larger crystal size and more fibrillar-like C-S-H, which have opposite effects on the carbonation rate of the mortar samples. Thus, it could be hypothesized that when the retardation effect of CH phase prevails, the carbonation rate would be slower; when the acceleration effect of the C-S-H phase prevails, the carbonation rate would be faster. The carbonation degree of mortar will be discussed in Section 4.3.3. The specific surface area of mortar is another significant factor for CO_2 attack. The presence of nano TiO_2 with different concentrations in mortar also affects the variation of the specific surface area of the mortar sample, which will be discussed in Section 4.4.2.

4.3.2   BET specific surface area of mortar

As discussed in Section 4.3.1, the crystal size and morphology of main cement hydrates after curing are significantly influenced by nano TiO_2 hydrosols, reflected by the variation of specific surface area (SSA) of hardened mortar. Fig. 4.6 presents the BET SSA of mortar with

and without TiO_2 hydrosols before and after different carbonation duration. Before carbonation, the SSA of mortar samples increases with the mass content of TiO_2 hydrosols, indicating TiO_2 hydrosols promotes dissolution and subsequent carbonation. The initial crystal morphology of CH and C-S-H phases in TiO_2 modified mortar influences the SSA during the carbonation. After 28 days of curing, the SSA of the mortar increases with the increase of TiO_2 content, confirming again that the morphology of cement hydrates is affected by the added TiO_2 hydrosols.

The SSA of mortar in each group increases with the increase of carbonation duration, attributed to the molar volume difference between the hydrates and the formed $CaCO_3$ [21]. In Fig. 4.6, the SSA of the mortar samples with 0.50 w/w % of TiO_2 hydrosols are less influenced by carbonation. While in the mortar with a lower content of TiO_2 (<0.1 w/w %), the SSA increases obviously with the increase of carbonation duration, attributing to the less molecular volume variation of carbonates in the mortar with 0.50 w/w % of TiO_2 hydrosols during carbonation. The $CaCO_3$ with different crystalline states shows quite different crystal morphology, which also influences the SSA of mortar. As discussed in Section 4.3.1(3), it could be inferred that the carbonation rate of C-S-H plays the leading role, and there are more crystalline phases of calcium carbonate in the mortar with 0.50 w/w % of TiO_2 hydrosols during carbonation. These results confirm that the presence of TiO_2 hydrosols influences the volume difference between the hydrates and the carbonation products.
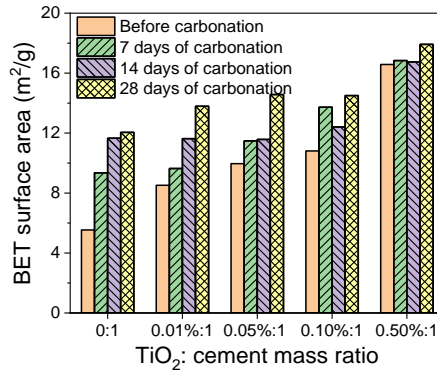
Fig. 4.6 BET surface area of mortar samples containing different amounts of nano TiO_2 undergo different durations of accelerating carbonation test.

4.3.3   Carbonation degree of mortar

The mass loss of mortar samples containing 0.01 w/w % and 0.50 w/w % of TiO_2 upon different carbonation duration are shown in Fig. 4.7. The plots of the reference sample and sample containing 0.05 w/w % and 0.10 w/w % of TiO_2 are shown in Fig. C-5 in Appendix III. The mass loss curves shown in Fig. 4.7 and Fig. C-5 are obtained by TGA.

As shown in Fig. 4.7, the temperature ranges of the endothermic peaks of C-S-H gel, CH in

all test mortar powder samples are relatively stable, while the endothermic peaks of poorly crystalline $CaCO_3$ in the test mortar containing lower TiO_2 (<0.1 w/w % of cement) moves towards the lower temperature. These results reveal that the concentration of nano TiO_2 hydrosols influences the thermo-stability of newly formed poorly crystalline $CaCO_3$. The mass ratios of amorphous $CaCO_3$ (ACC), poorly crystalline $CaCO_3$ (vaterite and aragonite), and well-crystalline $CaCO_3$ (calcite) in TiO_2 modified mortar at different carbonation durations are shown in Fig. 4.8. The ACC and poorly crystalline $CaCO_3$ increase with the carbonation duration, while the increase rate of calcite is slower in the reference mortar without TiO_2 hydrosols. With the increased content of TiO_2 hydrosols in the mortar, the increase rate of ACC is lower than that of crystalline $CaCO_3$, indicating that the existence of TiO_2 hydrosols can accelerate the transformation from ACC to calcite. As shown in Table 4.1, the molecular volume of calcite is smaller than the mean molecular volume of poor-crystalline calcium carbonates. Fig. 4.8 proves that before carbonation the mortar with 0.50 w/w % of TiO_2 has more well-crystalline $CaCO_3$ and less poorly crystalline $CaCO_3$, which explains the BET specific surface area results shown in Section 4.3.2.
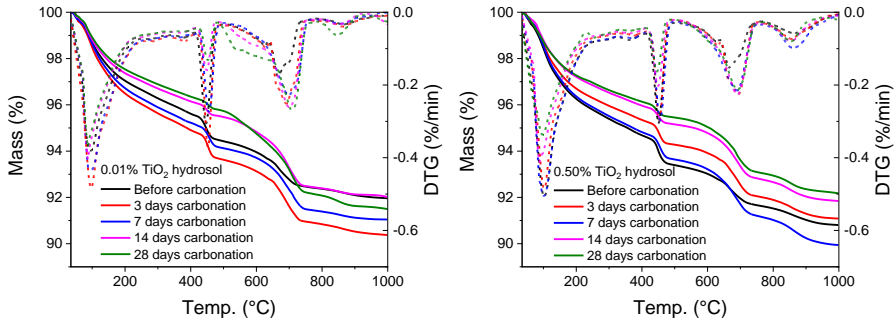
Fig. 4.7 Mass loss of 0.01 w/w % and 0.50 w/w % TiO_2 hydrosols modified mortar during carbonation.

The calculated average carbonation degree values (D_c) of mortar containing different amounts of TiO_2 hydrosols are shown in Fig. 4.9. Before the carbonation test, the initial D_c of mortar samples containing TiO_2 hydrosols are close to the reference mortar. During the carbonation, the D_c of the mortar increases with the content of TiO_2 when the dosage is lower than 0.05 w/w % of cement, while the D_c values of mortar are close when the TiO_2 dosage is higher than 0.05 w/w % of cement. These results prove the hypothesis in Section 4.3.1(2) that the carbonation rates of CH and C-S-H in the mortar samples show an opposite trend with the increase of nano TiO_2 in mortar. Thus, when the TiO_2 hydrosols concentration is lower than 0.05 w/w %, the carbonation rate of CH dominates the mortar carbonation, while when the TiO_2 hydrosols concentration is higher than 0.05 w/w %, the carbonation rate of C-S-H dominates the mortar carbonation. In sum, TiO_2 hydrosols influences the carbonation of C-S-H and CH phases, resulting in different $CaCO_3$ polymorphs in mortar during carbonation. The effects of TiO_2 hydrosols on the microstructure of mortar will be discussed in Section 4.3.5.

(a) TiO₂: cement = 0 %:1

(b) TiO₂: cement = 0.01 %:1

(c) TiO₂: cement = 0.05 %:1

(d) TiO₂: cement = 0.10 %:1

(e) TiO₂: cement = 0.50 %:1
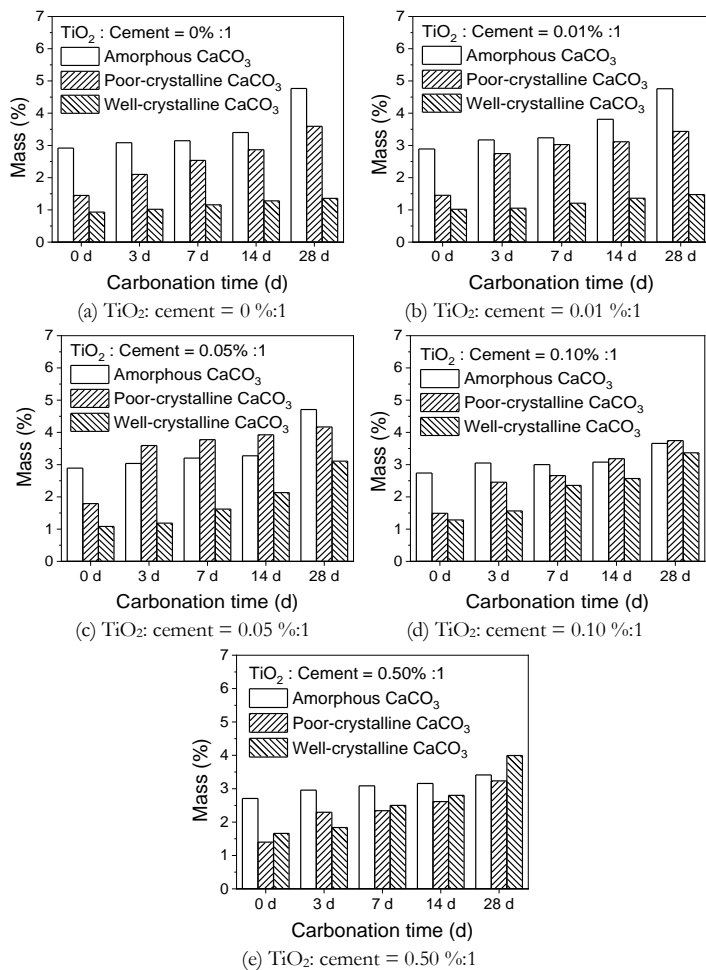
Fig. 4.8 The mass ratios of amorphous, poorly and well crystalline CaCO₃ in mortar samples during carbonation.
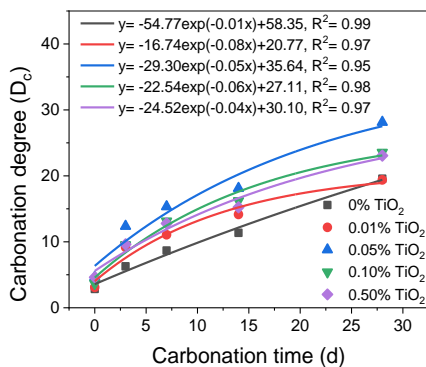
Fig. 4.9 The carbonation degrees of mortar containing different contents of TiO₂ after different carbonation durations.

4.3.4　Self-cleaning performance

(1)　Optical photocatalytic factors

The bandgap energy and Urbach energy are used to evaluate the photoactivity of nano TiO_2 [125,248,249]. The change of bandgap energy can represent the electronic structure change of photocatalysts. The Urbach energy can represent the defects and impurities caused by disorders of the electronic structure of photocatalysts when they are doped by metal, non-metal elements [152,156,187], or cement hydration products [125,126,186]. According to the previous study [199], the photocatalytic performance of nano TiO_2-modified cementitious material is strongly influenced by cement hydration and the age of cementitious materials. The changes in the surface condition of nano TiO_2 particles influence the photo-induced self-cleaning performance of the hardened mortar.
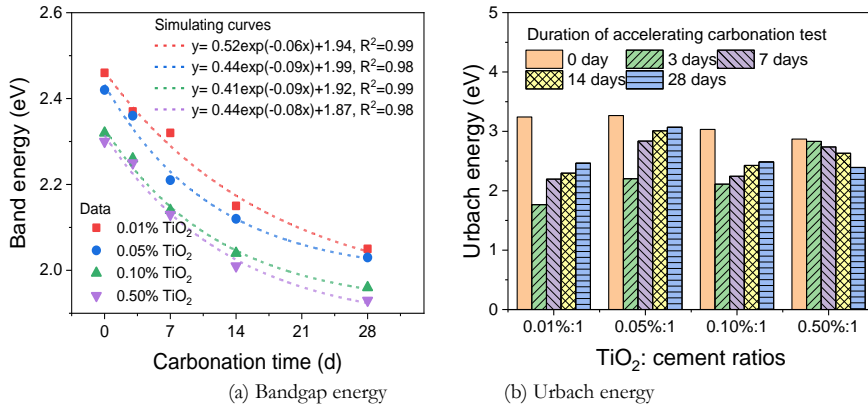
Fig. 4.10 The trends of optical bandgap energy and Urbach energy of TiO_2-mortar compounds along with the accelerating carbonation duration.

Fig. 4.10 shows the changes in bandgap energy and Urbach energy of TiO_2-mortar compounds at different carbonation durations. The detailed reflectance curves, Tauc's plots and simulating curves for calculating the Ubrach energy of mortar samples are shown in Figs. C-2 to C-4 in Appendix III. As shown in Fig. 4.10(a), the bandgap energy of all TiO_2-mortar compounds decreases with the carbonation duration exponentially. In TiO_2-mortar samples, the reduction in band edges may be due to locally defective states in the bandgap near the bottom or the top of the TiO_2-mortar conduction band or valence band. These results reflect that the mortar matrix (mainly hydrates and sands) may disrupt the semiconductor electronic structure of the TiO_2 by producing defects [125]. The carbonation of the mortar matrix significantly impacts the structural disorder of mixed nano TiO_2. As shown in Fig. 4.10(b), when the TiO_2 to cement ratio is lower than 0.10 w/w %, the Urbach energy decreases sharply after three days of carbonation and slowly increases during further carbona-

tion. The decrease of bandgap energy indicates that the Urbach tail of TiO_2-mortar compounds increases with the carbonation duration. The high value of Urbach energy means that impurities and defects (mainly the Ti^{3+} and oxygen vacancies) make the structure of TiO_2 highly disordered, forming an absorption tail that extends to the depth of the forbidden zone [125,155,228]. In general, the higher the Urbach energy, the better the photocatalytic performance of the sample is expected. The following Section 4.4.2 will discuss the self-cleaning performances of TiO_2-mortar samples.

The changes in surface defect status and disorder of the TiO_2-mortar during carbonation also prove that the photocatalytic self-cleaning property of mortar is closely related to the crystal pattern and morphology evolution of main cement hydrates. Section 4.4 will describe the relationship between the chemical conversions of cement hydrates and the photocatalytic activity of TiO_2-mortar compounds.

(2)   Chromatics factors

As to the influences of carbonation on the photo-activity of TiO_2 modified mortar, Fig. 4.11 shows the change of R_4 and R_{26} on the surface of the mortar at different carbonation durations. Before the accelerated carbonation test, except the sample containing 0.01 w/w % of TiO_2, the colour change rates of samples are greater than 25 % (R_4) and 50 % (R_{26}) after 4 hours and 26 hours of UV irradiation. These indicate that the low dosage TiO_2 hydrosols modified mortar samples are sufficiently photoreactive before carbonation. Fig. 4.11(a) shows that although the value of R_4 in each mortar sample decreases with the increase of carbonation duration, the R_4 of most mortar samples is still higher than 20 %, except for the mortar with 0.01 w/w % of TiO_2 after 28 days of carbonation. The influence of hydrates carbonation on the R_{26} value of the mortar sample is more remarkable in Fig. 4.11(b). After the first three days of carbonation, the R_{26} value of the mortar with 0.01 w/w %TiO_2 is reduced by 20.1 %, while the R_{26} values of the mortar with 0.01 w/w % to 0.50 w/w % of TiO_2 are reduced by about 30 %. However, it is worth mentioning that the R_{26} of mortar with 0.50 w/w % decreases after seven days of carbonation and then increases to 52.1 % after 28 days of carbonation, while the R_{26} values of mortar containing 0.05 w/w % and 0.10 w/w % TiO_2 starts to increase after three days of carbonation.

It is noted that the TiO_2-mortar sample containing 0.01 w/w % of TiO_2 presents similar values of Urbach energy with the sample containing 0.05 w/w % of TiO_2, but the RB degradation rate (R_{26}) is not as high as that in the sample containing 0.05 w/w % of TiO_2. These may be related to the amount of effective reaction sites and the amount of RB molecules during the self-cleaning test. When the TiO_2 to cement ratio is between 0.01 % and 0.10 %, the variation rule of the Urbach energy of TiO_2-mortar is similar to that of $R_{26,}$ as shown in Fig. 4.11(b). Therefore, the continuous decline of Urbach energy during carbonation will lead to the continuous decrease of photocatalytic self-cleaning performance of photocatalysts, assuming no other factors are involved. However, when the TiO_2 to cement ratio is

higher than 0.10 %, the R_{26} value of mortar slowly upswings after 28 days of carbonation.

(a) R_4 (b) R_{26}
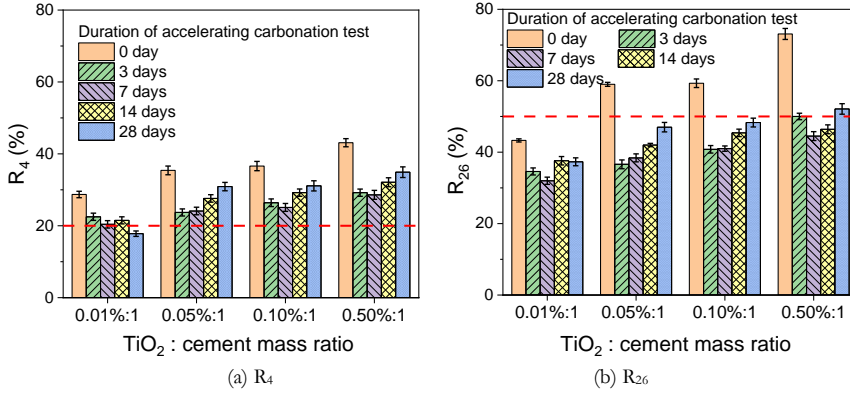
Fig. 4.11 Colour change rates R_4 and R_{26} of mortar in each test group.

In the previous study [228], the surface electron capture effect of hydration products plays an essential role in improving the self-cleaning performance of non-carbonated hardened cement paste with a higher dosage of TiO_2 hydrosols (>0.05 w/w % of cement). Based on the results in Section 4.3.1 and Section 4.3.2, the calcium carbonate phase in the sample containing 0.50 w/w % TiO_2 has several different polymorphs during carbonation, and the SSA increase induced by carbonation is much smaller than in the other samples. Thus, it is speculated that the recovery of the photocatalytic self-cleaning performance of carbonated mortar is closely related to the physical properties and morphologies of different polymorphs of $CaCO_3$. The relationships between carbonates and photocatalytic self-cleaning performance will be thoroughly discussed in Section 4.4.

4.3.5   Morphology evolution of $CaCO_3$

The SEM images of different mortars at different carbonation durations are shown in Fig. 4.12. Fig. 4.12(a, e, i) shows that both rhomboscalenohedral calcite crystal and vaterite aggerates are observed on the reference mortar after three days of carbonation. On the surface of mortar with 0.01 w/w % TiO_2, rod aragonite crystals are detected besides calcite and vaterite. More rod aragonite crystals are observed on the surface of mortar containing 0.05 w/w % TiO_2. In Fig. 4.12(b, f, j), after seven days of carbonation, the spherical vaterite crystals are observed on the surface of the reference mortar, while the vaterite particles tend to merge in the mortar containing 0.01 w/w % TiO_2. The rod-shaped aragonite crystals transform into larger flower-shaped and smaller cauliflower-shaped aragonite crystals on the mortar surface containing 0.50 w/w % TiO_2. Fig. 4.12(c, g, k) shows that the spherical vaterite crystals are merged, and the scalenorhombohedral calcite crystals are aggregated on the reference surface. On the surface of mortar with 0.01 w/w % TiO_2, aggregates of rhomboscalenohedral calcite crystals, and spherical aggregates of scalenorhombohedral calcite

crystals are observed. The flower-shaped aragonite crystals transform into smaller aragonite radiating clusters of tiny prismatic crystals in the mortar with 0.50 w/w % TiO_2. In Fig. 4.12(d, h, l), vaterite and calcite phases are observed on the surface of the reference mortar, and the mortar containing a lower dosage of TiO_2 (<0.05 w/w %), while aragonite is the main meta-stable phase of $CaCO_3$ in the surface of mortar sample containing a higher dosage of TiO_2 (>0.05 w/w %).

As discussed in Section 4.3.1(2) and Section 4.3.2, the TiO_2 hydrosols significantly impacts the crystal sizes and shapes of CH and C-S-H phases in hydrated mortar samples, further affecting the specific surface areas of mortar samples after the curing of 28 days. According to the previous studies [250,251] on the interaction of nitrogen oxides (NO_x) with the nano TiO_2 photocatalytic cementitious materials, the TiO_2 nanoparticles contribute to the NO_x absorption increase because of increasing the SSA of the matrix. Moreover, as mentioned in Section 4.3.1, the mortar containing a higher dosage of TiO_2 shows higher SSA and bigger CH and more fibrillar C-S-H phases. Thus, the addition of nano TiO_2 influences the CO_2 absorption and the crystal solubility in pore solution at the initial period of the carbonation test. As a result, the cement hydrates in the mortar with TiO_2 hydrosols show different morphological evolution during carbonation. In addition, the volume and size of polymorphs of $CaCO_3$ change with the increase of carbonation duration, indicating that the coverage effect of $CaCO_3$ on the mortar surface also changes during carbonation.

To further understand the distribution evolution of TiO_2, $CaCO_3$ polymorphs, and main hydrates (Portlandite and C-S-H phase), Fig. 4.13(a) shows the Raman images by CRM of mortar samples with 0.50 w/w % TiO_2 before and after carbonation. The Raman images of mortar samples containing 0.01 w/w %, 0.05 w/w % and 0.10 w/w % TiO_2 are shown in Fig. C-6 in Appendix III.

According to the previous studies, the Raman band of 144 cm^{-1} [168], 356 cm^{-1} [178], and 667 cm^{-1} [169] are referred to as the phase of anatase TiO_2, Portlandite, and C-S-H, respectively. For the polymorphs of $CaCO_3$, the Raman band of 7191 cm^{-1}, 703 cm^{-1}, and 750 cm^{-1} [252–255] refer to the phases of calcite, aragonite, and vaterite, respectively. In Fig. 4.13, the areas outlined in red, green, violet, blue, light blue, and yellow represent the anatase TiO_2, CH, C-S-H, calcite, aragonite, and vaterite, respectively. The area ratio of each phase in the CRM images is calculated and shown in Fig. 4.13(b). As shown in Fig. 4.13, before carbonation, the CH and C-S-H phases are the leading cement hydrates, while the vaterite crystals are scattered around the C-S-H phases, and the aragonite crystals are scattered among the CH, anatase TiO_2, and calcite crystals. After seven days of carbonation, the CH phase is carbonated to aragonite and vaterite. The sphere-shaped vaterite crystals are merged into more massive clusters covering the mortar surface. Simultaneously, the aragonite crystals grow more extensively and cover most areas of the tested surface. After 14 days and 28 days of carbonation, the calcite phase continuously increases due to the further carbonation of CH, aragonite, and vaterite phases, while the anatase TiO_2 crystal increases slightly.

Comparing the results of SEM and CRM of TiO_2-modified mortar, we can conclude that the exposure area of TiO_2 first reduces because of the coverage effect caused by the formed vaterite and aragonite phase at the initial seven days of carbonation. Then, the exposure area of the TiO_2 phase is regained, mainly because of the crystal shape and pattern evolution of the aragonite phase at a longer carbonation duration. Due to the photochemical reactions on the interfaces between pollution and photocatalysts, the exposure area of the TiO_2 anatase phase on the surface of mortar dominates the self-cleaning performance of TiO_2- mortar catalyst. The essential point is that the chemical reaction between CO_2 and cement hydrates involves a series of crystal phase and shape evolution processes that firmly control the exposure area of TiO_2 in the mortar. These results confirm that the photocatalytic self-cleaning performance of TiO_2 hydrosols modified mortar shows the first decline and then recovered trend, attributed to the crystal morphology evolution of $CaCO_3$ polymorphs caused by carbonation.

(a) The Raman images   (b) Statistical area values vs. carbonation duration
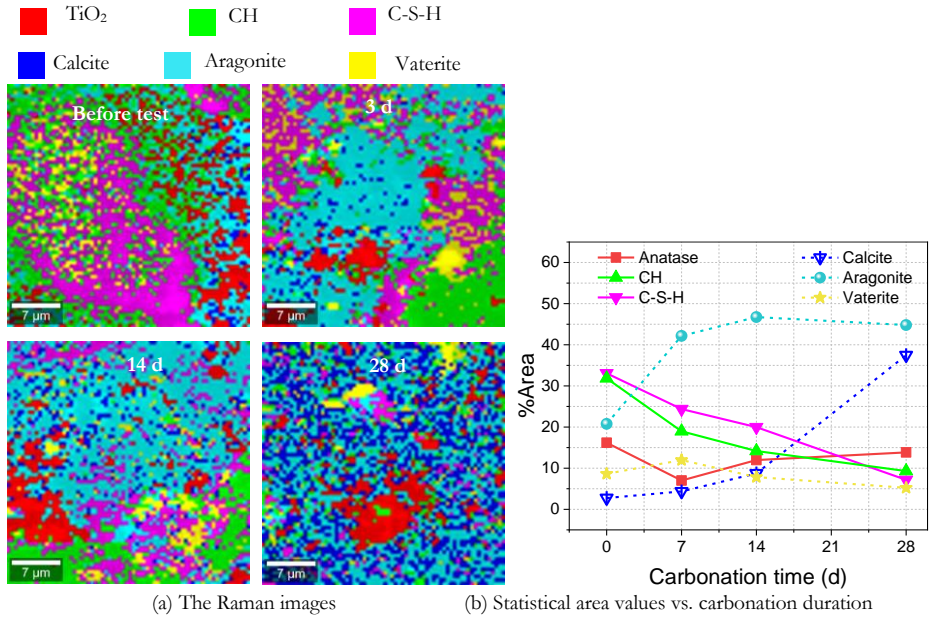
Fig. 4.13 (a) Raman mapping images by CRM of the evolution of the presence of the main phases in the mortar contains 0.50 w/w % TiO_2 at different accelerating carbonation test time (the scan area is 35 μm×35 μm) and (b) Semi-quantitative calculation of the presence of the main phases present of TiO_2 hydrosols modified mortar during the carbonation.
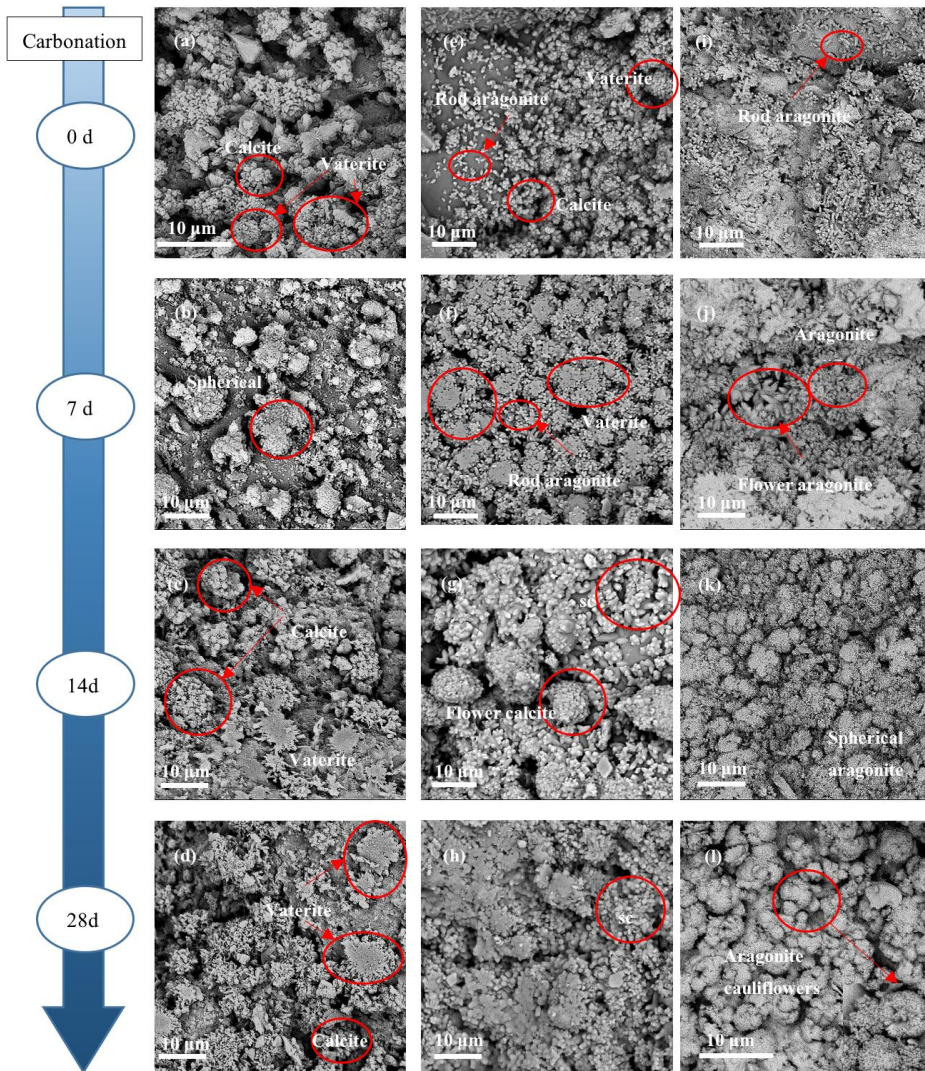
Fig. 4.12 SEM images of tested mortar samples containing TiO₂ hydrosols before and after accelerating carbonation test (Fig. (a-d) belong to the reference group; Fig. (e-h) belong to the mortar mixed 0.01 w/w % TiO₂; Fig. (i-l) belong to the mortar mixed 0.50 w/w % TiO₂; crystal shape of calcite, sc: scalenorhombohedral).

4.4   Discussions

Since the properties of the main hydration products change during carbonation, the influence of carbonation on self-cleaning performance needs to be considered. The photocatalytic activity of photocatalytic concrete is closely related to the effective exposure surface area of photocatalysts, cement hydrates and carbonates in the matrix surface. Therefore, the

discussion of the interrelated roles of individual cement hydrates and carbonates on the photocatalytic self-cleaning performance of mortar is essential to distinguish the significance of each factor.

4.4.1 Correlation analysis between photocatalytic performance and mortar composition

The principal factor analysis is used to analyse the factors that influence mortar's variation of photocatalytic self-cleaning performance during carbonation. Fig. 4.14 shows the correlation plot among R_{26}, anatase, cement hydrates and carbonates area ratios, carbonation degree (D_c) and carbonation duration.

The Spearman correlation coefficient measures the monotonic association between two variables in terms of rank. Spearman correlation coefficients are often used to measure whether one variable increases or decreases with another, even if the relationship between the two variables is not linear or bivariate normal. Considering that the relationships between R_{26} and its influential factors may not be linear, a heat map is used to display the features of the correlation matrix of Spearman correlation coefficients, as shown in Fig. 4.14. In the correlation matrix, Spearman's rank correlation coefficient values shown in the lower triangular matrix in Fig. 4.14 correspond to the colours in the upper triangular matrix.

Spearman's rank correlation coefficients with high absolute values (>0.50) indicate that this variable is monotonous consistent with the output. The asterisks in the upper triangular grids in Fig. 4.14 mean the p-values in the statistical analysis, representing the significant level of parameters on the horizontal axis to those on the vertical axis. An asterisk represents the p-value is smaller than 0.05, two asterisks represent the p-value is smaller than 0.01, while three asterisks represent the p-value is smaller than 0.001. For example, the change of R_{26} is monotonously corresponding to the area ratios of anatase, CH, C-S-H, $CaCO_3$ and the TiO_2 content, where the significant levels of the variation of the area ratio of anatase and the TiO_2 content are higher than that of the area ratio of C-S-H.

The anatase area ratio is closely influenced by the variation of CH, C-S-H, D_c and nano TiO_2 content in mortar while changing of D_c is associated with the variation of main cement hydrates and carbonates. As shown in Fig. 4.14, the total $CaCO_3$ area ratio is mainly monotonously related to the variation of D_c, carbonation duration and TiO_2 content. Since both CH and C-S-H area ratios are monotonously related to the variation of the anatase area ratio and the carbonation duration that is monotonously corresponding to the variation of D_c, the anatase area ratio and D_c are suitable as characteristic variables of R_{26}. Due to the data being more easily collected, the TiO_2 content is selected as the characteristic variable of the anatase area ratio, D_c is selected as the characteristic variable of $CaCO_3$ area ratio in this chapter. Therefore, it is feasible to establish a prediction model for the changing of R_{26} with the variation of characteristic components of photocatalytic mortar.
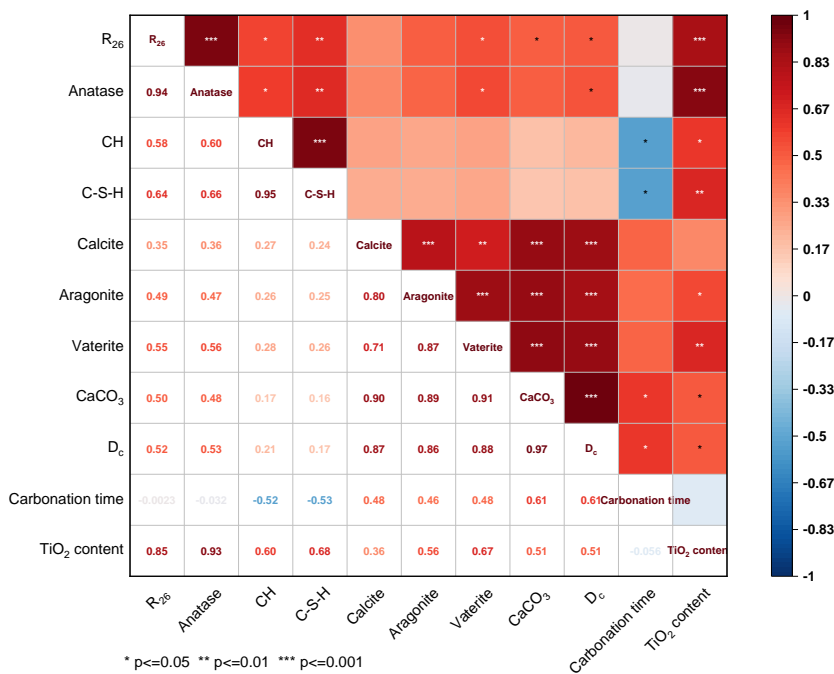
Fig. 4.14 Correlation matrix of the factors related to the photocatalytic self-cleaning performance.

4.4.2 Prediction model of photocatalytic self-cleaning performance during carbonation

Here, the variation of photocatalytic self-cleaning performance of mortar during carbonation can be predicted by two pairs of characteristic variables as mentioned in Section 4.4.1. A more straightforward intuitional relationship is expected to describe the R_{26} with the variation of anatase and $CaCO_3$ exposure area ratios. The binary functional relationship is established among the R_{26}, anatase area ratio, and $CaCO_3$ area ratio, the simulated 3D surface is shown in Fig. 4.15, and the following equation can describe the relationship:

$$R_{26} = 32.10 + 2.80\,A_{TiO_2} - 0.46 A_{CaCO_3} + 0.03 A_{TiO_2}^2 + 0.006 A_{CaCO_3}^2 - 0.03 A_{TiO_2} \times A_{CaCO_3} \quad (4.4)$$

The correlation of this fit is 0.95, indicating that this binary function can describe the change law of photocatalytic self-cleaning performance of mortar along with the change of carbonate area well.

R_{26} is the percentage of discolouration of RB on the surface of photocatalytic mortar after 26-hour irradiation of UV, representing the photocatalytic self-cleaning ability of mortar;

$ATiO_2$ and A_{CaCO3} are the area ratios of anatase and calcium carbonates in the surface of photocatalytic mortar detected by CRM, 3.5 %$<ATiO_2<$12 %.

Considering the difficulty of obtaining experimental data in the CRM analysis, we propose to quantify the influences of carbonation on the photocatalytic self-cleaning ability of nano TiO_2 hydrosols modified mortar by using the characteristic factors of anatase and $CaCO_3$ area ratios, namely nano TiO_2 (anatase) contents in the mortar and the carbonation degrees of mortar.

$$R_{26} = 48.0 + 204.0\, C_{TiO_2} - 4.5D_c - 276C_{TiO_2}^2 + 0.23D_c^2 - 2.17C_{TiO_2} \times D_c \qquad (4.5)$$

Fig. 4.16 presents the fitting surface and binary function of the variation of R_{26} along with the variation of nano TiO_2 content and D_c of mortar. R_{26} is the percentage of discolouration of RB on the surface of photocatalytic mortar after 26-hour irradiation of UV; C_{TiO2} is the initial weight content ratio of anatase mixed in the mortar, 0.01 % $< C_{TiO2} <$ 0.5 %; D_c is the carbonation degree of mortar calculated in Section 4.3.3.

The proposed model shows an excellent correspondence, with a high fitting degree of 0.93. It should be noted that the functional relationship shown in Eq. (4.5) is widely applicable because the variable of D_c is more easily collected in the lab than component area ratios. Based on this proposed model, the photocatalytic self-cleaning performances of nano TiO_2 hydrosols-modified cementitious materials during carbonation can be calculated if the carbonation degree and the anatase content in mortar are obtained. However, due to this numerical model being established on the limited tested data only in this chapter, the accuracy of this model may not be good enough for predicting the self-cleaning performances of the photocatalytic cementitious materials in other studies. At least, the processes of demonstration and the establishment of this model provide a feasible way to clarify the relationship between the hydrates carbonation and the variation of photocatalytic self-cleaning performance of photocatalytic cementitious materials.
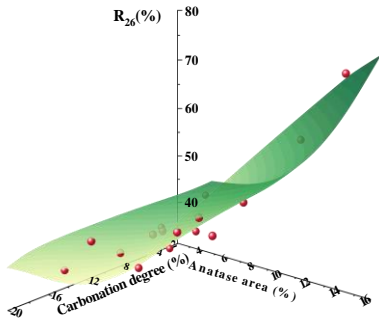
Fig. 4.15 Simulating surface among R_{26}, anatase and $CaCO_3$ area ratios.
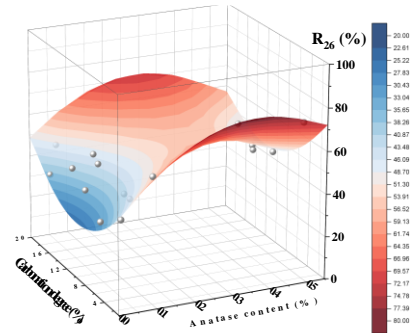
Fig. 4.16 Simulating surface among R_{26}, anatase content and carbonation degree.

4.5   Summaries

This chapter studies the effects of carbonation on the photo-induced self-cleaning performance of nano TiO_2 hydrosols-modified mortar. The coverage effect of cement hydration products and the evolution of crystal morphology during carbonization are considered in studying the relationship between carbonation and self-cleaning performance of mortar. The following conclusions can be drawn from the acquired results:

(1) Carbonation reduces the self-cleaning performance of the photocatalytic mortar. The photoactivity of TiO_2-mortar is seriously affected by aragonite, vaterite or intermediate products of calcium carbonate. After complete carbonation, a large amount of aragonite and unstable calcium carbonate transforms into a stable calcite phase with a smaller volume. The re-exposure of photocatalytic active sites leads to recovery of the self-cleaning performance of the carbonated mortar.

(2) Nano TiO_2 hydrosols affect the carbonation rate of cement hydrates. The amount of nano TiO_2 hydrosols significantly influences the crystal type and volume of carbonation products. When the dosage of nano TiO_2 is less than or equal to 0.05 w/w % of cement, the surface defects of nano TiO_2 decrease first and then increase with the carbonation duration; the carbonation rate of C-S-H dominates the carbonation process of mortar. When the nano TiO_2 dosage is greater than 0.05 w/w % of cement, the surface defects of nano TiO_2 decrease continuously, and the carbonation rate of CH dominates the carbonation process of mortar.

(3) During carbonation, the self-cleaning ability is closely related to the anatase exposure area ratio and the area ratio of $CaCO_3$ in the mortar surface. The anatase content and the carbonation degree are the characteristic variables of the photocatalytic self-cleaning performance of nano TiO_2-modified mortar during carbonation. A new model is proposed to describe the performance evolution of the photocatalytic self-cleaning property of mortar by TiO_2 content and the carbonation degree.

Chapter 5 Photocatalytic self-cleaning performance reactivation of nano TiO$_2$ hydrosols modified mortar during wetting and drying cycles in pure water

Dissolution and diffusion of hydrates caused by renewed and slightly ionized water not only lead to the degradation of the cementitious matrix but also affect the photo-induced function of nano TiO$_2$-modified concrete. This chapter focuses on the photocatalytic self-cleaning performance variation of mortar containing different dosages of nano TiO$_2$ hydrosols during wetting and drying cycling in pure water. The colourimetric analysis is used to evaluate the self-cleaning performances of mortar samples suffering pure water attack. The distribution areas of anatase TiO$_2$ and main hydrates in the mortar surface are characterized by the Confocal Raman Microscopy. The data recorded during the 40 times of wetting and drying cycles show that both the self-cleaning ability and optical parameters of photocatalytic mortar change sinusoidal with the number of cycles, which period is about 20 cycles. A possible changing law is suggested to describe the photocatalytic reactivation behaviours of nano TiO$_2$ hydrosols modified mortar during wetting and drying cycles.

5.1   Introduction

As one of the commonly used building materials for facades, cementitious materials always suffer the wetting and drying cycling effects caused by rainy days. The porous microstructure in the cementitious materials matrix will be influenced by the dissolution of the cement hydrates during the cyclic humidity change, resulting in the deterioration of concrete structures [256]. In general, the wetting and drying cycling effects, for example, rain, caused by erosion solutions, such as chloride or sulphate solutions, are common conditions in the field of concrete durability. Lots of works have studied the influence laws of wetting and drying cycles on the changes in porous structure, mechanical properties and the volume stability of concrete. The majority of results in the literature [257–260] prove that the feature parameters of mechanical and durability of cementitious materials decrease obviously in the conditions of wetting and drying cycles. Here, it should be pointed out that pure water is a kind of erosion solution for cementitious materials because of the high alkalinity in the pore solution. At the cement paste contact, pure water creates concentration gradients, which lead to the diffusion of ions from the interstitial solution to these aggressive solutions [261–264]. These transfers modify chemical balances and create leaching of the calcium hydroxide and then a progressive decalcification of the C-S-H [265–268].

As to photocatalytic cementitious materials, water from rain and tip water are the most common erosion solutions, and they barely contain ions. Therefore, the influences of wetting and drying cycles in pure water on the functional photo-induced self-cleaning properties of photocatalytic mortar are critical to practical applications. Several previous works [269–273] have paid attention to the damage and functional durability of photocatalytic coatings under the simulated wetting and drying cycles of rain. According to the results in the previous chapters, nano TiO_2 particles of hydrosols disperse evenly surrounded by the hydrates in the cementitious matrix, which deeply influence electronic structures via surface modification and surface-doping effects. The surfaces of nano TiO_2 particles are disordered because of the additional surface defects. The photon-induced electrons can be captured by hydrates with positive charges, enlonging the lifetime of hole-electron pairs and improving the photocatalytic activity of cementitious materials. Therefore, the electronic structure and the surface conditions of nano TiO_2 particles in cementitious materials could be affected by the changing of hydrate phases and volume variations, resulting in the variation of photocatalytic self-cleaning properties of the cementitious materials.

Moreover, an often-overlooked phenomenon of cementitious materials during the wetting and drying effects of rain is the change of colour due to the leaching of calcium in the matrix, resulting in the variation of the albedo of building facades. Compared with the deterioration of mechanical properties of normal buildings, the change in colour does not seem to be that much. However, for photocatalytic buildings, the change of solar reflectance caused by col-

our change directly affects the photocatalytic activity of the cementitious materials, influencing the photo-induced self-cleaning performance of the buildings.

However, a few studies have focused on the effects of the change of cement hydrates on the self-cleaning properties of photocatalytic cementitious materials under the attack of alternating wetting and drying in pure water. This chapter mainly studies the changing laws of photocatalytic self-cleaning performance of nano TiO_2 hydrosols modified mortar with the number of wetting and drying cycles in pure water. The kinetic processes of the photocatalytic reaction of TiO_2-mortar are analyzed, and the correlations between the exposure of nano TiO_2 in mortar and photocatalytic activity caused by the quantity change of hydration products are established.

5.2   Materials and methods

5.2.1   Materials

CEM I 52.5R cement, CEN-EN 196-1 standard sand and tip water are used to made mortar samples. The chemical components of cement are listed in Table 5.1. The water to binder ratio is 0.5, and the sand to cement ratio is 3. The nano TiO_2 hydrosols to cement mass ratios are 0 %; 0.01 %; 0.05 %; 0.10 % and 0.50 %. The size of each mortar sample is 40 mm × 40 mm × 160 mm. All the samples are demoulded after one day, and then cured in the curing room with the RH of 95 % and temperature of 20 °C until the test age. The chemical composition of cement is shown in Table 5.1, which is tested by X-ray fluorescence spectroscopy.

Table 5.1 Chemical composition of CEM I 52.5 R cement.

Components	CaO	SiO$_2$	Fe$_2$O$_3$	SO$_3$	Al$_2$O$_3$	MgO	K$_2$O	TiO$_2$	P$_2$O$_5$	Minor elements*
Content (%)	66.34	18.22	3.81	3.15	5.56	1.68	0.29	0.50	0.16	0.30

* V_2O_5+Cr_2O_5+MnO+CuO+ZnO+BaO+Cl

5.2.2   Methods

(1)   Wetting and drying cycles

In the wetting and drying cycles, a typical cycle parameter of the mortar sample is as follows: the sample is vacuum dried at 50 °C for seven hours, and then completely soaked in deionized water for 17 h. A total of 40 wetting and drying cycles are carried out for each test sample. The laboratory temperature is maintained at 20 ± 0.1 °C, and the relative humidity is maintained at 50 ± 0.1 %. The prismatic mortar samples for the wetting and drying cycles are all cured to 28 days of age. Before the experiment, the prismatic mortar samples are cut off 1 cm at both ends and then cut into flake samples with a side length of 4 cm and a

thickness of 1 cm. During the wetting and drying cycles, one sample is prepared every five cycles for each test group, and the deionized water is renewed every five cycles.

(2) Photocatalytic self-cleaning tests

The self-cleaning performances of the TiO_2-modified mortar slice samples are evaluated by the colourimetric analysis of the degradation of the organic dye Rhodamine B (RB) [228]. Each surface area of the paste sample is stained by painting 600 μL of 50 mg/L RB aqueous solution. Then, the samples are kept overnight in the dark at room temperature for drying. Subsequently, the samples are exposed to a UV lamp (10 ± 0.05 W/m²) to simulate UV light in natural conditions, and the discolouration of the samples is monitored. The UV lamp is composed of three UV tubes with a power of 25 W, the UV-A wavelength ranges from 300 nm to 400 nm, and the centre is at 345 nm. The reflected colour and the reflectance spectra measurements are taken on the sample's surface with a spectrometer (USB4000, Ocean optics, United Kingdom) equipped by a light resource with a wavelength range from 380 to 780 nm. For mortar with each dosage of nano TiO_2, two slices are used as the parallel samples. Nine points are recorded for the colourimetric tests for each sample, and each point is tested four times. The colour of each sample is measured after 0.5h, 1h, 2h, 4h, 8h, 16h and 26h of UV irradiation, respectively. The percentage of discolouration of RB on the surface of mortar (R_t) is expressed with a* value coordinate of the dominant colour of dye in the CIE Lab colour space [120,121,131], according Eq.(3.1) in Chapter 3.

5.2.3 Characterizations

Calorimetric tests are performed using an isothermal calorimeter (TAM Air, TA Instruments, USA) with a test temperature of 20 °C. The cement powders are first mixed with deionized water and nano TiO_2 hydrosols, then injected into the ampoule bottles, sealed with the lids, and loaded into the calorimeter. The total recorded data is over 140 hours. The crystal patterns of cement hydrates before and after the accelerated carbonation test are determined by the X-ray diffraction (XRD) pattern (Bruker D4 PHASER, Philips, The Netherlands) with a Co tube (40 kV, 40mA), with the test step size of 0.02°/min and dwell time of 0.5s. Thermal gravimetric analysis (TGA) is performed using a thermal analyser (STA 449 F1, NETZSCH, Germany), with nitrogen as a protective gas, and the test sample is heated from 40 °C to 1000 °C at a rate of 10 °C / min. Before the test, all the samples need to be crushed and soaked in acetone for seven days and dried in an oven at 40 °C to stop further hydration of the cement. Ultraviolet-vision-near-infrared spectrophotometer (PerkinElmer 750, USA) is used to measure the reflectance spectra of TiO_2-modified hardened cement paste samples at different ages (1d, 3d, 7d, 14d, 28d) before and after wetting and drying cycles. The test range is 200-2200 nm, and the scanning rate is 2 nm/s. To meet the test requirements, the samples are cut into slices with a thickness of about 1 cm. The phase distributions on the surface of hardened cement paste are observed by Confocal Raman Microscopy (CRM)

(Witec alpha300S, Witec, Ulm, Germany). The wave number of spectra recorded by Raman spectroscopy ranges from 0 to 3900 cm^{-1}. Confocal Raman measurements are performed using a 532 nm excited laser with a power of 30 mW. The collected Raman spectra are analyzed using WITec Suite 5.2 software (WITec, Ulm, Germany). In the process of obtaining the results of CRM spectroscopy, data processing methods such as cosmic ray removal and background deduction are carried out.

5.3   Results and discussions

5.3.1   Variation of optical photocatalytic factors

The diffuse reflection spectra of mortar samples with different wetting and drying cycles in pure water are measured by UV-VIS-NIR spectrophotometer, and the change curves of TiO$_2$-mortar band gap energy values and Urbach energy values with the number of wetting and drying cycles of pure water are obtained by calculation, as shown in Figure 5.1. Detailed solar reflectance curves, T$_{auc}$ curves and simulated curves of calculated Urbach energy values of mortar samples are shown in Fig. D-1 to D-3 in Appendix IV of this thesis.

It can be seen from Fig. 5.1 that the band gap energy values of the mortar without wetting and drying cycling decrease with the increase of the dosage of nano TiO$_2$ hydrosols, while the Urbach energy values increase with the increase of the dosage of nano TiO$_2$ hydrosols. With the increase in the number of wetting and drying cycles in pure water, the band gap energy curves show a fluctuating trend of 'W' shape. Urbach energy curves, on the other hand, show a wavy downward trend of 'M' shape. Taking TiO$_2$: cement as 0.10 % as an example, the band gap energy of TiO$_2$-mortar decreases from the initial value to a bottom after 10 wetting and drying cycles of pure water, and the Urbach energy increases from the initial value to the first peak. Then, after 20 wetting and drying cycles of pure water, the band gap energy of TiO$_2$-mortar increases again to the initial value, while the Urbach energy decreases from the initial value to the first valley bottom. After 30 wetting and drying cycles of pure water, the band gap energy of TiO$_2$-mortar decreases again to the second valley bottom, but this valley bottom is higher than the first valley bottom, while the Urbach energy increases from the initial value to the second peak, but this second peak value is lower than the first peak. After 40 wetting and drying cycles of pure water, the band gap energy of TiO$_2$-mortar increases to more than the initial value, while Urbach values decrease to less than the initial value. The decrease of band gap energy and the increase of Urbach energy indicate that the electronic structure of nano-TiO$_2$ particles has a serious imbalance after 10 wetting and drying cycles of TiO$_2$-mortar samples, which can be excited by photons with longer wavelengths, and there are more surface defects on the surface of the particles, such as oxygen holes and Ti^{3+}. These surface defects can trap photogenerated electrons or holes, prolong the life of photogenerated electrons and holes, and improve the photocatalytic activity of TiO$_2$-mortar. From the results of optical parameters of TiO$_2$-mortar, it can be predicted that the self-cleaning performances of photocatalytic mortar should show a wavy change

trend with the increase of the number of wetting and drying cycles of pure water.

(a) Bandgap energy   (b) Urbach energy
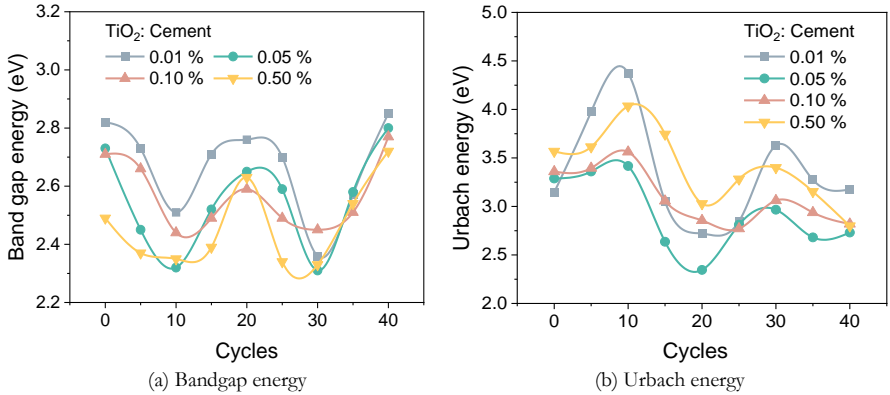
Fig. 5.1 The variations of optical bandgap energy and Urbach energy of TiO$_2$-paste compounds along with the cycles of wetting and drying tests.

5.3.2   Photocatalytic self-cleaning performance

The self-cleaning performances of photocatalytic mortar samples are characterized by the degradation rate of RB under mortar UV irradiation after different wetting and drying cycles of pure water with different dosages of nano TiO$_2$ hydrosols. The test results are shown in Fig. 5.2. As shown in Fig. 5.2, the results of RB degradation rates in the control group (without nano TiO$_2$) have not obtained obvious photocatalytic self-cleaning ability. When the TiO$_2$ to cement mass ratio is 0.01 % (in Fig. 5.2(b)), the RB degradation rate of mortar before the wetting and drying cycle test is close to 50 % after 26 hours of UV irradiation. However, after specific wetting and drying cycles, such as 10 or 30 cycles, the RB degradation rate of mortar exceeds 50 %, indicating the wetting and drying cycle process has a certain promotion effect on its self-cleaning performance that in such a low dosage of TiO$_2$ modified mortar. When the TiO$_2$ to cement mass ratio is greater than and equal to 0.05 %, the mortar shows good photocatalytic self-cleaning performance before and after the wetting and drying cycles.

Another interesting phenomenon that could be found in Fig. 5.2(c -e) is that the number of wetting and drying cycles of pure water leads to a certain regular fluctuation in the RB degradation rate of mortar at a certain UV irradiation time. Taking the mortar sample containing 0.1 % of TiO$_2$ hydrosols (Fig. 5.2(d)) as an example, after ten wetting and drying cycles of pure water, the R$_{26}$ of mortar increased from 73 % to 81 %. After 20 wetting and drying cycles of pure water, R$_{26}$ value decreases to 73 % again. After 30 wetting and drying cycles of pure water, R$_{26}$ re-increased to 79 %. After 40 wetting and drying cycles of pure water, R$_{26}$ re-decreased to 71 %.
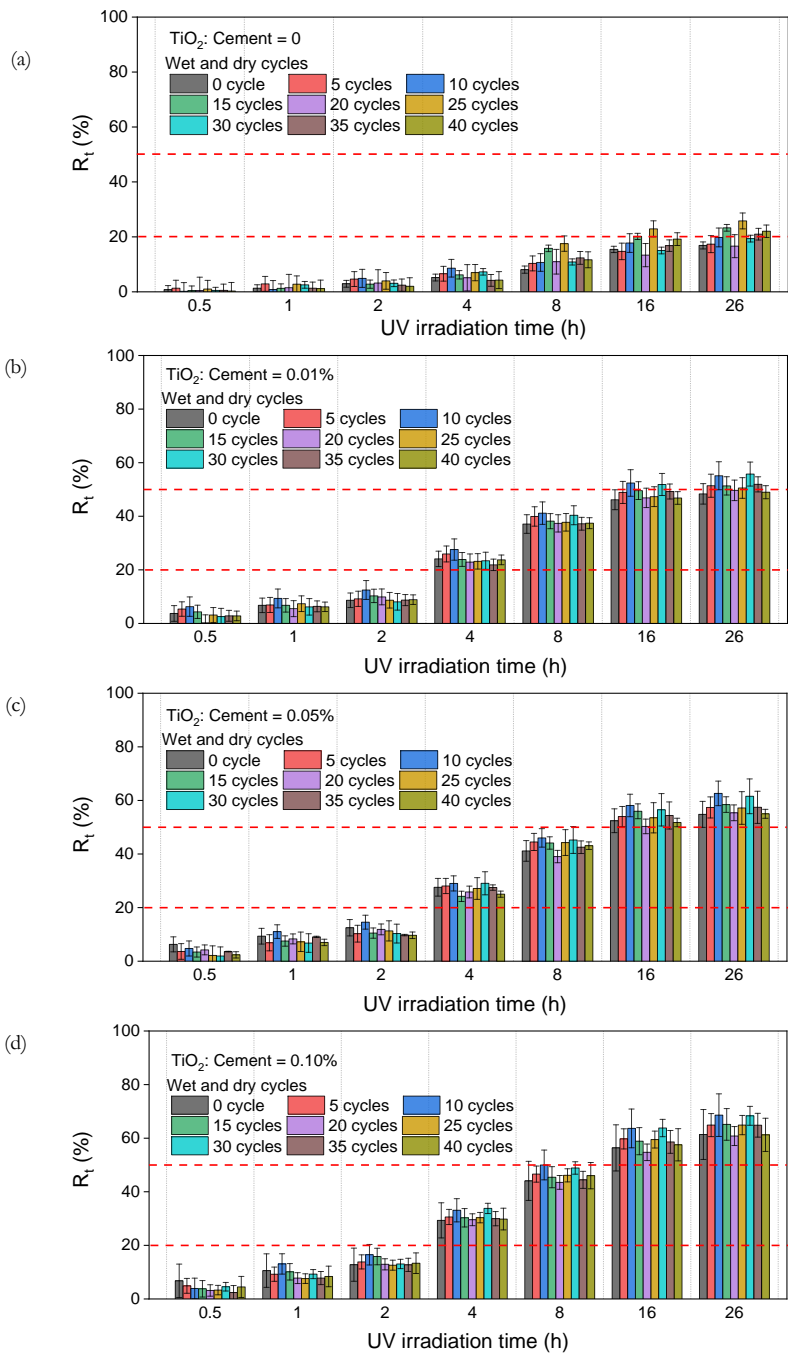
Fig. 5.2 RB degradation rate of mortar containing different contents of nano TiO₂ hydrosols after different wetting and drying cycles in pure water (a -e: the nano- TiO₂ hydrosols to cement ratios is 0, 0.01 %, 0.05 %, 0.10 % and 0.50 %, respectively).

(e)
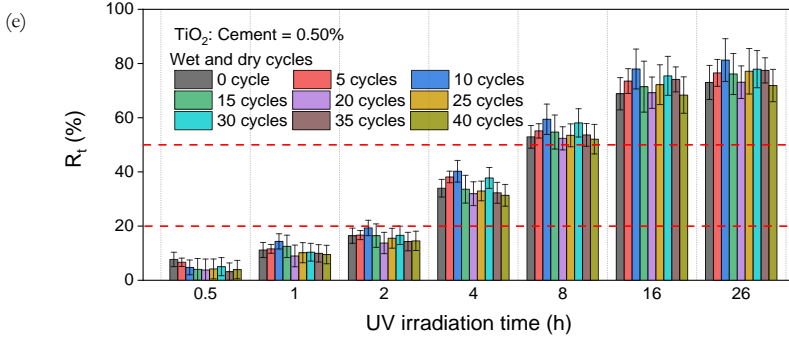
Fig. 5.2 continued.

In brief, the values of R_{26} present sinusoidal variation trends with the number of wetting and drying cycles as shown in Fig. 5.3(b). The values of R_4 also show a similar downward trend of fluctuation in Fig. 5.3(a). The above self-cleaning performances of TiO_2-mortar are consistent with the predicted results based on optical parameters in Section 5.3.1, indicating the influences of physical and chemical changes of cementitious materials on the electronic structure of TiO_2-mortar under the wetting and drying cycles of pure water accounts for a large proportion in the evolution of its self-cleaning performance.

In order to further determine the relationships between the photocatalytic activity of TiO_2-mortar and the number of wetting and drying cycles of pure water, Section 5.3.3 will analyze the photocatalytic reaction kinetics model of TiO_2-mortar from the perspective of catalytic reaction kinetics.

(a) R_4

(b) R_{26}
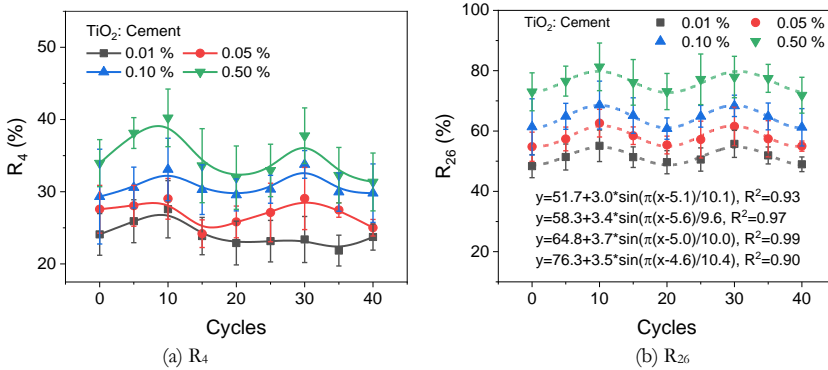
Fig. 5.3 R_4 and R_{26} of TiO_2-mortar samples after different cycles of wetting and drying tests.

5.3.3　Kinetic parameters of photocatalytic reactions

The pseudo-second-order reaction kinetics model is used to simulate the photocatalytic re-action kinetics of TiO_2-mortar under the wetting and drying cycles of pure water. Fig. 5.4 shows the kinetic model analysis of TiO_2-mortar samples with different dosages of nano

TiO$_2$ hydrosols after different times of wetting and drying cycles. Table 5.1 shows the reaction kinetic parameters of the photocatalytic self-cleaning kinetic processes. The linear fit degree (R²) of each group of TiO$_2$-mortars in the table is greater than 0.98, indicating that the concentration change rates of RB on the surface of each TiO$_2$-mortar sample meet the pseudo-second-order kinetic model. These results show that the pseudo-second-order kinetic model can reasonably predict the variation trend of RB degradation rate on the surface of TiO$_2$-mortar samples during the alternating wetting and drying action of pure water.

The photocatalytic reaction kinetic parameter C_e represents the concentration of RB that can be degraded when the effective photocatalytic reaction sites of TiO$_2$-mortar are involved in the photocatalytic processes. In other words, the value of C_e can be used to evaluate the photocatalytic activity of TiO$_2$-mortar. Fig. 5.5 shows the variation curve of C_e of TiO$_2$-mortar with the number of wetting and drying cycles for different nano-TiO$_2$ hydrosols contents. In Fig. 5.5, C_e of TiO$_2$-mortar in each group shows an 'M' shape change trend with the increase of the number of wetting and drying cycles, and there are two peaks in the curve of C_e values after 10 to 30 wetting and drying cycles. After 0, 20 and 40 wetting and drying cycles, there are three valley values in the curves. It is confirmed that the photocatalytic activity of TiO$_2$-mortar shows a 'M' wave trend with the increase in the number of wetting and drying cycles of pure water.

As a kind of nanoparticle, the existence of nano TiO$_2$ hydrosols will also have a certain impact on the hydration of cementitious materials and the deterioration processes of hydrates. In Section 5.3.4, the effects of nano TiO$_2$ hydrosols on the deterioration of hydrates of modified mortar under the action of a strong dissolution environment, such as the wetting and drying cycle of pure water, will be analyzed.

(a) 0 cycle   (b) 5 cycles
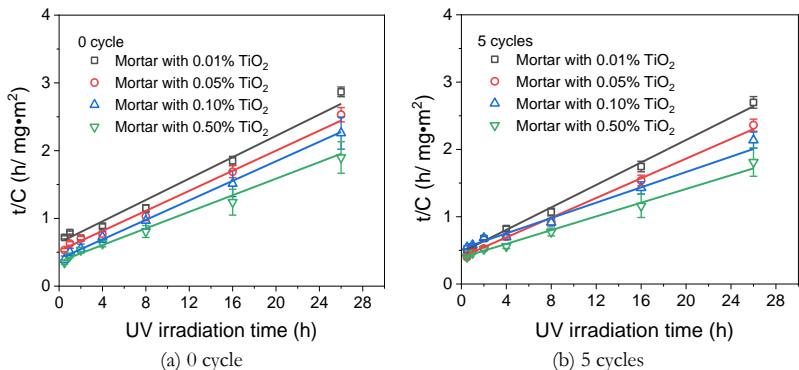
Fig. 5.4 Pseudo-second-order photocatalytic kinetic analysis of RB on TiO$_2$-mortars with different TiO$_2$ content and wetting and drying cycles.

(c) 10 cycles

(d) 15 cycles

(e) 20 cycles

(f) 25 cycles

(g) 30 cycles

(h) 35 cycles

(i) 40 cycles
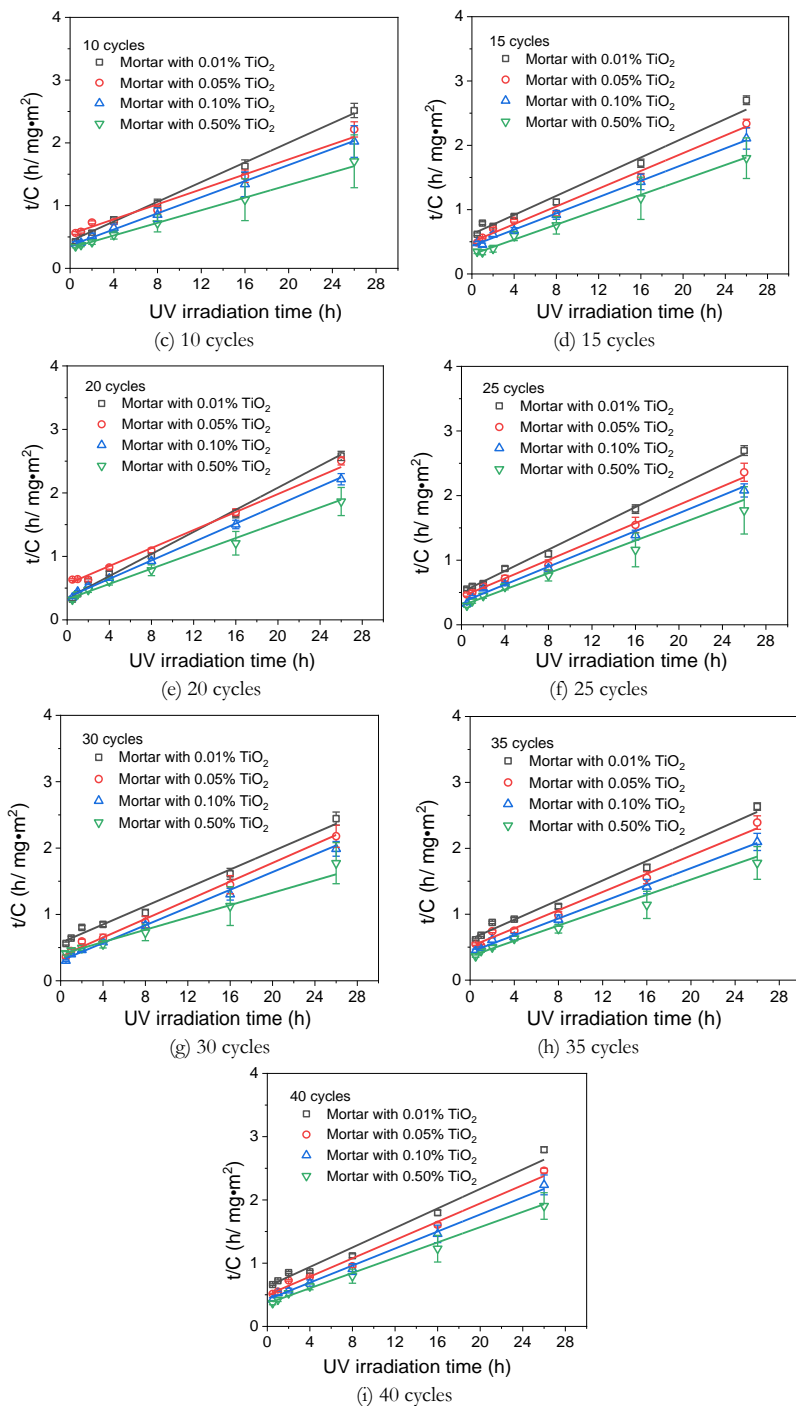
Fig. 5.4 continued.
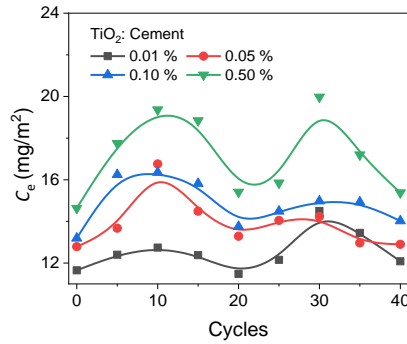
Fig. 5.5 The relationship between the degradation concentration of RB and the number of wetting and drying cycles in the equilibrium photocatalytic reactions on TiO$_2$-mortar.

Table 5.1 Photodegradation kinetic parameters in the processes of TiO$_2$-mortar degradation of RB during the wetting and drying cycles of pure water.

Cycles	TiO$_2$: Cement	k (m²/mg·h^{-1})	C_e(mg/m²)	r_{in} (mg/m² h^{-1})	R²
0	0.01 %	0.011	11.65	1.56	0.955
	0.05 %	0.012	12.79	1.93	0.981
	0.10 %	0.014	13.19	2.49	0.984
	0.50 %	0.013	14.63	2.76	0.924
5	0.01 %	0.014	12.40	2.12	0.993
	0.05 %	0.013	13.67	2.50	0.976
	0.10 %	0.007	16.24	1.91	0.963
	0.50 %	0.008	17.75	2.63	0.938
10	0.01 %	0.014	12.75	2.31	0.978
	0.05 %	0.007	16.76	1.84	0.938
	0.10 %	0.010	16.35	2.75	0.987
	0.50 %	0.008	19.36	3.09	0.995
15	0.01 %	0.011	12.38	1.62	0.959
	0.05 %	0.010	14.49	2.01	0.955
	0.10 %	0.009	15.82	2.29	0.962
	0.50 %	0.009	18.84	3.16	0.958
20	0.01 %	0.020	11.48	2.67	0.968
	0.05 %	0.010	13.29	1.77	0.978
	0.10 %	0.016	13.75	2.95	0.985
	0.50 %	0.013	15.41	3.08	0.965
25	0.01 %	0.013	12.15	1.98	0.995
	0.05 %	0.012	14.05	2.30	0.993

Cycles	TiO$_2$: Cement	k (m²/mg·h⁻¹)	C_e(mg/m²)	r_{in} (mg/m² h⁻¹)	R²
	0.10 %	0.014	14.49	2.88	0.932
	0.50 %	0.013	15.85	3.39	0.950
	0.01 %	0.008	14.50	1.74	0.952
30	0.05 %	0.013	14.23	2.70	0.949
	0.10 %	0.015	14.98	3.30	0.965
	0.50 %	0.006	19.98	2.52	0.964
	0.01 %	0.009	13.45	1.61	0.958
	0.05 %	0.012	12.97	1.96	0.923
35	0.10 %	0.011	14.93	2.35	0.984
	0.50 %	0.009	17.20	2.75	0.932
	0.01 %	0.011	12.09	1.58	0.969
	0.05 %	0.012	12.90	2.01	0.970
40	0.10 %	0.012	14.02	2.36	0.980
	0.50 %	0.012	15.38	2.76	0.965

5.3.4   Deteriorations of hydrates

(1)   XRD patterns

Fig. 5.6 lists the powder XRD spectra of the mortar with 0.10 w/w % nano TiO$_2$ hydrosols and the blank mortar samples after different wetting and drying cycles of pure water. The XRD spectra of the TiO$_2$-mortar samples of other groups are shown in Fig. D-4 in Appendix IV of this thesis. In Fig. 5.6, the main hydrates of cement in the blank sample are CH and C-S-H before the wetting and drying cycles. The main hydrates in nano TiO$_2$ hydrosols-modified mortar are CH, C-S-H and C-A-S-H. As the number of wetting and drying cycles of pure water increases to 30 cycles, the CH peak in both groups of samples gradually weakened. Then, when the number of cycles increased to 40, the peak values of CH rebounded.

Moreover, after 40 times of wetting and drying cycles in pure water, the peak value of calcium carbonate ($2\theta = 29.4°$) in the mortar of those two groups hardly changed, so it can be considered that no carbonization occurred in the mortar samples in this experiment. The peak values of C-S-H in mortar samples of those groups decrease with the increase in the number of cycles. Therefore, the experimental results support that the attack of wetting and drying cycles of pure water causes the dissolution of hydrates, such as CH and C-S-H, and causes the variation of CH content in the range of 10 mm below the sample surface.

(a) Mortar containing 0.10 w/w % nano TiO$_2$

(b) Blank mortar
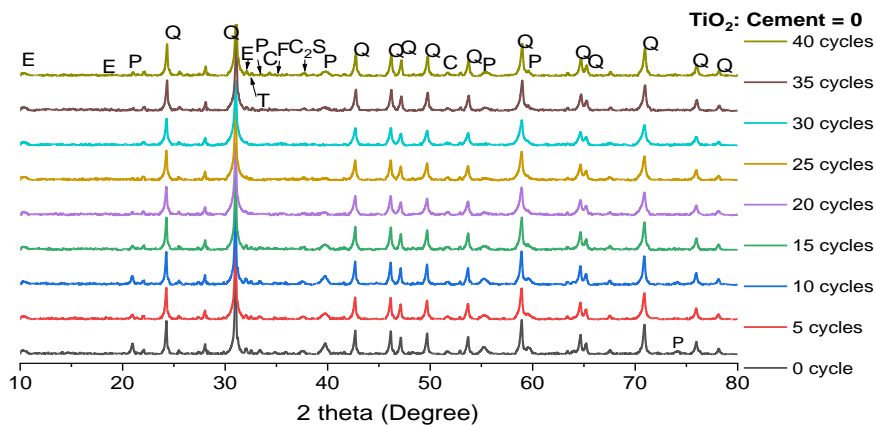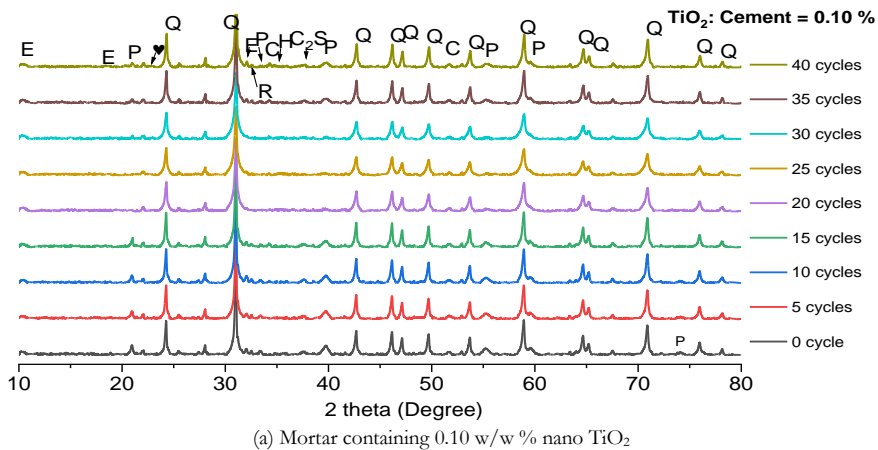
Fig. 5.6 XRD spectra of mortar with and without 0.10 w/w % nano TiO$_2$ after different wetting and drying cycles. Symbols: quartz: Q; Portlandite: P; Tobermorite: T; Foshagite: F; Ettringite: E; Hillebrandite: H; Rosenhahnite: R; C-A-S-H (Vertumnite): ♥.

(2)   TGA

According to the thermogravimetric curves of each group of modified mortar, the mass ratios of the main hydrates, such as CH and C-S-H, change with the number of wetting and drying cycles of pure water, as shown in Fig. 5.7. The thermogravimetric curves of each group of mortar are shown in Fig. D-5 in Appendix IV of this thesis. As can be seen from Figure 5.7(a), the proportions of CH in mortar samples of each group decrease in a fluctuating manner as the number of cycles increases. While the proportions of C-S-H in the

sample fluctuated greatly after the 15th, 25th and 30th cycles, there is no significant difference between the proportion of C-S-H in the sample after the end of the 40th cycles and the initial value. After 40 wetting and drying cycles, the mass ratios of CH in the mortar of the control group decrease by 45.6 %, and the mass ratios of CH in the mortar samples with different dosages of nano TiO_2 decrease by 40.5 % (TiO_2: cement = 0.01 %), 33.9 % (TiO_2: cement = 0.05 %) and 30.3 % (TiO_2: Cement = 0.10 %), 21.4 % (TiO_2: cement = 0.50 %). As shown in Fig. 5.8, after 40 wetting and drying cycles of pure water, the reduction rate of the CH ratio decreases exponentially with the increase of nano TiO_2 hydrosols in the matrix, indicating that the presence of nano-TiO_2 hydrosols could inhibit the CH mass loss in mortar caused by dissolution effects. Moreover, when the content of nano TiO_2 reaches a certain value (0.50 w/w % of cement mass), that inhibition effect will become stable.
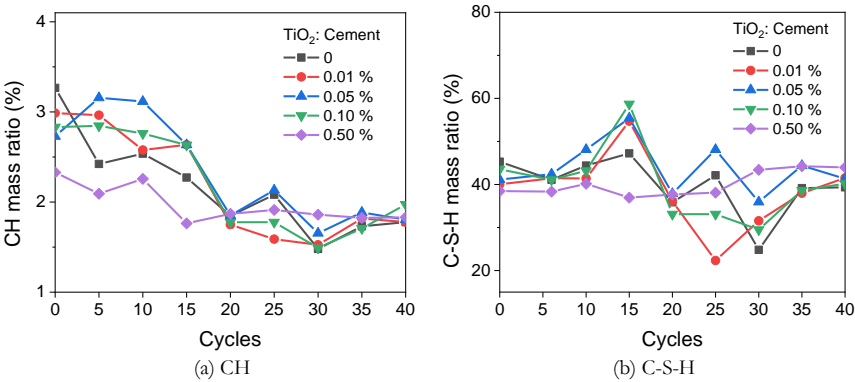
Fig. 5.7 Mass ratios of CH and C-S-H in mortar with different dosages of nano TiO_2 hydrosols after different wetting and drying cycles.
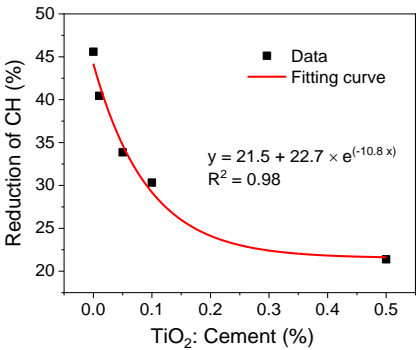
Fig. 5.8 Relationship between the proportion reduction rate of Portlandite in mortar and the dosages of nano TiO_2 hydrosols after 40 wetting and drying cycles of pure water.

For cementitious materials, the dissolution of hydrates is a series of processes of chemical solution-diffusion under the wetting and drying cycles of pure water. The dissolution of CH is closely related to the shape of the crystal [238], and dissolution is easier when the size of

the CH crystal is smaller [237]. The dissolution rate of C-S-H phase is also greatly affected by its Ca/Si ratio [274]. The dissolution rate of C-S-H with a low Ca/Si ratio is two to three orders of magnitude higher than that of C-S-H with a high Ca/Si ratio [275,276]. Since the Ca/Si ratio controls the crystal shape of C-S-H phase, it can be understood that the dissolution process of C-S-H is greatly affected by its crystal shape. In Chapter 4.3.1, the relationships between the crystal shapes of CH and C-S-H and the amount of nano TiO_2 hydrosols in mortar with different dosages are analyzed in detail. The ratio of $\{0001\}/\{10\text{-}10\}$ of CH crystals increases with the increase of the amount of nano TiO_2 hydrosols in the matrix. When the nano TiO_2 to cement ratio exceeds 0.5 w/w %, the ratio of $\{0001\}/\{10\text{-}10\}$ tends to be stable. The amount of filamentous C-S-H (high Ca/Si ratio) phase also increases with the increase in the amount of nano TiO_2 hydrosols. In other words, nano TiO_2 hydrosols affect the dissolution rate of CH and C-S-H under the alternating action of wetting and drying cycles of pure water by affecting the crystal shapes of CH and C-S-H. These results can reasonably explain the inhibitory effect of nano TiO_2 hydrosols on the dissolution of CH in mortar during the wetting and drying cycles of pure water. When the nano TiO_2 hydrosols to cement ratio reaches a certain value (0.50 w/w %), the size of CH crystals tends to be stable. That is, the inhibition effects of nano TiO_2 hydrosols on CH dissolution also tend to be stable.

5.3.5 Anatase exposure areas during wetting and drying cycles

A confocal Raman microscope is used to observe the area distribution of typical components such as CH, C-S-H, anatase TiO_2 and calcium carbonate on the surface of mortar samples containing 0.50 % nano TiO_2 hydrosols after different times of wetting and drying cycles, as shown in Fig. 5.9. In Fig. 5.9, the red region represents anatase TiO_2, the green region represents C-S-H phases, the blue region represents CH, and the magenta region represents the calcium carbonate. Raman characteristic peaks at the positions of 144 cm^{-1}, 356 cm^{-1}, 667 cm^{-1} and 1085 cm^{-1} are selected as the characteristic peaks of the Anatase, CH, C-S-H phases and calcium carbonate. Fig. 5.9(j) shows the variation curves of the area ratios of each typical component with the times of wetting and drying cycles.

It can be seen from Fig. 5.9(j) that the area ratios of anatase on the mortar surface present a wavy change trend with the number of wetting and drying cycles, in which the value increases first and then decreases periodically. This is consistent with the changing trend of the Urbach energy and self-cleaning efficiency of TiO_2-mortar with the number of wetting and drying cycles in Section 5.3.1 and Section 5.3.2. While the area variations of CH, C-S-H phase and calcium carbonate do not show a similar changing rule like anatase.

| TiO₂ | C-S-H | Portlandite | CaCO₃ |

(a) 0 cycle (b) 5 cycles (c) 10 cycles

(d) 15 cycles (e) 20 cycles (f) 25 cycles

(g) 30 cycles (h) 35 cycles (i) 40 cycles
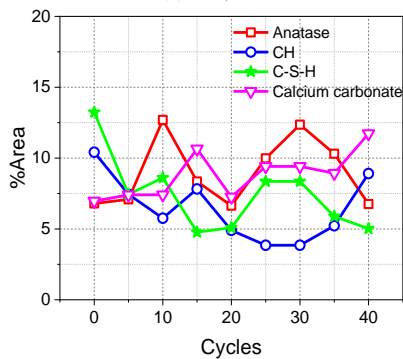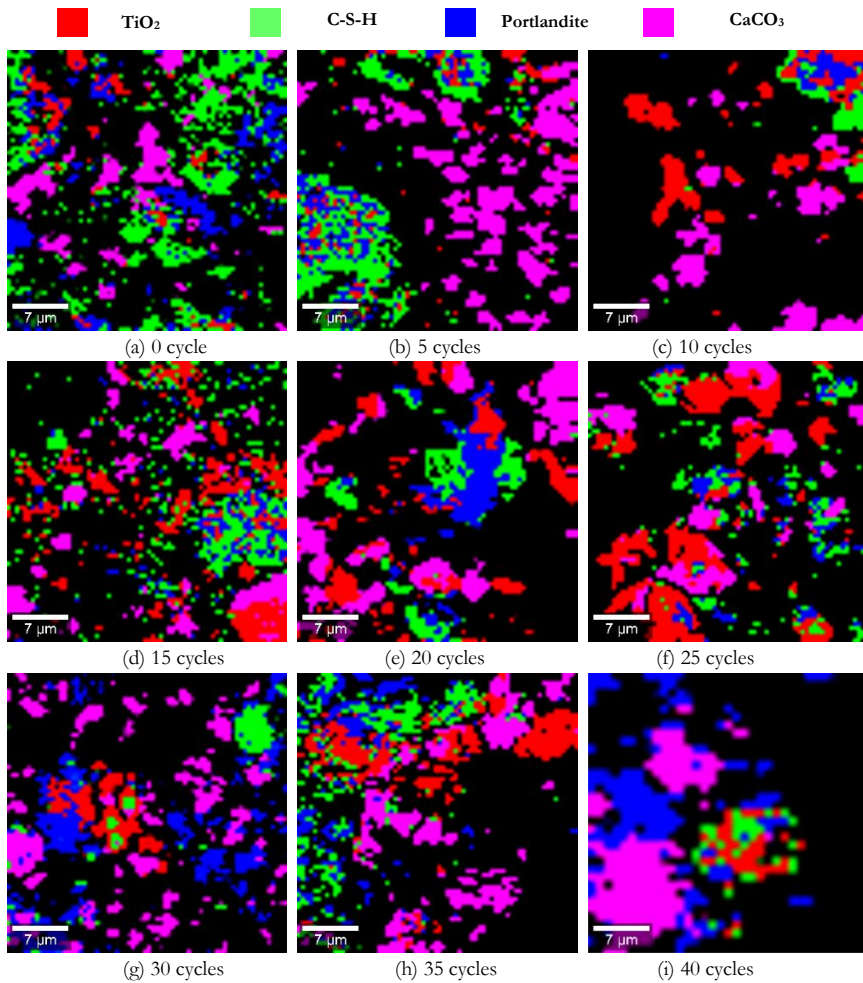
(j) Semi-quantitative calculation of the main phases in TiO₂-mortar surface

Fig. 5.9 Raman images of main components on the surfaces of the sample after different wetting and drying cycles of pure water mixed with 0.50 w/w % obtained by CRM (scanning area is 70μm×70μm).

By observing the distribution regions of anatase and CH and C-S-H in Fig. 5.9(a to i), a rule can be summarized during the wetting and drying cycles of pure water as follows. The distribution area of anatase has undergone periodic changes from being closely surrounded by hydration products such as CH and C-S-H at the beginning to being relatively independent and coherent after ten wetting and drying cycles and then being relatively closely surrounded by hydration products again after 20 wetting and drying cycles.

This phenomenon may be because the hydration products initially surrounded by anatase on the surface of the test sample dissolved and spread outside the sample with the dissolution and diffusion of hydrates such as CH under the action of the wetting and drying cycles of pure water. In this way, the surfaces of the test block that are initially tightly wrapped with TiO_2 particles are left empty so that more active surfaces of TiO_2 particles are exposed, which can participate in photocatalytic reactions. At the same time, the surfaces of those particles are relatively affected by the similar doping effects of cement hydration products, which have high instability and more surface defects, resulting in a small improvement in the self-cleaning performance of TiO_2-mortar. With the increase in the number of wetting and drying cycles, the hydration products in the inner regions of the surface layer of the slide samples dissolve and diffuse to the surface region and then diffuse again to the porous regions around the TiO_2 particles. Thus, the distributions of TiO_2, CH and C-S-H on the surfaces of the samples return to the distributions similar to that of the initial samples. These results also explain why the Urbach energy of TiO_2-mortar in Section 5.3.1 shows a similar sinusoidal trend with the number of wetting and drying cycles.

5.4   Summaries

In this chapter, the photocatalytic self-cleaning performance of nano TiO_2 hydrosols modified mortar (hereinafter referred to as TiO_2-mortar), the evolution of optical parameters with the number of wetting and drying cycles, the photocatalytic reaction kinetics, the dissolution of hydration products in TiO_2-mortar, and the typical phase distribution on the surface of the mortar are mainly studied under the action of pure water alternating wetting and drying cycles. The following conclusions are drawn:

(1) The self-cleaning performance of TiO_2-mortar showed a sinusoidal trend with the increase of the number of wetting and drying alternating cycles, and the period is 20 wetting and drying cycles. The band gap energy and Urbach energy of TiO_2-mortar showed a cyclical trend like the sine function as the number of wetting and drying cycles increased, and the period is 20 wetting and drying cycles. The photocatalytic self-cleaning kinetic process of TiO_2-mortar follows the pseudo-second-order reaction kinetic model and is not affected by the number of wetting and drying cycles. The kinetic parameter C_e, which represents the photocatalytic activity of TiO_2-mortar, also showed a periodic first increase and then decrease with the increase of wetting and drying cycles, and the change period is about 20 wetting and drying cycles.

(2) The possible reasons for the self-cleaning performance of TiO_2-mortar showing a change similar to a sine function with the number of wetting and drying cycles of pure water are as follows: The hydration product CH on the surface of the sample first dissolved and diffused into the erosion water, which exposed more photocatalytic reaction surfaces of the nano TiO_2 coated by the hydration product, and these surfaces affected by the doping effect of the hydration product had more defects, which made the self-cleaning performance of the TiO_2-mortar reach its peak in 10 cycles. In continuous wetting and drying cycles, the hydration products within the surface of TiO_2-mortar gradually dissolve and diffuse to the surface and re-aggregate around nano TiO_2 particles, making the self-cleaning performance of TiO_2-mortar gradually decrease from the peak value to the initial value after 20 cycles.

(3) Nano TiO_2 hydrosols can inhibit the dissolution and diffusion of hydrates caused by wetting and drying cycling of pure water in TiO_2-mortar. By delaying the early hydration of cement, nano TiO_2 hydrosols generated CH and thin filamentous C-S-H phases with low $\{0001\}/\{10\text{-}10\}$ ratio, refining the pore structure of mortar and affecting the dissolution and diffusion rates of CH and C-S-H under the alternating action of wetting and drying pure water. When the mass ratio of nano TiO_2 to cement exceeds 0.5 %, the shape of the CH crystal tends to be stable, and when nano TiO_2 exceeds 0.5 % of cement mass, the inhibition effect tends to be stable.

Chapter 6 Early-age and hardened performances of visible-light photocatalytic concrete with ultra-low dosages of CNF-TiO₂ hydrosols

There are still risks to using nano-dispersed TiO_2 hydrosols to prepare cementitious materials because of the inherent acidic properties. The study in this chapter investigates the negative influences and potential solutions of pure nano-dispersed TiO_2 hydrosols with ultra-low dosages to cement paste. The cellulose nanofibrils (CNF) are used to modify the TiO_2 hydrosols to prepare the visible-light photocatalysts (CNF-TiO_2 hydrosols). The mass ratios of CNF greatly influence the rheological parameters of paste slurries containing nano TiO_2 hydrosols-based photocatalysts to TiO_2 in photocatalysts. Compared with the reduction of compressive property caused by adding pure nano TiO_2 hydrosols, the compressive strength values of hardened cement paste samples containing CNF-TiO_2 hydrosols increase apparently when the CNF to TiO_2 ratio is less than 1.5. The presence of CNF-TiO_2 hydrosols does not affect the phase patterns of hardened paste but improves the portlandite mass ratios and the porosities of macro pores.

6.1   Introduction

Cementitious materials in buildings are directly and continuously exposed to various atmospheric pollutants and micro-organisms under different weather conditions, resulting in façade pollution and structural deterioration [1,2]. Nano-photocatalysts-modified cementitious materials have been rapidly developed in the past 20 years. Nano titanium dioxide (TiO_2) is the most widely used photocatalyst in cementitious materials due to its high cost-effectiveness, non-toxicity, and chemical inertia in the absence of light and nanometer size effects. In addition, the combination of TiO_2 and cement hydrates have some synergistic advantages because the reaction product can be adsorbed on the surface and then ished away by rain [9].

In most of the studies [21,22,277,278], the commercially available nano TiO_2 powder (for example, Degussa P25) is studied as concrete coatings to improve its photocatalytic activity. The inherent agglomeration and very poor dispersity of nano TiO_2 powders in an aqueous system caused by the calcination in the synthetic process may be the biggest holdback in making air-purifying and self-cleaning cementitious materials. The nano-dispersed TiO_2 hydrosols are usually synthesized by the sol-gel process using titanium alkoxide as precursor [279–281], where the solvent is water, in large excess with respect to the alkoxide [32,34,36,87,103,124,282]. The acids, such as nitric acid and hydrochloric acid, are used as peptizators that produce colloidal suspensions containing TiO_2 particles with size ranges of less than 100 nm. This route is a cheap and low-energy consumption method to obtain anatase and well-dispersed nano TiO_2 particles. TiO_2 hydrosols catalysts have a much larger surface area and are much more transparent than conventional TiO_2 nano powder catalysts, which have demonstrated better performance in the photocatalytic degradation of pollutants [197]. Moreover, the good dispersity of nano TiO_2 particles in cementitious materials is the critical point of self-cleaning and photocatalytic performances because the photodegrading reactions between pollutants and photocatalytic matrix occur on the surface of TiO_2 particles and the stable dispersion of nano TiO_2 particles in cementitious materials can provide more reaction areas because of the greater specific surface areas [283]. However, when it is applied to the high alkaline cementitious materials, there is one drawback of the acidic nano TiO_2 hydrosols is the risk of weakening the matrix and resulting in a decrease in mechanical properties. Therefore, minimizing this risk of nano TiO_2 hydrosols is still an urgent problem that needs to be solved.

In this chapter, a series of nano TiO_2 hydrosols-based visible light photocatalysts are synthesized by using nano fibril cellulose at low temperatures. The rheology properties and the hydration heat release processes of fresh paste samples and with different visible light photocatalysts are discussed. The mechanical properties and the pore size distribution curves of the hardened paste samples are also recorded. The photocatalytic air purification performances of visible light photocatalyst-modified cement paste are also investigated.

6.2　Materials and experimental

6.2.1　Materials

(1)　Preparation of nano TiO₂ hydrosols

Titanium tetra-isopropoxide (TTIP, 97.0 %) is purchased from Sigma-Aldrich. Glacial acetic acid (99.6 %), and absolute ethanol (99.9 %), are purchased from VWR Chemicals. Deionized water (18.2 MΩ.cm) is used throughout the preparation process of TiO_2 hydrosols. The nano TiO_2 powder (P25) is purchased from Evonik Industries AG company. The selected method in this chapter to produce anatase TiO_2 hydrosols are adapted from studies from Yang et al. [128] and Alphonse et al. [36], and the different synthesis temperatures are applied. The synthesis is as follows: TTIP is dissolved in absolute ethanol with the TTIP/ethanol molar ratio of 2.44, and then the solution is stirred for 30 min at different temperatures (50 °C and 40 °C) for comparison. The obtained solution is added drop by drop at the speed of 0.01 mL/s into a mixture containing acetic acid and deionized water with a molar ratio of 0.175. After that, the suspension is continuously stirred for 48 h at 50 °C or 40 °C by magnetic stirrers and then left to settle for at least 72 h at room temperature of 20 °C and relative humidity of 60 %.

(2)　Preparation of CNF-TiO₂ hydrosols

The method of synthesizing cellulose nanofibril (CNF) modified TiO_2 hydrosols are as follows: Dissolve TTIP in absolute ethanol, the molar ratio of TTIP: ethanol is 2.44, and stir at 40 °C for 30min. The mixture of acetic acid and deionized water with a molar ratio of 0.175 is added drop by drop at a rate of 0.01mL/s into the mixture of acetic acid and deionized water, in which cellulose nanofibril with different molar mass ratios of TiO_2 are added, and stirred at room temperature for 2 h. At 50 °C or 40 °C, the mixture is continuously stirred for 48 h, and then left for at least 72 h at room temperature and relative humidity of 60 %. Four kinds of CNF-modified TiO_2 hydrosols with different molar mass ratios are synthesized: CNF:TiO_2 = 1.0, 1.5, 2.0, and 2.5.

(3)　Preparation of the photocatalytic paste

P.W. 52.5 white cement and tip water are used to prepare the cement paste. The chemical components of white cement recorded by XRF are shown in Table 6.1. The water-to-cement ratio of the paste is 0.4, and the modified TiO_2 hydrosols to cement is 0.10 %. The cubic samples with the size of 10 mm × 10 mm × 10 mm are used to test the compressive strength of the hardened paste at different ages. The paste samples are demoulded after one day and placed in the curing room (95 % relative humidity, 20 °C) until the test ages. Cylindrical samples with a size of ф 65 mm × 2 mm are used to measure the thermal conductivity of

the hardened slurry at 28-day-age. According to the mass ratio of CNF:TiO$_2$ in photocatalysts, hardened cement paste samples are defined as different groups, which are: Ref (CNF:TiO$_2$ = 0:0), A1 (CNF:TiO$_2$ = 0:1), A2 (CNF:TiO$_2$ = 1:1), A3 (CNF:TiO$_2$ = 1.5:1), A4 (CNF:TiO$_2$ = 2.0:1), A5 (CNF:TiO$_2$ = 2.5:1).

Table 6.1 Chemical components of P.W. 52.5 cement.

Components	CaO	SiO$_2$	MgO	SO$_3$	Al$_2$O$_3$	MnO	K$_2$O	Na$_2$O	Fe$_2$O$_3$	TiO$_2$	Minor elements*
Contents (%)	64.51	20.34	5.70	4.62	2.04	0.83	0.71	0.59	0.26	0.05	0.35

* V$_2$O$_5$+Cr$_2$O$_5$+NiO+ZnO+BaO+Cl+SrO+Rb$_2$O+Y$_2$O$_3$

6.2.2   Methods

The particle size distribution and zeta potential of TiO$_2$ hydrosols are tested by the Zetasizer NanoSeries (Malvern Panalytical) at 25 °C. In these tests, the initial hydrosols are diluted 100 times in distilled water. The TiO$_2$ hydrosols samples are tested three times by Zetasizer Nano Series by using a process called dynamic light scattering. The Zetasizer Nano Series calculated the zeta potential by determining the electrophoretic mobility and then applying the Herny equation.

The UV-VIS absorbance spectra of TiO$_2$ hydrosols and P25 suspension samples are measured by the UV-VIS-NIR spectrophotometer (Perkin Elmer Lambda 750), the tested range is 250 nm to 800 nm, 1 nm per second. According to the Beer-Lambert law, the samples contents should be lower than 0.01M, and the absorbance should be set below 1.0. In this chapter, the hydrosols sample is diluted down to 1.0 % by distilled water. To measure the specific surface area and crystal phase pattern of TiO$_2$ hydrosols sample, a powder sample is prepared by drying the initial TiO$_2$ hydrosols in the oven at 105 °C for 24 hours.

The specific surface area values of dried hydrosols are measured by the Brunauer, Emmett and Teller (BET) method. The pore size distribution from the adsorption isotherm is evaluated by using the Barrett-Joyner-Halenda (BJH) interpretation. Nitrogen sorption isotherm experiments are carried out at 77 K temperature by a NAD device of type TriStar II 3020. The phase composition of the dried TiO$_2$ powder sample is investigated by comparing

A rheometer (RSX SST, AMETEK Brookfield, USA) and a rotor with the size of 40 mm × 20 mm are used to determine the effects of different types of modified photocatalysts on the dynamic shear rheological properties of cementitious materials. During the rheological test, the test protocol is adopted as shown in Fig. 6.1. In this chapter, the Herschel-Bulkley model is used to describe the rheological behaviours of slurry samples.

$$\tau = \tau_0 + K\gamma^n \tag{6.1}$$

Where, τ_0 is the yield stress, Pa; K is the coefficient of viscosity; γ is the shear rate; n is the rheological index. $n = 1$ means the slurry belongs to Newtonian fluids; $n > 1$ means the slurry belongs to yield swelling plastic fluids; $n < 1$ means the slurry belongs to yield pseudoplastic fluids.
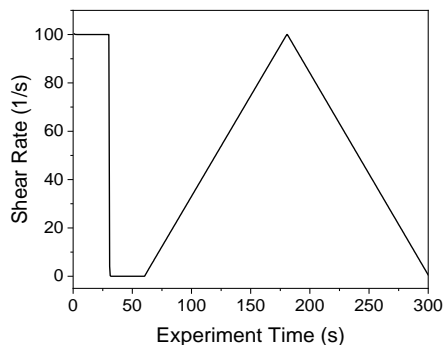
Fig. 6.1 Shear rate to time curve in rheological test.

X-ray diffraction (XRD) pattern (Bruker D4 PHASER, Philips, The Netherlands) with a Co tube (40 kV, 40 mA). A typical run used in this test is made with a step size of 0.02°/min and a dwell time of 0.5 s.

Thermal gravimetric analysis (TGA) is performed using a thermal analyser (SDT 650,WA-TERS, USA), with nitrogen as a protective gas, and the test sample is heated from 30 °C to 1000 °C at a rate of 10 °C / min. Before the test, all the samples need to be crushed and soaked in acetone for seven days and dried in an oven at 40 °C to stop further hydration of the cement.

The mercury intrusion pore size analyzer (PoreMaster 60, Anton paar, USA) is used to measure the pore size distribution curves of hardened paste samples. The maximum pressure applied is 420 MPa.

Parameters such as the thermal conductivity of hardened paste samples are measured by the ISOMET2114 portable heat conduction meter produced by Precision Instrument Co., Ltd in Slovakia.

A universal testing machine measures the compressive strength values of the hardened paste samples with a test limit of 100 kN (Wuhan Weiheng Industrial System Co., Ltd., P. R. China). During the compressive test, the dimension of the compressive surface is 40mm×40mm, and the loading rate is 2400 N/s.

6.3 Results and discussions

6.3.1 CNF-modified TiO₂ hydrosols

(1) Chemical and physical properties of TiO₂ hydrosols

The average particle size and Zeta potential values are shown in Table 6.2. For a physically stable nanosuspension stabilized by electrostatic repulsion, a zeta potential of approximately ± 30 mV is required as a minimum, while in a combined electrostatic and steric stabilization, as a rough guideline ± 20 mV is sufficient [284,285]. The average particle size (of intensity) of TiO₂ hydrosols samples at 40 °C and 50 °C are 19 nm and 38 nm, respectively. The zeta potential of TiO₂ hydrosols synthesized at 40 °C and 50 °C are 43 mV and 39 mV. These results indicated that the synthesis temperature had a great influence on the particle size of TiO₂ in hydrosols, while the influences on the zeta potential values of TiO₂ hydrosols are limited.

Increasing the reaction temperature increased the titania solubility, leading to the growth of larger particles at the expense of smaller ones by a classical dissolution-reprecipitation mechanism (Ostwald ripening) [286]. Another side effect of increasing the titania solubility is the progressive transformation of metastable crystalline phases, like brookite and anatase, into rutile, which is the stable phase [36]. Therefore, the TiO₂ hydrosols prepared at 40 °C presented better dispersion stability.

Table 6.2 The average particle size and zeta potential of TiO₂ hydrosols.

Synthesis temperatures	Hydrodynamic Size ± SD (d. nm)	%Intensity	Z-average ±SD (d. nm)	Polydispersity index	Zeta potential(mV)	Conductivity (mS/cm)
50 °C	38 ± 16	100	35 ± 13	0.14	39	0.12
40 °C	19 ± 6	100	17 ± 6	0.11	43	0.11

The diffraction angle 2θ of (101) crystal plane of anatase TiO₂ crystal is 29.4°, the (004) crystal plane is 44.2° and the (200) (105) and (204) crystal planes are 56.4°, 63.5° and 74.3°, respectively [287]. As can be seen in Fig. 6.2, the TiO₂ particles in hydrosols synthesized at 40 °C and 50 °C show all the typical diffraction peaks of anatase TiO₂, indicating the synthesized TiO₂ particles in TiO₂ hydrosols are pure anatase TiO₂ crystal. Since the TiO₂ hydrosols synthesized at a lower temperature presented smaller particle size, dispersity and same crystal form, the following characterisation tests are focused on the comparison between TiO₂ hydrosols synthesized at 40 °C and P25 suspension.
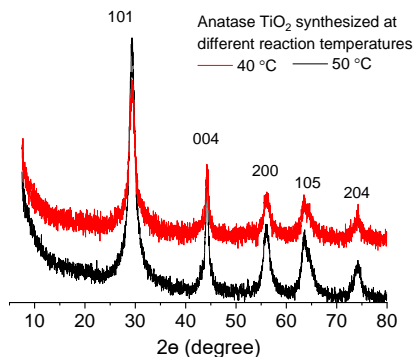
Fig. 6.2 XRD pattern of TiO₂ hydrosols dried at 105 °C.

The visual observation of colour changes, as well as UV-VIS absorbance spectra of both TiO₂ hydrosols and P25 suspension with the same mass content of 1.54 %, are shown in Fig. 6.3. In Fig. 6.3(a), TiO₂ hydrosols are transparent, while the P25 suspension sample with the same mass content is pure white and non-transparent. The visual observation results revealed that the particle size of suspended TiO₂ particles is much larger than the wavelength of visible light. Thus, the TiO₂ particles in the P25 suspension scattered and reflected all wave-lengths of visible light (400 to 800 nm) equally without wavelength selectivity, and the P25 suspension appeared white. In Fig. 6.3(b), the absorbance of TiO₂ hydrosols in the 250-300 nm range is higher than the P25 suspension. In general, the P25 powder is made of 20 % rutile crystal and 80 % anatase crystals, and in theory, the absorption band edge is near 380 nm for anatase and 300 nm for rutile [125]. In Fig. 6.3(b), it is clear that the visible light in the range from 400 nm to 800 nm is also absorbed by P25 suspension, which is induced by the scatter effect of huge clusters of TiO₂ particles. As a result, the nanoparticles in TiO₂ hydrosols are more stable than in P25 suspension.
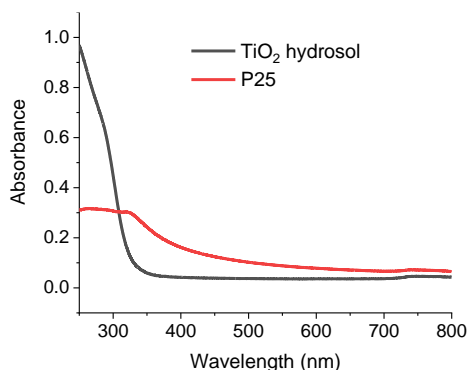
(a) UV-VIS spectra   (b) Visual observation

Fig. 6.3 The visual observation and UV-VIS absorbance spectra of TiO₂ hydrosols and P25 suspension.

The UV-VIS light absorption spectra of five groups of synthetic photocatalysts (TiO$_2$ contents in each photocatalysts are consistent, and the test solutions are diluted 100 times) are tested, as shown in Fig. 6.4. Based on the spectra, the mathematic relationships between the bandgap energy and absorbance of the photocatalysts are calculated, as shown in Fig. 6.4(a). The relationships between the bandgap energy values of each photocatalyst and the ratios of CNF to TiO$_2$ in the photocatalysts are shown in Fig. 6.4(b). It can be seen from the test data that the absorption of CNF in the UV and visible light wavelengths is very low, as shown by the grey curve in Fig. 6.4(a).

(a) UV-VIS spectra   (b) bandgap energy
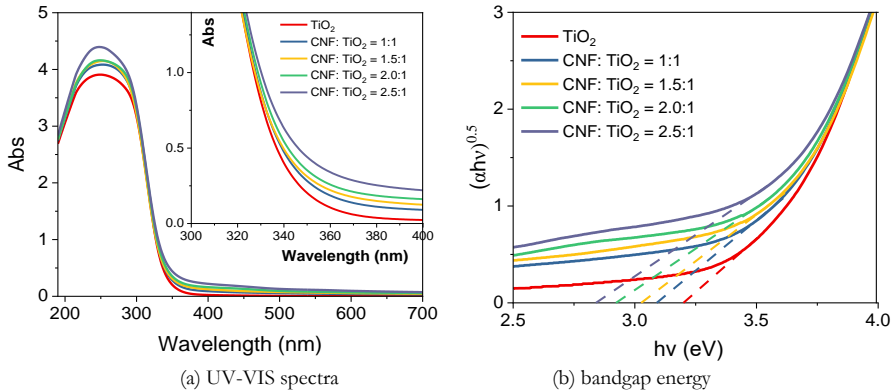
Fig. 6.4 UV-VIS spectra and the bandgap energy to light absorbance values curves.

In Fig. 6.4(b), with the increase of the mass ratios of CNF to TiO$_2$ in the photocatalysts, the absorption of the photocatalysts in both UV and visible light wavelengths gradually increase, which bandgap energy values gradually decrease from 3.20 eV to 2.84 eV. When the mass ratios of CNF to TiO$_2$ is greater than or equal to 1, the bandgap energy of the photocatalyst is 3.09 eV, indicating that the photocatalytic activity of the modified TiO$_2$ hydrosols can be excited by visible light with a wavelength larger than 401.5 nm (400 nm, 3.10 eV). As shown in Fig. 6.5, the bandgap energy values of the synthetic photocatalysts show a linear decrease with the increase of the mass ratios of CNF to TiO$_2$. These results indicate that TiO$_2$ hydrosols modified by CNF can be excited by visible light, which belongs to visible light photocatalysts. The mass ratios of CNF to TiO$_2$ catalyzed by modified visible light have a great influence on the surface charging states of particles, which will impact the hydration reaction processes of cementitious materials.
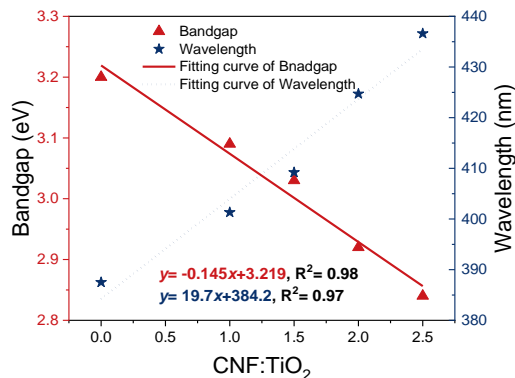
Fig. 6.5 Relationships between band energy values and CNF:TiO$_2$ mass ratios of photocatalysts.
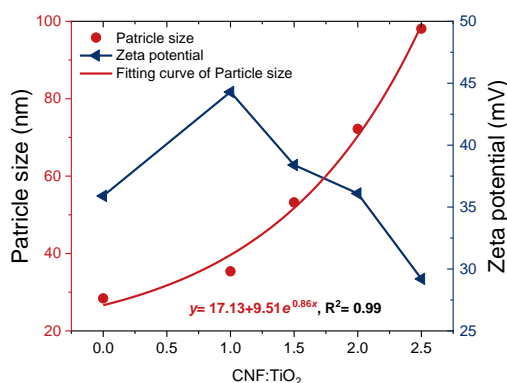
Fig. 6.6 Zeta potential values and the hydrodynamic diameters of modified hydrosols.

Fig. 6.6 shows the zeta potential values and hydrodynamic diameters of CNF and modified nano TiO$_2$ hydrosols. It can be seen that with the increase of the mass ratios of CNF and TiO$_2$, the zeta potential values of the modified hydrosols gradually decrease while the hydrodynamic diameter gradually increases. The hydrodynamic diameters of the synthetic photocatalysts showed an exponential increase with the increase of the mass ratios of CNF to TiO$_2$. When the mass ratio value of CNF and TiO$_2$ is 2.5, the hydrodynamic diameter of the modified photocatalyst hydrosols is about 98.1 nm, which is close to the upper limit of the size definition of nanoparticles. Therefore, considering the small size feature of nanoparticles, the mass ratios of CNF and TiO$_2$ in those modified TiO$_2$ visible light photocatalysts hydrosols in this chapter should be less than 2.5.

6.3.2 Dynamic shear rheology

The apparent viscosities changing curves of slurry samples in each group at different shear rates are shown in Fig. 6.7(a). In Fig. 6.7(a), the viscosity values of slurry samples in each group show a changing feature of first decreasing sharply and then decreasing slowly with

the increase of the shear rates. When the shear rate is small (≤ 5 s^{-1}), the apparent viscosity of slurry decreases rapidly in a short time with the increase of shear rate. The reason is that at a low shear rate, the particles and molecular structures inside the slurry are relatively static, and there is a strong interaction force between each other, resulting in a high apparent viscosity of the cement slurry. When the shear rate increases, the shear stress begins to act on the internal structure of the slurry, causing the particles or molecular structure to deform and rearrange. In a short period, the shear stress can rapidly destroy the structure in the slurry and weaken the interaction force between particles or molecules, resulting in a rapid decrease in the apparent viscosity of the slurry. This phenomenon is also known as shear thinning. When the shear rate is large (> 5 s^{-1}), the apparent viscosity of the slurry gradually decreases and becomes flat with the increase of the shear rate. The reason is that at larger shear rates, the action of shear stress gradually balances the interaction forces within the slurry, thereby rearranging the particles to form a new ordered structure. This ordered structure is relatively stable, resulting in a smooth apparent viscosity of the slurry. Thus, adding the CNF-modified TiO$_2$ hydrosols with a mass fraction of 0.10 % to the cement paste improves the viscosity of the cement paste.

(a) Viscosity   (b) Thixotropic loop
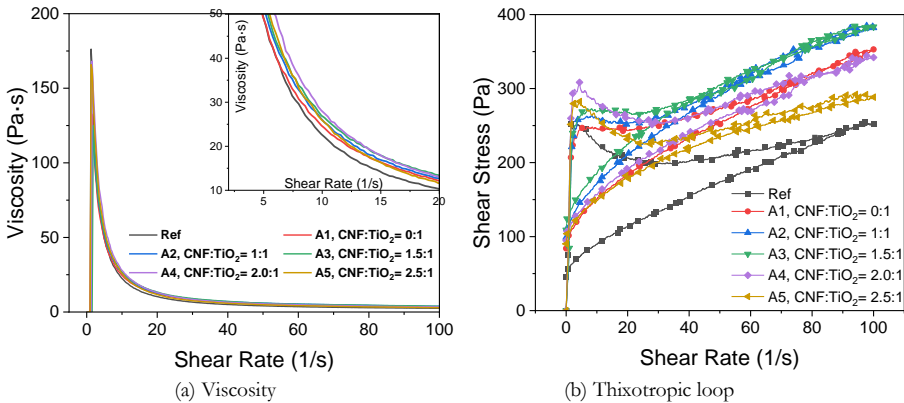
Fig. 6.7 The rheological curves of slurries with different CNF-TiO$_2$ hydrosols.

Table 6.3 Parameters of Herschel-Bulkley model and areas of thixotropic loops for slurry in each group.

Group name	CNF:TiO$_2$	τ_0 (Pa)	K (Pa·s)	n	R^2	Area (Pa/S)	Decrease ratio of loops (%)
Ref	0:0	54.019	6.043	0.762	0.9994	4974.7	-
A1	0:1	94.978	11.265	0.681	0.9988	2957.3	40.55
A2	1:1	99.868	17.962	0.604	0.9991	2133.4	57.12
A3	1.5:1	97.247	29.036	0.499	0.9989	1682.4	66.18
A4	2.0:1	99.313	14.146	0.618	0.9970	3679.9	26.03
A5	2.5:1	78.836	25.809	0.456	0.9983	3121.7	37.25

116

The influences of different photocatalysts on the rheological properties of slurry are studied, and the results are shown in Fig. 6.7(b). The H-B rheological model is used to simulate the rheological behaviours of slurry samples in the descending parts of the thixotropic rings. The calculated parameters and the areas of thixotropic loops are listed in Table 6.4. Thixotropy is an important property of the rheology behaviours of cement slurry samples. Under the action of an external force, the internal networks of slurry samples change with the variation of the shear force. The area of one hysteresis loop enclosed by the shear rise curve and shear fall curve is called the area of the thixotropic loop of the slurry. In general, a larger area of a thixotropic loop means a longer time required for the slurry to recover from the current shear force to the original state without the shear force. That is, the larger the area of the thixotropic loop, the stronger the thixotropy of the slurry, and the smaller the area of the thixotropic loop, the weaker the thixotropy of the paste.

In Table 6.3, the rheology index (n) values in each group are smaller than 1, meaning all slurries yield pseudoplastic fluid. That is, the addition of TiO_2 hydrosols and CNF-TiO_2 hydrosols does not influence the fluid type. The yield stress (τ_0) value of the slurry increases greatly when the pure nano TiO_2 hydrosols are mixed in the paste (A1 group). With the increase of mass ratio between CNF and TiO_2 in hydrosols, the τ_0 values are stable when the CNF to TiO_2 mass ratio is smaller than 2.0. At the same time, the τ_0 value of the slurry in the A5 group decreases. The coefficients of viscosity of slurry noticeably increase and then slightly decrease with the increase of CNF to TiO_2 mass ratio in hydrosols. Meanwhile, the thixotropic loop areas of slurries show the opposite changing low with the increase of CNF to TiO_2 mass ratio in hydrosols. When the CNF to TiO_2 mass ratio in hydrosols is smaller than 1.5, the thixotropic loop area of the slurry decreases with the increase of the CNF to TiO_2 mass ratio, indicating a poor thixotropic performance of the slurry. When the CNF to TiO_2 mass ratio in hydrosols is larger than 1.5, the thixotropic loop area of the slurry increases remarkably, suggesting a recovery of the thixotropy of the slurry.

According to the previous results, the presence of pure TiO_2 hydrosols significantly improves the viscosity but weakens the thixotropic performance of the slurry. Moreover, the modification of CNF to TiO_2 hydrosols enhances those test phenomena. The slurry obtains the largest apparent viscosity and the smallest thixotropic loop. Thus, the CNF to TiO_2 mass ratio in hydrosols influences the dynamic rheological behaviours greatly of the fresh paste, which may also influence the properties of the hardened paste.

6.3.3   Compressive strength

Fig. 6.8 shows the compressive strength values of hardened samples at different ages. At 1-day-age, the average compressive strength value of hardened paste samples containing pure nano TiO_2 hydrosols in the A1 group is smaller than that of the blank paste samples in the reference group. This result proves that mixing the pure acidic nano TiO_2 hydrosols in Port-

land cement paste negatively affects the compressive strength of the hardened paste. However, the CNF-modified TiO_2 hydrosols can offset those negative influences and improve the compressive strength of the hardened cement paste. At 28-day-age, the compressive strength values of hardened samples containing CNF-TiO_2 hydrosols (CNF:TiO_2 > 1.0:1) are much higher than that of the blank samples, indicating the CNF-modified nano TiO_2-based photocatalysts have no harm for the mechanical properties of the hardened cementitious materials.
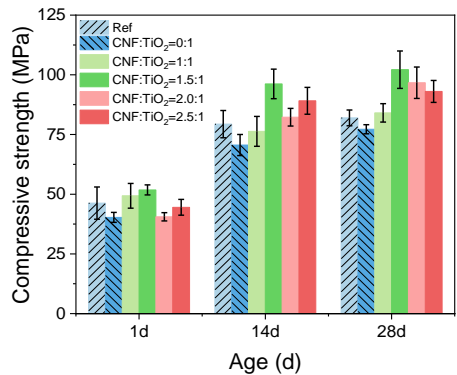
Fig. 6.8 Compressive strength values of hardened paste samples in each group at different ages.

6.3.4 Hydration heat flow and hydrates

(1) Heat flow

| (a) Heat flow | (b) Total heat |
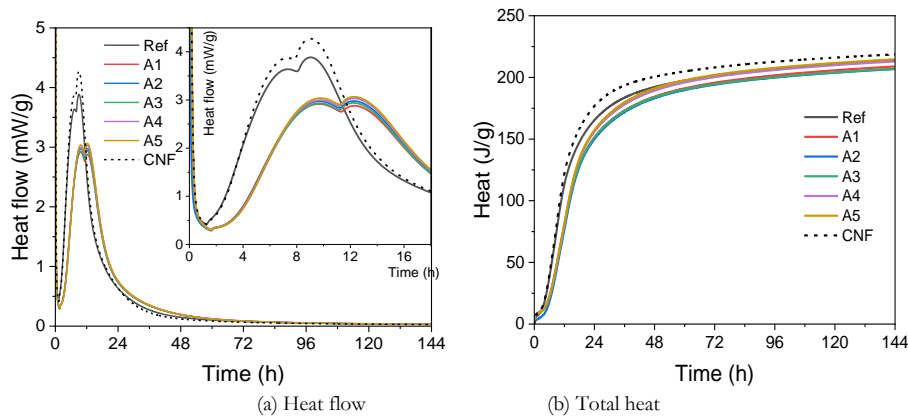
Fig. 6.9 Influences of photocatalysts to cement hydration heat release.

Fig. 6.9 shows the heat flow curves and the total heat curves of white cement containing different kinds of photocatalysts and cellulose nanofibrils in the first 6 days. In Fig. 6.9(a), it can be seen that the presence of all those photocatalysts (photocatalyst: cement = 0.10

w/w %) inhibits the cement hydration reactions at an early age. Compared with the heat flow curves in the reference group, the appearance time of the second and the third peaks in each heat flow curve of cement with photocatalysts is obviously delayed. The peak values of the third one are closer to the second one. Adding the same dosage of cellulose nanofibrils into cement paste accelerates the hydration of cement apparently, which peak values of the second and the third peaks in the heat flow curves are much larger than those in the reference curve, but the appearance time and the difference values of those peaks are almost the same.

These results indicate that the presence of cellulose nanofibrils does not influence the setting time of cement paste, while the presence of cellulose nanofibrils modified nano TiO_2 affects the setting time of the slurry apparently. Moreover, the peak values of heat flow curves of cement paste containing photocatalysts increase with the content ratios of CNF to TiO_2 in the modified photocatalyst. This indicates that the increased content of cellulose nanofibrils in the modified photocatalysts alleviates the inhibition of raw nano TiO_2 hydrosols on the hydration exothermic reactions of cement powders. Fig. 6.9(b) shows that the total heat release values of each curve are close to each other, meaning the ultra-low dosage of photocatalysts can hardly affect the cement hydration heat release.

(2)   XRD patterns

Two images in Fig. 6.10 show the XRD pattern curves of hardened paste containing different kinds of nano TiO_2-based photocatalysts at one day and 28 days of age. In Fig. 6.10, the cement hydrate patterns in hardened paste samples are not influenced by adding CNF-TiO_2 photocatalysts and cellulose fibrils with a dosage of 0.10 w/w % to cement. The main phases in the tested samples are Ettringite, Calcium hydroxide (CH), C-S-H, dolomite and the anhydrate C_3S and C_2S.

1. Ettringite, 2. CH, 3. C_3S, 4. C_2S, 5. C-S-H, 6. Dolomite

(a) 1-day-age
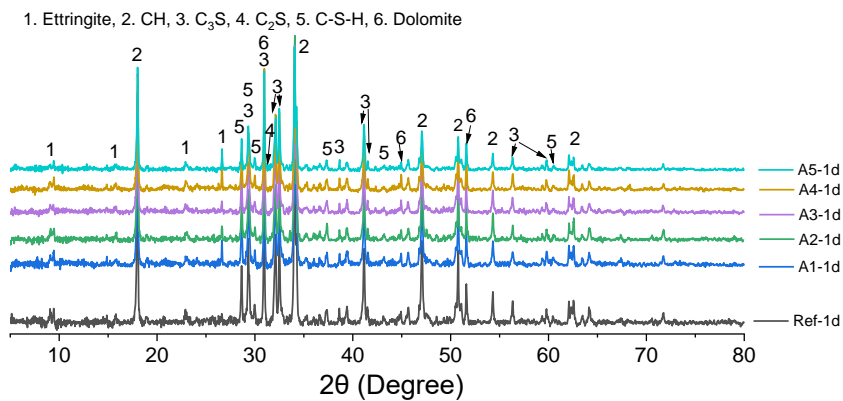
1. Ettringite, 2. CH, 3. C_3S, 4. C_2S, 5. C-S-H, 6. Dolomite
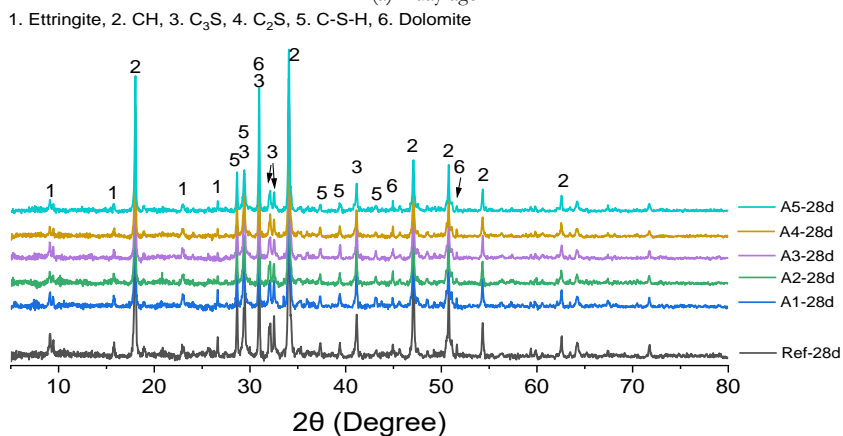
(b) 28-day-age

Fig. 6.10 Fig. 6.10 XRD pattern spectra of modified paste sample at different ages.

(3)   TGA

Fig. 6.11 shows the TGA curves of hardened paste samples in each group at 1-day-age and 28-day-age. Table 6.4 lists the mass ratios of calcium hydroxide (CH) and the non-evaporable water in hardened samples of each group at different ages. In Fig. 6.11, the mass loss between 400 °C and 500 °C represents the decomposition of CH, while the mass loss between 500 °C and 990 °C represents the decomposition of calcium carbonate (multi-phases). In Table 6.4, at 1-day-age and 28-day-age the non-evaporable water mass ratios of samples containing pure nano TiO_2 hydrosols in the A1 group are smaller than those of the blank samples in the Ref group. These results also prove that the presence of pure nano TiO_2 hydrosols has reduced mass ratios of main hydrates in hardened cement paste. While in the paste sample containing the CNF-modified TiO_2 hydrosols in A2 and A3 groups, both mass ratios of CH

and no-evaporable water are larger than those in the Ref group. However, when the CNF to TiO₂ mass ratio in the photocatalysts is higher than 1.5: 1, the CH mass and the non-evaporable water ratios of hardened paste samples decrease apparently at 1-day-age. While at 28-day-age, those phenomena of decrease are not obvious. The CH mass ratios in the paste samples containing pure and modified TiO₂ hydrosols are higher than that in the Ref group, while the non-evaporable water mass ratios are slightly smaller than that in the Ref group.
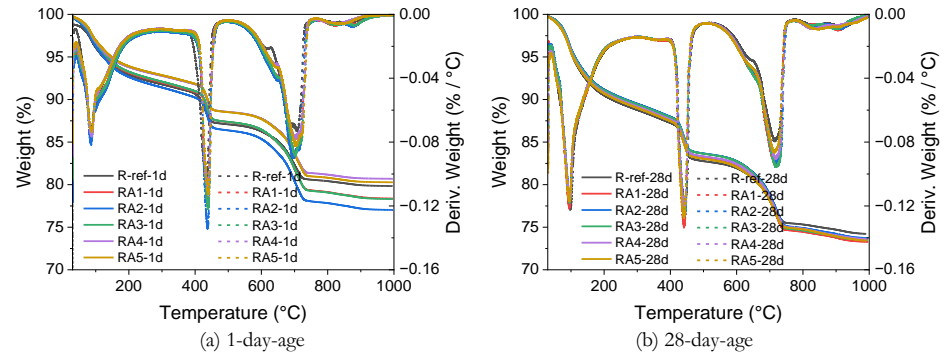
Fig. 6.11 TG-DTG curves of modified paste sample at different ages.

Table 6.4 Mass ratios of CH and non-evaporable water in the hardened paste of each group at different ages.

Group	CNF:TiO₂	CH (%)	Non-evaporable water (%)	CH (%)	Non-evaporable water (%)
		1-day-age		28-day-age	
Ref	0:0	27.861	8.977	33.641	12.573
A1	0:1	29.708	8.950	34.857	12.018
A2	1:1	31.570	9.615	34.433	11.927
A3	1.5:1	30.118	9.073	34.512	11.815
A4	2.0:1	26.550	8.020	34.132	11.937
A5	2.5:1	27.589	8.214	34.364	12.088

6.3.5 Thermal conductivity

Fig. 6.13 shows the thermal conductivity values of hardened cement paste with and without photocatalysts at 28-day-age. The thermal conductivity value of the blank sample is about 1.20 W/(m·K), while the thermal conductivity values of paste samples with nano TiO₂-based hydrosols are smaller than 1.10 W/(m·K). According to the results mentioned in Section 6.3.4, the addition of nano TiO₂-based hydrosols has not influenced the hydrate patterns in the hardened paste sample but has affected the mass ratios of hydrates. Based on the

compressive strength results in Section 6.3.3, the improvement of strength in the paste samples containing CNF-TiO$_2$ hydrosols predicates a denser matrix and a larger thermal conductivity. Thus, those unusual values of thermal conductivity may be the consequence of the re-distribution of pores in the hardened paste. The following section will talk about the pore size distribution and microstructure of samples in each group.
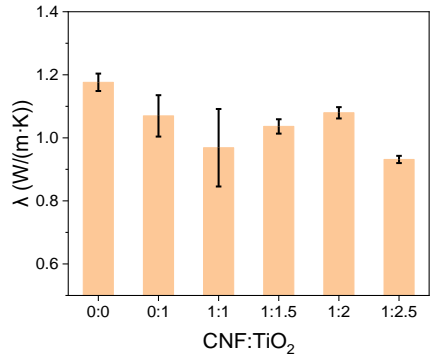
Fig. 6.13 The thermal conductivity coefficients of hardened paste samples in each group.

6.3.6   Porous structure analysis

(1)   MIP analysis
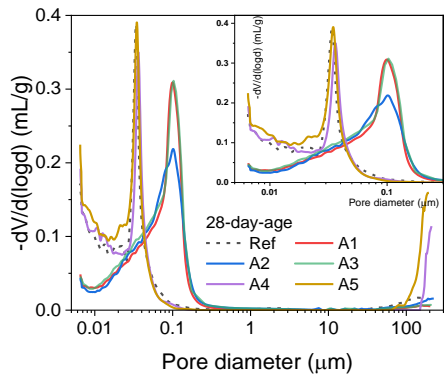
Fig. 6.14 Pore size distribution curves of paste samples in each group at 28-day-age.

Fig. 6.14 shows the pore sizes distribution curves of samples in each group at 28-day-age measured by MIP. In Fig. 6.14, the pore size distribution curve of the blank sample has two main peaks at about 35 nm and 150 μm. For the sample containing pure nano TiO$_2$ hydrosols in the A1 group, the pore size distribution curve has one obvious peak at about 100 nm. When the CNF to TiO$_2$ mass ratio in hydrosols is smaller than 1.5: 1, the pore size distribution curves of the hardened paste containing those modified hydrosols in the A2 and A3

groups have a similar obvious peak at about 100 nm. However, when the CNF to TiO$_2$ mass ratio in hydrosols is larger than 2.0: 1, the pore size distribution curves of the hardened paste containing those modified hydrosols in both A4 and A5 group have the two obvious peaks at about 100 nm and 200 μm.

Table 6.4 Porosity values of pores with different size ranges of samples in each group.

Group	Porosity (%)		
	2 to 50 nm (mesopores)	50 nm to 7.5 μm (macropores)	> 7.5 μm (megapores)
Ref	79.65	8.07	12.28
A1	33.75	63.49	2.76
A2	34.35	61.52	4.13
A3	35.15	62.66	2.19
A4	53.42	3.55	43.03
A5	74.24	3.47	22.29

Table 6.4 lists the porosity of three typical pore sizes in paste samples, which are mesopores (< 50 nm), macropores(50 to 7.5 μm) and mega pores (> 7.5 μm) [288,289]. In Table 6.4, it is easy to find that the sample in the A3 group has the smallest porosity values in the range of megapores, while the value of samples in the Ref group is larger than 12.0 % and the values of samples in the A4 and A5 groups are larger than 20.0 %. These results explain the reasons for the smaller compressive strength values of hardened samples in the A4 and A5 groups compared with the samples in the A3 group, as mentioned in Section 6.3.3.

(2)   SEM morphology

Fig. 6.14 shows the SEM images of hardened samples in each group at 1-day-age. In Fig. 6.14(a and b), compared with the blank sample from the Ref group, the shapes and sizes of AFt phases in the sample of the A2 group are much smaller. In Fig. 6.14(b to d), nano-size particles (nano TiO$_2$ particles and CNF-TiO$_2$ particles) are observed on the surfaces of hydrates (CH) and unhydrated cement. The edges of the CH crystals become blurred in the samples containing CNF-TiO$_2$ hydrosols when the CNF to TiO$_2$ mass ratio is larger than 1.5: 1, as shown in Fig. 6.14(d to f). Nanoholes are observed in the plate-like CH crystals in the sample of the A5 group, as shown in Fig. 5.14(f).
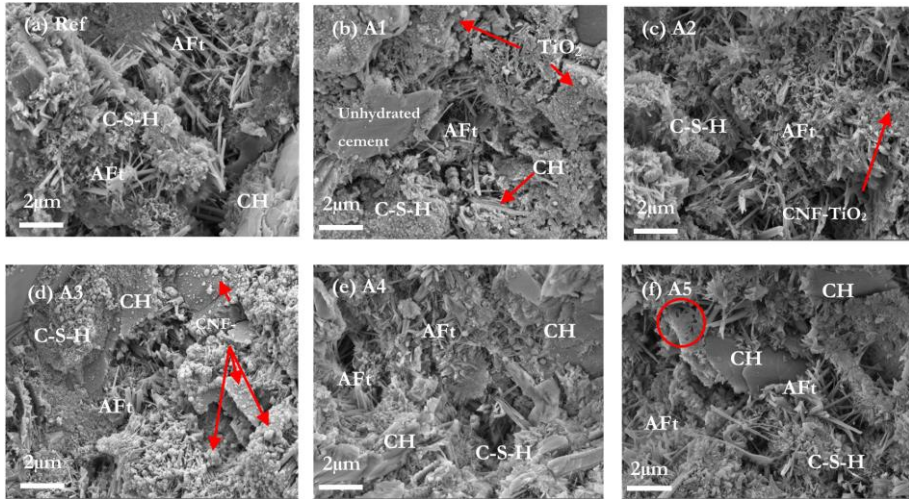
Fig. 6.14 SEM images of hardened paste samples in each group at 1-day-age.
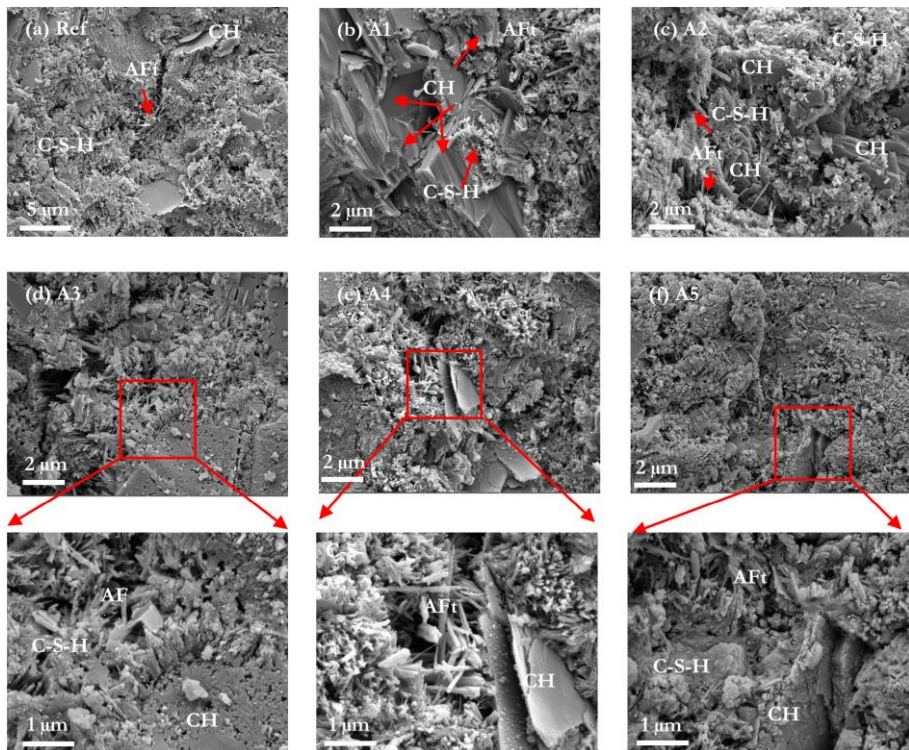
Fig. 6.15 SEM images of hardened paste samples in each group at 28-day-age.

Fig. 6.15 shows the SEM images of the hardened paste samples at 28 days of age at a comparable magnification. As can be seen from Fig. 6.15, there is no regularity in the microstructure of samples in each group, micro-pores are randomly distributed in the matrix. When the pure nano TiO_2 hydrosols are added to the cement paste, the microstructure of the hardened sample is refined, and the shapes of the hydrates are significantly reduced, which is related to the small size and filling effects of nanoparticles. With the increase of the mass ratio of CNF to TiO_2 in the modified hydrosols, the hexagonal flakes of calcium hydroxide crystals in the hardened paste show a growth pattern of layer upon layer, and the size of the ettringite decreases greatly, and the fine C-S-H gel phase is distributed among the crystals of the hardened paste. When the mass ratio of CNF to TiO_2 is larger than 1.5: 1, it can be seen from Fig. 6.15 (d-f) that pitting holes appear on the surface of CH crystals, showing a certain porous structure. The edges of CH crystals are gradually blurred, and the crystal size of the ettringite and C-S-H phases becomes smaller compared with those in the blank paste sample. These special porous features of CH and other hydrates can explain the increase of macropores in the hardened paste containing CNF-TiO_2 hydrosols, as mentioned in the MIP analysis section.

6.4   Summaries

This chapter studies the influences of synthetic cellulose nanofibrils modified nano TiO_2 hydrosols on the early-age and hardened properties of cement paste. The dynamic shear rheology performance and the compressive property are chosen to represent the properties of cement paste samples at an early age and 28-day-age. The following conclusions can be drawn from the acquired results:

(1) Cellulose nanofibrils (CNF) can effectively improve the visible light photocatalytic activity of nano TiO_2 hydrosols. The mass ratios of CNF to TiO_2 have a significant effect on the hydrodynamic sizes and surface charges of the modified CNF-TiO_2 hydrosols. The hydrodynamic sizes increase with the increase of these mass ratios, and the surface zeta potential values first increase and then sharply decrease with the increase of these mass ratios.

(2) Adding 0.10 w/w % of well-designed CNF-TiO_2 hydrosols to cement paste strengthens the hardened cement paste both at an early age and at 28-day-age, but does not change the hydrate patterns. Mixing pure nano TiO_2 hydrosols of the same dosage in cement paste has a negative effect of cement paste on mechanical properties. When the mass ratio of CNF to TiO_2 is 1.5: 1 in the modified hydrosols, adding it to the cement paste leads to the highest compressive strength increase rate of about 25 % at 28-day-age. The significant reduction of megapores' porosity and increase of macropores' porosity in the CNF-TiO_2 modified hardened paste sample are the reasons for the improvement of compressive strength values.

(3) The addition of both pure TiO_2 and CNF-TiO_2 hydrosols does not influence the fluid type of cement paste slurry, which belongs to yield pseudoplastic fluids. The rheology index

and shear stress values of paste slurry containing CNF-TiO$_2$ hydrosols first increase and then decrease with the increase of CNF to TiO$_2$ mass ratios in hydrosols. The thixotropic performances of these paste slurries show the opposite changing rule, the alleviation effects of CNF on the retardation of cement hydration caused by acidic nano TiO$_2$ hydrosols.

Chapter 7 Functional enhancements of ultra-low dosages of CNF-TiO₂ hydrosols modified photocatalytic concrete with designed directional porous channels

The cost-effectiveness of photocatalytic cementitious materials hindered their applications in construction and buildings. This chapter tries to propose a possibility of improving the functional properties of visible-light photocatalysts modified cement paste by using CNF-TiO₂ nano-refrigerants and freeze-casting methods. The results show that 0.10 w/w % CNF-TiO₂ modified hardened paste prepared via freeze-casting obtains much better compressive properties at both early ages and 28-day-age. Due to the pore structure rearrangement effects by freeze-casting processes optimised by CNF-TiO₂ nano-refrigerants, the photocatalytic NO$_x$ degradation rates of hardened cement paste improved more than 1000 times than that of the sample with the same nano-refrigerants prepared via regular casting methods. The CNF-TiO₂ nano-refrigerants modified hardened paste containing directional microchannels with widths of 0.38 to 2.5 μm obtains much better radiative cooling performance and receives less solar energy.

7.1   Introduction

Oxynitride (NO_x) is a major air pollutant produced by the burning of fossil fuels, chemical manufacturing processes, and the treatment of metal nitrification. NO_x not only causes environmental problems such as acid rain and PM2.5 but also is toxic to the human body. Even NO_x in an ultra-low concentration range of ppm can also cause adverse effects on human health and the environment [290]. High-temperature reduction methods can effectively remove high concentrations of NO_x with concentrations in the range from 200 to 2000 ppm in automobile exhaust and industrial manufacturing [291,292].

However, these reduction methods cannot effectively remove low concentrations of NO_x, for example, below one ppm, which is easy to find in a human settlement environment. Therefore, researchers are committed to finding ways to remove low-concentration NO_x with low energy consumption and high efficiency, of which photocatalytic degradation of NO_x is considered to be one of the most promising methods for removing low-concentration NO_x in indoor and outdoor environments [8,293]. As cementitious materials are the most widely used and the largest building materials in the world today, coupled with the huge surface area of buildings, cementitious materials become excellent carriers for photocatalytic degradation of NO_x. For this reason, photocatalytic cementitious materials came into being, among which nano-photocatalysts modified cementitious materials have been rapidly developed in the past 40 years. Nano titanium dioxide (TiO_2) powders are the most widely used photocatalyst in photocatalytic cementitious materials due to the high cost-effective, non-toxicity, chemical inertia in the absence of light and nanometer size effect. In addition, the combination of TiO_2 and cement hydrates have some synergistic advantages because the reaction product can be adsorbed on the surface and then wished away by rain [9].

Moreover, nano TiO_2-modified cementitious materials need to use ultraviolet photon energy to obtain the performance of photocatalytic degradation of gaseous pollutants. This feature is not conducive to the promotion and application of photocatalytic cementitious materials in residential buildings. Through screening and surface modification of photocatalysts, visible light photocatalysts can be obtained, with whom photocatalytic cementitious materials can degrade organic pollutants under the irradiation of visible light. Several studies [294–296] have reported some TiO_2-based visible-light photocatalysts and their applications in cementitious materials. Nevertheless, the reported photocatalytic cementitious materials are not highly cost-effective. Meanwhile, the synthesis conditions of previous visible-light photocatalysts are harsh and not suitable for large-scale production. For example, the UV-visible light catalyst (V-TiO_2 [296]) in the above literature is prepared by spray combustion thermal decomposition processes, which require precision instruments and high energy consumption. The preparation of UV-visible light catalyst (TiO_2@CoAl-LDH [294]) needs to react for 48 hours in 180 ℃ and high-pressure reactor, during which there is a certain explosion risk.

Moreover, for the concrete modified by nano TiO_2-based visible-light photocatalysts, a relatively high dosage is still needed to obtain a satisfying NO_x degradation efficiency. The costs of visible-light photocatalysts in existing reports are much higher than those of nano TiO_2, so their applications in concrete are very limited. Therefore, improving the effects of photocatalytic concrete with low cost and low dosages of photocatalyst on photocatalytic air purification in the UV-visible light bands is still an urgent problem that needs to be solved.

In view of the above-mentioned technical problems of photocatalytic concrete, based on the special low-temperature thermodynamic properties of nano-dispersed TiO_2 hydrosols, the possibility of using them as nano visible-light photocatalytic refrigerants to prepare visible-light photocatalytic concrete with directional channels is investigated in this chapter. In this chapter, by using a very small amount of visible light photocatalytic refrigerant, the visible-light degradation rates of NO_x of concrete can be significantly improved, and the daytime radiation cooling effects of concrete slabs can be improved.

7.2 Materials and experimental

7.2.1 Raw materials

P.W. 52.5 white cement and tip water are used to prepare the cement paste, the chemical components of white cement recorded by XRF are shown in Table 7.1. Tap water is used to prepare the cement paste sample with a water-to-cement ratio of 0.4, and the nano TiO_2-based hydrosols to cement is 0.10 w/w %. In this chapter, pure nano-dispersed TiO_2 hydrosols and CNF-modified TiO_2 hydrosols studied in Chapter 6 are used to prepare the photocatalytic cement paste.

Table 7.1 Chemical components of P.W. 52.5 cement.

Compo-nents	CaO	SiO_2	MgO	SO_3	Al_2O_3	MnO	K_2O	Na_2O	Fe_2O_3	TiO_2	Minor elements
Contents (%)	64.51	20.34	5.70	4.62	2.04	0.83	0.71	0.59	0.26	0.05	0.35

* V_2O_5+Cr_2O_5+NiO+ZnO+BaO+Cl+SrO+Rb_2O+Y_2O_3

7.2.2 Freeze-casting of samples

The cubic samples with the size of 10 mm × 10 mm × 10 mm are used to test the compressive strength of the hardened paste at different ages. Cylindrical paste samples with a size of ф 65 mm × 2 mm are used to measure the thermal conductivity of the hardened samples at 28-day-age. Plate samples with a size of 200 mm × 100 mm × 10 mm are prepared to measure the photocatalytic NO_x degradation and self-cooling performances. According to the mass ratio of CNF to TiO_2 in photocatalysts, hardened cement paste samples are defined as different groups, which are: F-ref (CNF:TiO_2 = 0:0), FA1 (CNF:TiO_2 = 0:1), FA2 (CNF:TiO_2 = 1:1), FA3 (CNF:TiO_2 = 1.5:1), FA4 (CNF:TiO_2 = 2.0:1), FA5 (CNF:TiO_2 =

2.5:1).
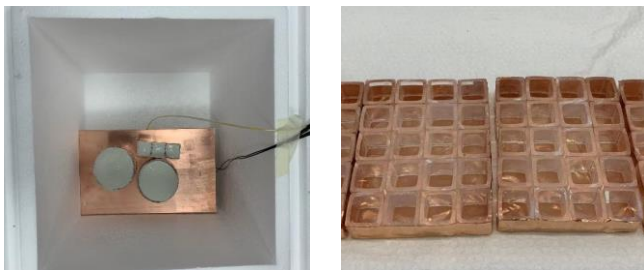
Fig. 7.1 Cubic and cylindrical moulds for freeze-cast samples.
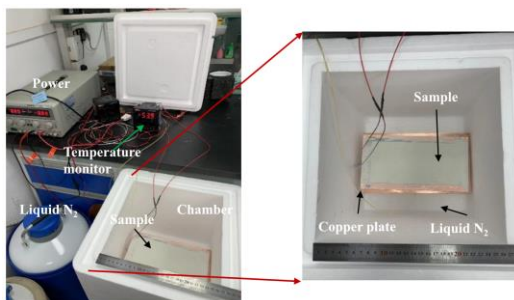
Fig. 7.2 The self-designed device for freeze-casting paste samples.

The specific processes of the unidirectional freezing moulding method are as follows: put the fresh slurry into the specific moulds made of copper and polytetrafluoroethylene or polymethyl methacrylate, as shown in Fig. 7.1. Then put the moulds on the self-designed cryogenic table (as shown in Fig. 7.2) for freeze-casting. In this chapter, the temperature of the cryogenic table for the freeze-casting process is -70 ℃, and the freezing time is determined according to the volume and height of the samples, which is generally about 10 to 15 minutes. After the sample is frozen, the mould is quickly removed. After that, the sample is put into a refrigerator at 5 ℃ immediately, and the sample is cured in that refrigerator for another 48 h. Then, the sample is placed in the curing box and cured at 20 ℃ and 95 % relative humidity until the test age.

7.2.3   Methods

(1)   Air purification performance

The air purification experiments [101,277,297,298] of plate samples are carried out in a homemade reactor designed in accordance with standard ISO 22197-1. The experimental setup, as shown in Fig. 7.3, consists of a reactor cell, a simulated solar light source, a chemiluminescent NO_x analyser, and two gas supplies. The main operating conditions of the system are as follows: the wavelength of solar light resource is 320 - 2500 nm, the irradiance

flux on the surface of flat cement paste samples is 10 ± 0.05 W/m², the pollutant source concentration is 0.5 ppm, the NO flow and air flow are 60 mL/min and 2.94 L/min, and the total gas flow is 3.0 L/min, the relative humidity in the reactor is 50 ± 1 %. The amount of NO_x converted in the reactor is calculated as the following:

$$NO_x Conversion(\%) = \frac{[C_{NO_x}]_{in} - [C_{NO_x}]_{out}}{[C_{NO_x}]_{in}} \times 100 \tag{7.1}$$

Where $[C_{NOx}]_{in}$ is the initial concentration [ppm], measured by taking the average value of the first 5 min of the test before turning on the light. The outlet concentration $[C_{NOx}]_{out}$ is measured by taking the average value of the last 5 min of the irradiation period [ppm]. The amount of NO converted in the reactor is calculated following:

$$NO Conversion(\%) = \frac{[C_{NO}]_{in} - [C_{NO}]_{out}}{[C_{NO}]_{in}} \times 100 \tag{7.2}$$

Where $[C_{NO}]_{in}$ is the initial concentration [ppm], measured by taking the average value of the first 5 min of the experiment, before turning on the light. The outlet concentration $[C_{NO}]_{out}$ is measured by taking the average value of the last 5 min of the irradiation period [ppm].
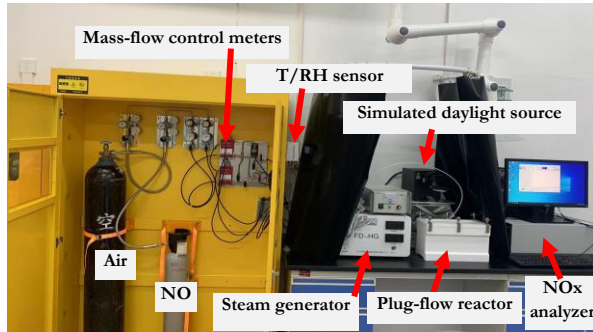
Fig. 7.3 The air purification experimental setup [298].
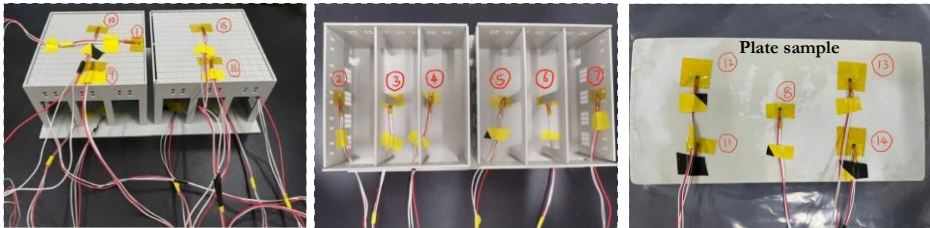
Fig. 7.4 The building model and positions of temperature sensors in it.

A simple test device is designed to record the temperature change of the test cementitious plate surface under simulated sunlight irradiation for a period of time with a temperature recorder, which has 24 test channels. The temperature changes at different test channels quantitatively characterize the daytime radiation cooling performance of the test plate. The experimental device is shown in Fig. 7.4, and the channel numbers and the locations of the test temperature sensors are shown on the building model.

7.2.4   Characterizations

X-ray diffraction (XRD) pattern (Bruker D4 PHASER, Philips, The Netherlands) with a Co tube (40 kV, 40 mA). A typical run used in this test is made with a step size of 0.02°/min and a dwell time of 0.5 s. Thermal gravimetric analysis (TGA) is performed using a thermal analyser (SDT 650, WATERS, USA), with nitrogen as a protective gas, and the test sample is heated from 30 °C to 1000 °C at a rate of 10 °C / min. Before the test, all the samples need to be crushed and soaked in acetone for seven days and dried in an oven at 40 °C to stop further hydration of the cement. The mercury intrusion pore size analyzer (PoreMaster 60, Anton paar, USA) is used to measure the pore size distribution curves of hardened paste samples. The maximum pressure applied is 420 MPa. Parameters such as the thermal conductivity of hardened paste samples are measured by the ISOMET2114 portable heat conduction meter produced by Precision Instrument Co., Ltd in Slovakia. The compressive strength values of the hardened paste samples are measured by a universal testing machine with a test limit of 100 kN (Wuhan Weiheng Industrial System Co., Ltd., P. R. China). During the compressive test, the dimension of the compressive surface is 40mm×40mm, and the loading rate is 2400 N/s.

7.3   Results and discussions

7.3.1   NO$_x$ degradation efficiency

Fig. 7.5 show the concentration change curves of photocatalytic degradation of NO$_x$ on the surface of cementitious plate samples under the irradiation of simulated solar light. In Fig. 7.5, the concentration of NO on the surface of plates mixed with different CNF-TiO$_2$ photocatalysts decreases to a stable value within 5 minutes after the light is turned on within two hours of sunlight exposure. When the light source is turned off, the concentration of NO in the test chamber returns to the original concentration of about 500 ppb within 2 minutes. As can be seen in Fig. 7.5, the regular casted cementitious plates containing CNF-TiO$_2$ photocatalysts in each group show barely any degradation effects on NO$_x$, indicating that mixing 0.1 w/w % photocatalysts in paste has a very poor effect on the photocatalytic degradation ability of hardened cement paste plates.

Table 7.2 NO$_x$ degradation rate of the plate containing photocatalysts in each group.

Group	Photocata- lyst: cement (w/w %)	NO Conversion (%)	NO$_x$ Conversion (%)	Increase rate of NO Conversion (%)	Increase rate of NO$_x$ Conversion (%)
FA1		17.8	18.0	546.4	651.0
FA2		12.5	12.4	273.6	267.6
FA3		9.6	9.8	196.5	218.4
FA4		11.4	10.3	905.4	809.9
FA5	0.10	6.2	5.5	587.5	460.4
A1		3.3	2.8	-	-
A2		4.6	4.6	-	-
A3		0.4	0.4	-	-
A4		0.2	0.5	-	-
A5		1.0	1.2	-	-
[296]	1.0	10.5	8.2	-	-
[294]	1.0	-	12.3	-	-

Table 7.2 lists the NO$_x$ degradation rates of cementitious plates in each tested group. In Table 7.2, the degradation rates of NO and NO$_x$ in the plate samples made of regular casting in the A1 and A2 groups are all lower than 5 %, and the degradation rates of NO and NO$_x$ in the A3 and A4 groups are smaller than 0.5 %. In contrast, the plate samples made by the freeze-casting method significantly improved the degradation rate of NO and NO$_x$. The degradation rate of NO in the FA1 group is 17.8 %, which is 546.4 % of that the samples in the A1 group. The degradation rate of NO in the FA2 group is 12.5 %, which is 273.6 % of that in the A2 group. The degradation rate of NO of the plate sample in the FA3 group is 9.6 %, which is 196.5 % of that in the A3 group. The degradation rate of NO of the plate sample in the FA4 group is 11.4 %, which is 905.4 % of that in the A4 group. The degradation rate of NO of the plate sample in the FA5 group is 6.2 %, which is 587.5 % of that in the A5 group. The above results show that the preparation processes of freeze-casting greatly improve the efficiency of photocatalytic degradation of NO and NO$_x$ in concrete with an ultra-low photocatalyst content.

Moreover, compared with the NO$_x$ degradation rate of concrete modified with 1.0 w/w % visible light photocatalysts reported in the literature [294,296], the NO$_x$ degradation rates of visible light photocatalytic concrete containing 0.10 w/w % photocatalysts studied in this chapter are comparable in the FA1 to FA4 groups. Therefore, the above results show that the preparation process of freezing forming can greatly improve the efficiency of photocatalytic degradation of nitrogen oxides in concrete with low photocatalyst content and can effectively improve the utilization rate of photocatalyst in concrete.

(a1) FA1, CNF:TiO₂ = 0:1, freezing-casted   (b2) A1, CNF:TiO₂ = 0:1, regular casted

(b1) FA2, CNF:TiO₂ = 1:1, freezing-casted   (c2) A2, CNF:TiO₂ = 1:1, regular casted

(c1) FA3, CNF:TiO₂ = 1.5:1,freezing-casted   (d2) A3, CNF:TiO₂ = 1.5:1,regular casted

(d1) FA4, CNF:TiO₂ = 2.0:1, freezing-casted   (e2) A4, rCNF:TiO₂ = 2.0:1, regular casted
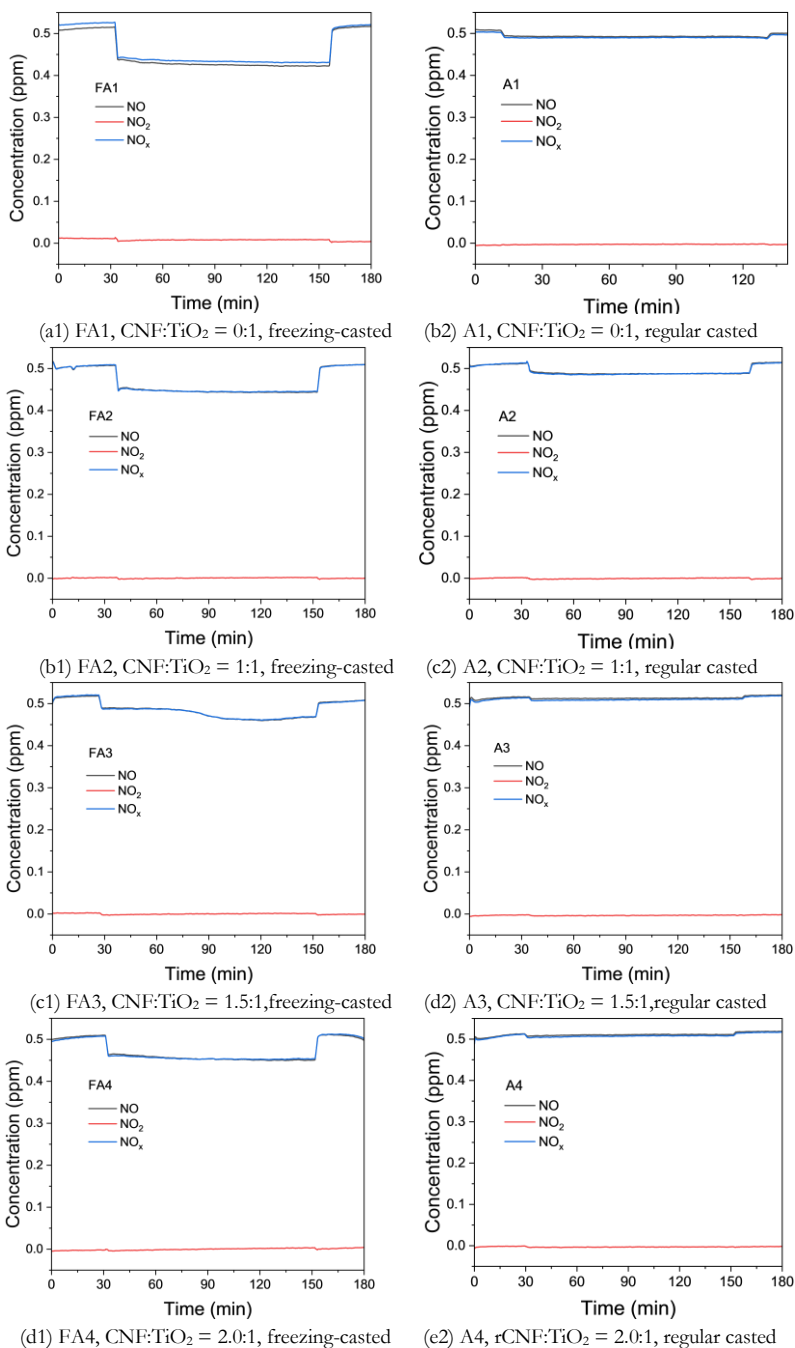
Fig. 7.5 The NOₓ concentration changing curves of tested plates during simulated solar light irradiation.

134
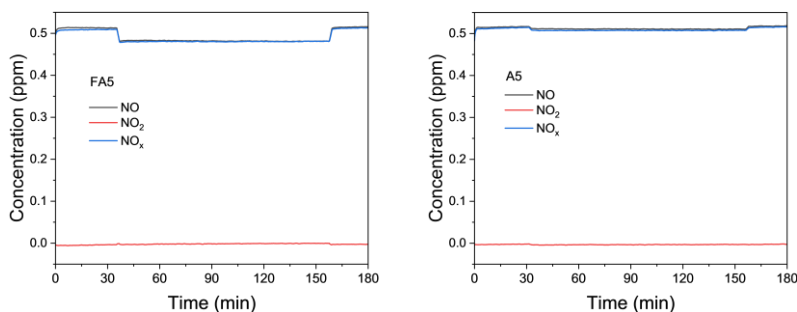
(e1) FA5, CNF:TiO₂ = 2.5:1, freezing-casted   (e2) A5, CNF:TiO₂ = 2.5:1, regular casted

Fig. 7.5 continued.

7.3.2   Radiative cooling performances

The temperature-changing curves of the surface and bottom of the tested plates containing photocatalysts with two casting methods and the bottom of the building model under simulated sunlight are recorded in this chapter. Fig. 7.6 shows the temperature change curves recorded by three temperature sensors of the plates with freeze-casting and regular casting, respectively. In Fig. 7.6, within 1 h irradiation by the simulated solar light source, the highest temperature on the upper surfaces of the freezing-casted plates does not exceed 34 ℃, and the highest temperature on the lower surfaces of the plates does not exceed 28 ℃. While, within 1 h irradiation by the simulated daylight light source, the upper surface temperatures of the regular casted plates are close to or exceed 34 ℃, and the highest temperature of the lower surfaces of the plates is close to 30 ℃. These results show that the freezing-casted photocatalytic paste plates received less radiation energy from the light source.

Table 7.3 lists the calculation values of the temperature-changing rate of plates in each group. The temperature difference ΔT of the upper and lower surfaces of the plate is calculated when the recorded temperature is relatively stable. In Table 7.3, for the freezing-casted plates (Group F-ref to FA5), ΔT values of the plate containing CNF-TiO₂ hydrosols are between 4.4 - 7.6 ℃, which first increase and then decrease with the CNF to TiO₂ mass ratios. For the regular casted plates (Group Ref to A5), ΔT values of the plate containing CNF-TiO₂ hydrosols are between 4.8 - 7.3 ℃, which also first increases and then decreases with the CNF to TiO₂ mass ratios. RR1 values in Table 7.3 are the reduction rate of ΔT to the Maximum temperature on the surface of the paste plate ($T_{max,s}$). When the CNF to TiO₂ mass ratio is larger than 1:1, the RR1 values of plates made by freeze-casting are larger than those by regular casting, indicating the presence of CNF-TiO₂ hydrosols improves the radiative cooling properties of hardened paste. RRS values in Table 7.3 are the reduction rate of $T_{max,s}$ of the tested plate to that of the Ref group. For regular casted plates, the differences in RRS values in each group are very subtle. The RRS values of the plates made by freeze-casting processes are much larger, meaning an apparent decrease in the temperature on the top surface of the plates compared with that of the Ref group (blank, regular cast samples). RRB

values show similar changing rules to the RRS values. RRC values are the reduction rate of $T_{max,s}$ of the tested plates made by freeze-casting and the regular casting processes. Besides the plate in the FA4 group, the RRC values of plates are larger than 4.0 %, meaning slight but important temperature reduction effects resulted from the casting methods.

The above results support the idea that regular casted cement paste plates with and without TiO$_2$-based photocatalysts cannot obtain effective radiative cooling performance. At the same time, the freezing-casted cement paste plates obtain lower temperature values on the top surfaces of plates, meaning a good radiative cooling performance, which seems more related to the special porous structure than the presence of nano photocatalysts. However, the mechanical properties of hardened paste samples will also be influenced by the porous structure of the samples. The following sections will discuss this.

Table 7.3 Temperature changing rates of the plates under the irradiation of simulated solar light source.

Group	$T_{max,s}$ (℃)	$T_{max,b}$ (℃)	ΔT (℃)	RR1 (%)	RRS (%)	RRB (%)	RRC (%)
F-Ref	31.2	26.8	4.4	14.10	9.83	7.27	9.83
FA1	32.7	26.7	6.0	18.35	5.49	7.61	5.76
FA2	33.2	26.9	6.3	18.98	4.05	6.92	4.32
FA3	33.5	27.0	6.5	19.40	3.18	6.57	5.37
FA4	34.3	26.7	7.6	22.16	0.87	7.61	0.00
FA5	33.3	28.0	5.3	15.92	3.76	3.11	5.93
Ref	34.6	28.9	5.7	16.47	-	-	-
A1	34.7	27.4	7.3	21.04	-0.29	5.19	-
A2	34.7	28.6	6.1	17.58	-0.29	1.04	-
A3	35.4	29.3	6.1	17.23	-2.31	-1.38	-
A4	34.3	29.5	4.8	13.99	0.87	-2.08	-
A5	35.4	29.4	6.0	16.95	-2.31	-1.73	-

$T_{max,s}$: Maximum temperature on the surface of the paste plate; $T_{max,b}$: Maximum temperature on the bottom of the paste plate;
$\Delta T = T_{max,s}-T_{max,b}$; RR1: Reduction rate of $T_{max,s}$, $RR1(T_{max,s}) = 100 \times \Delta T/T_{max,s}$; RRS: Reduction rate of $T_{max,s}$ compared with the Ref group, $RRS(T_{max,s}) = 100 \times (T_{max,s}-T_{max,s}$ of Ref$)/(T_{max,s}$ of Ref$)$; RRB: Reduction rate of $T_{max,b}$ compared with the Ref group, $RRB(T_{max,b}) = 100 \times (T_{max,b}-T_{max,b}$ of Ref$)/(T_{max,b}$ of Ref$)$; RRC: Reduction rate of $T_{max,s}$ compared with the relative group made by regular casting processes.

(a1) F-ref, CNF:TiO$_2$ = 0:0, freezing-casted

(a2) Ref, CNF:TiO$_2$ = 0:0, regular casted

(b1) FA1, CNF:TiO$_2$ = 0:1, freezing-casted

(b2) A1, CNF:TiO$_2$ = 0:1, regular casted

(c1) FA2, CNF:TiO$_2$ = 1:1, freezing-casted

(c2) A2, CNF:TiO$_2$ = 1:1, regular casted

(d1) FA3, CNF:TiO$_2$ = 1.5:1, freezing-casted

(d2) A3, CNF:TiO$_2$ = 1.5:1, regular casted
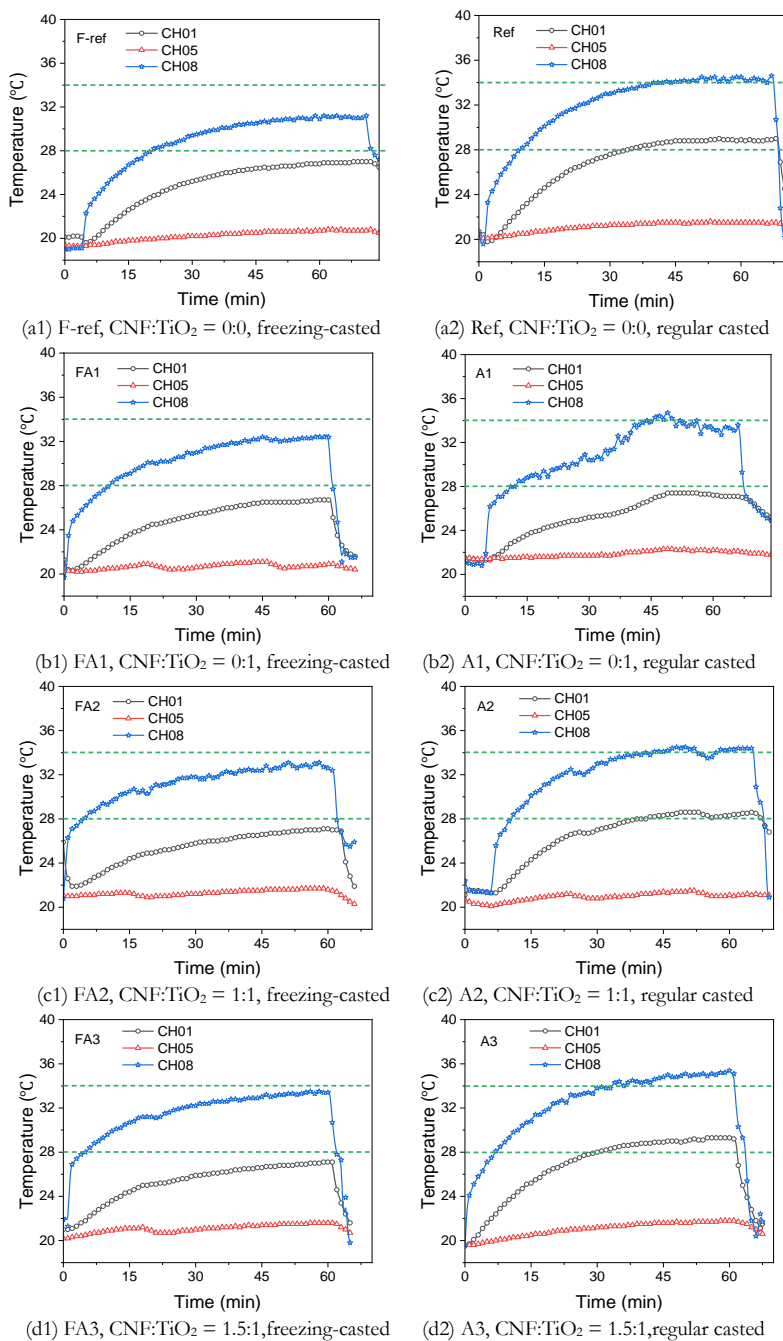
Fig. 7.6 Temperature changing curves of paste samples casted by regular and freeze-casting methods with and without CNF-TiO$_2$ photocatalysts under the irradiation of simulated solar light source for one hour.

(e1) FA4, CNF:TiO$_2$ = 2.0:1, freezing-casted

(e2) A4, rCNF:TiO$_2$ = 2.0:1, regular casted

(e1) FA5, CNF:TiO$_2$ = 2.5:1, freezing-casted

(e2) A5, CNF:TiO$_2$ = 2.5:1, regular casted
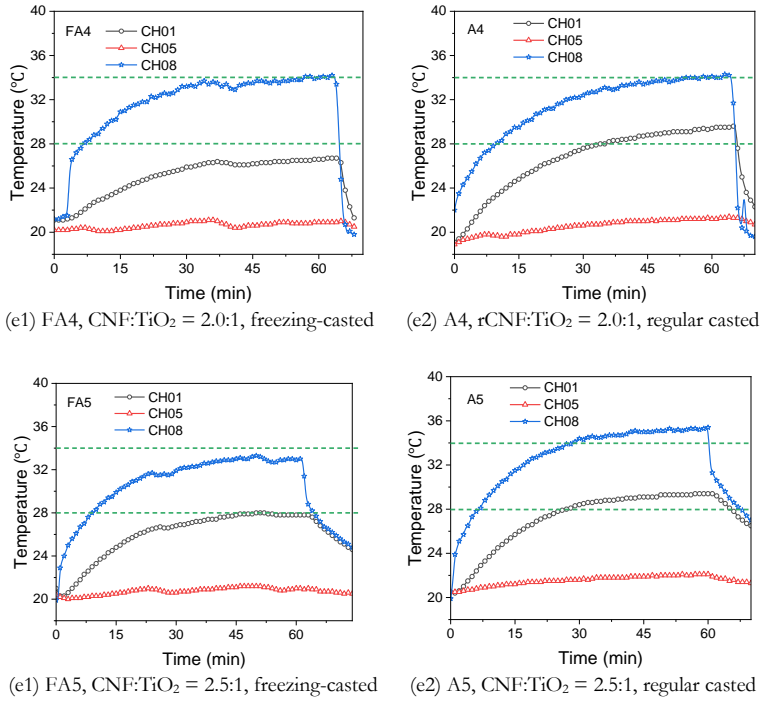
Fig. 7.6 continued.

7.3.3   Porous structures

(1)   SEM analysis

Fig. 7.7 shows SEM images of cross sections of freezing-casted hardened cement paste samples at 1 and 28 days of age. After one day and 28 days of curing, the samples in each group have obvious directional distributed micron channels, the directions of which are represented by red double arrows in Fig. 7.7. The widths of the micron channels are affected by the CNF to TiO$_2$ mass ratios of the synthetic photocatalysts, which is because the inhibition of the photocatalyst on the hydration reaction of cement causes the change of the amount of early hydration products, and thus the change of the morphology of the hydration products inside the pores. As shown in Fig. 7.7, the widths of the micron channels in samples decrease with the increase of the mass ratio of CNF:TiO$_2$ in the photocatalysts, which may be related to the thickening effects of the hydrophilic functional groups of cellulose nanofibrils. During the processes of water icing, rheological parameters of slurry samples, for example, the viscosity, will significantly affect the sizes of the ice crystals [299,300], thus causing changes in the widths of the micron channels.

According to Mi scattering theory, when the diameters of the particles in the atmosphere or the diameters of the holes (channels) are equivalent to the wavelengths of the electromagnetic waves, radiation scattering will occur, that is, the light scattering phenomenon. Moreover, the distribution of pores in the hardened paste samples will influence the absorption and desorption of gas molecules on the surface of samples [160], resulting in different photocatalytic NO_x degradation rates. Therefore, the discussion on the pore size distribution curves at specific size ranges is important for analyzing the reasons for the better cooling performances and NO_x degradation properties of freezing-casted samples with different CNF-TiO_2 photocatalysts.

CNF:TiO₂ = 0: 0   CNF:TiO₂ = 0: 1   CNF:TiO₂ = 1: 1

CNF:TiO₂ = 1.5: 1   CNF:TiO₂ = 2.0: 1   CNF:TiO₂ = 2.5: 1

(a) 1-day-age

CNF:TiO₂ = 0: 0   CNF:TiO₂ = 0: 1   CNF:TiO₂ = 1: 1

CNF:TiO₂ = 1.5: 1   CNF:TiO₂ = 2.0: 1   CNF:TiO₂ = 2.5: 1

(b) 28-day-age
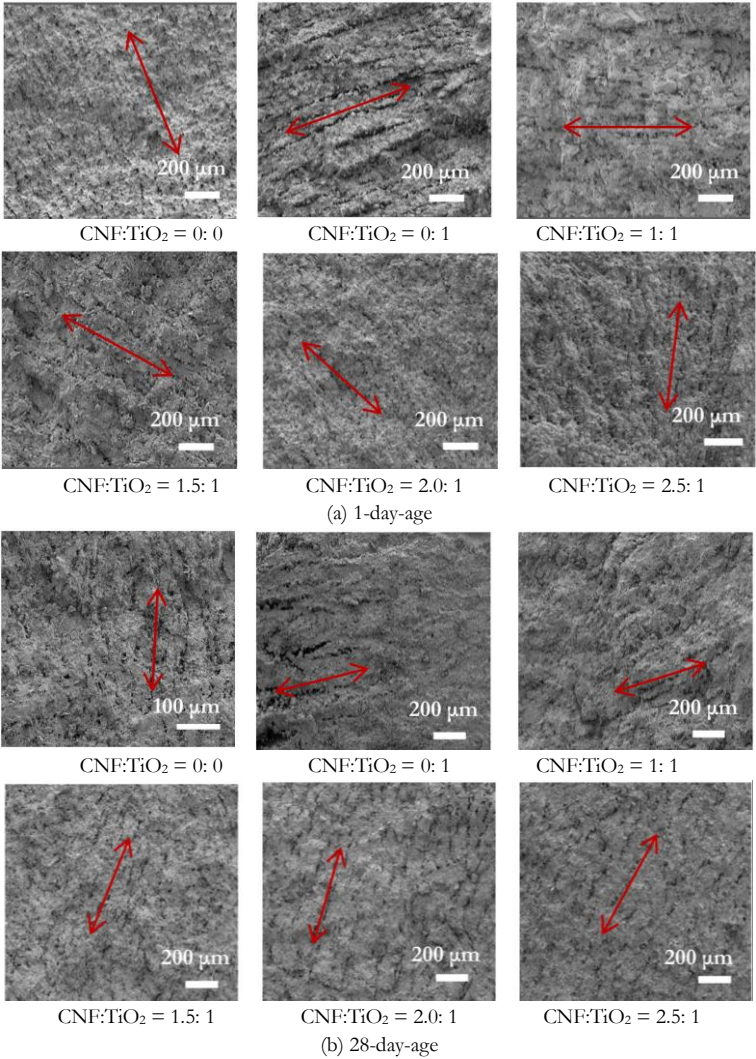
Fig. 7.7 SEM images of freezing-casted hardened cement paste at ages of 1 and 28 days (the direction of the pore is marked with red double arrows).

(2) MIP analysis

Fig. 7.8 shows the pore size distribution curves of hardened paste samples containing different CNF-TiO$_2$ photocatalysts at 28-day-age. In Fig. 7.8, the pore size distribution curve of the blank sample has one main peak at about 100 nm. For the sample containing pure nano TiO$_2$ hydrosols in the FA1 group, the pore size distribution curve has two obvious peaks at about 25 nm and 150 μm. When the CNF to TiO$_2$ mass ratio in hydrosols is larger than 1.5: 1, the pore size distribution curves of the hardened paste containing those CNF-TiO$_2$ hydrosols in the FA4 and FA5 groups have a similar one obvious peak at about 100 nm and 150 μm. However, when the CNF to TiO$_2$ mass ratio in hydrosols is 1.5: 1, the pore size distribution curves of the hardened paste containing CNF-TiO$_2$ hydrosols in the FA3 group have one obvious peak at about 9 nm. As shown in the partial zoom image in the upper right corner of Fig. 7.8, all the freezing-casted samples contain pores or channels with a size range between 0.38 to 2.5 μm. Compared with the MIP data in Fig. 6.14 in Chapter 6, the regular casted samples have barely any pores in the size range between 0.38 to 2.5 μm. These results can explain the better radiative cooling performances of the freezing-casted cement past samples via the improvement of solar light scattering behaviors.
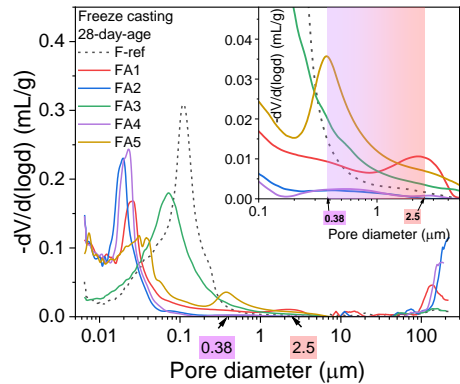
Fig. 7.8 Pore size distribution curves of paste samples made by freeze-casting processes in each group.

Table 7.4 Porosity values of pores with different size ranges of freezing-casted samples in each group.

Group	Porosity (%)		
	2 to 50 nm (mesopores)	50 nm to 7.5 μm (macropores)	>7.5 μm (megapores)
F-Ref	23.69	72.61	3.70
FA1	65.91	17.11	16.98
FA2	69.76	4.04	26.20
FA3	33.95	62.61	3.44
FA4	77.78	4.19	18.03
FA5	68.87	29.63	1.50

Table 7.4 lists the porosity of three typical pore sizes in paste samples, which are mesopores (< 50 nm), macropores(50 to 7.5 μm) and mega pores (>7.5 μm) [288,289]. In Table 7.4, it is easy to find that the sample containing CNF-TiO$_2$ hydrosols or pure nano TiO$_2$ hydrosols obtain more mesopores compared with the sample in the F-ref group. The changing rules of mesopores porosity values in samples containing CNF-TiO$_2$ hydrosols are similar to that of NO and NOx degradation rates, as mentioned in Section 7.3.1. The conclusions about the formation of pores in the size range of 10 to 50 nm lead to the increase of photocatalytic air purification efficiency in the literature [160] can be used to explain this phenomenon. Moreover, the formation of mesopores also results in a denser matrix and better mechanical compressive properties, which will be discussed in the next section.

7.3.4   Compressive strength

Fig. 7.9 shows the compressive strength values of the hardened cement paste samples made by freeze-casting processes at different ages. The directional arrangement of the internal micron channels and pores of the samples caused by the casting method and the direction of force loading are parallel to the freezing direction during the compressive tests. In Fig. 7.9, the compressive strength values of the hardened cement paste mixed with CNF-TiO$_2$ hydrosols with the CNF to TiO$_2$ mass ratios smaller than 2.0: 1 are much larger than that of the F-ref group (blank sample) at 1-day-age. At 28-day-age, the compressive strength values of all the samples containing CNF-TiO$_2$ hydrosols are larger than that of blank samples. This may be due to the microstructural changes caused by the synergistic effects of nano-particle refinement on pore sizes and frozen water on pore size rearrangement.
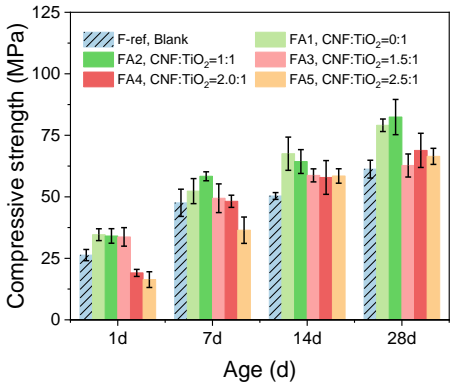
Fig. 7.9 Compressive strength values of hardened paste samples in each group at different ages.
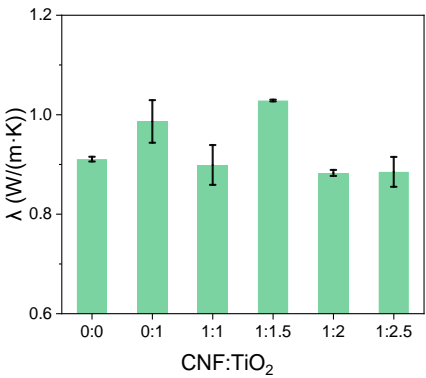
Fig. 7.10 The thermal conductivity coefficients of freezing-casted paste samples in each group.

7.3.5   Thermal conductivity

Fig. 7.10 shows the thermal conductivity values of hardened cement paste with and without photocatalysts made by freeze-casting processes at 28-day-age. The thermal conductivity value of the blank sample is about 0.91 W/(m·K), while the thermal conductivity values of paste samples with CNF-TiO_2 hydrosols in the FA3 group is about 1.03 W/(m·K). The thermal conductivity values of paste samples with CNF-TiO_2 hydrosols in FA2, FA4 and FA5 groups are smaller than 0.90 W/(m·K). According to the results mentioned in Section 6.3.4, the addition of nano TiO_2-based hydrosols has not influenced the hydrate patterns in the hardened paste sample but has affected the mass ratios of hydrates. Based on the compressive strength results in Section 7.3.4 and Section 7.3.3, the improvement of strength and the rearrangement of pore structures in the paste samples containing CNF-TiO_2 hydrosols result in the variation of thermal conductivity values.

7.3.6   Hydrates

(1)   XRD patterns

Fig. 7.11 shows the XRD pattern curves of hardened paste containing different kinds of nano TiO_2-based photocatalysts at 1-day-age and 28-day-age. The cement hydrate patterns in hardened paste samples are not influenced by adding CNF-TiO_2 photocatalysts and cellulose fibrils with a dosage of 0.10 w/w % to cement. The main phases in the tested samples are Ettringite, Calcium hydroxide (CH), C-S-H, dolomite and the anhydrate C_3S and C_2S.

1. Ettringite, 2. CH, 3. C$_3$S, 4. C$_2$S, 5. C-S-H, 6. C-A-S-H, 7. Dolomite

(a) 1-day-age

1. Ettringite, 2. CH, 3. C$_3$S, 4. C$_2$S, 5. C-S-H, 6. C-A-S-H, 7. Dolomite
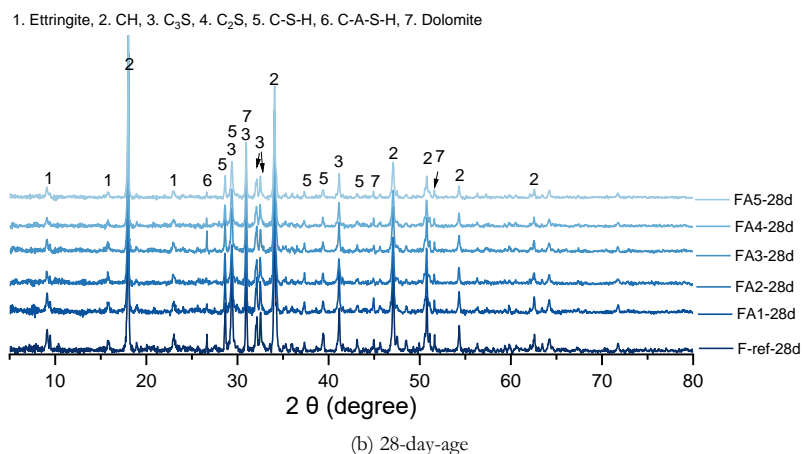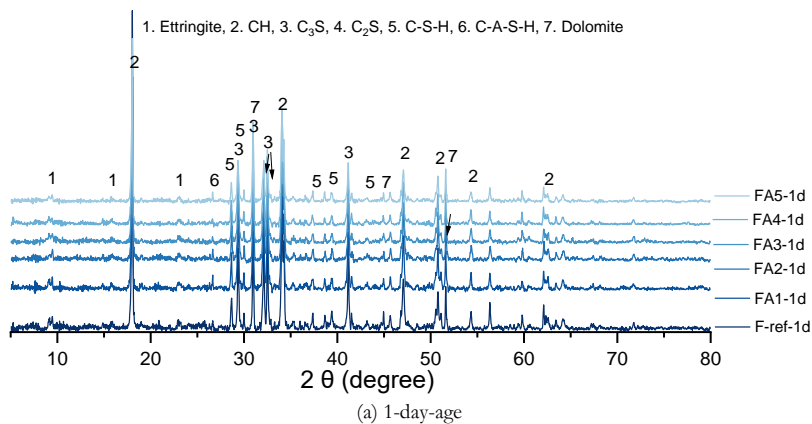
(b) 28-day-age

Fig. 7.11 XRD pattern spectra of modified paste sample made of freeze-casting at 28-day-age.

(a) 1-day-age
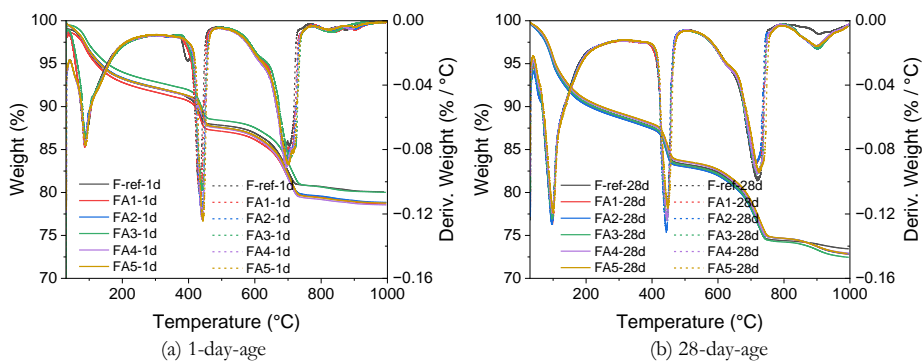
(b) 28-day-age

Fig. 7.12 TG-DTG curves of modified paste samples at different ages.

Fig. 7.12 shows the TGA curves of hardened paste samples in each group at 28-day-age. Table 7.5 lists the mass ratios of calcium hydroxide (CH) and the non-evaporable water in hardened samples of each group at different ages. In Fig. 7.12, the mass loss between 400 °C and 500 °C represents the decomposition of CH, while the mass loss between 500 °C and 990 °C represents the decomposition of calcium carbonate (multi-phases). In Table 7.5, at 1-day-age and 28-day-age, the non-evaporable water mass ratios of samples containing pure nano TiO_2 hydrosols in the FA1 group are larger than those of the blank samples in the F-ref group. These results suggest that in the freeze-casting processes, the retardation of cement hydration caused by pure nano TiO_2 hydrosols is cancelled and even promoted. Meanwhile, in the paste sample containing the CNF-modified TiO_2 hydrosols in FA2 and FA3 groups, both mass ratios of CH and non-evaporable water are larger than those in the F-ref group. The CH mass ratios in the paste samples containing pure and modified TiO_2 hydrosols are higher than that in the F-ref group, while the non-evaporable water mass ratios are slightly larger than that in the F-ref group.

Table 7.5 Mass ratios of CH and non-evaporable water in the hardened paste of each group at different ages.

Group	CNF:TiO$_2$	CH (%)	Non-evaporable water (%)	CH (%)	Non-evaporable water (%)
		1-day-age		28-day-age	
F-ref	0:0	26.187	8.271	34.412	11.375
FA1	0:1	28.698	8.636	35.203	11.736
FA2	1:1	29.716	8.745	35.189	11.513
FA3	1.5:1	28.670	8.615	36.196	11.659
FA4	2.0:1	30.176	8.721	35.620	11.554
FA5	2.5:1	29.901	8.676	36.065	11.761

7.4   Summaries

This chapter investigates the enhancement effects of the directional freeze-casting method on the photocatalytic air purification performance under simulated sunlight irradiation for photocatalytic concrete modified with visible light active bio-based modified nano TiO_2 hydrosols. It also studies the influences of the directional micro-channels on the compressive properties of hardened paste samples at different ages. The impacts of different photocatalysts on the morphology and distribution of cement hydrates are analyzed. The following conclusions are drawn:

(1) Freeze-casting processes significantly improve the air purification performance of ultra-low dosage of CNF-TiO$_2$ hydrosols-modified visible light photocatalytic concrete. The porosity increments in the pore size range of 10 to 50 nm resulting from the pore structure

rearrangement of water icing can explain the better NO_x degradation behaviours of hardened paste samples containing 0.10 w/w % of CNF-TiO_2 hydrosols.

(2) The directional arrangement of microchannels of the widths between 0.38 to 2.5 μm caused by the freeze-casting processes in the cement paste dominates the radiative cooling performance of the plate samples. The presence of CNF-TiO_2 hydrosols in paste slurries in such a small dosage affects the freezing rate of free water during casting, resulting in the difference in pore structure distribution and microchannel widths.

(3) In the processes of freeze-casting, the cement hydration retardation caused by water freezing is much worse than that by acidic nano-dispersed TiO_2 hydrosols. The CNF-TiO_2 hydrosols with high dispersion can be used as the nano-visible light catalytic refrigerant, which improves the thermal conductivity of the liquid phase in the fresh slurries, increases the average cooling rate, and influences the pore structure of the hardened paste. Therefore, the hardened paste containing pure nano TiO_2 hydrosols and CNF-modified TiO_2 hydrosols show much larger compressive strength values than that of the blank samples.

Chapter 8 Conclusions, innovations and recommendations

8.1   Conclusions

In this thesis, the improvement mechanism and functional degradation mechanism of photocatalytic self-cleaning performance of common Portland cementitious materials are studied by nano-dispersed TiO_2 hydrosols. From the perspective of the photocatalytic performance of nano TiO_2 hydrosols in the simulated pore solution, in the positive ion water environment, the photocatalytic performance of degradation of gaseous pollutants on the surface of cement paste and self-cleaning performance of degradation of dry solid organic dyes in cement paste and cement mortar. The feasibility of the application of nano TiO_2 hydrosols as photocatalysts in the improvement of the self-cleaning performance of cementitious materials is demonstrated. From the perspective of formation, growth, dissolution and degradation of cement hydration products, the effects of Portland cement at different service stages on the surface state, electronic band structure, optical properties and photocatalytic reaction kinetics of nano TiO_2 hydrosols are analyzed in detail. The effects of nano TiO_2 hydrosols on the cement hydration process, crystal morphology of hydration products, carbonization of cement mortar and dissolution of hydration products during the wetting and drying alternating cycle of pure water are analyzed. The potentials of preparing visible-light photocatalysts by cellulose nanofibrils (CNF) modifying nano TiO_2 hydrosols are discussed.

Through experimental research and theoretical analysis, this thesis draws the following conclusions:

1. The typical inorganic metal cation in the pore solution affects the photocatalytic degradation performance of organic dyes by affecting the dispersion stability of nano TiO_2 hydrosols and the concentration of hydrogen ions in a water environment.

The existence of Na^+, K^+, Ca^{2+} and Mg^{2+} ions inhibit the degradation of Rhodamine B by nano TiO_2 hydrosols, and the inhibition effect of bivalent cations is greater than that of univalent cations. The competitive adsorption between Rhodamine B molecules and anions on the surface of nano TiO_2 is intensified with the increase of cation concentration, which further inhibited the photocatalytic performance more obviously. Due to the hydrolysis of Al^{3+} in electrolytes, the photochemical reaction activity and photocatalytic reaction rate of TiO_2 hydrosols are increased. The different dispersion-agglomeration mechanisms of TiO_2 hydrosols in hydrolysable metal ion electrolytes are revealed. The isopotential point transfer to low pH caused by electrolyte can be partially offset by the hydrolysis of Al^{3+} in the measured system, thus inhibiting the aggregation of TiO_2 nanoparticles thereby improving the dispersion stability of nano TiO_2 hydrosols. Nano-dispersed TiO_2 hydrosols are suitable as

a photocatalyst containing Al^{3+} in strong ion environments such as municipal sewage and Portland cement.

2. The low dosages of nano-dispersed TiO_2 hydrosols can be used to improve the photocatalytic self-cleaning performance of cementitious materials.

Because nano TiO_2 particles in positively charged hydrosols carry functional group -COOH, by mixing water into the cement paste, the appearance of heat release peak in the early hydration stage of ordinary Portland cement is delayed, and the inhibition effect on cement hydration heat release is increased with the increase of mixing amount. Although nano TiO_2 hydrosols do not affect the types of cement hydration products, they have a great influence on the crystal shape of hydration products and the microstructure of cementitious materials at different ages. The surface defects of nano TiO_2 particles and the surface electron trapping effect caused by the special cluster structure of TiO_2 and main hydration products are observed. With the increase of TiO_2 aqueous sol content, the cement hydration products with greater influence become the binding agent of photoinduced electrons, which also improves the self-cleaning performance of modified cementitious materials. A new mechanism is proposed to improve the self-purification performance of the modified cement slurry by nano TiO_2 hydrosols, and the experimental phenomenon that the photocatalytic self-purification performance of the modified cement-based material increased with the increase of the concentration of TiO_2 hydrosols, but is not proportional to the amount of nano TiO_2 hydrosols in each test hydration age is reasonably explained.

3. The surface defect states change of nano TiO_2 caused by the evolution of the polycrystalline form of hydration products in the process of carbonization is the main reason for the attenuation of photocatalytic self-cleaning performance of modified cement mortar.

Carbonation reduces the self-cleaning performance of the photocatalytic mortar. During carbonation, the self-cleaning ability is closely related to the anatase exposure area ratio and the area ratio of $CaCO_3$ in the mortar surface. Nano TiO_2 hydrosols with different dosages affect the carbonation rate of cement hydrates and their carbonates' crystal patterns and volumes. When the nano TiO_2 dosage is greater than 0.05 w/w % of cement, the surface defects of nano TiO_2 decrease and the carbonation rate of CH dominates the carbonation process of mortar. After complete carbonation, aragonite and unstable calcium carbonate transforms into calcite phase with a smaller volume. The re-exposure of photocatalytic active sites leads to recovery of the self-cleaning performance of the carbonated mortar. The anatase content and the carbonation degree are the characteristic variables of the photocatalytic self-cleaning performance of nano TiO_2-modified mortar during carbonation. A new model is proposed to describe the performance evolution of the photocatalytic self-cleaning property of mortar by TiO_2 content and the carbonation degree.

4. The change of nano TiO_2 surface defect state caused by the periodic dissolution and migration of hydration products caused by the alternating circulation of pure water is the main reason for the sinusoidal change of photocatalytic self-cleaning performance of modified cement mortar.

The self-cleaning performance of TiO_2-mortar showed a trend of sinusoidal function with the increase of the number of wetting and drying alternating cycles, and the period is 20 wetting and drying cycles. The photocatalytic self-cleaning kinetic process of TiO_2-mortar follows the pseudo-second-order reaction kinetic model and is not affected by the number of wetting and drying cycles. Under the action of alternating wetting and drying cycles, the band gap energy, Urbach energy, and reaction kinetic parameters C_e of TiO_2-mortar show corresponding periodic changes, and the change period is about 20 wetting and drying cycles. Nano TiO_2 hydrosols can inhibit the dissolution and diffusion of the hydration products caused by the resistance of TiO_2-mortar to the wetting and drying cycling of pure water. By delaying the early hydration of cement, nano TiO_2 hydrosols affect the morphology of CH and C-S-H, and refine the pore structure of mortar, thus affecting the dissolution rate and diffusion rate of CH and C-S-H under the alternating action of wetting and drying pure water. Since the shape of CH crystals tends to be stable when the mass ratio of nano TiO_2 to cement exceeds 0.5 %, the inhibition of CH dissolution is exponentially related to the water-sol content of nano TiO_2. When nano TiO_2 exceeds 0.5 % of cement mass, the inhibition effect tends to be stable.

5. The influences of synthetic CNF-modified nano TiO_2 hydrosols on the early-age and hardened properties of cement paste are studied. The dynamic shear rheology performance and the compressive property are chosen to represent the properties of cement paste samples at an early age and 28-day-age.

The synthesis temperature of TiO_2 nanoparticles prepared by the sol-gel method had a great influence on the initial grain size and hydrodynamic particle size of TiO_2 nanoparticles in hydrosols. The pure anatase type TiO_2 hydrosols with good dispersion, low agglomeration and large specific surface area are prepared by sol-gel method at 40 ℃. CNF can effectively improve the visible light photocatalytic activity of nano TiO_2 hydrosols. The hydrodynamic sizes increase with the increase of these mass ratios, and the surface zeta potential values first increase and then sharply decrease with the increase of these mass ratios. Adding 0.10 w/w % of well-designed CNF-TiO_2 hydrosols to cement paste strengthens the hardened cement paste both at an early age and at 28-day-age but does not change the hydrate patterns. Mixing pure nano TiO_2 hydrosols of the same dosage in cement paste has a negative effect of cement paste on mechanical properties. When the mass ratio of CNF to TiO_2 is 1.5: 1 in the modified hydrosols, adding it to the cement paste leads to the highest compressive strength increase rate of about 25 % at 28-day-age. The significant reduction of megapores' porosity and increase of macropores' porosity in the CNF-TiO_2 modified hardened paste

sample are the reasons for the improvement of compressive strength values. The addition of both pure TiO_2 and CNF-TiO_2 hydrosols does not influence the fluid type of cement paste slurry, which belongs to yield pseudoplastic fluids. The rheology index and shear stress values of paste slurry containing CNF-TiO_2 hydrosols first increase and then decrease with the increase of CNF to TiO_2 mass ratios in hydrosols. While, the thixotropic performances of these paste slurries show the opposite changing rule, the alleviation effects of CNF on the retardation of cement hydration caused by acidic nano TiO_2 hydrosols.

6. The enhancement effects of the directional freeze-casting method on the photocatalytic air purification performance under simulated sunlight irradiation for photocatalytic concrete modified with visible light active bio-based modified nano TiO_2 hydrosols are studied. It also studies the influences of the directional micro-channels on the compressive properties of hardened paste samples at different ages.

Freeze-casting processes significantly improve the air purification performances of ultra-low dosage of CNF-TiO_2 hydrosols-modified visible light photocatalytic concrete. The porosity, in the pore size range of 10 to 50 nm, increases resulting from the pore structure rearrangement of water icing, which can explain the better NO_x degradation behaviours of hardened paste samples containing 0.10 w/w % of CNF-TiO_2 hydrosols. The directional arrangement of microchannels of the widths between 0.38 to 2.5 μm caused by the freeze-casting processes in the cement paste dominates the radiative cooling performance of the plate samples. The presence of CNF-TiO_2 hydrosols in paste slurries in such a small dosage affects the freezing rate of free water during casting, resulting in the difference in pore structure distribution and microchannel widths. In the processes of freeze-casting, the cement hydration retardation caused by water freezing is much worse than that by acidic nano-dispersed TiO_2 hydrosols. The CNF-TiO_2 hydrosols with high dispersion can be used as the nano-visible light catalytic refrigerant, which improves the thermal conductivity of the liquid phase in the fresh slurries, increases the average cooling rate, and influences the pore structure of the hardened paste. Therefore, the hardened paste containing pure nano TiO_2 hydrosols and CNF-modified TiO_2 hydrosols show much larger compressive strength values than that of the blank samples.

8.2   Main innovations

The main innovations of this thesis include the following aspects:

(1) Pure anatase-type TiO_2 hydrosols with good dispersion, low agglomeration and large specific surface area are prepared, and the self-cleaning performance of cementitious materials is realized under the condition of low dosage.

(2) The mechanism by which the hydrolysis of inorganic cations improved the dispersion

stability and photocatalytic performance of nano TiO$_2$ hydrosols is revealed. Cement hydration affects the surface defects, band electronic structure and surface stability of TiO$_2$, which is conducive to the improvement of self-cleaning performance.

(3) The evolution law of photocatalytic self-cleaning performance of nano TiO$_2$ hydrosols-modified cementitious materials under carbonization and alternating wetting and drying environments is investigated, which provided theoretical support for the long-term effective application of TiO$_2$-modified cementitious materials.

(4) The enhancements of CNF-TiO$_2$ visible-light photocatalysts on the physical and functional properties of cement paste via regular casting and freeze-casting methods, which proposed a possible strategy for cheap and high-efficiency photocatalyst concrete.

8.3   Recommendations

This thesis addresses the questions raised in the introduction through experimental research and theoretical analysis. Nano-dispersed TiO$_2$ hydrosols are obtained using the sol-gel method and the organic acid-assisted approach, achieving uniform dispersion of nano-TiO$_2$ in cementitious materials and excellent photocatalytic self-cleaning performance. The effects of the formation, phase transition, and deterioration of cement hydrates on the photocatalytic self-cleaning performance of nano-TiO$_2$ hydrosols-modified cement paste and mortar are identified, and the correlation between the photocatalytic reaction processes and the deterioration of hydrates are investigated. The possible methods for sharply improving the photocatalytic air purification properties of CNF-TiO$_2$ hydrosols-modified paste are studied under the irradiation of simulated solar light resource. During the completion of the research content of this thesis, new issues worthy of in-depth exploration are discovered. In future work, further investigations are planned to be conducted in the following aspects:

(1) Combining nano-TiO$_2$ hydrosol with admixtures that regulate the heat release processes of cement hydration, such as heat-regulating agents, to conduct in-depth research on their regulation of the nucleation and growth processes of hydrates.

(2) Exploring the application of nano TiO$_2$-based hydrosols in decorative concrete for achieving self-cleaning and air purification functions.

(3) The influences of nano TiO$_2$-based hydrosols on the regulation of water icing need to be studied thoroughly. More functions of the freezing-casted cementitious composites should be discovered and investigated, such as the electromagnetic wave absorption with different wavelength ranges.

Bibliography

[1] P. Berdahl, H. Akbari, L.S. Rose, Aging of reflective roofs: soot deposition, Appl. Opt. 41 (2002) 2355. https://doi.org/10.1364/AO.41.002355.

[2] M. Sleiman, T.W. Kirchstetter, P. Berdahl, H.E. Gilbert, S. Quelen, L. Marlot, C. V. Preble, S. Chen, A. Montalbano, O. Rosseler, H. Akbari, R. Levinson, H. Destaillats, Soiling of building envelope surfaces and its effect on solar reflectance - Part II: Development of an accelerated aging method for roofing materials, Sol. Energy Mater. Sol. Cells. 122 (2014) 271–281. https://doi.org/10.1016/j.solmat.2013.11.028.

[3] M.V. Diamanti, R. Paolini, M. Rossini, A.B. Aslan, M. Zinzi, T. Poli, M.P. Pedeferri, Long term self-cleaning and photocatalytic performance of anatase added mortars exposed to the urban environment, Constr. Build. Mater. 96 (2015) 270–278. https://doi.org/10.1016/j.conbuildmat.2015.08.028.

[4] L. Graziani, E. Quagliarini, F. Bondioli, M. D'Orazio, Durability of self-cleaning TiO_2 coatings on fired clay brick façades: Effects of UV exposure and wet & dry cycles, Build. Environ. 71 (2014) 193–203. https://doi.org/10.1016/j.buildenv.2013.10.005.

[5] R. Pires, J. de Brito, B. Amaro, Statistical survey of the inspection, diagnosis and repair of painted rendered façades, Struct. Infrastruct. Eng. 11 (2015) 605–618. https://doi.org/10.1080/15732479.2014.890233.

[6] C.C. Gaylarde, P.M. Gaylarde, A comparative study of the major microbial biomass of biofilms on exteriors of buildings in Europe and Latin America, Int. Biodeterior. Biodegrad. 55 (2005) 131–139. https://doi.org/10.1016/j.ibiod.2004.10.001.

[7] N. Marinoni, M.P. Birelli, C. Rostagno, A. Pavese, The effects of atmospheric multipollutants on modern concrete, Atmos. Environ. 37 (2003) 4701–4712. https://doi.org/10.1016/j.atmosenv.2003.06.001.

[8] J. Chen, C. Poon, Photocatalytic construction and building materials: From fundamentals to applications, Build. Environ. 44 (2009) 1899–1906. https://doi.org/10.1016/j.buildenv.2009.01.002.

[9] E. Boonen, A. Beeldens, Photocatalytic roads: From lab tests to real scale applications, Eur. Transp. Res. Rev. 5 (2013) 79–89. https://doi.org/10.1007/s12544-012-0085-6.

[10] A. Fujishima, X. Zhang, D.A. Tryk, TiO_2 photocatalysis and related surface phenomena, Surf. Sci. Rep. 63 (2008) 515–582. https://doi.org/10.1016/j.surfrep.2008.10.001.

[11] S. Guo, Z. Wu, W. Zhao, TiO_2-based building materials: Above and beyond traditional applications, Chinese Sci. Bull. 54 (2009) 1137–1142. https://doi.org/10.1007/s11434-009-0063-0.

[12] Z. Shayegan, C.S. Lee, F. Haghighat, TiO_2 photocatalyst for removal of volatile organic compounds in gas phase – A review, Chem. Eng. J. 334 (2018) 2408–2439. https://doi.org/10.1016/j.cej.2017.09.153.

[13] V. Etacheri, C. Di Valentin, J. Schneider, D. Bahnemann, S.C. Pillai, Visible-light activation of TiO_2 photocatalysts: Advances in theory and experiments, J. Photochem. Photobiol. C Photochem. Rev. 25 (2015) 1–29. https://doi.org/10.1016/j.jphotochemrev.2015.08.003.

[14] H. Ren, P. Koshy, W.F. Chen, S. Qi, C.C. Sorrell, Photocatalytic materials and technologies for air purification, J. Hazard. Mater. 325 (2017) 340–366. https://doi.org/10.1016/j.jhazmat.2016.08.072.

[15] A. Fujishima, T.N. Rao, D.A. Tryk, Titanium dioxide photocatalysis, J. Photochem. Photobiol. C Photochem. Rev. 1 (2000) 1–21. https://doi.org/10.1016/S1389-5567(00)00002-2.

[16] Y. Wang, Y. He, Q. Lai, M. Fan, Review of the progress in preparing nano TiO_2: An important environmental engineering material, J. Environ. Sci. 26 (2014) 2139–2177. https://doi.org/10.1016/j.jes.2014.09.023.

[17] D.P. MacWan, P.N. Dave, S. Chaturvedi, A review on nano-TiO_2 sol-gel type syntheses and its applications, J. Mater. Sci. 46 (2011) 3669–3686. https://doi.org/10.1007/s10853-011-5378-y.

[18] A. Yousefi, A. Allahverdi, P. Hejazi, Effective dispersion of nano-TiO_2 powder for enhancement of photocatalytic properties in cement mixes, Constr. Build. Mater. 41 (2013) 224–230. https://doi.org/10.1016/j.conbuildmat.2012.11.057.

[19] A. Folli, I. Pochard, A. Nonat, U.H. Jakobsen, A.M. Shepherd, D.E. Macphee, Engineering photocatalytic Cements: Understanding TiO_2 surface chemistry to control and modulate photocatalytic performances, J. Am. Ceram. Soc. 93 (2010) 3360–3369. https://doi.org/10.1111/j.1551-2916.2010.03838.x.

[20] A. Zhao, J. Yang, E.H. Yang, Self-cleaning engineered cementitious composites, Cem. Concr. Compos. 64 (2015) 74–83. https://doi.org/10.1016/j.cemconcomp.2015.09.007.

[21] C. Giosuè, Q.L. Yu, M.L. Ruello, F. Tittarelli, H.J.H. Brouwers, Effect of pore structure on the performance of photocatalytic lightweight lime-based finishing mortar, Constr. Build. Mater. 171 (2018) 232–242. https://doi.org/10.1016/j.conbuildmat.2018.03.106.

[22] S. Lorencik, Q.L. Yu, H.J.H. Brouwers, Design and performance evaluation of the functional coating for air purification under indoor conditions, Appl. Catal. B Environ. 168–169 (2015) 77–86. https://doi.org/10.1016/j.apcatb.2014.12.012.

[23] J. Chen, C. Poon, Photocatalytic construction and building materials: From fundamentals to applications, Build. Environ. 44 (2009) 1899–1906. https://doi.org/10.1016/j.buildenv.2009.01.002.

[24] A. Mills, S.K. Lee, A web-based overview of semiconductor photochemistry-based current commercial applications, J. Photochem. Photobiol. A Chem. 152 (2002) 233–247. https://doi.org/10.1016/S1010-6030(02)00243-5.

[25] D. Spasiano, L. Rodriguez, J. Olleros, TiO$_2$/Cu(II) photocatalytic production of benzaldehyde from benzyl alcohol in solar pilot plant reactor, Appl. Catal. B Environ. 136–137 (2013) 56–63. https://doi.org/10.1016/j.apcatb.2013.01.055.

[26] S. Malato, P. Fernández-Ibáñez, M.I. Maldonado, Decontamination and disinfection of water by solar photocatalysis: Recent overview and trends, Catal. Today. 147 (2009) 1–59. https://doi.org/10.1016/j.cattod.2009.06.018.

[27] D. Bahnemann, Photocatalytic water treatment: Solar energy applications, Sol. Energy. 77 (2004) 445–459. https://doi.org/10.1016/j.solener.2004.03.031.

[28] I. Dincer, Renewable energy and sustainable development: a crucial review, Renew. Sustain. Energy Rev. 4 (2000) 157–175. https://doi.org/10.1016/S1364-0321(99)00011-8.

[29] K. Hashimoto, H. Irie, A. Fujishima, TiO$_2$ photocatalysis: A historical overview and future prospects, Jpn. J. Appl. Phys. 44 (2005) 8269–8285. https://doi.org/10.1143/JJAP.44.8269.

[30] D. Jing, L. Guo, L. Zhao, Efficient solar hydrogen production by photocatalytic water splitting: From fundamental study to pilot demonstration, Int. J. Hydrogen Energy. 35 (2010) 7087–7097. https://doi.org/10.1016/j.ijhydene.2010.01.030.

[31] M.N. Chong, B. Jin, C.W.K. Chow, C. Saint, Recent developments in photocatalytic water treatment technology: A review, Water Res. 44 (2010) 2997–3027. https://doi.org/10.1016/j.watres.2010.02.039.

[32] E. Ghenne, F. Dumont, C. Buess-Herman, Stability of TiO$_2$ hydrosols synthesized by hydrolysis of titanium tetraethoxide, Colloids Surfaces A Physicochem. Eng. Asp. 131 (1998) 63–67.

[33] O.B. Pavlova-Verevkina, Y.A. Shevchuk, V. V. Nazarov, Coagulation peculiarities and fractionation of nanodispersed titanium dioxide hydrosol, Colloid J. Russ. Acad. Sci. Kolloidn. Zhurnal. 65 (2003) 474–477. https://doi.org/10.1023/A:1025125019994.

[34] O.B. Pavlova-Verevkina, S.N. Chvalun, E.D. Politova, V. V. Nazarov, L.A. Ozerina, A.N. Ozerin, Study of the stable nanocrystalline TiO$_2$ hydrosol and its fractions, J. Sol-Gel Sci. Technol. 35 (2005) 91–97. https://doi.org/10.1007/s10971-005-1311-7.

[35] E. Santacesaria, M. Tonello, G. Storti, R.C. Pace, S. Carrà, Kinetics of titanium dioxide precipitation by thermal hydrolysis, J. Colloid Interface Sci. 111 (1986) 44–53. https://doi.org/10.1016/0021-9797(86)90005-6.

[36] P. Alphonse, A. Varghese, C. Tendero, Stable hydrosols for TiO$_2$ coatings, J. Sol-Gel Sci. Technol. 56 (2010) 250–263. https://doi.org/10.1007/s10971-010-2301-y.

[37] Z. Abbas, J.P. Holmberg, A.K. Hellström, M. Hagström, J. Bergenholtz, M. Hassellöv, E. Ahlberg, Synthesis, characterization and particle size distribution of TiO$_2$ colloidal nanoparticles, Colloids Surfaces A Physicochem. Eng. Asp. 384 (2011) 254–261. https://doi.org/10.1016/j.colsurfa.2011.03.064.

[38] O.B. Pavlova-Verevkina, L.A. Ozerina, V. V. Nazarov, N.M. Surin, Electrolyte-induced destabilization of hydrosols containing uniform TiO$_2$ nanoparticles, Colloid J. 69 (2007) 492–497. https://doi.org/10.1134/S1061933X07040114.

[39] P. Leroy, C. Tournassat, M. Bizi, Influence of surface conductivity on the apparent zeta potential of TiO_2 nanoparticles, J. Colloid Interface Sci. 356 (2011) 442–453. https://doi.org/10.1016/j.jcis.2016.01.075.

[40] T. Liu, F. Li, X. Li, TiO_2 hydrosols with high activity for photocatalytic degradation of formaldehyde in a gaseous phase, J. Hazard. Mater. 152 (2008) 347–355. https://doi.org/10.1016/j.jhazmat.2007.07.003.

[41] J.X. Yu, R.A. Chi, X.Z. Su, Z.Y. He, Y.F. Qi, Y.F. Zhang, Desorption behavior of methylene blue on pyromellitic dianhydride modified biosorbent by a novel eluent: Acid TiO_2 hydrosol, J. Hazard. Mater. 177 (2010) 222–227. https://doi.org/10.1016/j.jhazmat.2009.12.021.

[42] A. Brunelli, G. Pojana, S. Callegaro, A. Marcomini, Agglomeration and sedimentation of titanium dioxide nanoparticles (n-TiO_2) in synthetic and real waters, J. Nanoparticle Res. 15 (2013). https://doi.org/10.1007/s11051-013-1684-4.

[43] J. Wang, Z. Liu, R. Cai, A New Role for Fe3+ in TiO_2 Hydrosol: Accelerated Photodegradation of Dyes under Visible Light, Environ. Sci. Technol. 42 (2008) 5759–5764. https://doi.org/10.1021/es800616b.

[44] A. V. Volkova, L.E. Ermakova, N.F. Bogdanova, E.A. Tarabukina, M.P. Sidorova, Electrosurface characteristics of titanium dioxide in solutions of simple electrolytes: I. Effect of nature of counterions on adsorption and electrokinetic parameters of TiO_2, Colloid J. 72 (2010) 743–748. https://doi.org/10.1134/s1061933x10060037.

[45] A. V. Volkova, E. V. Golikova, L.E. Ermakova, Photometric study of the kinetics of TiO_2 hydrosol coagulation in electrolyte solutions, Colloid J. 74 (2012) 32–37. https://doi.org/10.1134/S1061933X11060184.

[46] H. Yang, G. Li, T. An, Photocatalytic degradation kinetics and mechanism of environmental pharmaceuticals in aqueous suspension of TiO_2: A case of b-blockers, Catal. Today. 153 (2010) 200–207. https://doi.org/10.1016/j.cattod.2010.02.068.

[47] H.Y. Chen, O. Zahraa, M. Bouchy, Inhibition of the adsorption and photocatalytic degradation of an organic contaminant in an aqueous suspension of TiO_2 by inorganic ions, J. Photochem. Photobiol. A Chem. 108 (1997) 37–44. https://doi.org/10.1016/S1010-6030(96)04411-5.

[48] R. Terzian, N. Serpone, C. Minero, E. Pelizzetti, Photocatalyzed mineralization of mresols in aqueous media with irradiated titania, J. Catal. 128 (1991) 352–365. https://doi.org/10.1016/0021-9517(91)90294-E.

[49] H. Chen, C.E. Nanayakkara, V.H. Grassian, Titanium dioxide photocatalysis in atmospheric chemistry, Chem. Rev. 112 (2012) 5919–5948. https://doi.org/10.1021/cr3002092.

[50] H. Fu, C. Pan, W. Yao, Y. Zhu, Visible-light-induced degradation of Rhodamine B by nanosized Bi_2WO_6, J. Phys. Chem. B. 109 (2005) 22432–22439. https://doi.org/10.1055/s-2006-950183.

[51] E.M. Hotze, T. Phenrat, G. V. Lowry, Nanoparticle aggregation: challenges to understanding transport and reactivity in the environment, J. Environ. Qual. 39 (2010) 1909–1924. https://doi.org/10.2134/jeq2009.0462.

[52] R.A. French, A.R. Jacobson, B. Kim, S.L. Isley, R.L. Penn, P.C. Baveye, Influence of ionic strength, pH, and cation valence on aggregation kinetics of titanium dioxide nanoparticles, Environental Sci. Technol. 43 (2009) 1354–1359. https://doi.org/10.1021/es802628n.

[53] Y. Zhang, Y. Chen, P. Westerhoff, J. Crittenden, Impact of natural organic matter and divalent cations on the stability of aqueous nanoparticles, Water Res. 43 (2009) 4249–4257. https://doi.org/10.1016/j.watres.2009.06.005.

[54] F. Loosli, P. Le Coustumer, S. Stoll, Effect of electrolyte valency, alginate concentration and pH on engineered TiO_2 nanoparticle stability in aqueous solution, Sci. Total Environ. 535 (2015) 28–34. https://doi.org/10.1016/j.scitotenv.2015.02.037.

[55] R.J. Honda, V. Keene, L. Daniels, S.L. Walker, Removal of TiO_2 nanoparticles during primary water treatment: Role of coagulant type, dose, and danoparticle concentration, Environ. Eng. Sci. 31 (2014) 127–134. https://doi.org/10.1089/ees.2013.0269.

[56] H. Xu, F. Xiao, D. Wang, Effects of Al_2O_3 and TiO_2 on the coagulation process by $Al_2(SO_4)_3$ (AS) and poly-aluminum chloride (PACl) in kaolin suspension, Sep. Purif. Technol. 124 (2014) 9–17. https://doi.org/10.1016/j.seppur.2014.01.010.

[57] A.B. Đukić, K.R. Kumrić, NikolaS.Vukelić, M.S. Dimitrijević, Z.D. Baščarević, S. V. Kurko, L.L. Matović, Simultaneous removal of Pb^{2+}, Cu^{2+}, Zn^{2+} and Cd^{2+} from highly acidic solutions using mechanochemically synthesized montmorillonite–kaolinite/TiO_2 composite, Appl. Clay Sci. 103 (2015) 20–27. https://doi.org/10.1016/j.clay.2014.10.021.

[58] M. Kanna, S. Wongnawa, P. Sherdshoopongse, P. Boonsin, Adsorption behavior of some metal ions on hydrated amorphous titanium dioxide surface, Songklanakarin J. Sci. Technol. 27 (2005) 1017–1026.

[59] M.S. Islam, M.M. Hossain, T.S. Islam, Effect of pH, Ions and Ionic Strength on TiO_2- mediated photodegradation of Brilliant Orange, Dhaka Univ. J. Sci. 58 (2010) 187–190.

[60] J. Zhang, P. Jiang, P. Sun, Q. Wang, J. Kuang, W. Liu, W.-B. Cao, Role of ammonium ions on the stability of TiO_2 sol, J. Dispers. Sci. Technol. 2691 (2018) 1–6. https://doi.org/10.1080/01932691.2018.1472002.

[61] J. Farner Budarz, A. Turolla, A.F. Piasecki, J.Y. Bottero, M. Antonelli, M.R. Wiesner, Influence of aqueous inorganic anions on the reactivity of nanoparticles in TiO_2 photocatalysis, Langmuir. 33 (2017) 2770–2779. https://doi.org/10.1021/acs.langmuir.6b04116.

[62] T. Wu, G. Liu, J. Zhao, H. Hidaka, N. Serpone, Photoassisted degradation of dye pollutants. V. Self-photosensitized oxidative transformation of Rhodamine B under

visible light irradiation in aqueous TiO_2 dispersions, J. Phys. Chem. B. 102 (1998) 5845–5851. https://doi.org/10.1021/jp980922c.

[63] S.K. Kansal, M. Singh, D. Sud, Studies on photodegradation of two commercial dyes in aqueous phase using different photocatalysts, J. Hazard. Mater. 141 (2007) 581–590. https://doi.org/10.1016/j.jhazmat.2006.07.035.

[64] C. Galindo, P. Jacques, A. Kalt, Photooxidation of the phenylazonaphthol AO20 on TiO_2: Kinetic and mechanistic investigations, Chemosphere. 45 (2001) 997–1005. https://doi.org/10.1016/S0045-6535(01)00118-7.

[65] B. Lee, W. Liaw, J. Lou, Photocatalytic decolorization of Methylene Blue in aqueous TiO_2 suspension, Environ. Eng. Sci. 16 (1999) 165–175. https://doi.org/10.1089/ees.1999.16.165.

[66] I. Poulios, I. Aetopoulou, Photocatalytic degradation of the textile dye reactive orange 16 in the presence of TiO_2 suspensions, Environ. Technol. 20 (1999) 479–487. https://doi.org/10.1080/09593332008616843.

[67] I. Poulios, I. Tsachpinis, Photodegradation of the textile dye Reactive Black 5 in the presence of semiconducting oxides, J. Chem. Technol. Biotechnol. 74 (1999) 349–357. https://doi.org/10.1002/(SICI)1097-4660(199904)74:4<349::AID-JCTB5>3.0.CO;2-7.

[68] D. Chen, A.K. Ray, Photodegradation kinetics of 4-nitrophenol in TiO_2 suspension, Water Res. 32 (1998) 3223–3234. https://doi.org/10.1016/S0043-1354(98)00118-3.

[69] T. Sauer, G.C. Neto, H.J. José, E. Al., Kinetics of photocatalytic degradation of reactive dyes in a TiO_2 slurry reactor, J. Photochem. Photobiol. A Chem. 149 (2002) 147–154. https://doi.org/10.1016/S1010-6030(02)00015-1.

[70] M. Asilturk, F. Sayılkan, S. Erdemoglu, M. Akarsu, H. Sayılkan, M. Erdemoglu, E. Arpac, Characterization of the hydrothermally synthesized nano-TiO_2 crystallite and the photocatalytic degradation of Rhodamine B, J. Hazard. Mater. B129 (2006) 164–170. https://doi.org/10.1016/j.jhazmat.2005.08.027.

[71] Y.L. Pang, A.Z. Abdullah, Comparative study on the process behavior and reaction kinetics in sonocatalytic degradation of organic dyes by powder and nanotubes TiO_2, Ultrason. Sonochem. 19 (2012) 642–651. https://doi.org/10.1016/j.ultsonch.2011.09.007.

[72] Y.L. Pang, S. Bhatia, A.Z. Abdullah, Process behavior of TiO_2 nanotube-enhanced sonocatalytic degradation of Rhodamine B in aqueous solution, Sep. Purif. Technol. 77 (2011) 331–338. https://doi.org/10.1016/j.seppur.2010.12.023.

[73] L. Song, S. Zhang, X. Wu, Q. Wei, Synthesis of porous and trigonal TiO_2 nanoflake, its high activity for sonocatalytic degradation of rhodamine B and kinetic analysis, Ultrason. Sonochem. 19 (2012) 1169–1173. https://doi.org/10.1016/j.ultsonch.2012.03.011.

[74] M.H. Priya, G. Madras, Kinetics of TiO_2-catalyzed ultrasonic degradation of Rhodamine dyes, Ind. Eng. Chem. Res. 45 (2006) 913–921. https://doi.org/10.1021/ie050966p.

[75] W. Zhang, Y. Li, C. Wang, P. Wang, Kinetics of heterogeneous photocatalytic degradation of rhodamine B by TiO_2-coated activated carbon: Roles of TiO_2 content and light intensity, Desalination. 266 (2011) 40–45. https://doi.org/10.1016/j.desal.2010.07.066.

[76] S. Ortelli, M. Blosi, S. Albonetti, A. Vaccari, M. Dondi, A.L. Costa, TiO_2 based nano-photocatalysis immobilized on cellulose substrates, J. Photochem. Photobiol. A Chem. 276 (2014) 58–64. https://doi.org/10.1016/j.jphotochem.2013.11.013.

[77] P. Qu, J. Zhao, T. Shen, H. Hidaka, TiO_2-assisted photodegradation of dyes: A study of two competitive primary processes in the degradation of RB in an aqueous TiO_2 colloidal solution, J. Mol. Catal. A Chem. 129 (1998) 257–268. https://doi.org/10.1016/S1381-1169(97)00185-4.

[78] J. Zhao, T. Wu, K. Wu, K. Oikawa, H. Hisao, N. Serpone, Photoassisted degradation of dye pollutants. 3 . Degradation of the cationic dye Rhodamine B in aqueous anionic surfactant / TiO_2 dispersions under visible light irradiation: evidence for the need of substrate adsorption on TiO_2 part, Environmental Sci. Technol. 32 (1998) 2394–2400. https://doi.org/10.1021/es9707926.

[79] S. Wahyuningsih, C. Purnawan, P.A. Kartikasari, Visible light photoelectrocatalytic degradation of rhodamine B using a dye-sensitised TiO_2 electrode, Chem. Pap. 68 (2014) 1248–1256. https://doi.org/10.2478/s11696-013-0476-8.

[80] L. Zhu, S.B. Jo, S. Ye, K. Ullah, W.C. Oh, Rhodamine B degradation and reactive oxygen species generation by a ZnSe- graphene/ TiO_2 sonocatalyst, Chinese J. Catal. 35 (2014) 1825–1832. https://doi.org/10.1016/S1872-2067(14)60158-3.

[81] Z. Lei, T. Ghosh, C. Park, M. Zeda, O. Wonchun, Enhanced Sonocatalytic Degradation of Rhodamine B by Graphene-TiO_2 Composites Synthesized by an Ultrasonic-Assisted Method, Chinese J. Catal. 33 (2012) 1276–1283. https://doi.org/10.1016/S1872-2067(11)60430-0.

[82] F. Wang, K. Zhang, Reduced graphene oxide–TiO_2 nanocomposite with high photocatalystic activity for the degradation of rhodamine B, J. Mol. Catal. A Chem. 345 (2011) 101–107. https://doi.org/10.1016/j.molcata.2011.05.026.

[83] J. Wang, Z. Jiang, L. Zhang, P. Kang, Y. Xie, Y. Lv, R. Xu, X. Zhang, Ultrasonics Sonochemistry Sonocatalytic degradation of some dyestuffs and comparison of catalytic activities of nano-sized TiO_2, nano-sized ZnO and composite TiO_2/ ZnO powders under ultrasonic irradiation, Ultrason. - Sonochemistry. 16 (2009) 225–231. https://doi.org/10.1016/j.ultsonch.2008.08.005.

[84] C.A. Tyson, A.E. Martell, Equilibria of Metal Ions with Pyrocatechol and 3,5-Di-t-Butylpyrocatechol, J. Am. Chem. Soc. 90 (1968) 3379–3386. https://doi.org/10.1021/ja01015a015.

[85] M. Das, K.G. Bhattacharyya, Oxidation of Rhodamine B in aqueous medium in ambient conditions with raw and acid-activated MnO_2, NiO, ZnO as catalysts, J. Mol. Catal. A Chem. 391 (2014) 121–129. https://doi.org/10.1016/j.molcata.2014.04.019.

[86] Y. Mao, C. Schoeneich, K.D. Asmus, Identification of organic acids and other intermediates in oxidative degradation of chlorinated ethanes on titania surfaces en

route to mineralization: a combined photocatalytic and radiation chemical study, J. Phys. Chem. 95 (1991) 10080–10089. https://doi.org/10.1021/j100177a085.

[87] J.X. Yu, R.A. Chi, J. Guo, Desorption and photodegradation of methylene blue from modified sugarcane bagasse surface by acid TiO_2 hydrosol, Appl. Surf. Sci. 258 (2012) 4085–4090. https://doi.org/10.1016/j.apsusc.2011.12.106.

[88] J.P. Holmberg, E. Ahlberg, J. Bergenholtz, M. Hassellöv, Z. Abbas, Surface charge and interfacial potential of titanium dioxide nanoparticles: Experimental and theoretical investigations, J. Colloid Interface Sci. 407 (2013) 168–176. https://doi.org/10.1016/j.jcis.2013.06.015.

[89] P. V. Kamat, Photochemistry on nonreactive and reactive (semiconductor) surfaces, Chem. Rev. 93 (1993) 267–300. https://doi.org/10.1021/cr00017a013.

[90] M. Hoffmann, S. Martin, W. Choi, Environmental applications of photocatalysis, Chem. Rev. 95 (1995) 69–96. https://doi.org/10.1007/978-1-4471-5061-9_3.

[91] Y. Wang, A. Liu, D. Ma, S. Li, C. Lu, T. Li, C. Chen, TiO_2 Photocatalyzed C–H Bond Transformation for C–C Coupling Reactions, Catalysts. 8 (2018) 355. https://doi.org/10.3390/catal8090355.

[92] D. Ma, S. Zhai, Y. Wang, A. Liu, C. Chen, TiO_2 photocatalysis for transfer hydrogenation, Molecules. (2019) 330–352. https://doi.org/10.3390/molecules24020330.

[93] D. Ma, A. Liu, S. Li, C. Lu, C. Chen, TiO_2 photocatalysis for C-C bond formation, Catal. Sci. Technol. 8 (2018) 2030–2045. https://doi.org/10.1039/c7cy01458a.

[94] S. Hiradate, S. Taniguchi, K. Sakurai, Aluminum speciation in aluminum-silica solutions and potassium chloride extracts of acidic soils, Soil Sci. Soc. Am. J. 62 (1998) 630–636. https://doi.org/10.2136/sssaj1998.03615995006200030012x.

[95] B.L. Phillips, W.H. Casey, M. Karlsson, Bonding and reactivity at oxide mineral surfaces from model aqueous complexes, Nature. 404 (2000) 379–382. https://doi.org/10.1038/35006036.

[96] J.W. Akitt, J.M. Elders, Multinuclear magnetic resonance studies of the hydrolysis of aluminium(III). Part 8. Base hydrolysis monitored at very high magnetic field, J. Chem. Soc. Dalt. Trans. (1988) 1347–1355. https://doi.org/10.1039/DT9880001347.

[97] H. Tang, F. Xiao, D. Wang, Speciation, stability, and coagulation mechanisms of hydroxyl aluminum clusters formed by PACl and alum: A critical review., Adv. Colloid Interface Sci. 226 (2015) 78–85. https://doi.org/10.1016/j.cis.2015.09.002.

[98] J.E. Van Benschoten, J.K. Edzwald, Chemical Aspects of coagulation using aluminum salts-I. Hydrolytic reactions of alum and polyaluminum chloride, Water Res. 24 (1990) 1519–1526.

[99] B. Cao, W. Zhang, Q. Wang, Y. Huang, C. Meng, D. Wang, Wastewater sludge dewaterability enhancement using hydroxyl aluminum conditioning: Role of aluminum speciation, Water Res. 105 (2016) 615–624. https://doi.org/10.1016/j.watres.2016.09.016.

[100] C. Zhao, J. Zhang, Z. Luan, X. Peng, X. Ren, Preparation of high concentration polyaluminum chloride with high content of Alb or Alc, J. Environ. Sci. 21 (2009) 1342–1346. https://doi.org/10.1016/S1001-0742(08)62424-9.

[101] Q.L. Yu, Y. Hendrix, S. Lorencik, H.J.H. Brouwers, Field study of NO_x degradation by a mineral-based air purifying paint, Build. Environ. 142 (2018) 70–82. https://doi.org/10.1016/j.buildenv.2018.06.014.

[102] M.M. Ballari, M. Hunger, G. Hüsken, H.J.H. Brouwers, NO_x photocatalytic degradation employing concrete pavement containing titanium dioxide, Appl. Catal. B Environ. 95 (2010) 245–254. https://doi.org/10.1016/j.apcatb.2010.01.002.

[103] E. Burunkaya, M. Akarsu, H. Erdem Çamurlu, Ö. Kesmez, Z. Yeşil, M. Asiltürk, E. Arpaç, Production of stable hydrosols of crystalline TiO_2 nanoparticles synthesized at relatively low temperatures in diverse media, Appl. Surf. Sci. 265 (2013) 317–323. https://doi.org/10.1016/j.apsusc.2012.11.003.

[104] A. Molea, V. Popescu, N.A. Rowson, A.M. Dinescu, Influence of pH on the formulation of TiO_2 nano-crystalline powders with high photocatalytic activity, Powder Technol. 253 (2014) 22–28. https://doi.org/10.1016/j.powtec.2013.10.040.

[105] B.P. Singh, S. Nayak, S. Samal, S. Bhattacharjee, L. Besra, The role of poly(methacrylic acid) conformation on dispersion behavior of nano TiO_2 powder, Appl. Surf. Sci. 258 (2012) 3524–3531. https://doi.org/10.1016/j.apsusc.2011.11.107.

[106] H.S. Bae, M.K. Lee, W.W. Kim, C.K. Rhee, Dispersion properties of TiO_2 nano-powder synthesized by homogeneous precipitation process at low temperatures, Colloids Surfaces A Physicochem. Eng. Asp. 220 (2003) 169–177. https://doi.org/10.1016/S0927-7757(03)00077-3.

[107] K. Bourikas, M. Stylidi, D.I. Kondarides, X.E. Verykios, Adsorption of Acid Orange 7 on the surface of titanium dioxide, Langmuir. 21 (2005) 9222–9230. https://doi.org/10.1021/la051434g.

[108] Z. Wang, P. Feng, H. Chen, Q. Yu, Photocatalytic performance and dispersion stability of nanodispersed TiO_2 hydrosol in electrolyte solutions with different cations, J. Environ. Sci. 88 (2020) 59–71. https://doi.org/10.1016/j.jes.2019.07.013.

[109] S. Fazio, J. Guzm, M.T. Colomer, A. Salomoni, R. Moreno, Colloidal stability of nanosized titania aqueous suspensions, J. Eur. Ceram. Soc. 28 (2008) 2171–2176. https://doi.org/10.1016/j.jeurceramsoc.2008.02.017.

[110] M.K. Ridley, V.A. Hackley, M.L. Machesky, I. State, W. Sur, G.D. V, Characterization and surface-Reactivity of nanocrystalline anatase in aqueous solutions, Langmuir 2006,. 22 (2006) 10972–10982. https://doi.org/10.1021/la061774h.

[111] D. Marchon, R.J. Flatt, Mechanisms of cement hydration, Sci. Technol. Concr. Admixtures. 41 (2015) 129–145. https://doi.org/10.1016/B978-0-08-100693-1.00008-4.

[112] A.R. Jayapalan, B.Y. Lee, S.M. Fredrich, K.E. Kurtis, Influence of Additions of Anatase TiO_2 Nanoparticles on Early-Age Properties of Cement-Based Materials,

Transp. Res. Rec. J. Transp. Res. Board. 2141 (2010) 41–46.
https://doi.org/10.3141/2141-08.

[113] B.Y. Lee, K.E. Kurtis, Influence of TiO_2 nanoparticles on early C_3S hydration, J. Am. Ceram. Soc. 93 (2010) 3399–3405. https://doi.org/10.1111/j.1551-2916.2010.03868.x.

[114] J. Chen, S.C. Kou, C.S. Poon, Hydration and properties of nano-TiO_2 blended cement composites, Cem. Concr. Compos. 34 (2012) 642–649. https://doi.org/10.1016/j.cemconcomp.2012.02.009.

[115] A.R. Jayapalan, M.L. Jue, K.E. Kurtis, Nanoparticles and apparent activation energy of Portland cement, J. Am. Ceram. Soc. 97 (2014) 1534–1542. https://doi.org/10.1111/jace.12878.

[116] R. Zhang, X. Cheng, P. Hou, Z. Ye, Influences of nano-TiO_2 on the properties of cement-based materials: Hydration and drying shrinkage, Constr. Build. Mater. 81 (2015) 35–41. https://doi.org/10.1016/j.conbuildmat.2015.02.003.

[117] A.P. Werle, M.L. De Souza, K. Loh, R. Ando, V.M. John, The performance of a self-cleaning cool cementitious surface, Energy Build. 114 (2016) 200–205. https://doi.org/10.1016/j.enbuild.2015.06.025.

[118] M. Janus, J. Zatorska, A. Czyzewski, K. Bubacz, E. Kusiak-Nejman, A.W. Morawski, Self-cleaning properties of cement plates loaded with N,C-modified TiO_2 photocatalysts, Appl. Surf. Sci. 330 (2015) 200–206. https://doi.org/10.1016/j.apsusc.2014.12.113.

[119] A. Zhao, J. Yang, E.H. Yang, Self-cleaning engineered cementitious composites, Cem. Concr. Compos. 64 (2015) 74–83. https://doi.org/10.1016/j.cemconcomp.2015.09.007.

[120] M. V. Diamanti, B. Del Curto, M. Ormellese, M.P. Pedeferri, Photocatalytic and self-cleaning activity of colored mortars containing TiO_2, Constr. Build. Mater. 46 (2013) 167–174. https://doi.org/10.1016/j.conbuildmat.2013.04.038.

[121] M.V. Diamanti, R. Paolini, M. Rossini, A.B. Aslan, M. Zinzi, T. Poli, M.P. Pedeferri, Long term self-cleaning and photocatalytic performance of anatase added mortars exposed to the urban environment, Constr. Build. Mater. 96 (2015) 270–278. https://doi.org/10.1016/j.conbuildmat.2015.08.028.

[122] R. Khataee, V. Heydari, L. Moradkhannejhad, M. Safarpour, S.W. Joo, Self-cleaning and mechanical properties of modified white cement with nanostructured TiO_2, J. Nanosci. Nanotechnol. 13 (2013) 5109–5114. https://doi.org/10.1166/jnn.2013.7586.

[123] A. Folli, C. Pade, T.B. Hansen, T. De Marco, D.E. MacPhee, TiO_2 photocatalysis in cementitious systems: Insights into self-cleaning and depollution chemistry, Cem. Concr. Res. 42 (2012) 539–548. https://doi.org/10.1016/j.cemconres.2011.12.001.

[124] X. Ding, S. Pan, C. Lu, H. Guan, X. Yu, Y. Tong, Hydrophobic photocatalytic composite coatings based on nano-TiO_2 hydrosol and aminopropyl terminated

polydimethylsiloxane prepared by a facile approach, Mater. Lett. 228 (2018) 5–8. https://doi.org/10.1016/j.matlet.2018.05.103.

[125] E. Jimenez-Relinque, I. Llorente, M. Castellote, TiO_2 cement-based materials: Understanding optical properties and electronic band structure of complex matrices, Catal. Today. 287 (2017) 203–209. https://doi.org/10.1016/j.cattod.2016.11.015.

[126] E. Jimenez-Relinque, J.R. Rodriguez-Garcia, A. Castillo, M. Castellote, Characteristics and efficiency of photocatalytic cementitious materials: Type of binder, roughness and microstructure, Cem. Concr. Res. 71 (2015) 124–131. https://doi.org/10.1016/j.cemconres.2015.02.003.

[127] E. Cerro-Prada, M. Manso, V. Torres, J. Soriano, Microstructural and photocatalytic characterization of cement-paste sol-gel synthesized titanium dioxide, Front. Struct. Civ. Eng. 10 (2016) 189–197. https://doi.org/10.1007/s11709-015-0326-6.

[128] L. Yang, A. Hakki, F. Wang, D.E. Macphee, Photocatalyst efficiencies in concrete technology: The effect of photocatalyst placement, Appl. Catal. B Environ. 222 (2018) 200–208. https://doi.org/10.1016/j.apcatb.2017.10.013.

[129] Z. Wang, P. Feng, H. Chen, Q. Yu, Photocatalytic performance and dispersion stability of nanodispersed TiO_2 hydrosol in electrolyte solutions with different cations, J. Environ. Sci. 88 (2020) 59–71. https://doi.org/10.1016/j.jes.2019.07.013.

[130] T. Watanabe, T. Takizawa, K. Honda, Photocatalysis through excitation of adsorbates. 1. Highly efficient N-deethylation of rhodamine B adsorbed to CdS, J. Phys. Chem. 81 (1977) 1845–1851. https://doi.org/10.1021/j100534a012.

[131] E. Jimenez-Relinque, J.R. Rodriguez-Garcia, A. Castillo, M. Castellote, Characteristics and efficiency of photocatalytic cementitious materials: Type of binder, roughness and microstructure, Cem. Concr. Res. 71 (2015) 124–131. https://doi.org/10.1016/j.cemconres.2015.02.003.

[132] H. Suk, Y. Mu, J. Won, Y. Kyong, J. Kook, D. Cho, Characterization of bioactive RGD peptide immobilized onto poly (acrylic acid) thin films by plasma polymerization, Appl. Surf. Sci. 257 (2010) 596–602. https://doi.org/10.1016/j.apsusc.2010.07.040.

[133] E. Portenkirchner, G. Neri, J. Lichtinger, J. Brumbarov, C. Ru¨diger, R. Gernha¨user, J. Kunze-Liebha¨user, Tracking areal lithium densities from neutron activation – quantitative Li determination in self-organized TiO_2 nanotube anode materials for Li-ion batteries, Phys. Chem. Chem. Phys. (2017). https://doi.org/10.1039/c7cp00180k.

[134] M.R. Ayers, A.J. Hunt, Titanium oxide aerogels prepared from titanium metal and hydrogen peroxide, Mater. Lett. 34 (1998) 290–293. https://doi.org/10.1016/S0167-577X(97)00181-X.

[135] V. Etacheri, M.K. Seery, S.J. Hinder, S.C. Pillai, Oxygen Rich Titania: A Dopant Free , High Temperature Stable , and Visible-Light Active Anatase Photocatalyst, Adv. Funct. Mater. 21 (2011) 3744–3752. https://doi.org/10.1002/adfm.201100301.

[136] J.A. Davis, R.O. James, J.O. Leckie, Surface Ionization and Complexation at the Oxide/Water Interface I. Computation of Electrical Double Layer Properties in

Simple Electrolytes, J. Colloid Interface Sci. 63 (1977) 480–499. https://doi.org/10.1016/S0021-9797(78)80009-5.

[137] S. Liufu, H. Xiao, Y. Li, Adsorption of poly(acrylic acid) onto the surface of titanium dioxide and the colloidal stability of aqueous suspension, J. Colloid Interface Sci. 281 (2005) 155–163. https://doi.org/10.1016/j.jcis.2004.08.075.

[138] Y.R. Zhang, X.M. Kong, Z.B. Lu, Z.C. Lu, S.S. Hou, Effects of the charge characteristics of polycarboxylate superplasticizers on the adsorption and the retardation in cement pastes, Cem. Concr. Res. 67 (2015) 184–196. https://doi.org/10.1016/j.cemconres.2014.10.004.

[139] R.H. Rogue, W. Lerch, Hydration of Portland Cement Compounds, Ind. Eng. Chem. Res. 26 (1934) 837–847. https://doi.org/10.1021/ie50296a007.

[140] K.L. Scrivener, P. Juilland, P.J.M. Monteiro, Advances in understanding hydration of Portland cement, Cem. Concr. Res. 78 (2015) 38–56. https://doi.org/10.1016/j.cemconres.2015.05.025.

[141] K.L. Scrivener, A. Nonat, Hydration of cementitious materials, present and future, Cem. Concr. Res. 41 (2011) 651–665. https://doi.org/10.1016/j.cemconres.2011.03.026.

[142] J. Cheung, A. Jeknavorian, L. Roberts, D. Silva, Impact of admixtures on the hydration kinetics of Portland cement, Cem. Concr. Res. 41 (2011) 1289–1309. https://doi.org/10.1016/j.cemconres.2011.03.005.

[143] Z. Lu, X. Kong, C. Zhang, Y. Cai, Effect of highly carboxylated colloidal polymers on cement hydration and interactions with calcium ions, Cem. Concr. Res. 113 (2018) 140–153. https://doi.org/10.1016/j.cemconres.2018.08.010.

[144] F.R. Kong, L.S. Pan, C.M. Wang, D. La Zhang, N. Xu, Effects of polycarboxylate superplasticizers with different molecular structure on the hydration behavior of cement paste, Constr. Build. Mater. 105 (2016) 545–553. https://doi.org/10.1016/j.conbuildmat.2015.12.178.

[145] S. Tsivilis, G. Kakali, E. Chaniotakis, A. Souvaridou, A study on the hydration of Portland limestone cement by means of TG, J. Therm. Anal. Calorim. 52 (1998) 863–870. https://doi.org/10.1023/A:1010139312958.

[146] G. Kakali, S. Tsivilis, A. Tsialtas, Hydration of ordinary Portland cements made from raw mix containing transition element oxides, Cem. Concr. Res. 28 (1998) 335–340. https://doi.org/https://doi.org/10.1016/S0008-8846(97)00250-0.

[147] I. Pane, W. Hansen, Investigation of blended cement hydration by isothermal calorimetry and thermal analysis, Cem. Concr. Res. 35 (2005) 1155–1164. https://doi.org/10.1016/j.cemconres.2004.10.027.

[148] N. De Belie, J. Kratky, S. Van Vlierberghe, Influence of pozzolans and slag on the microstructure of partially carbonated cement paste by means of water vapour and nitrogen sorption experiments and BET calculations, Cem. Concr. Res. 40 (2010) 1723–1733. https://doi.org/10.1016/j.cemconres.2010.08.014.

[149] D.S. Klimesch, A. Ray, The use of DTA/TGA to study the effects of ground quartz with different surface areas in autoclaved cement : Quartz pastes. Part 1: A method for evaluating DTA/TGA results, Thermochim. Acta. 289 (1996) 41–54. https://doi.org/10.1016/S0040-6031(96)03033-X.

[150] T. Aarthi, G. Madras, Photocatalytic degradation of rhodamine dyes with nano-TiO_2, Ind. Eng. Chem. Res. 46 (2007) 7–14. https://doi.org/10.1021/ie060948n.

[151] A. Folli, U.H. Jakobsen, G.L. Guerrini, D.E. Macphee, Rhodamine B discolouration on TiO_2 in the cement environment: A look at fundamental aspects of the self-cleaning effect in concretes, J. Adv. Oxid. Technol. 12 (2009) 126–133. https://doi.org/10.1515/jaots-2009-0116.

[152] V. Nadtochenko, N. Denisov, A. Gorenberg, Y. Kozlov, P. Chubukov, J.A. Rengifo, C. Pulgarin, J. Kiwi, Correlations for photocatalytic activity and spectral features of the absorption band edge of TiO_2 modified by thiourea, Appl. Catal. B Environ. 91 (2009) 460–469. https://doi.org/10.1016/j.apcatb.2009.06.015.

[153] R. López, R. Gómez, Band-gap energy estimation from diffuse reflectance measurements on sol-gel and commercial TiO_2: A comparative study, J. Sol-Gel Sci. Technol. 61 (2012) 1–7. https://doi.org/10.1007/s10971-011-2582-9.

[154] M. Radecka, M. Rekas, A. Trenczek-Zajac, K. Zakrzewska, Importance of the band gap energy and flat band potential for application of modified TiO_2 photoanodes in water photolysis, J. Power Sources. 181 (2008) 46–55. https://doi.org/10.1016/j.jpowsour.2007.10.082.

[155] S. Karapati, T. Giannakopoulou, N. Todorova, N. Boukos, S. Antiohos, D. Papageorgiou, E. Chaniotakis, D. Dimotikali, C. Trapalis, TiO_2 functionalization for efficient NO_X removal in photoactive cement, Appl. Surf. Sci. 319 (2014) 29–36. https://doi.org/10.1016/j.apsusc.2014.07.162.

[156] R. Bhatt, I. Bhaumik, S. Ganesamoorthy, A.K. Karnal, M.K. Swami, H.S. Patel, P.K. Gupta, Urbach tail and bandgap analysis in near stoichiometric $LiNbO_3$ crystals, Phys. Status Solidi Appl. Mater. Sci. 209 (2012) 176–180. https://doi.org/10.1002/pssa.201127361.

[157] D.C. Cronemeyer, Electrical and optical properties of rutile single crystals, Phys. Rev. 87 (1952) 876–886. https://doi.org/10.1103/PhysRev.87.876.

[158] Franz Urbach, The long-wavelength edge of photographic sensitivity and of the electronic absorption of solids, Phys. Rev. 92 (1953) 1324–1324. https://doi.org/10.1103/PhysRev.92.1324.

[159] P.K. Mehta, P.J.M. Monteiro, Concrete: Microsturcture, Properties and Materials, Third Edit, The McGraw-Hill Companies, Inc. All, 2006. https://doi.org/10.1036/0071462899.

[160] A.M. Kaja, H.J.H. Brouwers, Q.L. Yu, NO_x degradation by photocatalytic mortars: The underlying role of the CH and C-S-H carbonation, Cem. Concr. Res. 125 (2019) 105805. https://doi.org/10.1016/j.cemconres.2019.105805.

[161] F. Goetz-Neunhoeffer, J. Neubauer, P. Schwesig, Mineralogical characteristics of Ettringites synthesized from solutions and suspensions, Cem. Concr. Res. 36 (2006) 65–70. https://doi.org/10.1016/j.cemconres.2004.04.037.

[162] E. Sakai, Y. Nikaido, T. Itoh, M. Daimon, Ettringite formation and microstructure of rapid hardening cement, Cem. Concr. Res. 34 (2004) 1669–1673. https://doi.org/10.1016/j.cemconres.2004.04.021.

[163] H.M. Jennings, B.J. Dalgleish, P.L. Pratt, Morphological development of hydrating tricalcium silicate as examined by Electron Microscopy Techniques, J. Am. Ceram. Soc. 64 (1981) 567–572. https://doi.org/10.1111/j.1151-2916.1981.tb10219.x.

[164] P.K. Mehta, Mechanism of sulfate attack on Portland cement concrete- Another look, Cem. Concr. Res. 13 (1983) 401–406. https://doi.org/10.1016/0008-8846(83)90040-6.

[165] J.H. Potgieter, K.A. Horne, S.S. Potgieter, W. Wirth, An evaluation of the incorporation of a titanium dioxide producer's waste material in Portland cement clinker, Mater. Lett. 57 (2002) 157–163. https://doi.org/10.1016/s0167-577x(02)00723-1.

[166] D. Shang, M. Wang, Z. Xia, S. Hu, F. Wang, Incorporation mechanism of titanium in Portland cement clinker and its effects on hydration properties, Constr. Build. Mater. 146 (2017) 344–349. https://doi.org/10.1016/j.conbuildmat.2017.03.129.

[167] O. Mikhailova, A. del Campo, P. Rovnanik, J.F. Fernández, M. Torres-Carrasco, In situ characterization of main reaction products in alkali-activated slag materials by Confocal Raman Microscopy, Cem. Concr. Compos. 99 (2019) 32–39. https://doi.org/10.1016/j.cemconcomp.2019.02.004.

[168] M. Torres-Carrasco, A. del Campo, M.A. de la Rubia, E. Reyes, A. Moragues, J.F. Fernández, New insights in weathering analysis of anhydrous cements by using high spectral and spatial resolution Confocal Raman Microscopy, Cem. Concr. Res. 100 (2017) 119–128. https://doi.org/10.1016/j.cemconres.2017.06.003.

[169] J. Higl, M. Köhler, M. Lindén, Confocal Raman microscopy as a non-destructive tool to study microstructure of hydrating cementitious materials, Cem. Concr. Res. 88 (2016) 136–143. https://doi.org/10.1016/j.cemconres.2016.07.005.

[170] F. Liu, Z. Sun, Chemical mapping of cement pastes by using confocal Raman spectroscopy, Front. Struct. Civ. Eng. 10 (2016) 168–173. https://doi.org/10.1007/s11709-015-0323-9.

[171] I.R. Beattie, T.R. Gilson, Single crystal laser Raman spectroscopy, Proc. R. Soc. A, Math. Phys. Eng. Sci. 307 (1968) 407–429. https://doi.org/10.1098/rspa.1968.0199.

[172] T. Ohsaka, F. Izumi, Y. Fujiki, Raman spectrum of anatase, TiO_2, J. Raman Spectrosc. 7 (1978) 321–324. https://doi.org/10.1002/jrs.1250070606.

[173] L. Black, C. Breen, J. Yarwood, C.S. Deng, J. Phipps, G. Maitland, Hydration of tricalcium aluminate (C_3A) in the presence and absence of gypsum - Studied by Raman spectroscopy and X-ray diffraction, J. Mater. Chem. 16 (2006) 1263–1272. https://doi.org/10.1039/b509904h.

[174] G. Renaudin, R. Segni, D. Mentel, J.-M. Nedelec, F. Leroux, C. Taviot-Gueho, A Raman study of the sulfated cement hydrates: Ettringite and Monosulfoaluminate, J. Adv. Concr. Technol. 5 (2007) 299–312. https://doi.org/10.3151/jact.5.299.

[175] S. Gunasekaran, G. Anbalagan, S. Pandi, Raman and infrared spectra of carbonates of calcite structure, J. Raman Spectrosc. 37 (2006) 892–899. https://doi.org/10.1002/jrs.1518.

[176] R. Masmoudi, K. Kupwade-Patil, A. Bumajdad, O. Büyüköztürk, In situ Raman studies on cement paste prepared with natural pozzolanic volcanic ash and Ordinary Portland Cement, Constr. Build. Mater. 148 (2017) 444–454. https://doi.org/10.1016/j.conbuildmat.2017.05.016.

[177] F. Liu, Z. Sun, C. Qi, Raman pectroscopy study on the hydration behaviors of Portland cement pastes during setting, J. Mater. Civ. Eng. 27 (2014) 04014223. https://doi.org/10.1061/(asce)mt.1943-5533.0001189.

[178] T. Schmida, P. Dariz, Shedding light onto the spectra of lime: Raman and luminescence bands of CaO, Ca(OH)$_2$ and CaCO$_3$, J. Raman Spectrosc. 46 (2015) 141–146. https://doi.org/10.1002/jrs.4622.

[179] L. Black, Raman spectroscopy of cementitious materials, in: J. Yarwood, R. Douthwaite, S.B. Duckett (Eds.), Spectrosc. Prop. Inorg. Organomet. Compd. Vol. 40, The Royal Society of Chemistry, Cambridge, 2009: pp. 72–127. https://doi.org/10.1039/b715000h.

[180] T. Wu, G. Liu, J. Zhao, H. Hidaka, N. Serpone, Photoassisted degradation of dye pollutants. V. Self-photosensitized oxidative transformation of Rhodamine B under visible light irradiation in aqueous TiO$_2$ dispersions, J. Phys. Chem. B. 102 (1998) 5845–5851. https://doi.org/10.1021/jp980922c.

[181] R. Wang, K. Hashimoto, A. Fujishima, M. Chikuni, E. Kojima, A. Kitamura, M. Shimohigoshi, T. Watanabe, Photogeneration of highly amphiphilic TiO$_2$ surfaces, Adv. Mater. 10 (1998) 135–138. https://doi.org/10.1002/(SICI)1521-4095(199801)10:2<135::AID-ADMA135>3.0.CO;2-M.

[182] N. Sakai, A. Fujishima, T. Watanabe, K. Hashimoto, Quantitative evaluation of the photoinduced hydrophilic conversion properties of TiO$_2$ thin film surfaces by the reciprocal of contact angle, J. Phys. Chem. B. 107 (2003) 1028–1035. https://doi.org/10.1021/jp022105p.

[183] N. Sakai, A. Fujishima, T. Watanabe, K. Hashimoto, Enhancement of the photoinduced hydrophilic conversion rate of TiO$_2$ Film electrode surfaces by anodic polarization, J. Phys. Chem. B. 105 (2001) 3023–3026. https://doi.org/10.1021/jp003212r.

[184] T. Zubkoy, D. Stahl, T.L. Thompson, D. Panayotov, O. Diwald, J.T. Yates, Ultraviolet light-induced hydrophilicity effect on TiO$_2$(110) (1×1). Dominant role of the photooxidation of adsorbed hydrocarbons causing wetting by water droplets, J. Phys. Chem. B. 109 (2005) 15454–15462. https://doi.org/10.1021/jp058101c.

[185] S.H. Elder, F.M. Cot, Y. Su, S.M. Heald, A.M. Tyryshkin, M.K. Bowman, Y. Gao, A.G. Joly, M.L. Balmer, A.C. Kolwaite, K.A. Magrini, D.M. Blake, The discovery and study

of nanocrystalline TiO_2 -(MoO_3) core-shelf materials, J. Am. Chem. Soc. 122 (2000) 5138–5146. https://doi.org/10.1021/ja992768t.

[186] B. Choudhury, A. Choudhury, Oxygen defect dependent variation of band gap, Urbach energy and luminescence property of anatase, anatase-rutile mixed phase and of rutile phases of TiO_2 nanoparticles, Phys. E Low-Dimensional Syst. Nanostructures. 56 (2014) 364–371. https://doi.org/10.1016/j.physe.2013.10.014.

[187] M.M. Khan, S.A. Ansari, D. Pradhan, M.O. Ansari, D.H. Han, J. Lee, M.H. Cho, Band gap engineered TiO_2 nanoparticles for visible light induced photoelectrochemical and photocatalytic studies, J. Mater. Chem. A. 2 (2014) 637–644. https://doi.org/10.1039/c3ta14052k.

[188] M.M. Ballari, Q.L. Yu, H.J.H. Brouwers, Experimental study of the NO and NO_2 degradation by photocatalytically active concrete, Catal. Today. 161 (2011) 175–180. https://doi.org/10.1016/j.cattod.2010.09.028.

[189] Q.L. Yu, M.M. Ballari, H.J.H. Brouwers, Indoor air purification using heterogeneous photocatalytic oxidation. Part II: Kinetic study, Appl. Catal. B Environ. 99 (2010) 58–65. https://doi.org/10.1016/j.apcatb.2010.05.032.

[190] Q.L. Yu, H.J.H. Brouwers, Indoor air purification using heterogeneous photocatalytic oxidation. Part I: Experimental study, Appl. Catal. B Environ. 92 (2009) 454–461. https://doi.org/10.1016/j.apcatb.2009.09.004.

[191] Q.L. Yu, M.M. Ballari, H.J.H. Brouwers, Heterogeneous photocatalysis applied to indoor building material: Towards an improved indoor air quality, Adv. Mater. Res. 255–260 (2011) 2836–2840. https://doi.org/10.4028/www.scientific.net/AMR.255-260.2836.

[192] M.V. Diamanti, M. Ormellese, M. Pedeferri, Characterization of photocatalytic and superhydrophilic properties of mortars containing titanium dioxide, Cem. Concr. Res. 38 (2008) 1349–1353. https://doi.org/10.1016/j.cemconres.2008.07.003.

[193] F. Gherardi, A. Colombo, M. D'Arienzo, B. Di Credico, S. Goidanich, F. Morazzoni, R. Simonutti, L. Toniolo, Efficient self-cleaning treatments for built heritage based on highly photo-active and well-dispersible TiO_2 nanocrystals, Microchem. J. 126 (2016) 54–62. https://doi.org/10.1016/j.microc.2015.11.043.

[194] Q. Jin, M. Faraldos, A. Bahamonde, B.H. Zaribaf, K.E. Kurtis, Titania and silica nanoparticle-modified coatings for cementitious materials, in: ACI Symp. Publ., 2019: pp. 97–111. https://doi.org/10.14359/51720218.

[195] E. Burunkaya, M. Akarsu, H. Erdem Çamurlu, Ö. Kesmez, Z. Yeşil, M. Asiltürk, E. Arpaç, Production of stable hydrosols of crystalline TiO_2 nanoparticles synthesized at relatively low temperatures in diverse media, Appl. Surf. Sci. 265 (2013) 317–323. https://doi.org/10.1016/j.apsusc.2012.11.003.

[196] T. Liu, F. Li, X. Li, TiO_2 hydrosols with high activity for photocatalytic degradation of formaldehyde in a gaseous phase, J. Hazard. Mater. 152 (2008) 347–355. https://doi.org/10.1016/j.jhazmat.2007.07.003.

[197] T.X. Liu, Y. Liu, Z.J. Zhang, F.B. Li, X.Z. Li, Comparison of aqueous photoreactions with TiO_2 in its hydrosol solution and powdery suspension for light utilization, Ind. Eng. Chem. Res. 50 (2011) 7841–7848. https://doi.org/10.1021/ie102584j.

[198] N. Serpone, D. Lawless, R. Khairutdinov, Size effects on the photophysical properties of colloidal Anatase TiO_2 particles: size quantization versus direct transitions in this indirect semiconductor?, J. Phys. Chem. 99 (2002) 16646–16654. https://doi.org/10.1021/j100045a026.

[199] M. Lackhoff, X. Prieto, N. Nestle, F. Dehn, R. Niessner, Photocatalytic activity of semiconductor-modified cement---Influence of semiconductor type and cement ageing, Appl. Catal. B Environ. 43 (2003) 205–216. https://doi.org/10.1016/S0926-3373(02)00303-X.

[200] L. Cardellicchio, Self-cleaning and colour-preserving efficiency of photocatalytic concrete: case study of the Jubilee Church in Rome, Build. Res. Inf. (2019) 1–20. https://doi.org/10.1080/09613218.2019.1622405.

[201] A. Hartmann, D. Schulenberg, J.-C. Buhl, Synthesis and Structural Characterization of CSH-Phases in the Range of C/S = 0.41 - 1.66 at temperatures of the tobermorite xonotlite crossover, J. Mater. Sci. Chem. Eng. 03 (2015) 39–55. https://doi.org/10.4236/msce.2015.311006.

[202] M. Castellote, L. Fernandez, C. Andrade, C. Alonso, Chemical changes and phase analysis of OPC pastes carbonated at different CO_2 concentrations, Mater. Struct. Constr. 42 (2009) 515–525. https://doi.org/10.1617/s11527-008-9399-1.

[203] G.W. Groves, D.I. Rodway, I.G. Richardson, The carbonation of hardened cement pastes, Adv. Cem. Res. 3 (1990) 117–125. https://doi.org/https://doi.org/10.1680/adcr.1990.3.11.117.

[204] D.J. Anstice, C.L. Page, M.M. Page, The pore solution phase of carbonated cement pastes, Cem. Concr. Res. 35 (2005) 377–383. https://doi.org/10.1016/j.cemconres.2004.06.041.

[205] M. Auroy, S. Poyet, P. Le Bescop, J.M. Torrenti, T. Charpentier, M. Moskura, X. Bourbon, Comparison between natural and accelerated carbonation (3% CO_2): Impact on mineralogy, microstructure, water retention and cracking, Cem. Concr. Res. 109 (2018) 64–80. https://doi.org/10.1016/j.cemconres.2018.04.012.

[206] C. Xiantuo, Z. Ruizhen, C. Xiaorong, Kinetic study of ettringite carbonation reaction, Cem. Concr. Res. 24 (1994) 1383–1389. https://doi.org/10.1016/0008-8846(94)90123-6.

[207] T.Nishikawa, K.Suzuki, S.Ito, K.Sato, T.Takebe, Decomposition of synthesized ettringite by carbonation, Cem. Concr. Compos. 22 (1992) 6–12. https://doi.org/10.20595/jjbf.19.0_3.

[208] Q. Zhou, F.P. Glasser, Kinetics and mechanism of the carbonation of ettringite, Adv. Cem. Res. 12 (2000) 131–136. https://doi.org/10.1680/adcr.2000.12.3.131.

[209] L. Black, C. Breen, J. Yarwood, K. Garbev, P. Stemmermann, B. Gasharova, Structural features of C-S-H(I) and its carbonation in air-A Raman spectroscopic study. Part II:

Carbonated phases, J. Am. Ceram. Soc. 90 (2007) 908–917. https://doi.org/10.1111/j.1551-2916.2006.01429.x.

[210] A. Morandeau, M. Thiéry, P. Dangla, Investigation of the carbonation mechanism of CH and C-S-H in terms of kinetics, microstructure changes and moisture properties, Cem. Concr. Res. 56 (2014) 153–170. https://doi.org/10.1016/j.cemconres.2013.11.015.

[211] M. V. Diamanti, F. Lollini, M.P. Pedeferri, L. Bertolini, Mutual interactions between carbonation and titanium dioxide photoactivity in concrete, Build. Environ. 62 (2013) 174–181. https://doi.org/10.1016/j.buildenv.2013.01.023.

[212] E. Drouet, S. Poyet, P. Le Bescop, J.M. Torrenti, X. Bourbon, Carbonation of hardened cement pastes: Influence of temperature, Cem. Concr. Res. 115 (2019) 445–459. https://doi.org/10.1016/j.cemconres.2018.09.019.

[213] S. von Greve-Dierfeld, B. Lothenbach, A. Vollpracht, B. Wu, B. Huet, C. Andrade, C. Medina, C. Thiel, E. Gruyaert, H. Vanoutrive, I.F. Saéz del Bosque, I. Ignjatovic, J. Elsen, J.L. Provis, K. Scrivener, K.C. Thienel, K. Sideris, M. Zajac, N. Alderete, Ö. Cizer, P. Van den Heede, R.D. Hooton, S. Kamali-Bernard, S.A. Bernal, Z. Zhao, Z. Shi, N. De Belie, Understanding the carbonation of concrete with supplementary cementitious materials: a critical review by RILEM TC 281-CCC, Mater. Struct. 53 (2020). https://doi.org/10.1617/s11527-020-01558-w.

[214] A. Leemann, F. Moro, Carbonation of concrete: the role of CO_2 concentration, relative humidity and CO_2 buffer capacity, Mater. Struct. 50 (2017) 1–14. https://doi.org/10.1617/s11527-016-0917-2.

[215] Y. Li, W. Liu, F. Xing, S. Wang, L. Tang, S. Lin, Z. Dong, Carbonation of the synthetic calcium silicate hydrate (C-S-H) under different concentrations of CO_2: Chemical phases analysis and kinetics, J. CO_2 Util. 35 (2020) 303–313. https://doi.org/10.1016/j.jcou.2019.10.001.

[216] J. Chang, Y. Fang, Quantitative analysis of accelerated carbonation products of the synthetic calcium silicate hydrate(C-S-H) by QXRD and TG/MS, J. Therm. Anal. Calorim. 119 (2015) 57–62. https://doi.org/10.1007/s10973-014-4093-8.

[217] M. Fernández Bertos, S.J.R. Simons, C.D. Hills, P.J. Carey, A review of accelerated carbonation technology in the treatment of cement-based materials and sequestration of CO_2, J. Hazard. Mater. 112 (2004) 193–205. https://doi.org/10.1016/j.jhazmat.2004.04.019.

[218] J.M. Marangu, J.K. Thiong'O, J.M. Wachira, Review of Carbonation Resistance in Hydrated Cement Based Materials, J. Chem. 2019 (2019). https://doi.org/10.1155/2019/8489671.

[219] I. Galan, C. Andrade, M. Castellote, Natural and accelerated CO_2 binding kinetics in cement paste at different relative humidities, Cem. Concr. Res. 49 (2013) 21–28. https://doi.org/10.1016/j.cemconres.2013.03.009.

[220] F. Georget, W. Soja, K.L. Scrivener, Characteristic lengths of the carbonation front in naturally carbonated cement pastes: Implications for reactive transport models, Cem. Concr. Res. 134 (2020) 106080. https://doi.org/10.1016/j.cemconres.2020.106080.

[221] I. Monteiro, F.A. Branco, J. De Brito, R. Neves, Statistical analysis of the carbonation coefficient in open air concrete structures, Constr. Build. Mater. 29 (2012) 263–269. https://doi.org/10.1016/j.conbuildmat.2011.10.028.

[222] Z. Wang, Q. Yu, P. Feng, H.J.H. Brouwers, Variation of self-cleaning performance of nano-TiO_2 modified mortar caused by carbonation : From hydrates to carbonates, Cem. Concr. Res. 158 (2022) 106852. https://doi.org/10.1016/j.cemconres.2022.106852.

[223] X. Gan, K. He, B. Qian, Q. Deng, L. Lu, Y. Wang, The effect of glycine on the growth of calcium carbonate in alkaline silica gel, J. Cryst. Growth. 458 (2017) 60–65. https://doi.org/10.1016/j.jcrysgro.2016.11.027.

[224] R. Ševčík, M. Pérez-Estébanez, A. Viani, P. Šašek, P. Mácová, Characterization of vaterite synthesized at various temperatures and stirring velocities without use of additives, Powder Technol. 284 (2015) 265–271. https://doi.org/10.1016/j.powtec.2015.06.064.

[225] F.C. Meldrum, Calcium carbonate in biomineralisation and biomimetic chemistry, Int. Mater. Rev. 48 (2003) 187–224. https://doi.org/10.1179/095066003225005836.

[226] Y. Ding, Y. Liu, Y. Ren, H. Yan, M. Wang, D. Wang, X.Y. Lu, B. Wang, T. Fan, H. Guo, Controllable synthesis of all the anhydrous $CaCO_3$ polymorphs with various morphologies in $CaCl_2$-NH_3-CO_2 aqueous system, Powder Technol. 333 (2018) 410–420. https://doi.org/10.1016/j.powtec.2018.04.056.

[227] E.T. Stepkowska, M.A. Aviles, J.M. Blanes, J.L. Perez-Rodriguez, Gradual transformation of $Ca(OH)_2$ into $CaCO_3$ on cement hydration XRD study, J. Therm. Anal. Calorim. 87 (2007) 189–198. https://doi.org/https://doi.org/10.1007/s10973-006-7840-7.

[228] Z. Wang, Q. Yu, F. Gauvin, P. Feng, Q. Ran, H.J.H. Brouwers, Nanodispersed TiO_2 hydrosol modified Portland cement paste: The underlying role of hydration on self-cleaning mechanisms, Cem. Concr. Res. 136 (2020). https://doi.org/10.1016/j.cemconres.2020.106156.

[229] V.S. Harutyunyan, A.P. Kirchheim, P.J.M. Monteiro, A.P. Aivazyan, P. Fischer, Investigation of early growth of calcium hydroxide crystals in cement solution by soft X-ray transmission microscopy, J. Mater. Sci. 44 (2009) 962–969. https://doi.org/10.1007/s10853-008-3198-5.

[230] G. Villain, M. Thiery, G. Platret, Measurement methods of carbonation profiles in concrete: Thermogravimetry, chemical analysis and gammadensimetry, Cem. Concr. Res. 37 (2007) 1182–1192. https://doi.org/10.1016/j.cemconres.2007.04.015.

[231] X. Pan, C. Shi, X. Hu, Z. Ou, Effects of CO_2 surface treatment on strength and permeability of one-day-aged cement mortar, Constr. Build. Mater. 154 (2017) 1087–1095. https://doi.org/10.1016/j.conbuildmat.2017.07.216.

[232] Z. Tu, M.Z. Guo, C.S. Poon, C. Shi, Effects of limestone powder on $CaCO_3$ precipitation in CO_2 cured cement pastes, Cem. Concr. Compos. 72 (2016) 9–16. https://doi.org/10.1016/j.cemconcomp.2016.05.019.

[233] F. Matsushita, Y. Aono, S. Shibata, Carbonation degree of autoclaved aerated concrete, Cem. Concr. Res. 30 (2000) 1741–1745. https://doi.org/10.1016/S0008-8846(00)00424-5.

[234] D. Feng, N. Xie, C. Gong, Z. Leng, H. Xiao, H. Li, X. Shi, Portland Cement Paste Modified by TiO_2 Nanoparticles: A Microstructure Perspective, Ind. Eng. Chem. Res. 52 (2013) 11575–11582. https://doi.org/10.1021/ie4011595.

[235] S. Steiner, B. Lothenbach, T. Proske, A. Borgschulte, F. Winnefeld, Effect of relative humidity on the carbonation rate of portlandite, calcium silicate hydrates and ettringite, Cem. Concr. Res. 135 (2020) 106116. https://doi.org/10.1016/j.cemconres.2020.106116.

[236] L. Black, K. Garbev, I. Gee, Surface carbonation of synthetic C-S-H samples: A comparison between fresh and aged C-S-H using X-ray photoelectron spectroscopy, Cem. Concr. Res. 38 (2008) 745–750. https://doi.org/10.1016/j.cemconres.2008.02.003.

[237] M.G. Margalha, A.S. Silva, M.D.R. Veiga, J. De Brito, R.J. Ball, G.C. Allen, Microstructural changes of lime putty during aging, J. Mater. Civ. Eng. 25 (2013) 1524–1532. https://doi.org/10.1061/(ASCE)MT.1943-5533.0000687.

[238] E. Ruiz-Agudo, K. Kudlacz, C. V. Putnis, A. Putnis, C. Rodriguez-Navarro, Dissolution and carbonation of portlandite $[Ca(OH)_2]$ single crystals, Environ. Sci. Technol. 47 (2013) 11342–11349. https://doi.org/10.1021/es402061c.

[239] G. Mascolo, M.C. Mascolo, A. Vitale, O. Marino, Microstructure evolution of lime putty upon aging, J. Cryst. Growth. 312 (2010) 2363–2368. https://doi.org/10.1016/j.jcrysgro.2010.05.020.

[240] R. Camerini, G. Poggi, D. Chelazzi, F. Ridi, R. Giorgi, P. Baglioni, The carbonation kinetics of calcium hydroxide nanoparticles: A boundary nucleation and growth description, J. Colloid Interface Sci. 547 (2019) 370–381. https://doi.org/10.1016/j.jcis.2019.03.089.

[241] C. Rodriguez-Navarro, K. Elert, R. Ševčík, Amorphous and crystalline calcium carbonate phases during carbonation of nanolimes: Implications in heritage conservation, CrystEngComm. 18 (2016) 6594–6607. https://doi.org/10.1039/c6ce01202g.

[242] L.S. Gomez-Villalba, P. López-Arce, M. Alvarez De Buergo, R. Fort, Atomic defects and their relationship to aragonite-calcite transformation in portlandite nanocrystal carbonation, Cryst. Growth Des. 12 (2012) 4844–4852. https://doi.org/10.1021/cg300628m.

[243] P. López-Arce, L.S. Gómez-Villalba, S. Martínez-Ramírez, M. Álvarez de Buergo, R. Fort, Influence of relative humidity on the carbonation of calcium hydroxide nanoparticles and the formation of calcium carbonate polymorphs, Powder Technol. 205 (2011) 263–269. https://doi.org/10.1016/j.powtec.2010.09.026.

[244] Ö. Cizer, C. Rodriguez-Navarro, E. Ruiz-Agudo, J. Elsen, D. Van Gemert, K. Van Balen, Phase and morphology evolution of calcium carbonate precipitated by

carbonation of hydrated lime, J. Mater. Sci. 47 (2012) 6151–6165. https://doi.org/10.1007/s10853-012-6535-7.

[245] O. Cazalla, C. Rodriguez-Navarro, E. Sebastian, G. Cultrone, M.J. De la Torre, Aging of lime putty: Effects on traditional lime mortar carbonation, J. Am. Ceram. Soc. 83 (2000) 1070–1076. https://doi.org/10.1111/j.1151-2916.2000.tb01332.x.

[246] K. Elert, C. Rodriguez-Navarro, E.S. Pardo, E. Hansen, O. Cazalla, Lime mortars for the conservation of historic buildings, Stud. Conserv. 47 (2002) 62–75. https://doi.org/10.1179/sic.2002.47.1.62.

[247] A. Trapote-Barreira, J. Cama, J.M. Soler, Dissolution kinetics of C-S-H gel: Flow-through experiments, Phys. Chem. Earth. 70–71 (2014) 17–31. https://doi.org/10.1016/j.pce.2013.11.003.

[248] R. Amadelli, L. Samiolo, M. Borsa, M. Bellardita, L. Palmisano, N-TiO$_2$ Photocatalysts highly active under visible irradiation for NO$_x$ abatement and 2-propanol oxidation, Catal. Today. 206 (2013) 19–25. https://doi.org/10.1016/j.cattod.2011.11.031.

[249] M. Gao, L. Zhu, W.L. Ong, J. Wang, G.W. Ho, Structural design of TiO$_2$ -based photocatalyst for H$_2$ production and degradation applications, Catal. Sci. Technol. 5 (2015) 4703–4726. https://doi.org/10.1039/c5cy00879d.

[250] Q. Jin, E.M. Saad, W. Zhang, Y. Tang, K.E. Kurtis, Quantification of NO$_x$ uptake in plain and TiO$_2$ -doped cementitious materials, Cem. Concr. Res. 122 (2019) 251–256. https://doi.org/10.1016/j.cemconres.2019.05.010.

[251] Q. Jin, S.L. Hordern, Y. Tang, K.E. Kurtis, NO$_x$ sequestration by calcium aluminate cementitious materials, Cem. Concr. Res. 142 (2021) 106381. https://doi.org/10.1016/j.cemconres.2021.106381.

[252] G. Gao, P. Huang, K. Wang, R. He, D. Cui, Gram-scale synthesis and shape evolution of micro-CaCO$_3$, Powder Technol. 205 (2011) 270–275. https://doi.org/10.1016/j.powtec.2010.09.032.

[253] U. Wehrmeister, A.L. Soldati, D.E. Jacob, T. Häger, W. Hofmeister, Raman spectroscopy of synthetic, geological and biological vaterite: A Raman spectroscopic study, J. Raman Spectrosc. 41 (2010) 193–201. https://doi.org/10.1002/jrs.2438.

[254] J.D. Rodriguez-Blanco, S. Shaw, L.G. Benning, The kinetics and mechanisms of amorphous calcium carbonate (ACC) crystallization to calcite, via vaterite., Nanoscale. 3 (2011) 265–271. https://doi.org/10.1039/c0nr00589d.

[255] Z. Zhang, Y. Xie, X. Xu, H. Pan, R. Tang, Transformation of amorphous calcium carbonate into aragonite, J. Cryst. Growth. 343 (2012) 62–67. https://doi.org/10.1016/j.jcrysgro.2012.01.025.

[256] C. Pereira, J. de Brito, J.D. Silvestre, Contribution of humidity to the degradation of façade claddings in current buildings, Eng. Fail. Anal. 90 (2018) 103–115. https://doi.org/10.1016/j.engfailanal.2018.03.028.

[257] S. Zuo, J. Xiao, Q. Yuan, Comparative study on the new-old mortar interface deterioration after wet-dry cycles and heat-cool cycles, Constr. Build. Mater. 244 (2020) 118374. https://doi.org/10.1016/j.conbuildmat.2020.118374.

[258] R. He, S. Zheng, V.J.L. Gan, Z. Wang, J. Fang, Y. Shao, Damage mechanism and interfacial transition zone characteristics of concrete under sulfate erosion and Dry-Wet cycles, Constr. Build. Mater. 255 (2020) 119340. https://doi.org/10.1016/j.conbuildmat.2020.119340.

[259] K. Wang, J. Guo, H. Wu, L. Yang, Influence of dry-wet ratio on properties and microstructure of concrete under sulfate attack, Constr. Build. Mater. 263 (2020) 120635. https://doi.org/10.1016/j.conbuildmat.2020.120635.

[260] M.Z.Y. Ting, K.S. Wong, M.E. Rahman, S.J. Meheron, Deterioration of marine concrete exposed to wetting-drying action, J. Clean. Prod. 278 (2021) 123383. https://doi.org/10.1016/j.jclepro.2020.123383.

[261] F. Adenot, M. Buil, Modelling of the corrosion of the cement paste by deionized water, Cem. Concr. Res. 22 (1992) 489–496. https://doi.org/10.1093/iclqaj/41.1.137.

[262] M. Buil, E. Revertegat, J. Oliver, A model of the attack of pure water or undersaturated lime solutions on cement, ASTM Spec. Tech. Publ. (1992) 227–241. https://doi.org/10.1520/stp19554s.

[263] P. Faucon, B. Gerard, J.F. Jacquinot, J. Marchand, Water attack of a cement paste: Towards an improved accelerated test?, Adv. Cem. Res. 10 (1998) 67–73. https://doi.org/10.1680/adcr.1998.10.2.67.

[264] M. Mainguy, C. Tognazzi, J.M. Torrenti, F. Adenot, Modelling of leaching in pure cement paste and mortar, Cem. Concr. Res. 30 (2000) 83–90. https://doi.org/10.1016/S0008-8846(99)00208-2.

[265] Q.T. Phung, N. Maes, D. Jacques, G. De Schutter, G. Ye, Investigation of the changes in microstructure and transport properties of leached cement pastes accounting for mix composition, Cem. Concr. Res. 79 (2016) 217–234. https://doi.org/10.1016/j.cemconres.2015.09.017.

[266] P. Hartwich, A. Vollpracht, Influence of leachate composition on the leaching behaviour of concrete, Cem. Concr. Res. 100 (2017) 423–434. https://doi.org/10.1016/j.cemconres.2017.07.002.

[267] Y. Yang, R.A. Patel, S. V. Churakov, N.I. Prasianakis, G. Kosakowski, M. Wang, Multiscale modeling of ion diffusion in cement paste: electrical double layer effects, Cem. Concr. Compos. 96 (2019) 55–65. https://doi.org/10.1016/j.cemconcomp.2018.11.008.

[268] H. Di, X. Guan, S. Liu, Changes in mechanical performance and pore structure of hardened cement paste under the combined effect of calcium leaching and dry/wet cycles, Constr. Build. Mater. 407 (2023) 133519. https://doi.org/10.1016/j.conbuildmat.2023.133519.

[269] P.M. Carmona-Quiroga, S. Martínez-Ramírez, H.A. Viles, Efficiency and durability of a self-cleaning coating on concrete and stones under both natural and artificial ageing

trials, Appl. Surf. Sci. 433 (2018) 312–320.
https://doi.org/10.1016/j.apsusc.2017.10.052.

[270] J. Zhou, Z. Tan, Z. Liu, M. Jing, W. Liu, W. Fu, Preparation of transparent fluorocarbon/TiO_2-SiO_2 composite coating with improved self-cleaning performance and anti-aging property, Appl. Surf. Sci. 396 (2017) 161–168. https://doi.org/10.1016/j.apsusc.2016.11.014.

[271] G.B. Goffredo, V. Terlizzi, P. Munafò, Multifunctional TiO_2-based hybrid coatings on limestone: Initial performances and durability over time, J. Build. Eng. 14 (2017) 134–149. https://doi.org/10.1016/j.jobe.2017.10.006.

[272] M. Baudys, J. Krýsa, M. Zlámal, A. Mills, Weathering tests of photocatalytic facade paints containing ZnO and TiO_2, Chem. Eng. J. 261 (2015) 83–87. https://doi.org/10.1016/j.cej.2014.03.112.

[273] M.Z. Guo, T.C. Ling, C.S. Poon, Nano-TiO_2-based architectural mortar for NO removal and bacteria inactivation: Influence of coating and weathering conditions, Cem. Concr. Compos. 36 (2013) 101–108. https://doi.org/10.1016/j.cemconcomp.2012.08.006.

[274] J. Jain, N. Neithalath, Analysis of calcium leaching behavior of plain and modified cement pastes in pure water, Cem. Concr. Compos. 31 (2009) 176–185. https://doi.org/10.1016/j.cemconcomp.2009.01.003.

[275] A. Trapote-Barreira, J. Cama, J.M. Soler, Dissolution kinetics of C-S-H gel: Flow-through experiments, Phys. Chem. Earth. 70–71 (2014) 17–31. https://doi.org/10.1016/j.pce.2013.11.003.

[276] A. Trapote-Barreira, L. Porcar, J. Cama, J.M. Soler, A.J. Allen, Structural changes in C-S-H gel during dissolution: Small-angle neutron scattering and Si-NMR characterization, Cem. Concr. Res. 72 (2015) 76–89. https://doi.org/10.1016/j.cemconres.2015.02.009.

[277] Y. Hendrix, A. Lazaro, Q.L. Yu, H.J.H. Brouwers, Influence of synthesis conditions on the properties of photocatalytic titania-silica composites, J. Photochem. Photobiol. A Chem. 371 (2019) 25–32. https://doi.org/10.1016/j.jphotochem.2018.10.040.

[278] E. Luévano-Hipólito, A. Martínez-De La Cruz, E. López-Cuellar, Q.L. Yu, H.J.H. Brouwers, Synthesis, characterization and photocatalytic activity of WO_3/TiO_2 for NO removal under UV and visible light irradiation, Mater. Chem. Phys. 148 (2014) 208–213. https://doi.org/10.1016/j.matchemphys.2014.07.034.

[279] Y. Wang, Y. He, Q. Lai, M. Fan, Review of the progress in preparing nano TiO_2: An important environmental engineering material, J. Environ. Sci. 26 (2014) 2139–2177. https://doi.org/10.1016/j.jes.2014.09.023.

[280] M. Malekshahi Byranvand, A.N. Kharat, L. Fatholahi, Z. Malekshahi Beiranvand, A review on synthesis of nano-TiO_2 via different methods, J. Nanostructures. 3 (2013) 1–9. http://jns.kashanu.ac.ir/article_5436_20d28461e8600e7c915eab3d24924117.pdf.

[281] R. Vijayalakshmi, V. Rajendran, Synthesis and characterization of nano-TiO_2 via different methods, Arch. Appl. Sci. Res. 4 (2012) 1183–1190. https://doi.org/10.11648/j.nano.20140201.11.

[282] M.M. Soderzhinova, D. V. Tarasova, F.K. Chibirova, Aging of titania hydrosols prepared via ultrasonic processing, Inorg. Mater. 52 (2016) 470–475. https://doi.org/10.1134/S0020168516050162.

[283] S. Singh, T. Shi, R. Duffin, C. Albrecht, D. van Berlo, D. Höhr, B. Fubini, G. Martra, I. Fenoglio, P.J.A. Borm, R.P.F. Schins, Endocytosis, oxidative stress and IL-8 expression in human lung epithelial cells upon treatment with fine and ultrafine TiO_2: Role of the specific surface area and of surface methylation of the particles, Toxicol. Appl. Pharmacol. 222 (2007) 141–151. https://doi.org/10.1016/j.taap.2007.05.001.

[284] C. Jacobs, R.H. Müller, Production and characterization of a budesonide nanosuspension for pulmonary administration, Pharm. Res. 19 (2002) 189–194. https://doi.org/10.1023/A:1014276917363.

[285] S. Bhattacharjee, DLS and zeta potential - What they are and what they are not? J. Control. Release. 235 (2016) 337–351. https://doi.org/10.1016/j.jconrel.2016.06.017.

[286] G. Oskam, A. Nellore, R.L. Penn, P.C. Searson, The growth kinetics of TiO_2 nanoparticles from titanium(IV) alkoxide at high water/titanium ratio, J. Phys. Chem. B. 107 (2003) 1734–1738. https://doi.org/10.1021/jp021237f.

[287] O.B. Pavlova-Verevkina, N. V. Kul'kova, E.D. Politova, Y.A. Shevchuk, V. V. Nazarov, Preparation of thermostable highly dispersed titanium dioxide from stable hydrosols, Colloid J. Russ. Acad. Sci. Kolloidn. Zhurnal. 65 (2003) 226–229. https://doi.org/10.1023/A:1023329527799.

[288] D.H. Everett, Manual of Symbols and Terminology for Physicochemical Quantities and Units, Appendix II: Definitions, Terminology and Symbols in Colloid and Surface Chemistry, Pure Appl. Chem. 31 (1972) 577–638. https://doi.org/10.1351/pac197231040577.

[289] Y. Luo, S.H. Li, K.M. Klima, H.J.H. Brouwers, Q. Yu, Degradation mechanism of hybrid fly ash/slag based geopolymers exposed to elevated temperatures, Cem. Concr. Res. 151 (2022) 106649. https://doi.org/10.1016/j.cemconres.2021.106649.

[290] S. Mukherjee, G. Kalra, S.C. Bhatla, Atmospheric nitrogen oxides (NO_x), hydrogen sulphide (H_2S) and carbon monoxide (CO): Boon or Bane for plant metabolism and development? Environ. Pollut. 367 (2025) 125676. https://doi.org/10.1016/j.envpol.2025.125676.

[291] S. Elkaee, A.D. Phule, J.H. Yang, Advancements in (SCR) technologies for NO_x reduction: A comprehensive review of reducing agents, Process Saf. Environ. Prot. 184 (2024) 854–880. https://doi.org/10.1016/j.psep.2024.02.046.

[292] A.A. Abdelaziz, A. Komuro, Y. Teramoto, M. Schiorlin, D.Y. Kim, T. Nozaki, H.H. Kim, Atmospheric-pressure plasmas for NO_x production: Short review on current status, Curr. Opin. Green Sustain. Chem. 50 (2024) 100977. https://doi.org/10.1016/j.cogsc.2024.100977.

[293] X. Zhou, J. Xie, R. Zhang, M. Ma, X. Li, P. Gong, Recent advances in different catalysts for synergistic removal of NO_x and VOCs: A minor review, J. Environ. Chem. Eng. 12 (2024) 111764. https://doi.org/10.1016/j.jece.2023.111764.

[294] J. Xu, H. Yang, Z. Yang, M. Huang, Y. Zhang, C. Yang, The effect of TiO_2@CoAl-LDH nanosphere on early hydration of cement and its photocatalytic depollution performance under UV–visible light, Constr. Build. Mater. 319 (2022) 126227. https://doi.org/10.1016/j.conbuildmat.2021.126227.

[295] S. Khannyra, M.J. Mosquera, M. Addou, M.L.A. Gil, Cu-TiO_2/SiO_2 photocatalysts for concrete-based building materials: Self-cleaning and air de-pollution performance, Constr. Build. Mater. 313 (2021) 125419. https://doi.org/10.1016/j.conbuildmat.2021.125419.

[296] M. Pérez-Nicolás, I. Navarro-Blasco, J.M. Fernández, J.I. Alvarez, Atmospheric NO_x removal: Study of cement mortars with iron- and vanadium-doped TiO_2 as visible light–sensitive photocatalysts, 2017. https://doi.org/10.1016/j.conbuildmat.2017.05.132.

[297] S. Lorencik, Q.L. Yu, H.J.H. Brouwers, Photocatalytic coating for indoor air purification: Synergetic effect of photocatalyst dosage and silica modification, Chem. Eng. J. 306 (2016) 942–952. https://doi.org/10.1016/j.cej.2016.07.093.

[298] S. Lorencik, Q.L. Yu, H.J.H. Brouwers, Design and performance evaluation of the functional coating for air purification under indoor conditions, Appl. Catal. B Environ. 168–169 (2015) 77–86. https://doi.org/10.1016/j.apcatb.2014.12.012.

[299] Thomas W. Patapoff, David E. Overcashier, Importance of Freezing on Lyophilization Development, BioPharm. (2002).

[300] J.C. Kasper, W. Friess, The freezing step in lyophilization: Physico-chemical fundamentals, freezing methods and consequences on process performance and quality attributes of biopharmaceuticals, Eur. J. Pharm. Biopharm. 78 (2011) 248–263. https://doi.org/10.1016/j.ejpb.2011.03.010.

Abbreviations

AFt	Alumina, ferric oxide, trisulpate
BET	Brunauer, Emmett and Teller
BJH	Barrett-Joyner-Halenda
CH	Calcium hydroxide
C_2S	Dicalcium silicate
C_3S	Tricalcium silicate
C-S-H	Calcium silicate hydrate
EDX	Energy-dispersive X-ray spectroscopy
FTIR	Fourier-transform infrared spectroscopy
LOI	Loss on ignition
SEM	Scanning Electron Microscope
SEM-EDS	Scanning Electron Microscope Energy Dispersive Spectrometer
TGA	Thermal gravimetric analysis
V	Volume
v/v %	Volume fraction
w/w %	Weight fraction
W/C	Water to cement ratio
XRD	X-ray diffraction
XRF	X-ray fluorescence

Appendix I
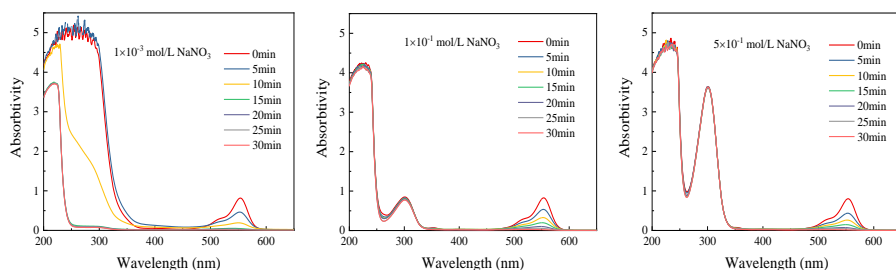
Fig. A-1 Absorption spectra of RB during UV degradation in NaNO$_3$ solution with TiO$_2$ hydrosols.
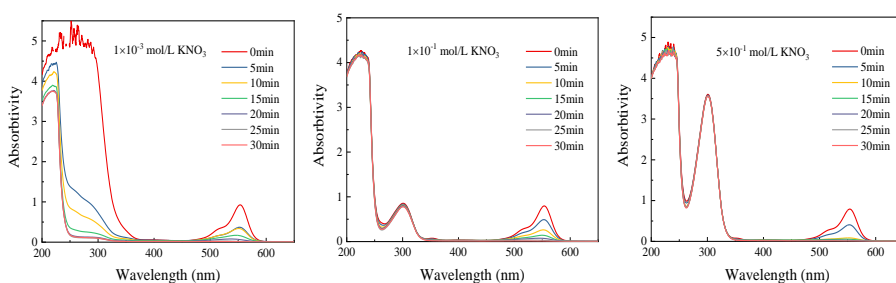
Fig. A-2 Absorption spectra of RB during UV degradation in KNO$_3$ solution with TiO$_2$ hydrosols.
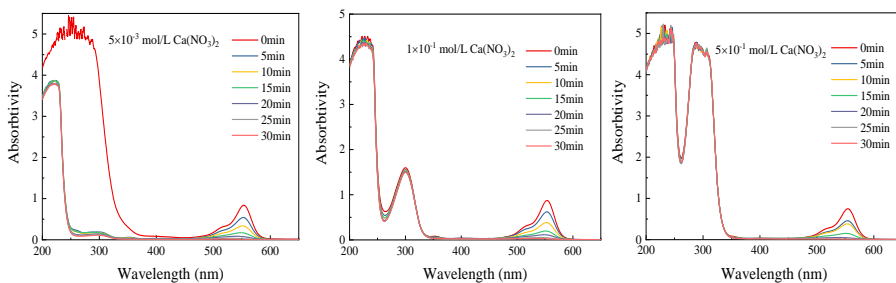
Fig. A-3 Absorption spectra of RB during UV degradation in Ca(NO$_3$)$_2$ solution with TiO$_2$ hydrosols.
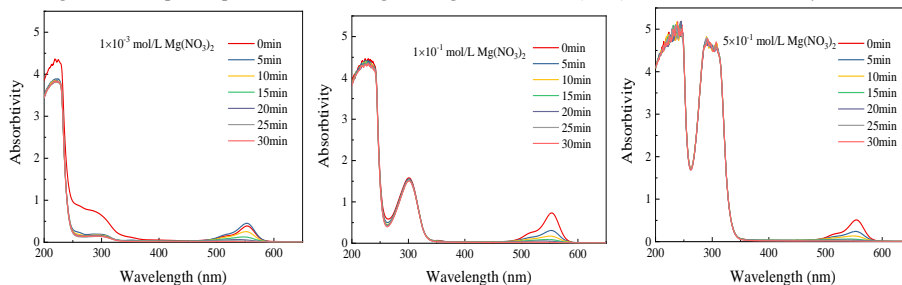
Fig. A-4 Absorption spectra of RB during UV degradation in Mg(NO$_3$)$_2$ solution with TiO$_2$ hydrosols.
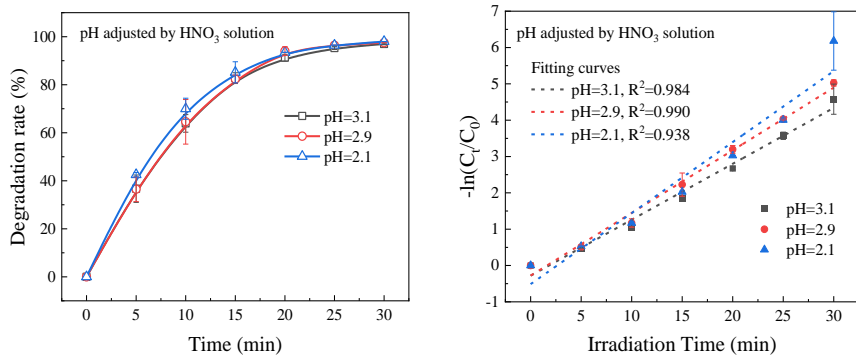
Fig. A-5 Kinetic analysis of RB degradation and reaction rates in solutions with different pH regulated by HNO_3 (R^2 value is the correlation coefficient).

Appendix II

(a) Blank sample

(b) sample with 0.01w/w %TiO₂

(c) sample with 0.05w/w %TiO₂

(d) sample with 0.10w/w %TiO₂
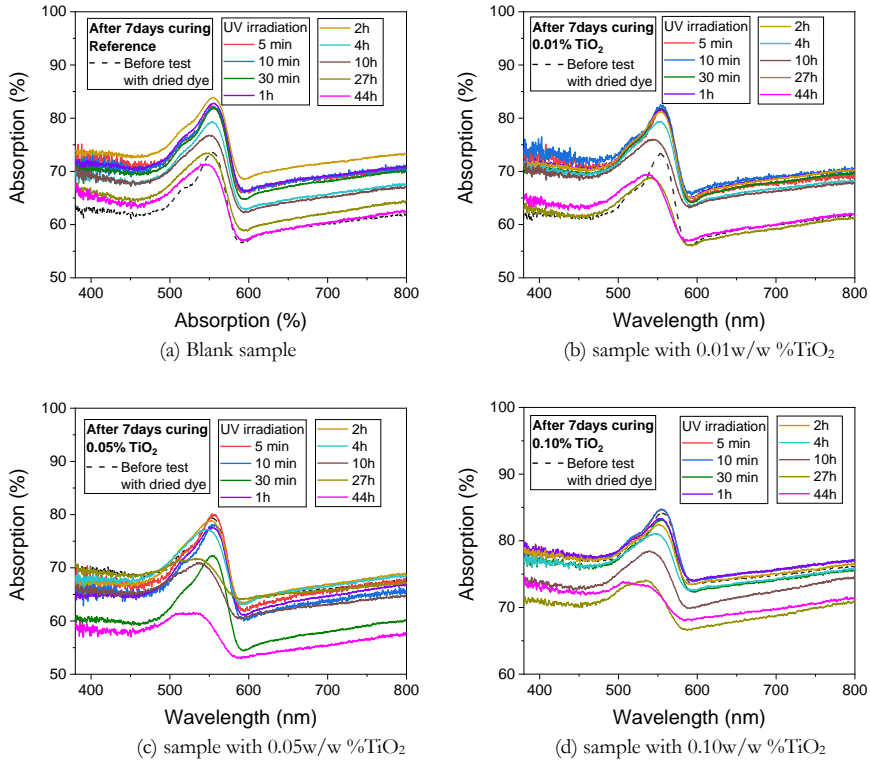
Fig. B-1 Absorption spectra of hardened samples with different dosages of nano TiO₂ hydrosols at 7-day-age.

(a) Blank sample

(b) sample with 0.01w/w %TiO₂
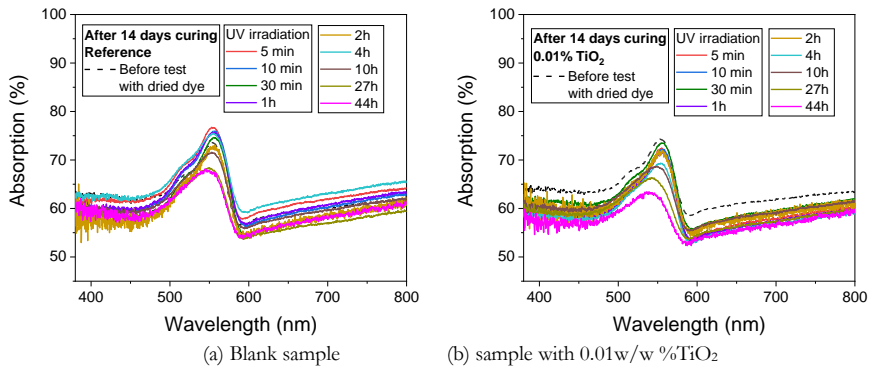
Fig. B-2 Absorption spectra of hardened samples with different dosages of nano TiO₂ hydrosols at 14-day-age.

(c) sample with 0.05w/w %TiO₂   (d) sample with 0.10w/w %TiO₂

Fig. B-2 continued.

(a) Blank sample   (b) sample with 0.01w/w %TiO₂

(c) sample with 0.05w/w %TiO₂   (d) sample with 0.10w/w %TiO₂
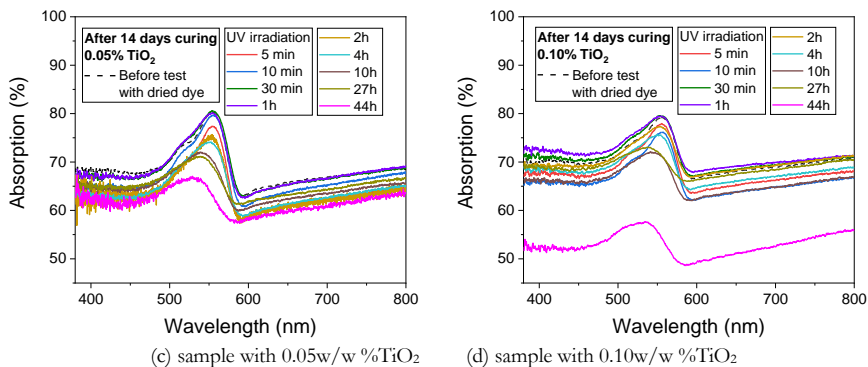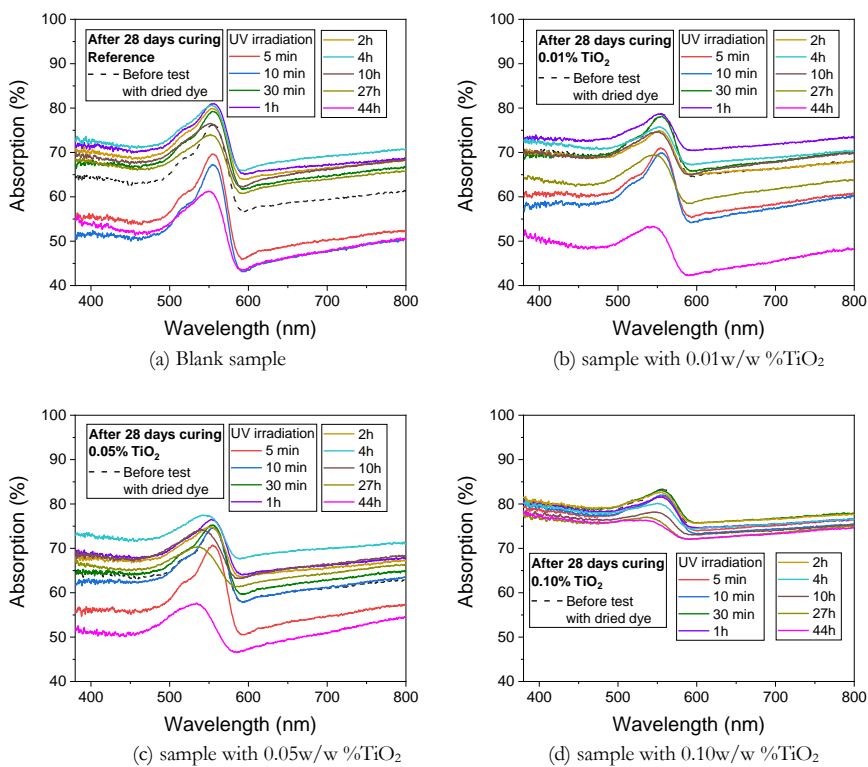
Fig. B-3 Absorption spectra of hardened samples with different dosages of nano TiO₂ hydrosols at 28-day-age.
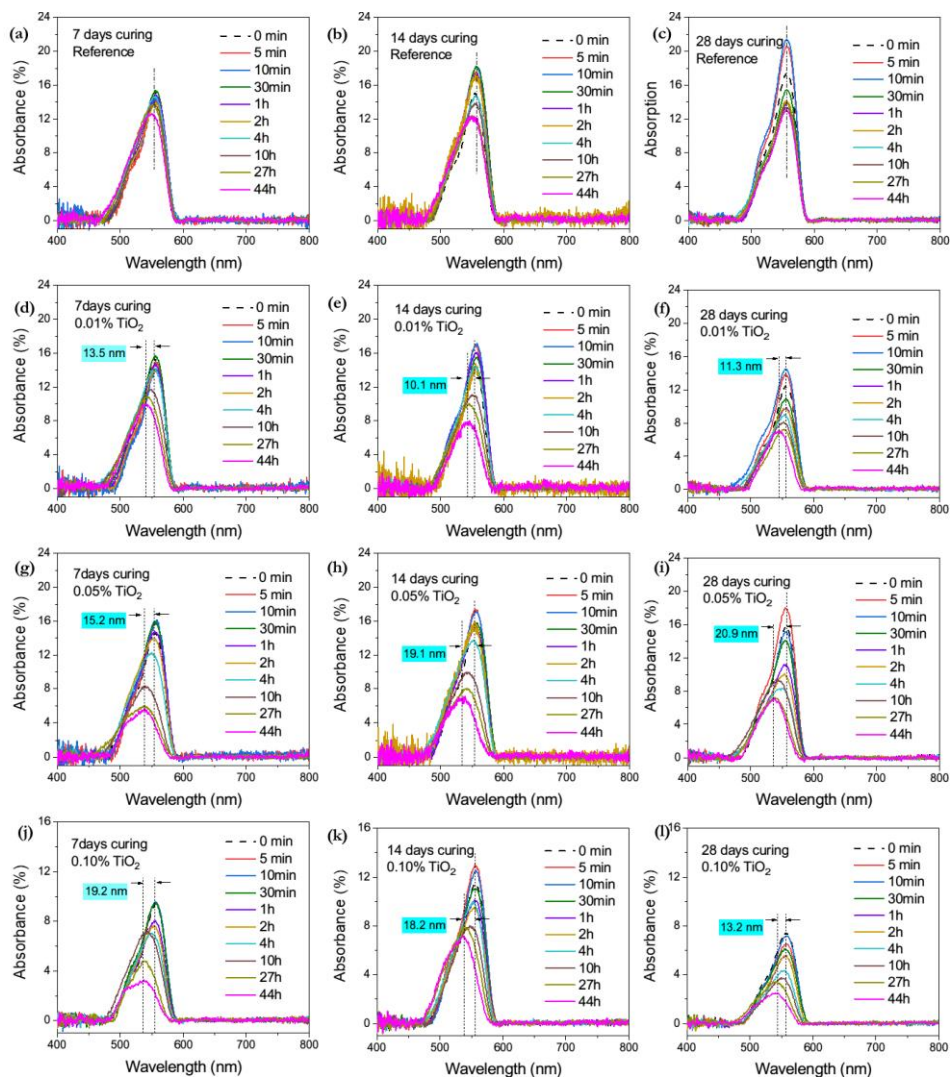
Fig. B-4 The absorbance spectra curves with the baseline removed of HPCP at different curing age under UV ir-radiation during UV irradiation.

(a, b, c) are spectra of the HPCP without TiO_2 tested at 7, 14, and 28 days; (d, e, f) are spectra of the HPCP with 0.01 % TiO_2 tested at 7, 14, and 28 days; (g, h, i) are spectra of the HPCP with 0.05 % TiO_2 tested at 7, 14, and 28 days; (j, k, l) are spectra of the HPCP with 0.05 % TiO_2 tested at 7, 14, and 28 days.

Table B-1 Visual images of HPCP samples after 44 hours of UV irradiation.

TiO₂: cement ratio	Age	0:1	0.01 %:1	0.05 %:1	0.10 %:1
After 44 hours of UV irradiation	7 d				
	14d				
	28d				

Appendix III
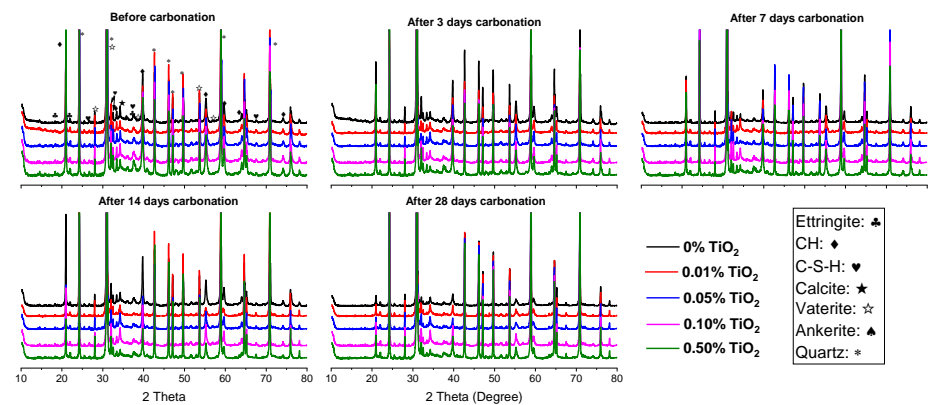
Fig. C-1 XRD pattern of mortar sample before and after accelerating carbonation test.

(a) Before carbonation

(b) After three days carbonation

(c) After seven days carbonation

(d) After 14 days carbonation

(e) After 28 days carbonation tests
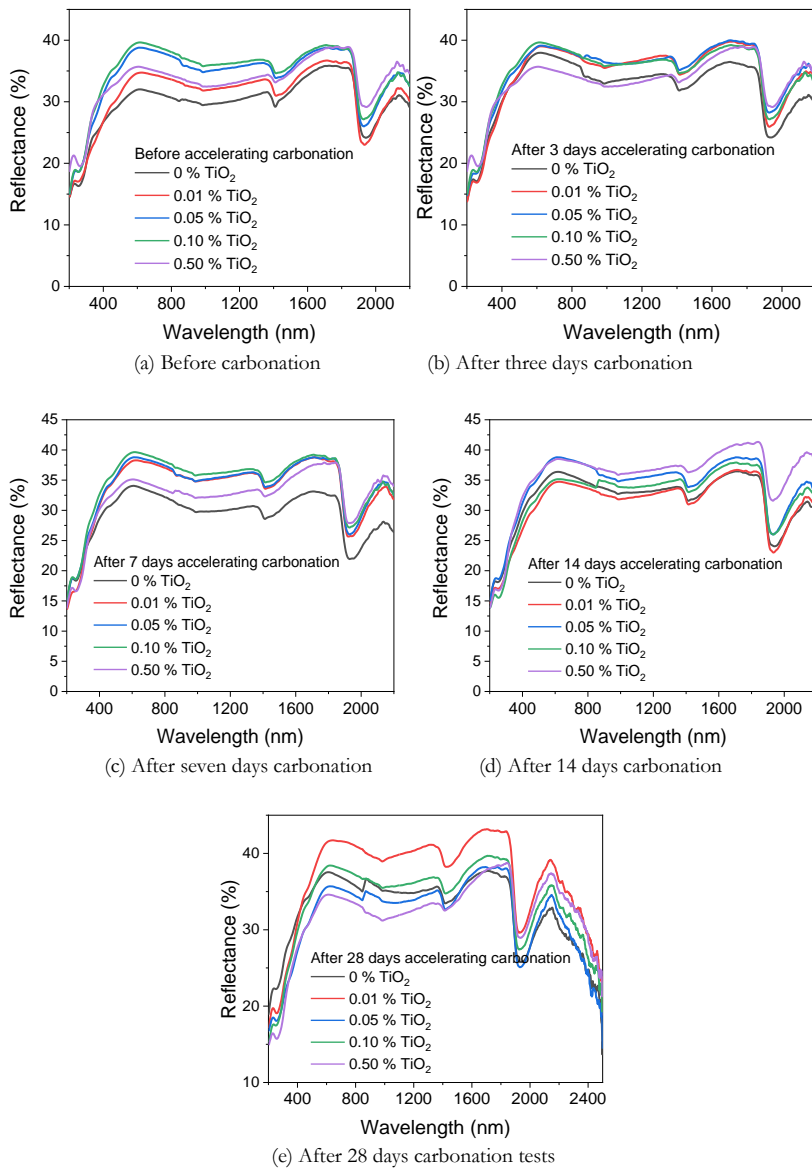
Fig. C-2 Reflectance of mortar with different TiO_2 hydrosols before and after carbonation.
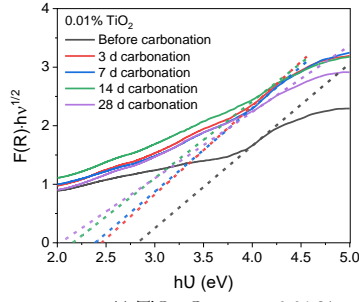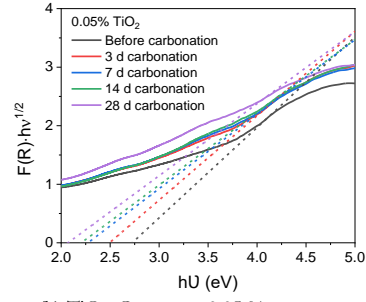
(a) TiO₂: Cement = 0.01 % (b) TiO₂: Cement = 0.05 %
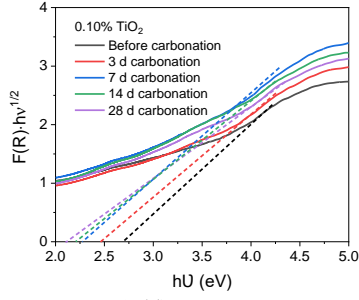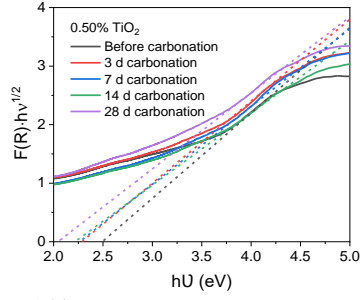
(c) TiO₂: Cement = 0.10 % (d) TiO₂: Cement = 0.50 %

Fig. C-3 Tauc's plots of the TiO₂-mortar samples before and after carbonation.
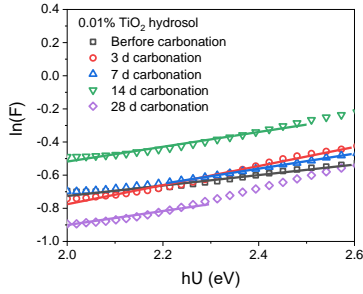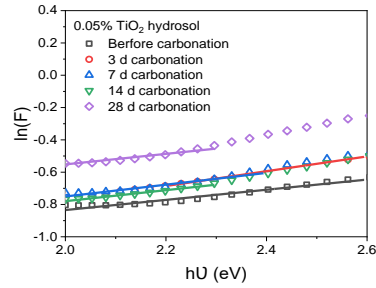
(a) TiO₂: Cement = 0.01 % (b) TiO₂: Cement = 0.05 %
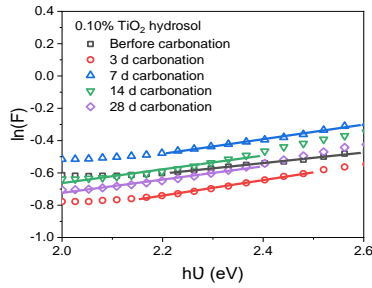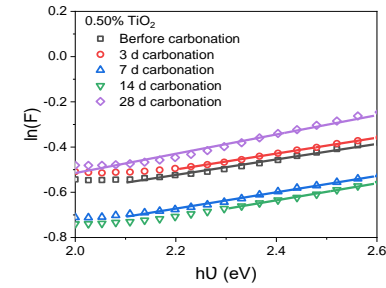
(c) TiO₂: Cement = 0.10 % (d) TiO₂: Cement = 0.50 %

Fig. C-4 Urbach energy of TiO₂- mortar samples before and after carbonation.

(a) TiO$_2$: Cement = 0

(b) TiO$_2$: Cement = 0.01 %

(c) TiO$_2$: Cement = 0.05 %

(d) TiO$_2$: Cement = 0.10 %

(d) TiO$_2$: Cement = 0.50 %
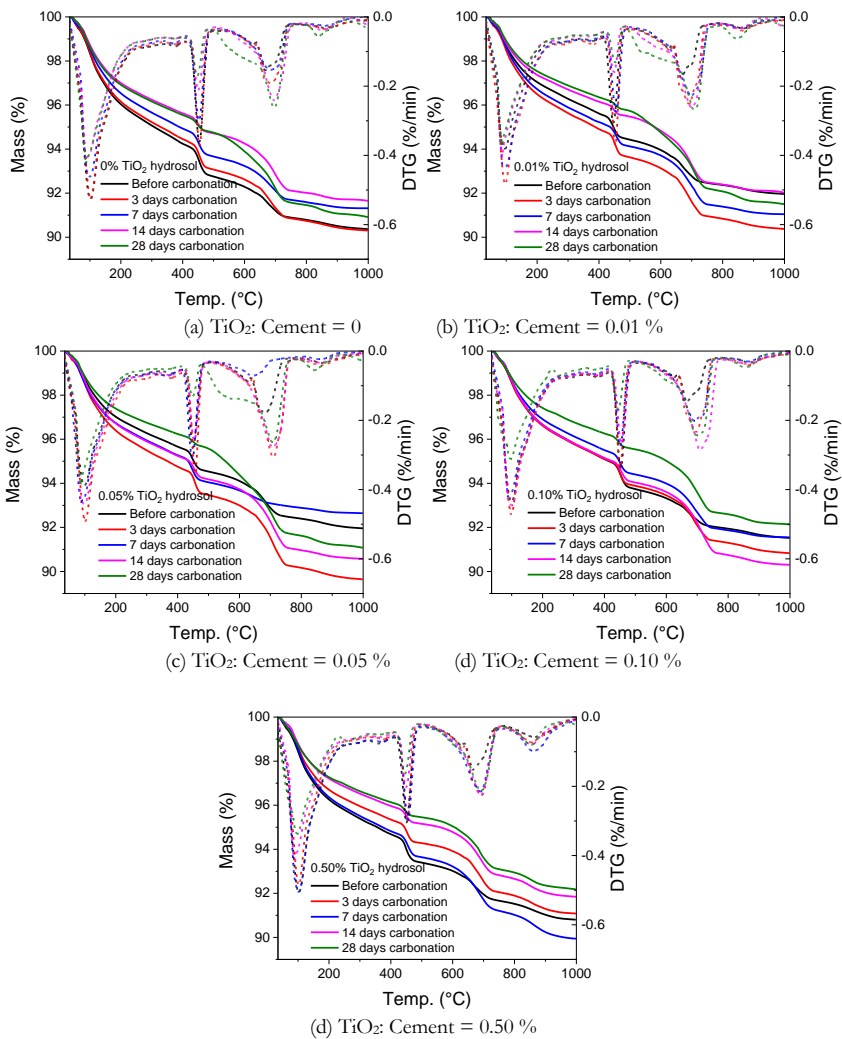
Fig. C-5 Mass loss and rate of TiO$_2$ hydrosols modified mortar.
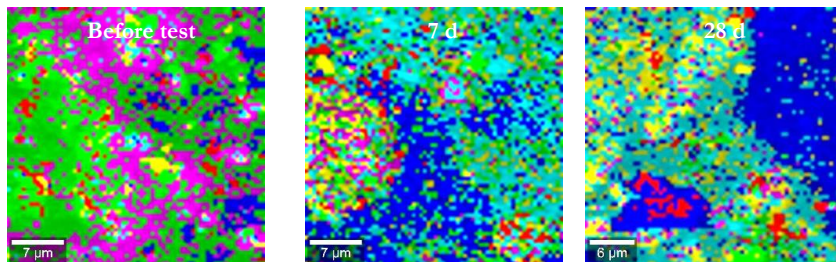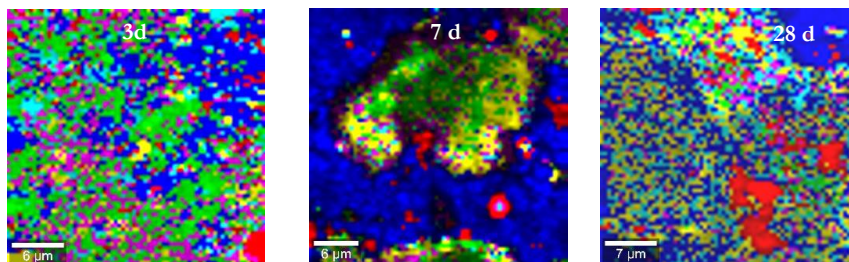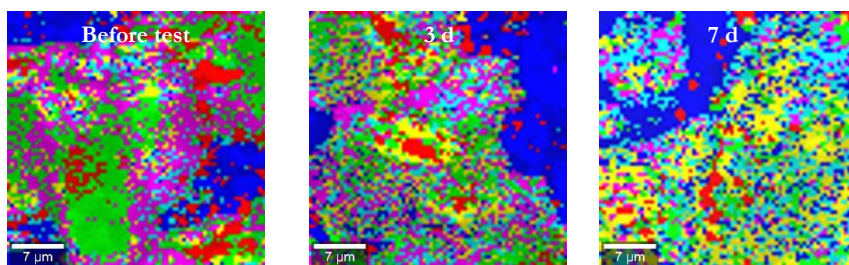
Fig. C-6 Raman images by CRM of the evolution of the presence of the main phase in the mortar containing TiO_2 at different accelerating carbonation duratioons (the scan area is 70 μm×70 μm).

* p<=0.05 ** p<=0.01 *** p<=0.001
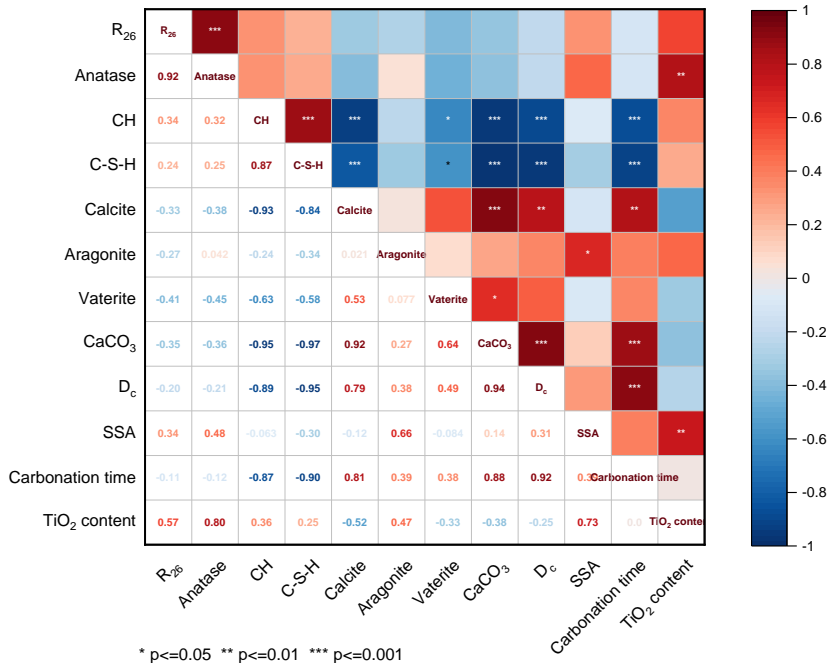
Fig. C-7 Correlation matrix of the factors related to the photocatalytic self-cleaning performance considering the influences of SSA.

* p<=0.05 ** p<=0.01 *** p<=0.001
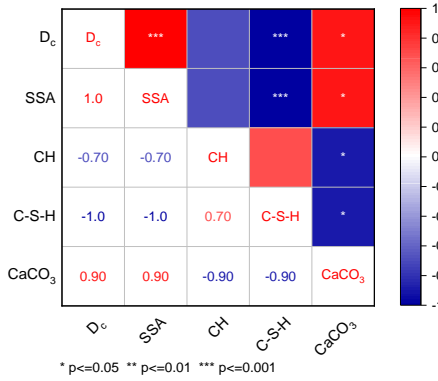
Fig. C-8 Correlation matrix of the factors related to the carbonation degree of mortar (D_c).
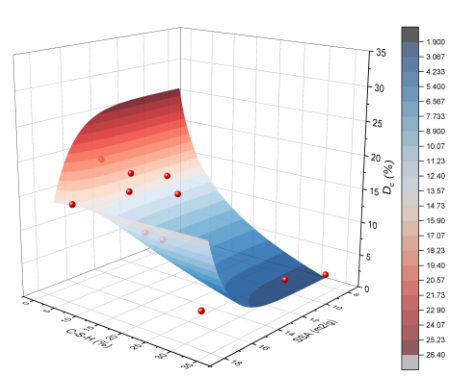
Fig. C-9 Simulating surface among D_c, C-S-H area ratios and SSA.

$$D_c = -1520.11 + 2.4 \times 10^{-13} * x^{12.62} + 1532.44 * y^{-0.005} - 2.43 * 10^{-13} * x^{12.62} y^{-0.005}$$
$$R^2 = 0.972 \quad (S1)$$

192

Appendix IV

(A) TiO$_2$: cement = 0.01 %

(B) TiO$_2$: cement = 0.05 %

(C) TiO$_2$: cement = 0.10 %

(D) TiO$_2$: cement = 0.50 %

(E) TiO$_2$: cement = 0
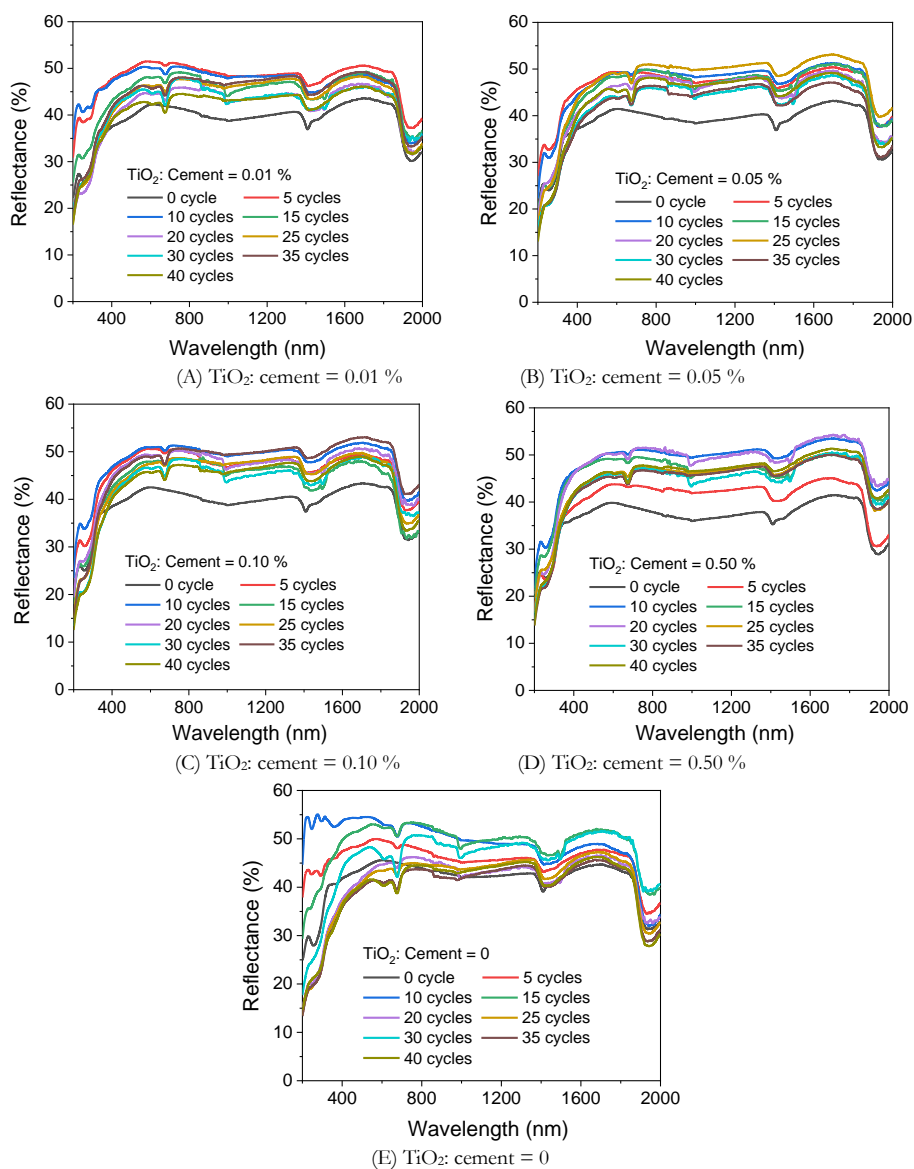
Fig. D-1 UV-VIS-NIR reflection spectra of nano-TiO$_2$ hydrosols modified mortar after different wetting and dry-ing cycles in pure water.
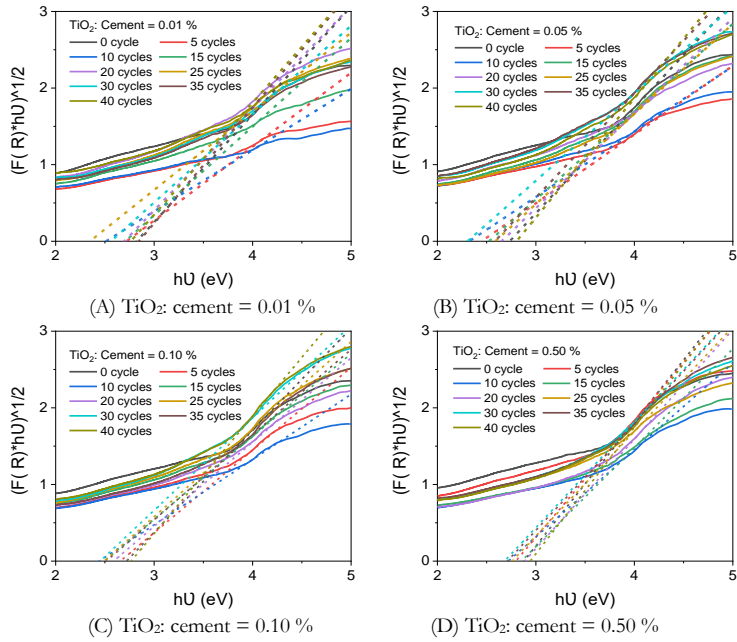
Fig. D-2 T$_{auc}$ curves of nano-TiO$_2$ hydrosols modified mortar after different wetting and drying cycles.
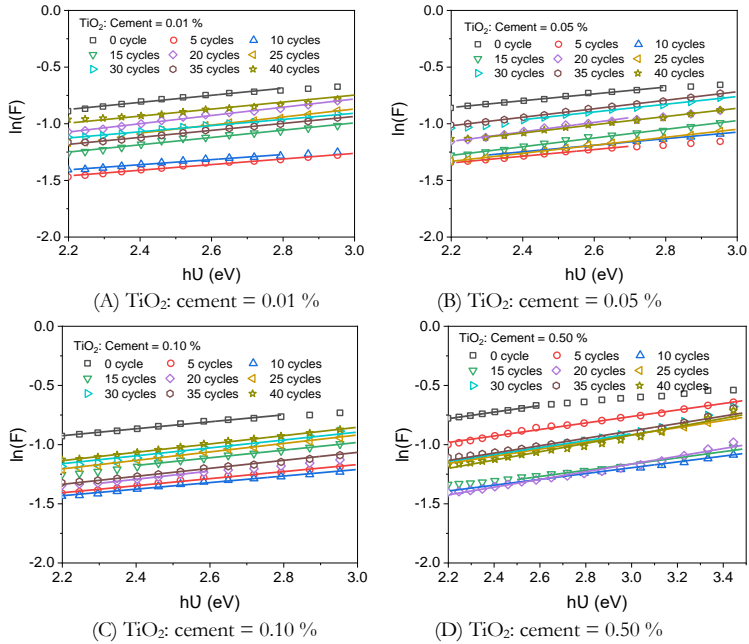
Fig. D-3 Urbach energy calculations of nano-TiO$_2$ hydrosols modified mortar after wetting and drying cycles.
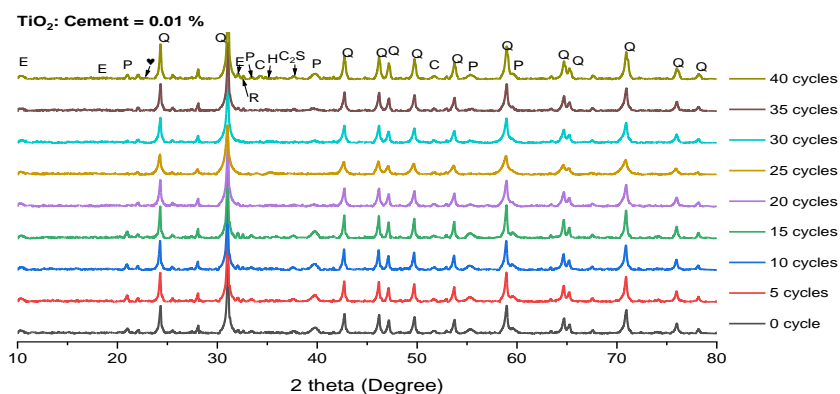
(A) TiO₂: cement = 0.01 %
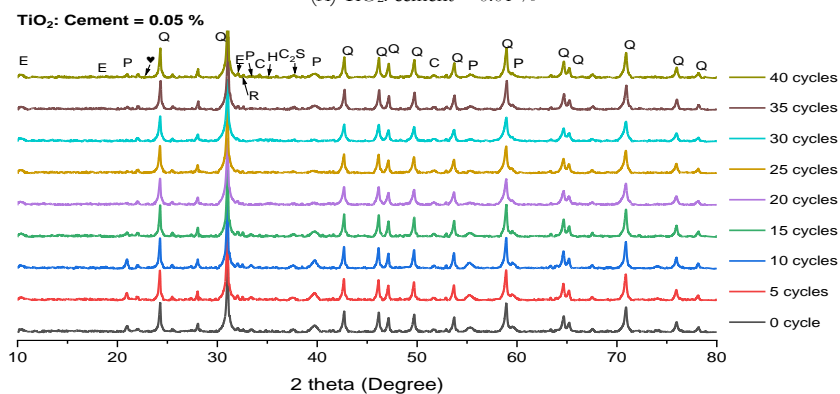
(B) TiO₂: cement = 0.05 %
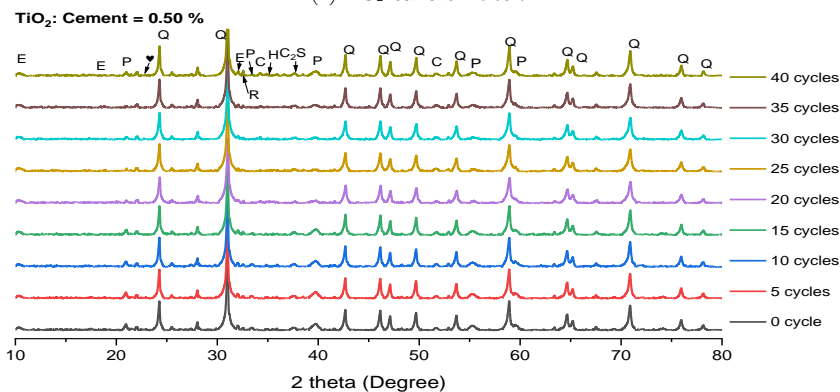
(C) TiO₂: cement = 0.50 %

Fig. D-4 XRD spectra of nano-TiO₂ hydrosols modified mortar after different wetting and drying cycles in pure water.

(A) TiO₂: cement = 0

(B) TiO₂: cement = 0.01 %

(C) TiO₂: cement = 0.05 %

(D) TiO₂: cement = 0.10 %

(E) TiO₂: cement = 0.50 %
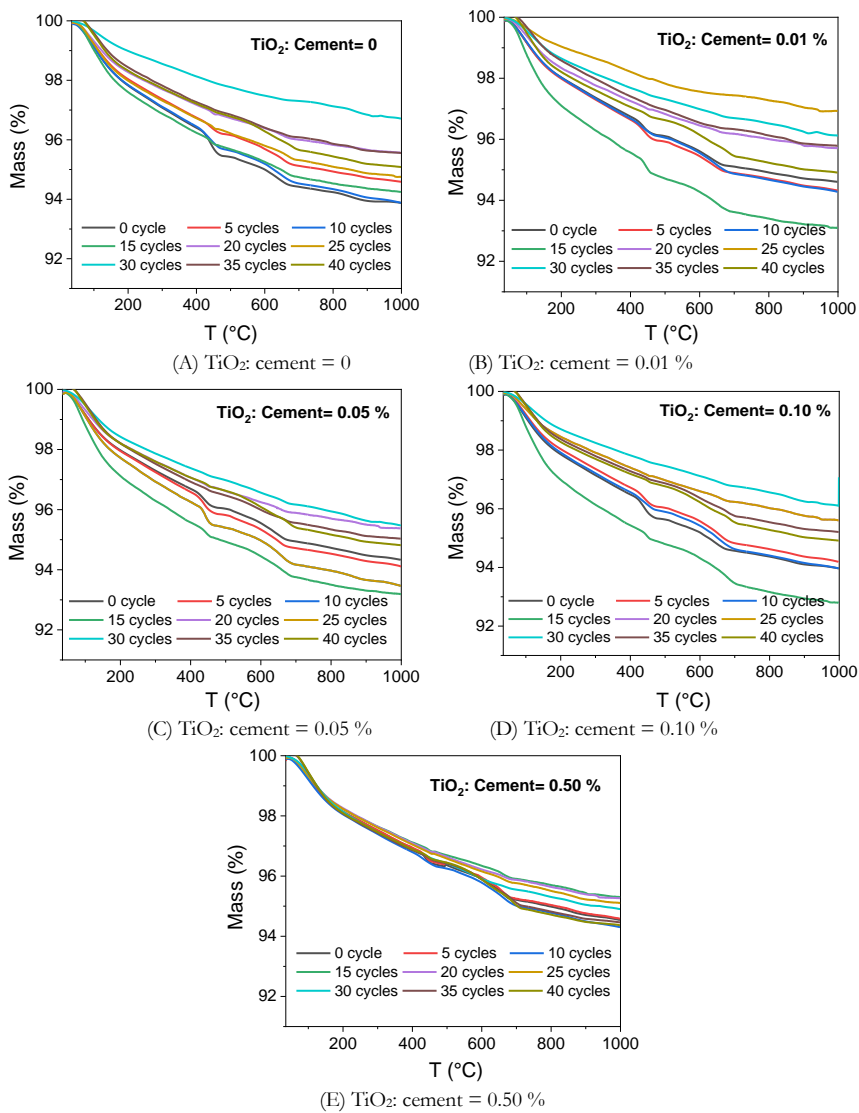
Fig. D-5 TGA curves of nano-TiO₂ hydrosols modified mortar after different wetting and drying cycles in pure water.

List of publications

Peer-reviewed journal papers

1. **Z. Wang**, Q. Yu*, P. Feng*, H.J.H. Brouwers, Variation of self-cleaning performance of nano TiO_2 modified mortar caused by carbonation: From hydrates to carbonates, Cem. Concr. Res. 158 (2022) 106852. doi:10.1016/j.cemconres.2022.106852.

2. **Z. Wang**, Q. Yu*, F. Gauvin, P. Feng*, Q. Ran, H.J.H. Brouwers, Nano-dispersed TiO_2 hydrosols modified Portland cement paste: The underlying role of hydration on self-cleaning mechanisms, Cem. Concr. Res. 136 (2020). doi:10.1016/j.cemconres.2020.106156.

3. **Z. Wang**, F. Gauvin, P. Feng*, H.J.H. Brouwers, Q. Yu*, Self-cleaning and air purification performance of Portland cement paste with low dosages of nano-dispersed TiO_2 coatings, Constr. Build. Mater. 263 (2020) 120558. doi:10.1016/j.conbuildmat.2020.120558.

4. **Z. Wang**, P. Feng*, H. Chen, Q. Yu*, Photocatalytic performance and dispersion stability of nano-dispersed TiO_2 hydrosols in electrolyte solutions with different cations, J. Environ. Sci. 88 (2020) 59–71. doi:10.1016/j.jes.2019.07.013.

5. **Z. Wang**, H. Zhang, Z. Wang, Q. Yu*, Rheological and mechanical performances of ultralightweight expanded polystyrene concrete: Synergistic effect of accelerator and multiscale fibers, Constr. Build. Mater. 476 (2025) 141265. https://doi.org/10.1016/j.conbuildmat.2025.141265.

6. **Z. Wang**, Q. Yu*, H.J.H. Brouwers, Self-cleaning performance reactivation of nano TiO_2 hydrosols modified photocatalytic mortar during wetting and drying cycles in pure water (in preparation).

7. **Z. Wang**, Q. Yu*, H.J.H. Brouwers, Early age and hardened properties of CNF-TiO_2 hydrosols modified visible-light photocatalytic concrete (in preparation).

8. **Z. Wang**, Q. Yu*, H.J.H. Brouwers, Performances enhancement of CNF-TiO_2 hydrosols modified photocatalytic concrete with designed directional porous channels (in preparation).

9. Q. Yu, X. Liu, **Z. Wang***, S. Wei, H. Gao, C. Lei, Effects of hybrid carbon and steel fibres on self-sensing and electromagnetic wave absorbing properties of concrete, Constr. Build. Mater. 460 (2025) 139848. https://doi.org/10.1016/j.conbuildmat.2024.139848.

10. M. Wu, **Z. Wang**, Y. Chen, M. Zhu, Q. Yu*, Effect of steel slag on rheological and mechanical properties of sulfoaluminate cement-based sustainable 3D printing concrete, J. Build. Eng. 98 (2024) 111345. https://doi.org/10.1016/j.jobe.2024.111345.

11. Z. Liu, W. Zhang, D. Zhang, J. Ouyang, **Z. Wang***, Y. Chen, Case Studies in Construction

Materials Case Study A review of penetrating corrosion inhibitors (PCIs): Molecular and compositions design, transport performance, anti-corrosion mechanisms , and long-term performance evaluation in engineering application, Case Stud. Constr. Mater. 21 (2024) e04031. https://doi.org/10.1016/j.cscm.2024.e04031.

12. Q. Deng, **Z. Wang**, S. Li, Q. Yu*, Salt scaling resistance of pre-cracked ultra-high performance concrete with the coupling of salt freeze-thaw and wet-dry cycles, Cem. Concr. Compos. 146 (2024) 105396. https://doi.org/10.1016/j.cemconcomp.2023.105396.

13.   Y. Chen, S. Li, Z. Liu, **Z. Wang***, Anticorrosion property of alcohol amine modified phosphoric and tannic acid based rust converter and its waterborne polymer-based paint for carbon steel, Coatings. 11 (2021). https://doi.org/10.3390/coatings11091091.

14.   M. Li, Z. Liu, Z. Yang, **Z. Wang***, H. Yuan, Bond-slip behaviors between reinforced concrete and coated rebar via a new strain monitoring method and FEA simulation, Constr. Build. Mater. 262 (2020). https://doi.org/10.1016/j.conbuildmat.2020.120402.

15. Z. Liu*, L. Bu, **Z. Wang**, G. Hu, Durability and microstructure of steam cured and autoclaved PHC pipe piles, Constr. Build. Mater. 209 (2019) 679–689. https://doi.org/10.1016/j.conbuildmat.2019.03.166.

Curriculum vitae

Zixiao Wang was born on April 16, 1991, in Nanyang, China. In September 2008, she started her Bachelor's study at Nanjing University of Science and Technology in Nanjing, majoring in Civil Engineering and received her Bachelor degree in June 2012. In September 2013, she started her Master's study at Yantai University supervised by Prof. Zhiyong Liu, majoring in Structural Engineering and received her Master degree in June 2016. She Master's project focused on the design of migrating corrosion inhibitors for reinforcements in buildings. In September 2016, she returned to Nanjing and began her PhD study under the supervision of Prof. Changwen Miao in Southeast University. In September 2018, she got a scholarship from China Scholarship Council (CSC) to support her PhD study at Eindhoven University of Technology (TU/e), Eindhoven, the Netherlands under the supervision of Prof. H.J.H. Brouwers and Dr. Q.L. Yu. Her PhD research interests include the performances enhancement of nano TiO_2-based photocatalytic cementitious materials.

Reeds verschenen in de serie
Bouwstenen

The façades of concrete buildings are continuously exposed to dust and organic matter in the living environment, which can compromise the aesthetic quality of the buildings. In particular, white facades of high-rise buildings are especially susceptible to such environmental influences. For example, the Nanjing Youth Olympic Center (completed in 2014), as depicted on the cover of this thesis, features white glass fiber-reinforced concrete (GRC) panels. Even though the silicon-containing coatings were used to protect these GRC panels, the facades have been stained and discoloured by moss over the past decade of service.

Using cement-based materials containing nano-photocatalysts as façade materials can mitigate air pollution near buildings and reduce dirt accumulation on facades, thereby lowering maintenance costs. This thesis aims to investigate the photocatalytic self-cleaning mechanisms of nano-dispersed TiO_2 hydrosols in Portland cement-based materials, as well as explore efficient methods for practical application. Firstly, the photocatalytic self-cleaning performances and mechanisms of nano-dispersed TiO_2 hydrosols in the positive ions water solutions and hardened cement paste are investigated. Secondly, the effects of environmental parameters, such as carbonation and wetting & drying cycles, on the photocatalytic self-cleaning performances of TiO_2 hydrosols-modified mortar are studied. Thirdly, the functional performance improvement methods of cement paste with directional micro-channels and cellulose nanofibrils (CNF)-modified nano TiO_2 hydrosols visible-light photocatalysts are discussed. The findings presented in this thesis can provide a promising guide to the application of photocatalytic cement-based materials.

DEPARTMENT OF THE BUILT ENVIRONMENT

TU/e **EINDHOVEN UNIVERSITY OF TECHNOLOGY**